

Deposition, Topographic and Spectroscopic Studies of Metal Nanoclusters on Photocatalytic Surfaces

By

Jesse Daughtry
BSc (Hons) Science (1st)

*Thesis
Submitted to Flinders University
for the degree of*

Doctor of Philosophy
College of Science and Engineering
18/10/2023

TABLE OF CONTENTS

TABLE OF CONTENTS	II
ABSTRACT	V
DECLARATION	VII
ACKNOWLEDGEMENTS	VIII
PUBLICATIONS	X
LIST OF ABBREVIATIONS	XI
LIST OF FIGURES	XII
LIST OF TABLES	XVII
1 INTRODUCTION	19
Solar Energy, Photocatalysis and Semi-conductors	19
Metal Clusters and Catalysis	22
1.1 Synthetic Methods and Approaches.....	24
1.1.1 Chemical Synthesis	24
1.1.2 Inverse Micelle and Micro-emulsion Synthesis.....	25
1.1.3 Chemical Reduction of Metal Salts in the presence of Stabilisers	27
1.1.4 'Magic Number' Clusters	29
1.1.5 Ligand-supported Synthesised' Magic Clusters'	31
1.2 Supported Catalysis and Nanocluster-Support Interaction	32
1.2.1 Nano-Structures for Catalysis	32
1.2.2 Clusters for Catalysis	33
1.2.3 Metal Oxides and Photocatalytic Surfaces for Catalysis.....	36
1.2.4 Au/TiO ₂ Heterogeneous Nanocluster Catalysis.....	39
1.3 Structural and electronic characterisation of clusters	41
1.3.1 Structural characterisation	41
1.3.2 Electronic Characterisation	44
1.4 Conclusion.....	48
1.5 Aims and Scope.....	49
2 EXPERIMENTAL METHODS	52
2.1 Electron Spectroscopy	52
2.1.1 Photoelectron Overview.....	52
2.1.2 Density of States and the Fermi Level	57
2.2 Surface Microscopy	62
2.2.1 Electron Microscopy Techniques	62
2.2.2 Scanning Probe & Atomic Force Microscopy	64
2.3 X-Ray Diffraction.....	66
3 COMPOSITION AND PROPERTIES OF RF-SPUTTER DEPOSITED TITANIUM DIOXIDE THIN FILMS	67
3.1 Abstract	68

3.2	Introduction:.....	68
3.3	Experimental Details.....	69
3.3.1	Preparation of TiO ₂ Thin Films.....	69
3.3.2	Spectroscopy.....	72
3.4	Results and Discussion.....	73
3.4.1	Chemical composition.....	73
3.4.2	Morphological Characterisations.....	80
3.4.3	Crystal Structure.....	85
3.5	Conclusions.....	87
4	SUB-MONOLAYER AU₉ NANOCUSTER FILM FORMATION VIA PULSED NOZZLE CLUSTER DEPOSITION.....	88
4.1	Abstract.....	89
4.2	Introduction:.....	89
4.2.1	Experimental Methodology.....	90
4.2.2	AFM.....	93
4.2.3	XPS.....	93
4.2.4	TEM.....	94
4.3	Results.....	94
4.3.1	Controlling and Optimising Deposition:.....	94
4.3.2	XPS results and analysis.....	97
4.3.3	AFM Results and Analysis.....	101
4.3.4	TEM Results and analysis.....	105
4.3.5	Solvent Removal – Effect of heating.....	107
4.4	Pulsed Nozzle Cluster Deposition Modelling.....	108
4.5	Conclusions.....	113
4.5.1	Acknowledgements.....	113
5	SPECTROSCOPIC COMPARISON OF ELECTRONIC STRUCTURE VIA GOLD METAL NANOCUSTER IMMERSION AND PULSE NOZZLE CLUSTER DEPOSITIONS ON DEFECT RICH TITANIA.....	114
5.1	Abstract.....	114
5.2	Introduction.....	114
5.3	Experimental Methodology.....	117
5.3.1	Chemically Synthesised, Atomically Precise NC Materials and Preparation.....	117
5.3.2	Substrate Selection, Surface Treatment and Deposition Techniques.....	118
5.3.3	X-Ray Photoelectron Spectroscopy (XPS).....	119
5.3.4	Metastable Impact Electron Spectroscopy (MIES) and Ultraviolet Photoelectron Spectroscopy (UPS).....	119
5.4	Results and Discussion.....	120
5.4.1	Carbon contamination from PNCD – Effect of heating.....	120
5.4.2	Surface Treatment and Elemental Composition of Immersion and PNCD deposited TiO ₂	122
5.4.3	Au ₉ NC De-Ligation and Agglomeration Effects.....	130

5.4.4	MIES/UPS analysis and XPS correlation	134
5.5	Conclusions	140
5.6	Acknowledgements.....	141
6	INVESTIGATIONS INTO THE ELECTRONIC STRUCTURE AND INTERACTION OF <i>IN-SITU</i> VACUUM-DEPOSITED AU AND RU METAL NANOCLUSTERS ON TiO₂.....	142
6.1	Introduction.....	142
6.2	Methods and Materials.....	143
6.2.1	Substrate Information.....	143
6.2.2	Vapour Pressure Deposition	144
6.2.3	Pulsed Nozzle Cluster Deposition.....	144
6.2.4	XPS, UPS and MIES Instrumentation	145
6.3	Results and Discussion.....	145
6.3.1	X-Ray Photoelectron Spectroscopy	145
6.3.2	MIES Results and Discussion	162
6.4	Conclusions	175
7	CONCLUSIONS	178
7.1	Composition and Properties of RF-Sputter Deposited Titanium Dioxide Thin Films	178
7.2	Sub-monolayer Au ₉ nanocluster film formation via pulsed nanocluster vapour deposition 179	
7.3	Spectroscopic Comparison of Electronic Structure through Gold Metal NC Immersion and Pulse Nozzle Cluster Depositions on Defect-Rich Titania.....	179
7.4	Chemical and electronic investigations into in-situ co-deposited chemically synthesised Au and Ru nanoclusters under vacuum conditions	180

ABSTRACT

Photocatalysis, the catalysis of chemical reactions using energy from solar photons, offers promising pathways to the production of fuel, chemical storage of solar energy and industrial catalysis. However photocatalytic materials such as TiO_2 require improvements to their properties and performance. The deposition of co-catalysts such as chemically-synthesised, atomically-precise nanoclusters, which have been shown to improve photocatalytic performance due to their size-specific properties and quantised energy levels, have been proposed as a pathway to improving performance and tuning the electronic structure of photocatalytic systems. To facilitate and improve the design of such systems, it is imperative to develop new methods to better characterise the physical and electronic surface interactions between metal nanoclusters and their photocatalytic supports. Ultra-high vacuum based spectroscopic techniques, offer extreme surface sensitivity, and are uniquely positioned for investigations into the surface interactions of nanoscale objects and their supporting surfaces.

Obtaining electronic information from nanocluster adorned photocatalytic surfaces has been a challenge without powerful, specialised equipment and delicate sample preparation techniques. These factors have meant that isolating the effects of deposited nanoclusters with respect to surface conditions has been difficult. The approach to improving investigations in such systems was three-fold. Firstly, an improved method of synthesising photocatalytic TiO_2 substrates for surface sensitive spectroscopies was required. Secondly, a deposition method which would allow for chemically-synthesised metal clusters to be deposited directly onto sample surfaces *in-situ* without causing the loss of surface treatments, or introducing unwanted species. Finally, the use of newly developed techniques was compared against legacy methods and used to investigate and isolate the electronic structure of nanoclusters, photocatalyst surfaces and the interactions between them using vacuum spectroscopy.

To build a complete picture of these methods and systems, a combination of scanning probe microscopy, electron microscopy, surface-sensitive spectroscopies and other methods were required. Topographical characterisation of surfaces and any deposited nanoclusters was achieved through a combination of atomic force microscopy, scanning electron microscopy and transmission electron microscopy, while material phase analysis was performed using x-ray diffraction methods. Elemental compositions and chemical states were investigated using x-ray photoelectron spectroscopy, which in turn informed the analysis of meta-stable ion electron spectroscopy and ultraviolet photon spectroscopy measurements which probe the electronic structure and density of states of these systems.

The development of a new method of nanoparticulate, amorphous TiO_2 thin film was achieved. These films were characterised and found to not only reduce undesirable chemical species, but

also enabled simple surface modification through sample heating introducing Ti^{3+} defects and transition to anatase and rutile crystallinity. A method for *in-situ* deposition of solvated chemically synthesised metal nanoclusters was developed, allowing for the controlled deposition of disperse sub-monolayer nanocluster films onto target samples under vacuum conditions. These photocatalyst and pulsed nanocluster deposition (PNCD) innovations were combined in a comparison of legacy deposition methods to PNCD samples with PNCD showing improvements in surface treatment retention, and improvements to XPS and MIES analysis of electronic DOS. Finally, the concept of an experimental system allowing the deposition of multiple chemically synthesised nanoclusters into vacuum was explored, showing inter-cluster and cluster-surface impacts on electronic DOS.

The developments presented in this thesis outline a complete system for the deposition and spectroscopic study of chemically synthesised metal nanoclusters onto photocatalytic TiO_2 surfaces. The results achieved offer pathways for the preparation, investigation, and analysis of the electronic structure and surface coverage for these photocatalytic systems, as well as pointing to the possibility for some techniques to find more general utility.

DECLARATION

I certify that this thesis:

1. does not incorporate without acknowledgment any material previously submitted for a degree or diploma in any university
2. and the research within will not be submitted for any other future degree or diploma without the permission of Flinders University; and
3. to the best of my knowledge and belief, does not contain any material previously published or written by another person except where due reference is made in the text.
4. was prepared without the use of professional editing services.

Signed.....JESSE DAUGHTRY.....

Date.....28/02/2023.....

ACKNOWLEDGEMENTS

This research is supported by an Australian Government Research Training Program (RTP) Scholarship.

I would first like to acknowledge my supervisor Professor Gunther Andersson, whose guidance, knowledge and patience have allowed me to complete a journey that began in the early years of undergraduate studies. The opportunities that Gunther presented welcoming me into his research group, setting me up with active research from my undergraduate years, through summer research scholarships, honours, international internships and finally, my PhD studies, kept me engaged and pushing forward in science. His calm, gracious and patient nature has been a constant, even when experiments are not going to plan, deadlines are fast approaching, and equipment is malfunctioning. Over my time under his supervision, I have come to appreciate how special his ability to push the boundaries of scientific inquiry and support a large group of students and researchers, all while juggling the many demands of modern academia, really is. I'm unsure how he does it some days, and I'm eternally grateful for his patience in helping me see this project to completion. Thank you, Gunther; you helped me see the bigger picture in science and life, and I only hope to pass that on to others where I can.

I'd also like to acknowledge the input and impact of Professor Greg Metha for his assistance, collaboration and advice on all things nanocluster and pulse nozzle related. Greg's advice in Japan and Adelaide often led to breakthroughs when I became stuck, and his editorial inputs have improved my writing to no end.

I also need to thank Professor Tomonobu Nakayama, 'Tomo' in Australia and Nakayama-Sensei in Japan, without whose gracious hosting of my research internship at NIMS-MANA large portions of my PhD wouldn't have been possible. Your advice, insight and experience were invaluable to my projects. Both in your generosity in sharing knowledge, and in sharing your love of your home country's amazing culture, I plan on revisiting Japan for years to come. The time, advice and rich ideas shared by my pseudo-supervisor Dr Adrian Diaz-Alvarez, who kept me sane and helped me stay the distance. I couldn't have done it without your help.

Thanks for everything to all my fellow students and collaborators during my time in the Andersson group, especially Hassan, Herri, Gowri, Liam, Abdul, Ben, Altaf, Amira and Chris. Your help in the lab and the office and your questions and advice were all valued. I hope that I managed to return the favour in some way.

I'd also especially thank Professor Jamie Quinton, who spearheaded the HAPS program at Flinders University. That program forged real researchers; your belief in your students, your open mind to their potential and the environment you created were truly special. To those early

classmates, especially Zoe, Tom, Joel, and Nathan, I can only hope I wasn't too much of a distraction.

This PhD would not have been possible without my family's love, support and understanding. Firstly my nana, Dr Anne Daughtry, who sat and watched Catalyst every week all those years ago with a little boy, nurturing in him a love of asking questions and seeking answers which persists to this day. My parents, Stephen and Vanessa Daughtry, twin spirits of love, support and understanding, have shown me the strength of faith and the power of creativity in the world. They sacrificed a lot to enable my opportunities and education, and words aren't enough to express my gratitude. You are both my heroes. To my siblings, Miranda and Liam, I'm sorry that pursuing my studies sometimes took me away from being there as a big brother for you, and I'm so grateful for the times we've had together; you're both so much cooler than I'll ever be. To my son Orlando, I was meant to have this all finished long before you were born, but I wouldn't change a thing about you or how you came to us, you are the light of our lives.

Finally, to my wife Laura, who has been there since the start and rode with me through the highs and the lows of life in the PhD, I can't thank you enough. Your love and constant support have been more than I deserved at times, and you have carried the load for both of us when I've been unable. You do nothing but impress me with how you conduct yourself and understand the world. You've taught me so much about living well and working hard at what matters, more than all my studies combined. We've walked this path through so much of our life together, and now we've reached its end, stronger, wiser, and so excited for what might come next. I love you

PUBLICATIONS

The following list contains all publications submitted during the authors PhD candidature which resulted from research presented within this thesis.

Book Chapters

Hudson, R., J. Daughtry, G. G. Andersson and G. F. Metha (2018). Deposition, Ligand Removal, and Applications of Atomically Precise, Chemically Synthesized Clusters on Metal Oxide Surfaces. *Encyclopedia of Interfacial Chemistry*. K. Wandelt. Oxford, Elsevier: 672-679.

Journal Articles

Daughtry, J., G. G. Andersson, G. F. Metha, S. Tesana and T. Nakayama (2020). "Sub-monolayer Au₉ cluster formation via pulsed nozzle cluster deposition." *Nanoscale Advances* **2**(9): 4051-4061.

Daughtry, J., A. S. Alotabi, L. Howard-Fabretto and G. G. Andersson (2021). "Composition and properties of RF-sputter deposited titanium dioxide thin films." *Nanoscale Advances* **3**(4): 1077-1086.

Oral Presentations

Daughtry, J. (2019, June). *Chemically Synthesized, Size Specific Metal Clusters on Surfaces for Photocatalysis* [Conference session] Flinders 8th Annual Nanoscale Conference, Adelaide, Australia

Poster Presentations

J. Daughtry, S. Krishana, T. Nakayama, G. Metha, V. Golovko, D. Lewis, G. Andersson (2020, February 9-13) *Pulsed Ultrasonic Vapour Deposition of Atomically Precise, Chemically Synthesized Metal Clusters in Vacuum* [Poster Presentation]. ICONN 2020, Brisbane Convention & Exhibition Centre, Brisbane, Australia

J Daughtry, G. G. Andersson, S. Hussain, V. B. Golovko, G. F. Metha (2016, February 7-11) *Characterisation of size-specific Au₉ nanoclusters on Titania Particles* [Poster Presentation]. ICONN 2016, National Convention Centre, Canberra, Australia

LIST OF ABBREVIATIONS

AD	Auger De-excitation
AFM	Atomic Force Microscopy
ALD	Atomic Layer Deposition
AN	Auger Neutralisation
CPS	Counts Per Second
CTAB	Cetrimonium Bromide
CVD	Chemical Vapour Deposition
DFT	Density Functional Theory
DOS	Density of States
EDX	Energy Dispersive X-ray
FWHM	Full Width Half Maximum
HAADF	High Angle Annular Dark Field
HBP	High Binding energy Peak
HCF	Hydrocarbon Fuels
HER	Hydrogen Evolution Reaction
HOMO	Highest Occupied Molecular Orbital
HOPG	Highly Oriented Pyrolytic Graphite
HPLC	High Purity Liquid Chromatography
HV	High Vacuum
IMFP	Inelastic Mean Free Path
IR	Infra-Red
LSPR	Localised Surface Plasmon Resonance
LUMO	Lowest Unoccupied Molecular Orbital
MBA	Mercaptobenzoic Acid
MIES	Meta-stable Ion Electron Spectroscopy
NC	Nanocluster
NIMS	National Institute for Materials Science (Japan)
NIST	National Institute of Standards and Technology (USA)
PNCD	Pulsed Nozzle Cluster Deposition
PVP	poly(N-vinyl-2-pyrrolidone)
RF	Radio Frequency
RI	Resonance Ionisation
SC	Single Crystal
SEM	Scanning Electron Microscopy
STEM	Scanning Transmission Electron Microscopy
STM	Scanning Tunnelling Microscopy
STS	Scanning Tunnelling Spectroscopy
SVD	Single Value Decomposition
TEM	Transmission Electron Microscopy
TPP	Tri Phenyl Phosphene
UHV	Ultra High Vacuum
UPS	Ultra-violet Photoelectron Spectroscopy
XAFS	X-ray Absorption Fine Structure
XPS	X-ray Photoelectron Spectroscopy
XRD	X-Ray Diffraction

LIST OF FIGURES

Figure 1-1 The production of solar Fuel hydrocarbons is proposed above. The system illustrates how this system would fit into existing energy production systems.....	20
Figure 1-2 Photocatalytic H ₂ production showing solar photons incident on TiO ₂ (yellow Sphere) and the excitation process. Attached metal clusters (green spheres) can improve catalytic performance as n-type electron sinks, reducing electron-hole recombination.....	21
Figure 1-3 Au ₉ (PPh ₃) ₈ nanocluster simulations, yellow atoms represent Au and the grey represent triphenylphospene (PPh ₃) ligands. Note the closed structure created by PPh ₃ orbitals in the right-most simulation, creating a steric hindrance for reactant species to reach the nanocluster core. Used with permission for the Andersson research group.	23
Figure 1-4 Cartoon representation of Au catalysts displaying a variety of observed surface and electronic features in Au nanoparticles and nanoclusters which lead to higher catalytic activity and tuneable properties [41].	24
Figure 1-5 Synthetic process for synthesising AU:PVP-n (n=1-10), a polymer-capped nanocluster species [50].....	28
Figure 1-6 Electronic properties of Au _n clusters by nanocluster size (a) Second difference of nanocluster energies $\Delta^2E(n)=E(n+1)+E(n-1)-2E(n)$; (b) HOMO-LUMO gap (eV) [1]	29
Figure 1-7 Diagram showing the size and sequence of "magic number" clusters. Note that increasing size corresponds to a reduced percentage of surface atoms correlating strongly with reduced catalytic performance.	30
Figure 1-8 A comparison between calculated electronic densities for Au nanocluster geometric isomers of clusters between 15-24 constituent atoms. Calculated spectra are seen in the top three traces in each section, and experimental photoelectron spectra denoted by <i>exp</i> prepared by Yoon et al[36]......	34
Figure 1-9 Schematic cross section of a metal co-catalyst before and after being covered with a Cr ₂ O ₃ shell. The reaction notation illustrates how such an arrangement can block photocatalytic back reactions involving O ₂ [128]	35
Figure 1-10 Simulated interactions between Au and a reduced 3x2 TiO ₂ surface with vacancy sites. The inset boxes represent a top view of the system, with O denoting an bridging oxygen site and v denoting a vacancy. Au binding to vacancies is presented for (a) single vacancy system, (b),(c) and (d): three arrangements of multi-vacancy systems [179].	40
Figure 1-11 High resolution, aberration corrected HAADF-STEM images of Au ₉ nanoclusters on TiO ₂ nanosheets alongside DFT models of the same nanocluster showing the variety of nanocluster geometric structures observable in experimental depositions [195].	43
Figure 1-12 Synchrotron XPS spectra of chemically synthesised, atomically precise Au ₈ , Au ₉ , Au ₁₁ and Au ₁₀₁ nanoclusters showing the distinct shifts in Au 4f peak binding energy with change in nanocluster size. The ~1.1 eV difference in binding energy observed for Au ₁₀₁ indicates the onset of metallic properties associated with Bulk Au at that nanocluster size [234]......	46
Figure 2-1 Diagram illustrating the excitation of core-level electrons through X-Ray illumination...	52
Figure 2-2 XPS scan trace recorded from a sample of TiO ₂ indicating the characteristic peak positions for Ti 2p, O 1s and C 1s orbitals.....	54
Figure 2-3 The changing conditions of the Fermi function within a semiconductor over a range of temperatures, not the small but noticeable probability for conduction band electrons in the third case (high temp.)	57
Figure 2-4 Representative diagrams of resonance ionisation and Auger neutralisation processes, modified from Harada et al.[245]	60
Figure 2-5 Schematic illustrating the process of Auger De-excitation (AD), the dominant process for He* neutralisation in this study, modified from [245].....	61

Figure 2-6 A simplified cartoon cross-section showing the similarities and differences between SEM and TEM experimental apparatus and lens and sample arrangements. Note the position of the sample and detector(s) in each technique.....	63
Figure 2-7 Diagram showing the basic principles of AFM measurement control. The movement or deflection of the tip and cantilever is recorded through a reflected laser source onto a photodiode sensor or similar. This signal is interpreted by computer analysis software, and signals to direct the cantilever in x, y, and z-planes are fed back to the scanning probe.....	65
Figure 3-1 XPS relative elemental composition comparison between the as-prepared and heated RF sputter samples.....	74
Figure 3-2: XPS high-resolution scan fitting for Vacuum Heated Ti 2p region showing As-made (left) and 500C heated (right) with Ti 3+ defect showing in the heated sample at around 457eV binding energy	76
Figure 3-3 UPS scans from a range of heated FT-RF samples and rutile (110) single crystal TiO ₂ showing broad range electronic structure on the left (series are offset in the y-axis) and the near-fermi valence band on the right.	79
Figure 3-4 SEM image of 90min-RF-As Made Sample, the arrow indicates TiO ₂ film thickness of approximately 153nm.....	80
Figure 3-5 High magnification SEM scans on RF-TiO ₂ after different heat treatments, clockwise from top left: As made, 300°C, 500°C, 700°C showing the transition from smaller, spherical particles on the film surface into aggregation and alignment into larger TiO ₂ grains	82
Figure 3-6 AFM scans on a) As-made, 1x1µm b) 500C Vacuum Heated, 1x1µm c) As-made, 3x3µm d) 500C Vacuum Heated, 3x3µm	83
Figure 3-7 SEM scans showing the morphological changes to FT-RF sputtered TiO ₂ films as they are heated, clockwise from top left, 500°C 1h, 600°C 1h, 900°C 1h, 1100°C 24h. The particle shown in the 500°C image was included to aid focussing of the measurement.	84
Figure 3-8 offset XRD scans on as-made and heated samples showing the transition from amorphous TiO ₂ towards anatase phase. Rutile phase formation was detected only within the 1100C heated sample. Anatase and Rutile main XRD peaks shown on the x-axis, in blue and orange respectively. XRD spectra shown are i) Si, ii) as-made RF-TiO ₂ , iii) as-made atomic layer deposition TiO ₂ , iv) 500°C atmosphere heated RF-TiO ₂ (1h), v) 600°C atmosphere heated RF-TiO ₂ (1h), vi) 900°C atmosphere heated RF-TiO ₂ (3h) and vii) 1100°C atmosphere heated RF-TiO ₂ (24h)	86
Figure 4-1 Representation of the PNCD system, mounted to a high vacuum load lock (cutaway). Au ₉ is loaded into the liquid reservoir and then backed with argon to 2 bar of pressure. The pulse nozzle control unit was operated with a programmed frequency to drive the opening/closing of the solenoid valve. Inside the vacuum chamber, a fabricated metal channel allows the pulsed vapour to reach the sample via line of sight while collecting the more dispersed vapour. The sample is held in a sample manipulator in the path of the vapour pulse and once deposited, can be inserted into the ultra-high vacuum for XPS measurement. AFM measurement requires removal to atmosphere.	91
Figure 4-2 AFM measurements displaying non-optimal regions from PNCD on mica surfaces, displaying droplet impacts (top left, 0.125mM Au ₉ /methanol, 30x pulses, 250µs, B4) mutli-layer coverages (top right, 0.125mM Au ₉ /methanol, 100x pulses, 250µs) and nanocluster aggregations (bottom, 0.04 mM Au ₉ /methanol, 10x pulses, 150µs)	95
Figure 4-3 (left) AFM scan on freshly cleaved mica, (right) AFM scan on mica after 50 pulses of methanol, some larger features are clipped out of scale range.	96
Figure 4-4 AFM scans of mica control images showing a methanol-only (no nanocluster) deposition (left) resulting in partial removal of the particles seen in fresh cleaved mica samples and some larger particles/residue (approx. 10-20 nm high) across the surface (right). This was only for the one sample presented and was attributed to sub-optimal deposition conditions.....	96

Figure 4-5 High resolution XPS scan at the Au 4f region. 2 distinct species are evident with gold cluster 4f _{7/2} Au peak at 85 eV while bulk Au peak can be seen at 84.2 eV showing that some cluster agglomeration has occurred.	98
Figure 4-6 Example XP spectra of sample B6 showing Au 4f region, with the characteristic nanocluster Au 4f _{7/2} peak at 85.2 eV.	98
Figure 4-7 Relative elemental concentration of Au ₉ clusters from XPS analysis across series A (concentration change) and series B (pulse number change). No trend is evident in series A, whereas series B shows a clear reduction in gold nanocluster conc. with lower pulse no. and, when normalised per pulse, reveals that the initial pulse deposits far more Au than subsequent pulses.	100
Figure 4-8 Top - A: 0.125mM Au ₉ /Methanol single pulse (sample B7) on mica. B: higher magnification scan of A C: High magnification scan on a single nanocluster-sized object found on the same sample. Particle height distribution for 5 μm ² scan of 0.125 mM from one pulse. Some larger particles are clipped out of scale range.	101
Figure 4-9 AFM scans of sample B6 (on mica) at different locations showing largely homogenous depositions of cluster sized particles with no droplet-like features. Bottom - Particle height distribution for 10 μm scan of sample B6 show the weighting of maximum and mean particle heights for each scan, with the distributions for both in agreement for large numbers of sub-nanometer (gold cluster sized) particles.	102
Figure 4-10 AFM scans of pulsed vapour deposited Au ₉ onto Mica. All scans were performed at the same location with top and bottom being 3μm ² and middle being 500nm ² . The blue frame indicates common scan regions. The top and bottom images are 3μm ² AFM scans taken before (top) and after (bottom) the central 500nm ² scan.	103
Figure 4-11. Above - Darkfield TEM of microgrids deposited with 10 pulses of 0.125 mM Au ₉ /methanol solution. Below – intensity profile along the white trace of the image	105
Figure 4-12 TEM scan on a 40x pulse deposited 0.125mM Au ₉ /Methanol sample using amorphous carbon microgrid. The top part shows a TEM scan of a PNCD deposition on to carbon microgrid with a region of dense coverage of metallic species. The bottom part shows the EDX result. Au was found (~ 2.1 keV) on this sample. In other TEM samples the Au concentration was below the threshold for detection using EDX. Cu signal seen in the EDX comes from the microgrid structure.	106
Figure 4-13 Mathematica code used to model the PNCD evaporation time and velocity	112
Figure 5-1 High-resolution XPS spectra of the C 1s region showing the change in C-C sp ³ and C-O fitted peaks across a heated and sputtered TiO ₂ surface (A), the same surface after PNCD deposition (B), and after post-deposition heating to 200°C (C). The change in the C-O peak through this range illustrates the removable nature of the low levels of carbon introduced through PNCD.	121
Figure 5-2 High resolution XPS scans showing typical spectra from the Oxygen 1s, and Silicon 2p regions.....	124
Figure 5-3 High resolution XPS scans on the Au 4f region of 0.006mM PNCD before (A) and after (B) post-deposition heating with peaks showing typical Au HBP and LBP fitting analysis.....	125
Figure 5-4 Ti high resolution XPS region before (A) and after (B) exposure to air as a form of immersion deposition simulation. Ti high res XPS region before (C) and after (D) PNCD in vacuum conditions.....	129
Figure 5-5 - Immersion deposited series Au ₉ HBP peak position and relative elemental concentration post immersion and after heating to remove PPh ₃ ligands showing the full range of concentrations in the immersion deposited samples. The control sample has been excluded as no Au was deposited or recorded on that sample. Any lower Au relative elemental concentration between Immersed and Heated values is mainly due to Au HBH agglomeration into the LBP state.	131

Figure 5-6 - PNC deposited series Au ₉ HBP peak position and relative elemental concentration after PNCD and heating to remove PPh ₃ ligands showing PNCD samples 0.01mM-0.0001mM; control sample was excluded as no Au was deposited or measured on that sample.....	132
Figure 5-7 Plot of HBP fraction of total Au XPS signal against total Au XPS creative concentration. Both immersion and PNCD samples show lower HBP fractions at higher total Au concentrations.	133
Figure 5-8 UPS scan traces from the I1-6 immersion deposition series, showing the characteristic doublet peak structure of TiO ₂ between 2-8 eV.....	134
Figure 5-9: Immersion Series MIES SVD reference spectra. Through correlations with XPS relative elemental concentrations and binding energies, Alpha has been associated with the TiO ₂ substrate, while Beta correlates to the Au ₉ AuAu NCs.	135
Figure 5-10 A- Immersion series MIES SVD weighting factors; B – MIES SVD weighting correlation with XPS Au ₉ HBP relative concentration, the near 100% correlation of 0.0006mM sample to the Beta reference spectrum corresponds to the highest concentration of non-agglomerated Au ₉ NCs across the sample range. This indicates a strong correlation with the Beta electronic structure and un-agglomerated, size specific Au ₉ NCs.	136
Figure 5-11 Top - Deconvoluted reference spectra from samples P1-P6 after undergoing MIES SVD analysis. Middle - The Alpha and Beta weighting factor breakdown for samples P1-P6. Bottom – Au ₉ HBP overlaid on SVD weighting factors showing a strong correlation to the Alpha reference spectra.....	139
Figure 6-1 Example high resolution XPS scans exhibiting all fitted chemical species for (A) O 1s after heating and sputtering (B) C 1s after heating and sputtering, and (C) Ti 2p after heating sputtering and Ru ₃ deposition	146
Figure 6-2 Stacked comparison between the XPS raw data of as made, heated (300°C) and sputtered stages of sample treatment on Sample 1. O 1s scans (A) show the reduction of the C=O peak at 532eV present in an as made sample, through sputtering and heating.....	150
Figure 6-3 XPS high resolution scan of the C 1s/Ru 3d region after Ru ₃ (CO) ₁₂ vapour deposition processing	151
Figure 6-4 XPS high-resolution scans of the C 1s/Ru 3d region showing (A) the comparison between as-deposited and heated scan traces for sample 1, displaying a clear shift in Ru 3d 5/2 peak shape and position, and (B) the fitted scan for the same sample after heating.	152
Figure 6-5 Au 4f high resolution XPS scans showing (A) An example of the fitted Au 4f region for post-PNCD, as-made Au NC species doublets as measured for Sample 1. (B) The fitted Au 4f region for heated, partially de-ligated Au NCs from Sample 1, showing the presence of characteristic HBP and LBP Au doublets associated with Au NCs and agglomerated Au respectively. (C) the stacked traces of all co-deposited samples after PNCD Au NC deposition and (D) the stacked traces of the same samples after heating, showing the partial Au NC agglomeration across the series.	155
Figure 6-6 Fitted high-resolution XPS scan traces on Sample 1, showing the C 1s/Ru 3d region both immediately after Au NC PNC deposition (A) and after subsequent heat treatment to 200C in order to partially de-ligate Au NCs (B) it can be seen that the post-PNCD scan shows the presence of Ru NCs correlating to an as-made chemical state in addition to the already deposited Ru species. This suggests that the PNCD process resulted in the deposition of residual Ru NCs onto the sample surface. The subsequent fitting after heating suggests that these Ru NCs undergo some level of agglomeration through the subsequent heating process.	156
Figure 6-7 Stacked, normalised MIES (A) and UPS (B) raw scan data measured from the sample series directly after Ru NC de-ligation was completed. Each trace has been offset on the vertical axis to display differences in the electronic structure more clearly between samples. MIES scans display some variation between samples in the 4-9 eV region, and no clear difference to ALD TiO ₂ in the 0-3 eV region. UPS scans display a clear increase in electronic structure in the 0-3 eV region, while some variation in intensity is seen between samples in the peak located at around 8 eV.....	162

Figure 6-8 The MIES reference spectra determined through SVD using three basis spectra (top) resulted in clearly differentiated Alpha, Beta and Gamma spectra, each with defining DOS features at 3 eV, 4.5 eV and 5-8 eV, respectively. The relevant weighting factors for each sample are presented (bottom), showing the respective trends throughout the sample series and the sum of weighting factors for each sample as determined by SVD..... 164

Figure 6-9 Resultant reference spectra, Alpha D & Beta E, produced from SVD of the Ru₃ sample series UPS scans (top), with Alpha D associated with typical Ti UPS features and Beta E associated with Ru NC DOS, the resultant weighting factors and their sum for each sample is seen below. 166

Figure 6-10 normalised and stacked UPS (A) and MIES(B) scan traces from across the sample range as measured after the Au₉ NC calcination step. UPS scans display increased DOS in the sub-3.5 eV region and slightly suppressed intensities in the 4-9 eV range. MIES Scans display a distinct shoulder peak at around 5 eV in the control, and some NC deposited samples, with smaller peaks at various lower energy positions. The UPS scan results display visibly increased uniformity between samples compared to the MIES scans, indicating higher variability of surface species DOS compared to combined surface & bulk DOS. 168

Figure 6-11 Three-basis SVD analysis results from co-deposited and calcined Au₉ and Ru₃ NC MIES scans. Distinct reference spectra (top) are Alpha F, Beta G and Gamma H. The per-sample weighting factors for each reference spectra are shown (below), along with each sample's overall weighting factor sum. This three-basis system still struggles to achieve series-wide convergence of weighting factor sums to unity. The control sample contains residual weightings of all three reference spectra, suggesting that even a three-basis interpretation may not account for the variety of final surface species..... 170

Figure 6-12 Two-basis SVD analysis results from co-deposited and calcined Au₉ and Ru₃ NC UPS scans. Two distinct reference spectra have been deconvoluted and can be seen (top) in the form of Alpha I, and Beta J. Per-sample weighting factors for each reference spectra and the sum of factors are presented (below). While there is some deviation from unity in the weighting factor sums across the sample series, convergence is improved from MIES results and within reasonable bounds when considering the complex co-deposited surface conditions..... 172

Figure 6-13 A comparison between the relative atomic percentages (At%) for both Ruthenium II and Au₉ NCs as determined by XPS against the respective weighting factors for Alpha I and Beta J across the sample series. It can be seen that a strong correlation in the trend of Beta J and Ruthenium II exists, while a weak correlation between the Au₉ species is also suggested. 174

Figure 6-14 The reference spectra associated with Ru and Au NCs, Epsilon B and Beta J are presented here as normalised spectra, along with their difference spectra, produced through the subtraction of Beta J's intensity from Epsilon B. The difference spectrum highlights the changes in DOS between the Ru₃ CVD samples and the co-deposited Ru/Au₉ samples, seen to primarily express in the -0.2-4 eV range, with some other minor differences at higher energies..... 175

LIST OF TABLES

Table 2-1 X-Ray satellite energies and intensities for Mg and Al X-Ray Sources [243]	55
Table 2-2 Atomic Sensitivity Factors for X-Ray Sources at 54.7°[243]	56
Table 3-1 Sample series for comparison of deposition methods (measured As-made and heated 500°C in vacuum) and vacuum heated series using an FT-RF sample.	70
Table 3-2 Sputter dose calculations for a range of argon ion currents, determining the required exposure time to receive the specified sputter dose.	71
Table 3-3 Analysis XPS taken from a sample of Single Crystal (SC) Rutile TiO ₂ after argon sputtering and heating to 625°C under vacuum. This sample served as an ideal TiO ₂ reference.	72
Table 3-4 Analysis of an XP Spectra from FT-RF TiO ₂ in as made condition, showing the energy peak positions, FWHM and intensities found in each region scanned (No Na was found in this sample). These values are typical for such a sample.	74
Table 3-5: XPS relative elemental compositions of TiO ₂ samples prepared with 90 min pre-sputtering (90m-RF), 30 min pre-sputtering (30m-RF) and 30 min pre-sputtering and a fresh TiO ₂ target (FT-RF). Samples designated As-made has received no further treatment after deposition. Samples designated – Heated, have been heated to 500°C in UHV Conditions before measurement.	75
Table 3-6 XPS Relative elemental compositions from an FT-RF sample, heated under UHV conditions to increasing temperatures to determine the change in C contribution through sequential heating. It can be seen that the level of C contribution in an As-made sample is significantly reduced by 300°C, decrease through 500°C and show a slight increase at 700°C. Sputtering an FT-RF sample with Ar ions at a set dose after heating to 300°C shows a reduction in C contribution over solely heating, as well as an increase in Ti ³⁺ defects.	77
Table 3-7 Ti ³⁺ defects as a proportion of total Ti 2p signal	78
Table 3-8 Average roughness characteristics from as-made and 500C heated sputtered TiO ₂ samples	83
Table 4-1 Deposition series for concentration change (A) and pulse number change (B). Series A were all deposited for 30x pulses. Series B used 0.125 mM Au ₉ in methanol solution. All samples were simultaneously deposited onto both mica and TiO ₂ substrates for AFM.....	97
Table 4-2 XPS relative elemental contributions for series A & B across C 1s, O 1s, Ti 2p and Au 4f regions.....	99
Table 4-3 Carbon 1s XPS percentages for the 3 measured steps, cleaning, deposition, and decontamination of a PNCD preparation of gold clusters	107
Table 4-4 Values for modelling methanol droplet evaporation after pulsing.....	108
Table 4-5 values used to model the number of monolayers deposited per pulse using Equation 4-1	109
Table 4-6 values for use with equation 4-4 to estimate pulsed packet velocity on exiting nozzle bore.	110
Table 5-1 Carbon 1s XPS relative intensities for the three measured steps displayed in Figure 1, substrate cleaning (A), deposition (B), and decontamination (C) of a single PNCD preparation of Au NCs.	122
Table 5-2 XPS relative concentrations (At%) measured directly after nanocluster deposition via PNCD (P1-6) and immersion deposition (I1-6)	123
Table 5-3 XPS relative concentrations for PNCD and Immersion depositions, all measurements presented here were recorded after deposition and post-deposition heating (@ 200°C, 10 mins) for surface carbon and ligand removal had occurred.....	126

Table 5-4 PNCD deposited sample Ti ³⁺ defects as a proportion of total Ti signal (%) showing the changes in each sample through different deposition steps.	130
Table 6-1 Elemental relative concentrations and primary species binding energy positions were determined by fitting XPS data collected after ALD TiO ₂ substrate treatment (Calcine @ 300°C, 10 mins & Ar sputtered). The ratio of Ti ⁴⁺ /Ti ³⁺ defects is recorded as an indication of substrate treatment results.	147
Table 6-2 XPS relative At%, primary peak positions and Ti ³⁺ /Ti ⁴⁺ ratio for the sample range after Ru ₃ (CO) ₁₂ deposition and calcination at 450°C for 10 minutes.....	153
Table 6-3-i Relative atomic percentages (At%) as determined through fitting XPS scans on the sample series directly after Au ₉ NCs through PNCD. Ru 3d I corresponds to the symmetrical Ru peak doublet, as measured for as-made Ru ₃ clusters. Ru 3d II corresponds to the asymmetric Ru doublet peak observed after Ru ₃ NCs are heated and delegation occurs. Au 4f – HBP is the high binding energy position of Au observed in Au ₉ NC samples which originates from ligated Au ₉ PPh ₃ nanoclusters.	157
Table 6-4-i Relative atomic percentages (At%) as determined through fitting XPS scans measured directly after calcination of the dual Au and Ru NC deposited sample series at 473 K for 10 minutes. Compared to Table 3, some species observed after PNCD have changed. Only Ru 3d II was detected after calcination, and two Au species, the Au HBP seen in the previous step and Au LBP associated with agglomerated Au NCs, were detected.....	159

1 INTRODUCTION

Solar Energy, Photocatalysis and Semi-conductors

The development of renewable, clean and cheap energy production methods has been identified as the key challenges facing much of the modern world if the challenges of climate change are to be met[1]. To meet this challenge, novel methods of energy generation and storage have come to the fore of the global scientific mind. Current energy production methods, largely based on hydrocarbon fuels (HCF) such as coal, oil and gas form the bulk of energy production[2] although this majority is steadily shrinking as countries attempt to reign in CO₂ emissions[3]. These efforts take the form of multiple, mixed technologies such as wind, solar (thermal and photovoltaic), and nuclear generation along with battery storage systems. However, many of these technologies have drawbacks, either lacking short-medium term reliability, long-term energy storage or high-risk (at least in the public mind) generation and waste scenarios, as well as critical risks to the supply chains required to build and maintain their ongoing operation[4]. When considered with some global regions lacking appropriate sites to capture large scale solar and wind energy, and the difficulty to efficiently transport the electricity produced by these methods over large distances, these technologies alone are not currently viable to completely replace HCF infrastructure. Global energy demands are not only growing in national power grids but for transport demands and more portable energy solutions, with petroleum and its derivatives accounting for up to 32% of all energy requirements in 2013[5].

A replacement energy source would preferably be carbon neutral, renewable, easily storable and transportable[6]. Solar energy, the harnessing of which has been a great success story and future hope of global energy production, is a practically inexhaustible, carbon-neutral energy source meeting the first two requirements but not the third[2, 7]. I. Ganesh observed that "The Department of Energy (DoE), USA, predicted that if the solar irradiance of 1% of the Earth's surface is converted into a storable energy with 10% efficiency, it would provide a resource base of 105 TW that is equal to the several times of the estimated world energy requirement in the year 2050" [7]. However the conversion of solar energy into an easily storable medium would make this method viable, especially if it provided a pathway to reducing existing CO₂ emissions due to petroleum fuels[8].

The conversion of solar energy into chemical fuel is evidenced in nature through photosynthesis, the abundant atmospheric CO₂ and incident light allowing plants leaves to synthesise their own fuel with nearly 100% quantum efficiency[9]. A synthetic "artificial leaf" with even a fraction of this efficiency would provide human civilisation with similarly renewable fuel sources, or Solar Fuels.

Taking the “artificial leaf” to its extreme example has been proposed through the use of Proteins films[10] and Microbial pathways[11] and while the harnessing of naturally occurring photosensitive proteins has shown successes, they often require integration with artificial interfaces as electrodes and are delicate and are difficult to produce at scale[9]. Their efficiencies are also reliant on large solar irradiation areas and require large arrays of infrastructure to ensure the biological components survival, reducing durability and increasing cost.

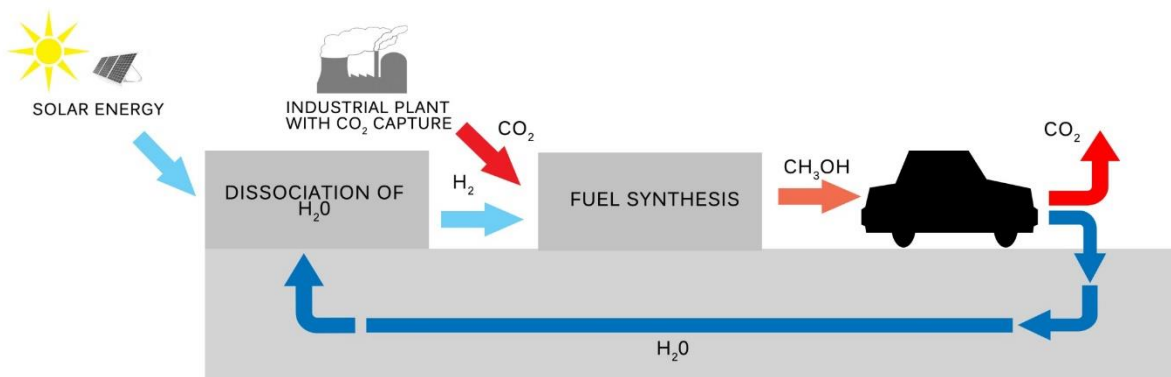


Figure 1-1 The production of solar Fuel hydrocarbons is proposed above. The system illustrates how this system would fit into existing energy production systems.

The conversion of solar energy to hydrocarbon fuels provides is one pathway being explored globally for solar-to-fuel energy production as seen in Figure 1-1. Hydrocarbon fuels offer advantages in their high energy density (33 GJ/m³ for gasoline)[2], stability and available existing global infrastructure. Fuels such as methane are ideally desired for their high energy density and its common usage throughout much of Europe, Asia and America’s heating and energy systems.

The pathway for producing hydrocarbons from solar energy involves capturing CO₂ and H₂O, dissociating into CO and H₂, using Solar or another source of energy[12] to finally recombine into a hydrocarbon fuel such as CH₄ [8, 12].

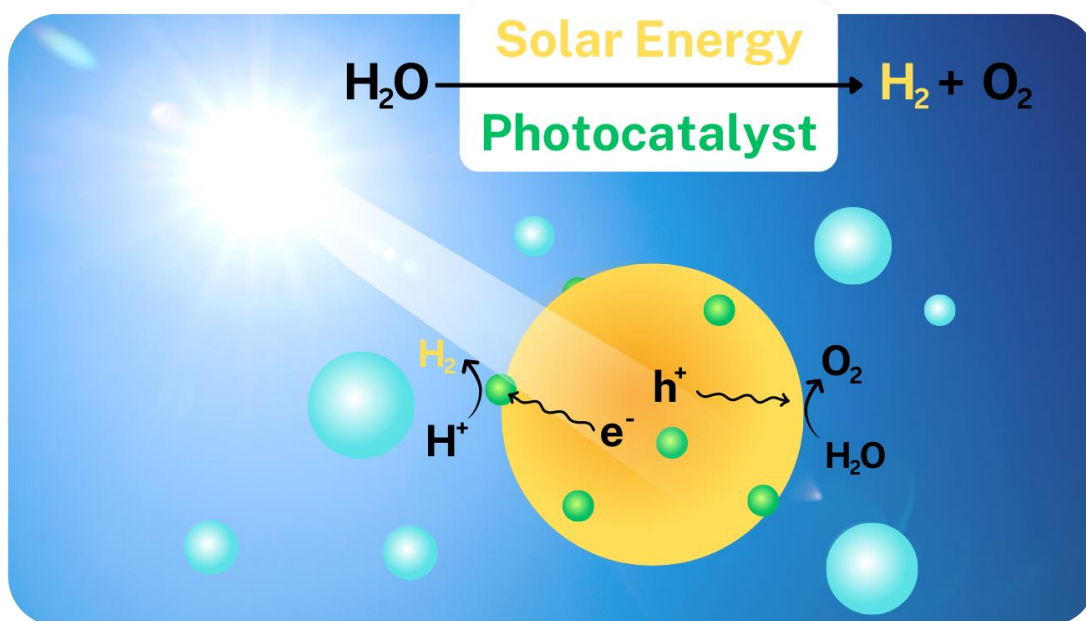


Figure 1-2 Photocatalytic H₂ production showing solar photons incident on TiO₂ (yellow Sphere) and the excitation process. Attached metal clusters (green spheres) can improve catalytic performance as n-type electron sinks, reducing electron-hole recombination.

Solar-fuelled hydrogen production is another promising potential pathway for solar fuel production shown in Figure 1-2. Hydrogen has been produced and used for much of the 20th century but would require extensive new global infrastructure to be used at the increased scale being investigated by many countries. Hydrogen is also difficult to store[7] due to its gaseous state at standard temperatures and steel embrittlement effects[13]. However, these challenges have not stopped hydrogen from being considered a key technology in global renewable transitions, particularly for heavy industry and large-scale transport applications.

The primary current source of Hydrogen is hydrocarbon fuels, which produce hydrogen by releasing the abundant hydrogen found in their molecules through a range of partial oxidations or gasifications[14]. Renewable hydrogen has been proposed and piloted in commercial projects through electrolysis, with renewable electricity supplying the energy required to break H₂O bonds[15]. Development and improvement of electrolyzers to facilitate these water-splitting processes have occurred over the past 200 years[16] with efficiencies now reported to reach 70-80% for the generation step [17]. However, long-term storage, handling and transport still pose issues for electrolysis at scale[18].

Photoelectrochemical water-splitting has also been investigated extensively as a pathway to solar fuel, with reports showing efficiencies as high as 12-20% are possible in a Hydrogen-production set-up depending on the intensity of the solar source [19-21]. Considering the relatively low efficiencies when compared to traditional electrolysis scaling, such technologies require further development to improve its solar-to-hydrogen efficiencies and protect against photoconversion and photoelectrode stability [22].

One of the most promising pathways for commercially relevant photocatalysis is seen in semiconductor-based photocatalysis. Discovered originally in 1972 by Akira Fujishima, Titanium Dioxide was shown to be capable of “splitting” water into H₂ and O₂ under ultraviolet irradiation[23]. These properties are due to TiO₂'s semiconductor nature causing incident light to excite electrons from the higher energy states of the valence band (HOMO) to the conduction band (LUMO) across the bandgap, leading to the separation of charges, which on reaching the surface can interact with adsorbed molecules.

TiO₂ has many positive characteristics, such as its low toxicity and cost, high photo-corrosion resistance[17], and earth-abundance. Its major drawback is the relatively wide bandgap of its two major forms, Anatase (3.2 eV, see fig. 1) and Rutile (3.0eV). These characteristics result in a limited percentage of the solar spectrum being of appropriate wavelength, with only around 6% of solar light (UV region) being harvestable[24]. This restriction limits the possible quantum efficiency of unmodified TiO₂, the ratio of collected photons to electrons excited by the cell.

The balance of these attributes has resulted in extensive efforts to utilise TiO₂ while narrowing its bandgap through doping with N, F, C or S[25, 26]. Although this can lead to new valence states by forming Ti³⁺ sites, which have proved useful in some catalytic processes[27], extreme doping can cause excess recombination sites within the bulk, reducing crucial surface charge availability[28]. Optimisations of TiO₂ crystal size have also been explored as changes in particle size and morphology, such as nanoscale crystals[28] and cuboid or pyramidal structures[29]. Electron beam treatment has also been used to decrease the band gap but compromises the integrity of surface constituents[27].

Metal Clusters and Catalysis

While doping and size control can lead to greater quantum efficiency for photocatalysis on TiO₂ by narrowing the bandgap, the matter of ensuring charge recombination does not occur before the desired catalytic reaction takes place will remain. A co-catalyst, being a species deposited on the photocatalytic surface that would “trap” excited charges at the surface is desirable to maximise electron lifetime and optimise surface reactions. Metal clusters within the range of 0.2-2nm, when attached to TiO₂, have shown dramatically improved catalytic performance while acting as ‘electron sinks’ for catalysis[30] [31]. Au and Ru clusters have been of specific interest for photocatalytic production of hydrogen and other solar fuels as part of nanocluster-modified surface systems [32]. Metal clusters have shown promise in areas other than photocatalysis, with Au₈ clusters on MgO substrate reducing the reaction temperature for CO oxidation from 400-500K for Pd/Pt catalyst to 150k[33].

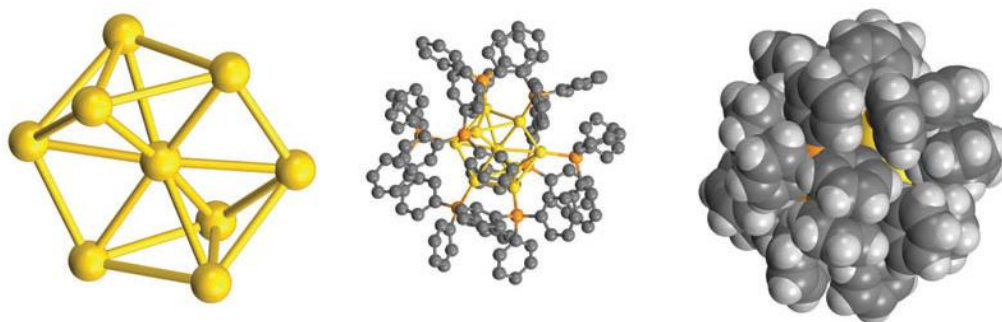


Figure 1-3 Au₉(PPh₃)₈ nanocluster simulations, yellow atoms represent Au and the grey represent triphenylphospene (PPh₃) ligands. Note the closed structure created by PPh₃ orbitals in the right-most simulation, creating a steric hindrance for reactant species to reach the nanocluster core. Used with permission for the Andersson research group.

Catalytic performance improvements when using metal clusters have been seen across various reactions, using elemental clusters including Ni, Pd, Pt and Ru[34, 35] and oxide supports. The improved efficiencies observed, both solar-to-hydrogen and for alternative catalytic pathways, are strongly linked to several key factors. Firstly, nanocluster size is crucial to performance. The above-reported results for CO oxidation using Au₈ proved drastically less effective when repeated using Au₇ or Au₉[33]. Other results have also pointed to the idea that a specific nanocluster size, where a specific number of atoms bring unique morphologies and electronic states, is crucial for optimal catalysing specific reactions[36].

Metal nanoclusters have vastly different valence structures to bulk materials, influenced by their more amorphous structure. The type of substrate the NC is attached to is also important affecting charging and geometric arrangement and adsorption sites for catalysis[33]. Substrate defect sites have also been observed to increase catalytic activity by introducing new, more favourable valence states [37]. However, they have also led to an increase in agglomeration effects, impacting nanocluster size homogeneity in some cases[38].

The size-dependant properties of these clusters as catalysts have led to two main pathways of proposed size control. The major method in the past 10 years has been gas-phase nanocluster formation, using sputtering and mass spectrometers resulting in highly size-selective nanocluster production[39]. However effective at size-control these methods have proved, unclear pathways to scalability for such a technique could be a major roadblock to commercialisation. Chemically-synthesised nanoclusters have shown great progress in refining the synthesis process towards producing a comparable range of sizes to gas-phase[40, 41] with the added benefit of ligand or polymer protection, as seen in the simulations is Figure 1-3 with Au₉ nanocluster cores protected by PPh₃ ligands, which increases nanocluster stability and provides synthetic pathways to large-scale production. These chemically synthesised clusters also have a variety of synthetic pathways and ligands available for tailoring catalytic properties, owing to a variety of surface features such as

active perimeter sites, excess electronic charge and non-metallic quantum size effects[42] as represented in Figure 1-4.

Clusters from both methods have been seen to have size-specific properties attributed to unique electronic structures appearing as nanocluster size goes below 3.5nm[43]. These changes in electronic structure have been explored using XPS techniques, and shifts in binding energy characteristic of nanoclusters have been found, especially in the Au 4f_{7/2} region where clusters show binding energies of the order of 1.1eV higher than bulk counterparts[44]. Experimental results showing these electrically unique properties have built on theoretical models and investigations suggesting that at these small numbers of constituent atoms, the density of states (DOS) changes, and the electrical properties and available energy levels in both conduction and valence bands can exhibit large shifts with small changes in constituent atoms.

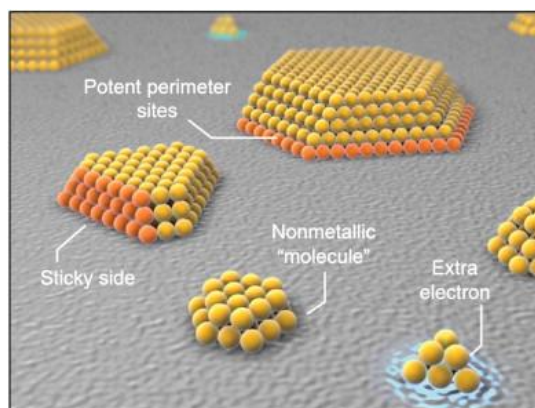


Figure 1-4 Cartoon representation of Au catalysts displaying a variety of observed surface and electronic features in Au nanoparticles and nanoclusters which lead to higher catalytic activity and tuneable properties [42].

1.1 Synthetic Methods and Approaches

1.1.1 Chemical Synthesis

Nano-sized gold particles have been known and used by humans for quite some time, but Faraday is credited with the first scientific investigations into their properties and synthesis. His colloidal solutions of gold were readily obtained from metal salts in an aqueous solution, and he observed that “the state of division of these [gold] particles must be extreme; they have not as yet been seen by any power of the microscope”. The stability of Au colloidal particles meant that modern analysis of these substances shows gold particles averaging 6-30nm depending on the solution[45].

While Faraday's clusters were charge stabilised, leading to polydispersity of resulting sized particles and limited candidate metals (Ag and Pt cannot be used this way), the recent explosion in research focusing on catalytic activity in nanostructured Au, Ru, Pt and Ag, the chemical route to synthesising nanostructures in general and nanoclusters, in particular, has been one of many novel advances [46] [47].

It has been relatively recent developments utilising steric control to control these reactions. This was first achieved using the thermolysis of organometallic precursors to create Co colloids through dispersion with polymers[48]. This technique was useable to create colloids in the range of 1-100nm through the attachment of polymers to the metal's surface, preventing aggregation through collision. This technique can be considered the basis for most modern efforts to synthesise and isolate size-specific clusters in non-aqueous media. While this technique has led to patentable technology[49] the issues of unwanted metal films, air sensitivity, and the lack of organometallic precursors for many metals make this approach impractical for many nano-catalytic contenders.

While organometallic decomposition has proved unsuitable for the large-scale production of monodisperse nanoclusters, one area of this synthesis resulted in the crucial development of nanocluster understanding. Schmid et al. managed to produce monodisperse metal clusters through the reduction of Au, Co and Ru precursors in reducing agents such as benzene or methyl chloride to form M_{55} clusters[50]. The specific number of constituent atoms (55) represented a highly stable and favoured "magic number" nanocluster around an M_{13} nanocluster core. This nanocluster's stability is explained through its spherical jellium potential, denoting a full outer shell[51, 52]. Schmid used these magic numbers similarly to polymer synthesis, "seeding" the larger nanocluster size with the smaller to achieve clusters with constituent atoms numbering up to the thousands[53]. These larger clusters were facilitated through the use of PPh_3 ligands as capping agents on the inorganic nanocluster core. Though this technique was limited in its efficiency in producing catalysts, it established the role of ligands as effective steric capping agents and showed that they could be used with Cu, Pd, and Pt as well as to form nano-alloys[54]. These developments fueled investigations into the next generation of chemical nanocluster synthesis.

While some organometallic investigation is an ongoing field, most recent innovations in chemical methods for nanocluster synthesis can be grouped into two methods; Inverse micelle synthesis and chemical reduction of metal salts in stabilisers.

1.1.2 Inverse Micelle and Micro-emulsion Synthesis

The first technique distinguishes itself from gas and liquid-phase reactions by using simple metal salts as nanocluster feedstock and droplet-like inverse micelles or micro-emulsions to control nanocluster size and growth. Several reported methods have utilised this technique [55-59] using a range of metal salt precursors, with $HAuCl_4$ or $NaAuCl_4$ being the most common.

The concept behind this technique is to use “nanoreactors” formed by thermodynamically stable nano-dispersions of oil in water (or vice versa) stabilised by some surfactant film. In a microemulsion system, several factors, including the surfactant, thermodynamic conditions and any additives (alcohols, electrolytes. Etc.), determine the size and shape of the nanodroplets. The dispersal and interaction of these droplets are determined through Brownian motion, with colliding droplets fusing briefly to allow reactant exchange. Internal micro-environments allow the particle and nanocluster-forming reactions to proceed. The adjustable variables for this control include reactant concentration, predicted to increase particle size and the range of polydispersity with increasing concentration [56]. These effects have been demonstrated in synthesising magnetite nano-particles [60].

Surfactant species also play a large effect in determining the micellar shape, with evidence from Pt nano-particle synthesis showing that using either alcohol ethoxylates or sodium bis(2-ethylhexyl)sulphosuccinate allowed control of reaction rates, as well as some coarse tuning of particle size[61]. The water-to-surfactant ratio has also been crucial to a final particle size with minimum stable sizes predicted for surfactant in excess, with increasing particle size for decreasing surfactant concentration[57]. The addition of co-surfactant species has also been investigated regarding particle size and has proven effective at reducing particle size through increasing inter-micellar exchange and increased droplet curvature[62].

Methods of particle size control in micro-emulsions are poor compared to the other methods described in this review. The polydispersity of microemulsion synthesised nano-species is undesirable when dealing with catalytic applications.

The exclusion of water (necessary for a micro-emulsion) in inverse micellar synthesis has proven to allow a greater range of synthetic options and products in these systems. Where water-containing systems are limited in useful reducing agent options (NaBH_4 , hydrazine), the cationic surfactants used in inverse micelles directly solubilise a wider range of metal salts, eliminating the need for water within the micelle. The removal of water also opens up pathways of stronger chemical-reducing agents such as LiBH_4 , Toluene and LiAH_4 [63]. This approach has been shown to work for Au, Pd, Ag, Rh, Ir, Ni, Pt and Md salts[64].

These micelles are considered “inverse” as when added to apolar solvents, they expose hydrophobic tails to the solvent, shielding the polar groups and surfactant counter-ions in a nanoscale cavity. These inverse micelles can stabilise the decomposed metal salt ions and form them into clusters [65]. As these micellar species usually contain around 1-4 ions, limited by the solubility of the precursor salts, the final sizes observed are dependent on micellar diffusion, collision, and atomic interchange. The diffusion rate of micelles, therefore, controls the nanocluster growth rate. This is an order of magnitude slower than for metal atoms in the continuous liquid

phase[63] and so allows for structural adjustments to clusters, leading to nanocrystalline products[66]}.

The choice of strongly binding ligands, such as alkyl thiols, has resulted in smaller clusters and a narrower size dispersion. These thiol ligands will compete with the higher concentrations of longer-chain surfactants used to initiate micellar growth and effectively cap the newly formed clusters, facilitating purification and characterisation through liquid chromatography[63]. It should be noted that synthesis of specific clusters of Pt, Rh, Pd and Ir in the 2-5nm range does exhibit near independence from surfactant and reactant concentration effects [67]. So the usefulness of this technique to control final size does have intrinsic limits that the use of ligands as stabilising agents can overcome.

1.1.3 Chemical Reduction of Metal Salts in the presence of Stabilisers

The power of strongly interacting ligands to control and restrict the growth of clusters to very small sizes is the basis of the second major technique for the chemical synthesis of clusters. The first direct report of chemical reduction leading to nano-particle formation in the presence of stabilisers was reported by Hirai et al.[68]. Their use of an organic soluble metal-salt precursor for chemical reduction in a strong reducing agent such as NaBH_4 resulted in metal nano-particles. Initial investigations utilised polymers such as poly(N-vinyl-2-pyrrolidone) (PVP) or poly(vinyl alcohol) as capping agents, and these early investigations showed promise as synthetic pathways as well as for catalytic properties. The choices of reducing agent such as NaBH_4 , H_2 or a polyol, stabilising agent (ligand or polymer), and solvent medium (water, alcohol) are all crucial factors in determining final nanocluster size, structure and properties[69].

Distinct from micelle-forming surfactant control, polymers coordinate onto the surface of reduced metal salt. Rather than allowing the reaction conditions to dictate the formation rates and final size of reaction products, polymer stabilisers allow for finer control of particle synthesis. They do this if their interaction with the metal precedes the reduction step. If this occurs, a 'complex' of polymer-stabilised metal ions form that maintains its interaction throughout reduction and can affect the structural properties of the final particle. This process has given simple, reproducible reactions, small particles with narrow size distribution and high particle stability[70].

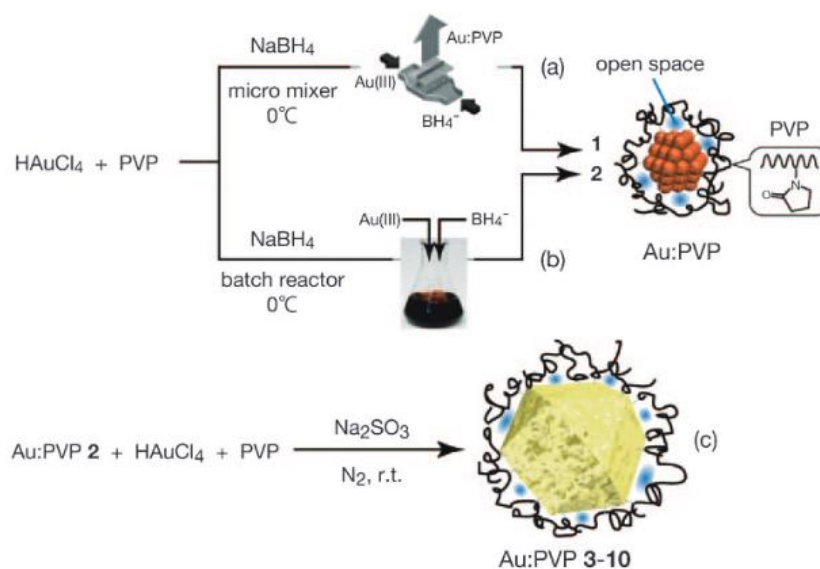


Figure 1-5 Synthetic process for synthesising AU:PVP-n (n=1-10), a polymer-capped nanocluster species [51].

The pathway of polymer stabilisation has shown synthetic potential, especially in the area of bimetallic nano-particles such as Pd-Pt[71], Au-Pd and Au-Pt[72]. These processes have also proved useful more recently in synthesising Au nanoclusters, viewed more favourably for future catalysis due to economic factors and impressive catalytic potential[73]. Examples of Nanosized products from 1.5-5nm covering clusters to particles using polystyrene poly-block-poly diblock P2VP copolymers with polar “heads” and non-polar “tails”. Control of nanocluster size was found to be tuneable through the “heads” molecular weight and the ratio of metal salt (chloroauric acid):polymer ratio[58].

Reaction conditions such as the mixing mechanism have also proved influential over final outcomes. Differences in final product between microfluidic mixing[74] and standard batch mixing[75] showed that the rapid, homogenous mixing in the micromixer resulted in finer particles with a finer range of sizes than the traditional method. Results such as these have led to an understanding that to produce small, narrowly size-distributed nanoclusters, a homogenous reduction is favourable. This type of synthetic control may be transferrable to other methods of synthesis involving mixing. ‘Seeding’ of polymer-stabilised nanoclusters is also possible. Using weaker reducing agents like Na₂SO₃ allows the reduction of Au(III) exclusively onto the surface of ‘seed’ Au(0):PVP complexes with variations in Au(0)/Au(III) concentration ratios producing clusters from 2-10nm in size as seen in Figure 1-5.

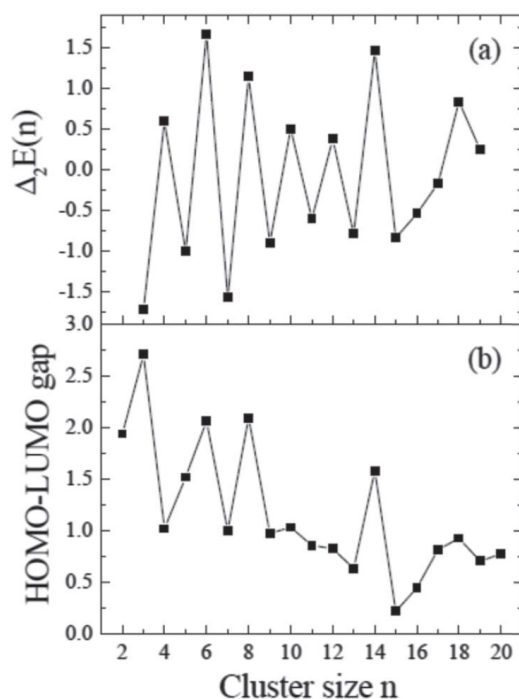


Figure 1-6 Electronic properties of Au_n clusters by nanocluster size (a) Second difference of nanocluster energies $\Delta^2 E(n)=E(n+1)+E(n-1)-2E(n)$; (b) HOMO-LUMO gap (eV) [1]

While polymer-stabilised nanocluster research is still ongoing, and polymer stabilisation (especially PVP) could be considered superior to other ligands for nano-particles greater than 8nm[63] they are not the only or most effective method of stabilising all clusters. It has been proposed that a synthesis system allowing for similar stabilisation during synthesis with greater selectivity for Au may help unravel and control these clusters' potential as tuneable catalysts[37]. Theoretical studies on small clusters of Au have been active for some time and provide, as with other metal clusters, reference points for comparison and refinement of nanocluster synthesis[76, 77].

Sulphur and phosphorous have a high affinity for gold, readily stabilising nanocluster growth. Subsequently, many synthetic pathways achieve stable thiolate (SR)[78] or phosphine (PR₃) ligated clusters[57]. Early investigations into this field were capable only of crude mixtures containing many sizes of nanocluster[54, 79]. These mixtures were size selectable generally through extraction[79], chromatography[80] or electrophoresis[81]. But as simpler, more efficient and higher-yielding systems were required, investigations turned to exploit the observed Au' magic clusters' detected in certain synthetic methods and crude mixtures.

1.1.4 'Magic Number' Clusters


Au Nano-particles and nanoclusters containing total electron numbers of

$$n^* = 2, 8, 18, 34, 58, 92, 138, \dots$$

are known to have huge effects on stabilising clusters due to the closing of electron shells at these states[82]. Investigated clusters have also shown periodic stability increases and electron affinity in odd/even alternation up to sizes of 58 atoms for Au and Ag[83]. Several simulated studies have

shown that the electronic structure of these clusters is the determining factor of stability[37, 52, 82]. While Au can form clusters of varying shapes, with Au clusters of 12 atoms or less predicted to be flat flakes, spherical nanocluster structures have been predicted when the total number of valence electrons within the nanocluster is at or near the 'magic numbers' stated above[84]. These numbers correspond to filled *s*, *p*, *d*, *f* and *g* orbitals.

'Magic Number' Clusters



Number of Full Shells	1	2	3	4	5
Number of atoms in cluster	13	55	147	309	561
Surface atoms as percentage of all atoms	92%	76%	63%	52%	45%

Figure 1-7 Diagram showing the size and sequence of "magic number" clusters. Note that increasing size corresponds to a reduced percentage of surface atoms correlating strongly with reduced catalytic performance.

While clusters at or near magic numbers show exceptional self-stability, the shell closures that make them useful can be further stabilised through ligand bonding. An understanding of these nanocluster complexes has been proposed in the form.

$$n^* = N\nu_A - M - z \quad \text{Equation 1-1}$$

Where n^* satisfies the above numbers, $N\nu_A$ is the product of the number of core metal atoms N and the atomic valence ν_A , and M is the number of electron localising ligands[82]. These predictive models have proved accurate for gas-phase metallic nanocluster size [85] and Ga clusters with and without ligand attachment[86]. However, applying theoretical models like these into wet-synthesised nanocluster catalysts has been slow, with further refinement of theoretical understanding required.

Opportunities for further understanding the practical implications of magic number theory for solvated, chemically synthesised clusters are crucial to refine this model. Discoveries such as the thiolated nanocluster $\text{Au}_{102}(\text{p-MBA})_{44}$ with its closed 58-electron shell [87] and its experimentally determined structure allow refining of DFT 'magic number' models[82] allowing more accurate predictions of structure both electronic and morphological. However, regardless of still-developing precision, the template for understanding stable nanocluster growth that magic numbers offers has found vast practical application and informs many fields of nanocluster catalysis.

1.1.5 Ligand-supported Synthesised' Magic Clusters'

Utilising theoretical ideas around 'magic' stable states, size-selective synthesis regimes were developed, allowing well-defined Au:SR thiolated nanocluster synthesis[88]. Ligation with thiols has been shown to influence nanocluster structure and change the core, especially for Au clusters[89]. Thiolate-mediated changes were confirmed in 2007 when X-Ray diffraction studies showed an oligomer 'staple' (-SR-[Au-SR-]) form at the metal-ligand interface and are responsible for stability that affects morphology[87].

Observations of ligand-nanocluster interactions have led to the current understanding of thiolated Au clusters with high stability consisting of Au core with high symmetry and stable geometry surrounded by surface Au anchored by thiolate oligomer -SR-[Au-SR-] 'staples' [90]. The Au atoms show different chemical behaviour depending on whether they are bound to ligands or are core constituents[91]. The size of these clusters is offered some control through the change in length of oligomer species, with larger clusters preferring longer oligomers[92]. The differences in structural and chemical environments for Au surface atoms vs core Au make thiolate synthesis methods somewhat unique. To date, only eight thiol clusters have been fully structurally solved[93], including the well-established $\text{Au}_{25}(\text{SCH}_2\text{CH}_2\text{Ph})_{18}$ [94],[95] $\text{Au}_{38}(\text{SCH}_2\text{CH}_2\text{Ph})_{24}$ [96] and $\text{Au}_{102}(\text{p-MBA})_{44}$ [87].

Phosphine-protected clusters, mainly of Au ($\text{Au}:\text{PR}_3$) have been investigated since before nanoscience, and nanotechnology emerged as research fields. $\text{Au}:\text{PR}_3$ chemical composition occurs in the general form of $[\text{Au}_N(\text{PR}_3)_M\text{X}_L]^Z$ where N, M and L represent the number of Au atoms, phosphine ligands and counter-ions, respectively and Z shows the net charge of the nanocluster. $\text{Au}:\text{PR}_3$ clusters stability is distinct from thiolated Au clusters in that the previously mentioned thiol oligomer 'staples' and their effect on Au chemical behaviour is not present in these systems. Instead, Au atoms form generally icosahedral cores with coordinating ligands and counter-ions above that core.

Phosphine ligand synthesis has been used to synthesise and isolate a variety of Au nanocluster species, offering a variety of useful properties and characteristics for catalysis[97]. Monodentate phosphine ligands like Tri-Phenyl Phosphine (TPP) have produced clusters such as $\text{Au}(\text{PPh}_3)$ [98], $\text{Au}_6(\text{PPh}_3)_6$ [99], $\text{Au}_9(\text{PPh}_3)_8$ [44, 100] and $\text{Au}_{55}(\text{PPh}_3)_{12}$ [54], [101]. Bi-dentate phosphine ligands have also been investigated over Au_n ranges ($n=7-11$) and showed reduced Au-Au bond lengths, suggesting they can reduce interatomic strain and increase stability [102]. 1,8-bis(diphenylphosphino)octane (L^8) has also been used in the synthesis of $\text{Au}_{22}(\text{L}^8)_6$ with each monodentate ligand coordinating one phosphine with each Au_{11} nanocluster 'building block' and 'clipping' them together[103]. This method leaves some surface Au atoms completely uncoordinated and, therefore, sterically available for catalysis. Recent synthetic methods have also allowed for one-pot

synthesis of Au from ultra-small nanocluster size to plasmonic nano-particles at slow growth rates due to methionine/CTAB mixed ligand systems[104]. Methods such as these allow for effective studies of nanocluster-particle growth regimes and kinetics; however, CTAB ligands strongly bind to Au and inhibit effective catalysis.

Magic number theory of clusters also informs pathways towards stable bi-metallic clusters such as $[\text{Pt}(\text{AuPPh}_3)_8]$ and $[(\text{PPh}_3)\text{Pt}(\text{AuPPh}_3)_6]$ [105] using monodentate TPP. As metals such as Au may not have electrons in the orbital shells corresponding to higher 'magic numbers'. Metals like copper have also shown isolated and characterised bi-metallic clusters in $\text{Au}_{13}\text{Cu}_2$, $\text{Au}_{13}\text{Cu}_4$ and $\text{Au}_{13}\text{Cu}_8$ using mixed thiol/phosphine ligand stabilisers [106]. These processes also occur through the reduction of multiple metal salts in stabiliser presence, with Cu acting as a face-capping species on the Au nanocluster core.

1.2 Supported Catalysis and Nanocluster-Support Interaction

1.2.1 Nano-Structures for Catalysis

Nanoclusters have shown huge potential in over the past 30+ years as catalytic agents with the potential for precise, highly active processes at favourable conditions. These somewhat unexpected catalytic properties point to a new generation of catalysts that might be 'tailorable' towards specific reactions through control of size, morphology and nanocluster-surface interactions [107, 108]. The surprise in these results comes from the clusters of major interest Pt[109], Ag[110, 111], Ru[112] and Au[54, 101] is known to be largely chemically inert when in bulk form.

The size reduction and the structural and electronic changes that small size expresses in these elements have consistently been found to determine the specific catalytic usefulness of these clusters. This is evident in the transition from bulk to nano-particle scale where localised surface plasmon resonances (LSPR) are excited by the resonant incident light in the solar emission spectrum (UV-Vis), making nano-particles catalysts possible pathways to homogenous catalysis. This absorbance[88] is strongly influenced by the nanoparticle's size and geometry[113]. Nanoclusters, however, do not exhibit the LSPR band, providing a pathway towards cluster/particle size distinction and making such clusters more useful in heterogeneous catalysis in conjunction with a support system. Au nanostructures in heterogeneous systems have been shown to improve important catalytic processes like water splitting over TiO_2 -Au complexes through the modification

of wide-bandgap semiconductors such as TiO₂ and MgO, extending absorbance into the visible spectrum[114].

The effect of size on the catalytic activity of particular species of nanoclusters is well understood, with intrinsic properties relevant to catalysis, including electronic state and structure, proving to be tuneable through size control[33]. In general, CO adsorption under IR spectroscopy has been used to probe the electronic state of Au clusters[115], with near-neutral or negatively charged Au showing increased performance in CO oxidation[116]. Observations through differential pulse voltammetry have shown a size-dependent shift to more bulk-like properties in the final particles from molecule-like initial clusters. This size-dependent shift has been seen to reduce catalytic activity, depending on the reaction, and can even nullify activity[101]. Au thiolate clusters were similarly explored through a mixture of applied and simulated experiments, and it was determined that the molecule-bulk transition occurs between 144-187 atomic constituents. The transition again expresses itself as plasmonic resonances[117] as the nanocluster become particle-sized and change the catalytic usefulness of the nano-species. These observations of change in catalytic and chemical properties with size allow the definition of nanoclusters to be determined as nanostructures without LSPR effects, while those that display LSPR fall under the nano-particle regime.

1.2.2 Clusters for Catalysis

Nanoclusters offer particular promise in catalytic applications given their particular properties and the incredibly high surface area-to-volume ratio they offer as a catalytic compound. There are emerging trends in real-world catalytic reports of a shift towards sub-nanometer nanoclusters or even single atom catalysts that offer these preferable ratios in particular[118, 119]. These promising properties are particularly obvious when nanoclusters have been examined while supported on both catalytic (NC as co-catalyst) or non-catalytic substrate surfaces.

Au clusters were predicted to have different electronic and therefore, catalytic properties at different sizes[77],[82] [51] offering the potential for tailoring catalytic properties for the desired reaction[108], such as Au clusters for CO reduction [120, 121], well below 0°. This specific reaction displays nanocluster size sensitivity as Au₈ nanocluster on MgO corresponds to far greater production rates than either Au₇ or Au₉ on MgO for the same reaction.

Some of the observable changes in nanocluster properties can be seen in their optical absorbance spectra. Optical spectra from 'magic' Au clusters of Au_nSR clusters (n=11-39)[122] have shown that as nanocluster size decreases, the optical features dramatically blue-shift after absorption onset below 1.2eV[88]. The onset of such a feature precedes a nanocluster "fingerprint" of

characteristic absorption peaks. The unique electronic properties of such spectra suggest the potential of catalytic performance being tailorable through nanocluster size.

Nanocluster catalytic potential is also structure-dependent, with important features such as O₂ absorption, predicted to depend on the coordination of the absorbing atom[80]. A nanocluster's structure and coordination are highly dependent on the number of atoms in the nanocluster and the energy conformation of the structure. This is observable in simulated models of clusters of Au[37] as well as other metallic nanoclusters. Even for nanoclusters of identical numbers of constituent elemental atoms, electronic structure can differ based on the geometric confirmation of the resulting nanocluster as seen in Figure 1-8.

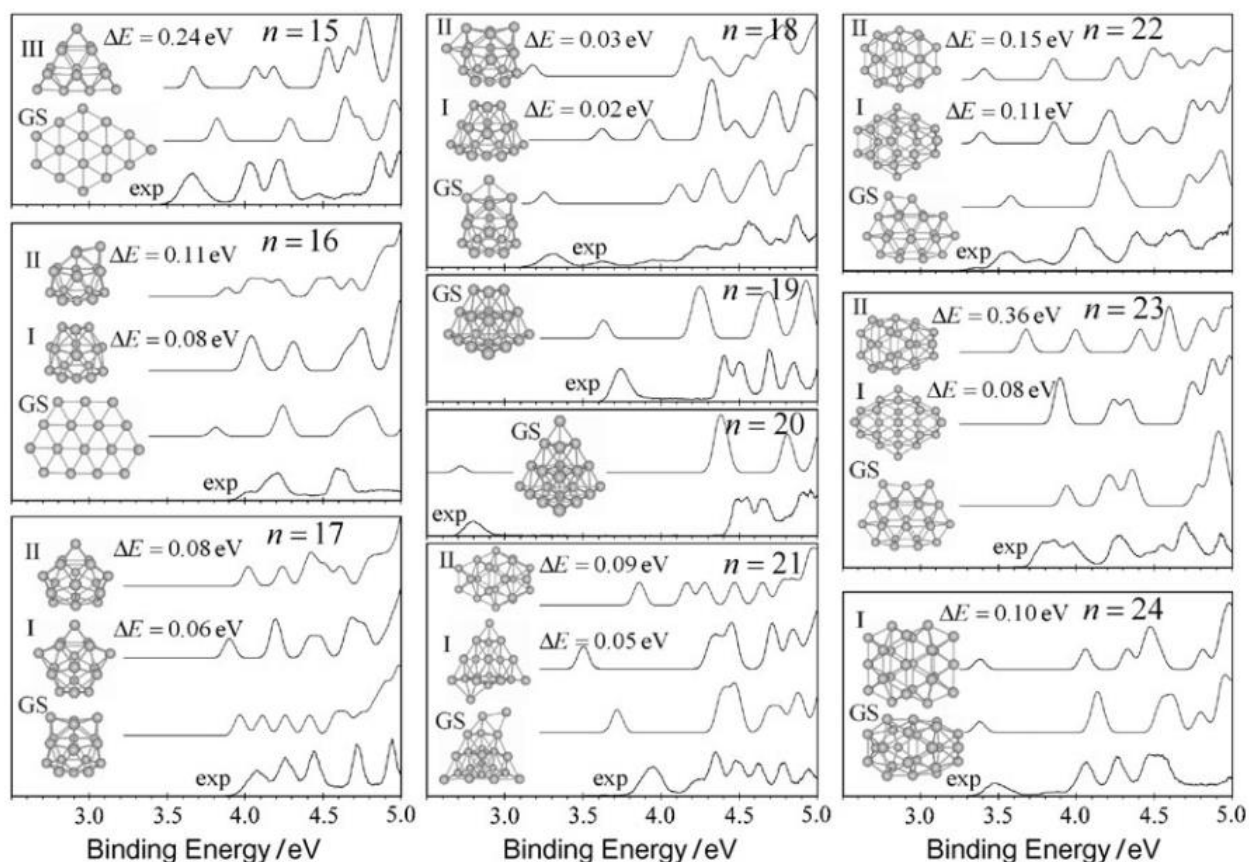


Figure 1-8 A comparison between calculated electronic densities for Au nanocluster geometric isomers of clusters between 15-24 constituent atoms. Calculated spectra are seen in the top three traces in each section, and experimental photoelectron spectra denoted by *exp* prepared by Yoon et al[37].

Some evidence of hetero-metallic clusters enhancing catalytic effects has been found with Au₁₃Cu₈ showing 13.7% increase in selective oxidation of benzyl alcohol over Au₂₅ under the same conditions[106]. Au/Pd and Au-Ni bimetallic clusters also have been shown to increase efficiency in a range of reactions compared to their elemental counterparts[123]. Stability and resistance to degradation in bi-metallic clusters has been shown to improve in addition to affecting chemical properties [124]. This was keenly demonstrated in comparing Au₂₅:SR clusters to Au₂₄Pd:SR in

toluene, with the substituted Pd atom increasing the structural integrity of the nanocluster greatly[40]. However, given the specificity of nanocluster catalysis for certain reactions, this may not point to a general trend but rather another method of control over nanocluster properties. Such Cr_2O_3 films have also been explored with regard to Au_9 metal nanoclusters, improving nanocluster agglomeration resistance when used in conjunction with a TiO_2 substrate[125, 126].

For nanoclusters used as co-catalysts on photocatalytic surfaces, a key challenge towards increasing photocatalytic performance has been to reduce the ratio of back reactions, the recombination of photogenerated electrons and holes before they have been used in catalysis. Modification of sample surfaces with a layer of amorphous hydroxide, most famously Cr_2O_3 , as seen in Figure 1-9 produced by Takata et al, after the photo-deposition of metal nanoclusters has proven successful at reducing back reactions and increasing catalytic performance of the cluster[127]. This is due to Cr_2O_3 layers being permeable to protons and H_2 molecules, but not O_2 , reducing the opportunity for back reactions involving O_2 at the metal nanocluster. A variety of hydroxide species have been explored to date, including TiO_2 , Nb_2O_3 , Ta_2O_5 , SiO_2 and MoO_x [128].

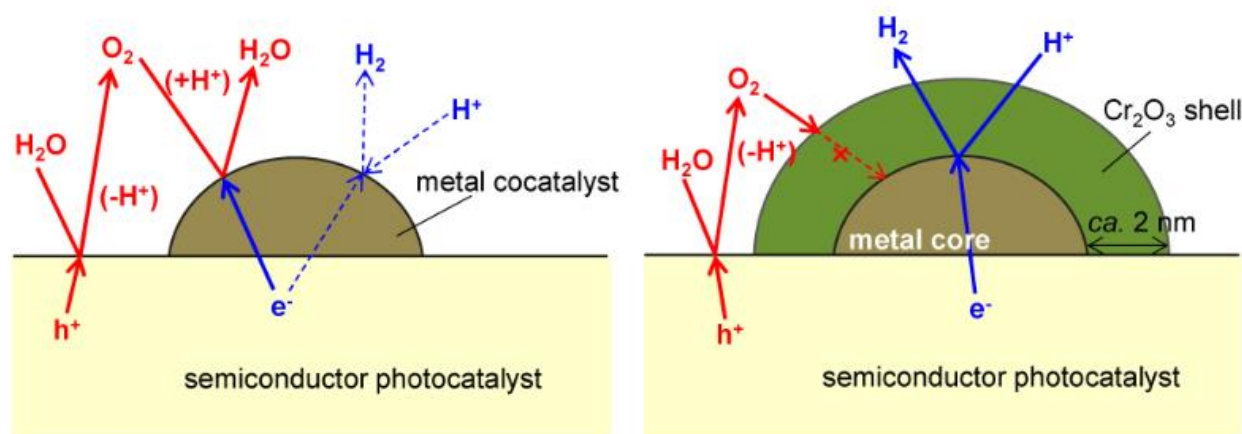


Figure 1-9 Schematic cross section of a metal co-catalyst before and after being covered with a Cr_2O_3 shell. The reaction notation illustrates how such an arrangement can block photocatalytic back reactions involving O_2 [129]

Carbonyl-ligated clusters have become commonly reported, particularly for group 8 and 9 metals, such as Rh[130], Ir[131], Os[132] and, more commonly, Ru in the form of $\text{Ru}_3(\text{CO})_{12}$. Such Ru clusters have been explored extensively for their catalytic properties and are among the most active reported catalysts for Co and CO_2 hydrogenation[133]. Supported Ru clusters, including Ru-CO ligated clusters, have displayed catalytic viability for a range of reactions, including gas-phase hydrogenations for previously mentioned CO & CO_2 [134, 135], and N_2 dissociations for ammonia production, more recently[136].

Ru as a co-catalyst has also been explored, particularly within hydrogen-producing reactions, as a potential enhancement for HER performance. Nanoscale RuO species deposited onto TiO_2 have shown increased quantum efficiency yields under UV and visible spectrums with optimal loadings

at around 3% w/w[137]. Surfactant-free Ru nanoclusters have also shown promise in increasing HER activity and catalytic stability across a wide pH range in electrocatalysis using defect-rich carbon nanotubes[138]. Density function theory (DFT) calculations have also theoretically compared Ru/TiO₂ and Au/TiO₂ photocatalytic systems and found that such pairings can narrow band-gaps while forming strong surface bonds that can act as electron sinks to capture photogenerated electrons, providing enhancements to such co-catalytic systems[139].

1.2.3 Metal Oxides and Photocatalytic Surfaces for Catalysis

With developments in the field of photocatalysis since the discovery of water splitting over TiO₂[23] and the heterogeneous combination of nanocatalysts and photo-active supports[33], heterogeneous pathways are some of the most promising for nanoclusters. Heterogeneous catalysis, or the utilisation of a mixture of clusters, supports, and even nano-particles, promises the benefits of utilising positive characteristics in each medium to overcome weaknesses in the others and lead to a more effective overall catalyst. Oxide surfaces are one of the most promising areas of interest, with theoretical studies showing a range of metal clusters becoming catalytically active on deposition[140, 141].

Au clusters have been predicted to have particular activity on photocatalytic metal oxide surfaces due to structural dynamical fluxionality, quantum size effects, and effective charge transfer from support to nanocluster[142]. The changes in nanocluster structure and electronic properties induced by the attachment to such a surface greatly affect the observed catalytic behaviour. Specifically, that support can potentially modify the utility of a given nanocluster. Studies over ideal, flat surfaces such as single crystal surfaces as model studies have proved useful for initial investigations in understanding the nanocluster-oxide interface and interactions. Utilising heterogeneous catalysts requires a fundamental understanding of the nature and structure of the surface as well as the interface between surfaces acts and reacts to environmental conditions and changes.

A combination of theoretical and experimental approaches has focused on developing novel nanoparticulate photocatalytic substrates, aiming to improve physical factors in oxide nanoparticles affecting photon absorption, the lifetime and distribution of charge carriers, electron-hole recombination rates and defect site location and concentrations. All of these factors are considered critical in developing more efficient, economically viable photocatalysts, especially for H₂ evolution reactions[128]. Such efforts have involved photocatalyst metal oxides such as GaN:ZnO[143, 144], SrTiO₂ [145] and Bi_{0.5}Y_{0.5}VO₄[146] in studies that have also shown the use of co-catalysts improve overall photocatalytic performance.

Some other surfaces used for these heterogeneous investigations include SiO₂, an inert support useful for determining the nanocluster's intrinsic activity in comparison to other, more active supports[147, 148]. Although it is abundant, economical and stable in many crystal forms, it has no photocatalytic properties. Due to availability and stability, quartz SiO₂ is the major crystal form utilised as a support. Attempts towards nano-sized impregnation using Ni have shown that such methods result in lower surface areas, pore volumes and dispersion of nano-species compared to other methods[149]. Impregnated SiO₂ also showed fragmentation after steam reforming catalysis. SiO₂ is also commonly used as a composite component for structural substrates such as sol-gels [150]. The increased porosity and surface area of SiO₂ sol-gel particles result in uniform pore size suggesting a mesostructured support capable of increasing [150]. SiO₂ has been of particular interest with Ni nanocatalysts. The use of sol-gel[150] and fumed SiO₂[151] has demonstrated increased performance of these catalysts on SiO₂, possibly explained by the interaction between Ni and SiO₂ surfaces controlling Ni particle size through etching resulting in improved ammonia-borane hydrolysis[151]. For other metals, however, the weak interaction between SiO₂ and compared to other oxide surfaces (TiO₂, FeO₂) has been identified through Pt₃ nanocluster agglomeration on SiO₂ surfaces without significant pre-treatment for defect creation as well as higher required operating temperature to achieve similar results [152]. Poor catalytic results for benzyl alcohol oxidation have also been observed in Au nano clusters on fumed SiO₂ when compared to alternate substrates[147].

Magnesium oxide has been viewed favourably for its usefulness in heterogenous catalytic systems. As an organic ceramic with versatile uses and high chemical reactivity, it is useful as a homogenous catalyst and a strong candidate for nanocluster-support systems. It has an octahedrally coordinated crystal structure, resulting in a diamagnetic material with a wide band gap of 7.8eV for bulk[153]. The synthetic method is crucial in determining the properties and subsequent utility of MgO as support. Decomposing Magnesium salts can result in MgO with high grain size variation, small surface area, and many defect sites[154]. To better control these variables and subsequent catalytic properties, synthetic methods via sol-gel, chemical precipitation, and thermal decomposition have been established[155]. Using various Mg precursors in synthesis can also affect and tailor the basicity of the support and change the catalytic nature of the resultant MgO[156].

The primary drawbacks of MgO as a support are its thermal instabilities, leading to sintering and loss of properties such as high surface area and defect sites crucial for nanocluster heterogeneous systems. These limitations are compounded by the ionic nature of the oxide, leading to dissolution in acidic solutions and strong sintering in aqueous environments[157], ruling out the wet preparation of MgO heterogeneous systems.

MgO has shown many useful results in nanocluster-assisted heterogeneous catalysis as a chemically inert substrate. MgO is also a useful model surface showing promising catalytic potential in single-crystal studies. Pd on MgO(1 0 0) revealed CO oxidation was possible at 260 and 500K and that surface defects played an important role[158]. Studies on larger Pd₁₃ clusters again show that non-symmetric Pd clusters can exhibit lower activation energies on MgO supports, facilitating useful reactions such as CO oxidation and Acetylene polymerisation when surface bonds form on the removal of the protecting ligands[159]. These reactions can occur down to cryogenic temperatures.

Studies on catalysis over Pd and Pt nano catalysts showed that the MgO(100) substrate had some effect on stabilising and affixing adorned metal species relative to each other but no noticeable effect on interatomic spacing or chemical activity and poor improvement of charge transfer[140]. Ni clusters on MgO have been predicted to have substrate-induced stability improvements beyond those of Pd and Pt[160]. Experiments using Ni on ultrathin MgO films show Ni clusters forming through oxidation at the interface, leading to 2D nanocluster morphology[161] that is not predicted to appear on other oxide surfaces, highlighting these materials' affinity. MgO surfaces are also shown to be capable of controlling Au nanocluster growth to nanoclusters approximately 30Å in size regardless of initial nanocluster size[162], effective for CO oxidation.

TiO₂ has shown perhaps some of the most promising results towards heterogeneous nano-catalytic systems, especially when coupled with co-catalysts. TiO₂ has also been shown to specifically enable Au clusters catalytic activity over other supports such as SiO₂ and BN, which show no influence on nanocluster properties[33]. The relatively wide band-gap of titania (3.2eV for Anatase and 3.0V for Rutile) in its most common forms means that its photocatalytic activity is only active for the UV region, around 4% of the total solar spectrum. Given that the band-gap of TiO₂ is a limitation towards photocatalytic homogenous catalysis, treatments have been explored to overcome this include doping with transition ions including Fe, Mo, and Ru[163] to induce band-gap narrowing. However, this approach often traps electron-hole pairs in the substrate bulk, allowing recombination before reaching the surface where useful reactions occur. Engineering heterojunctions with smaller band-gap semiconductors (CdS, GaAs) is also possible but has toxicity and facile photodegradation drawbacks [164]. It is worth noting however, that metal nitride nanowire photocatalysts, using InGaN and GaN have shown photocatalytic performance under irradiation at wavelengths up to ~560 nm with efficiencies of up to 13% in the visible spectrum[165]. Tuning supported catalysis through optimising charge transfer and stability with nanocluster adornment offers a more versatile and effective route while minimising charge recombination.

Whether TiO₂ has been prepared via sol-gel routes[166, 167],[168], Magnetron sputtering [169-171], or structural layers [30], the higher surface area supports exhibit common characteristics of

more defect and therefore binding sites, and increased charge migration to the surface. Phase-mixing of TiO₂, such as in the case of P-25 nano-particles, has shown decreased electron-hole recombination[172], allowing charges to migrate to surface species more efficiently. TiO₂ Nano-particle size can be effectively controlled through synthetic parameters [173] to further optimise the charge transfer mechanism and tune titania phase type and catalytic performance.

In pursuing nanocluster-assisted heterogeneous catalysis and solar fuel synthesis, the relative stability of TiO₂ surfaces and photocatalytic nature make them the preferred catalytic support over MgO and SiO₂. Especially in the case of Au catalysts, where there are established examples of improved heterogeneous catalysis[115]. This is not to discount the usefulness of the other oxide support for different metal clusters[158] and catalytic reactions[151].

1.2.4 Au/TiO₂ Heterogeneous Nanocluster Catalysis

Titania, owing largely to its intrinsic stability and simplicity, its photocatalytic activity, easy and varied preparation methods and usefulness as a model system as a single crystal[23],[171, 174, 175],[176] has been thoroughly explored as a photocatalyst and nanocluster substrate. The suitability of single crystal models adorned with nanocluster to surface science characterisation techniques allowed new knowledge of how these systems act at working temperatures and under realistic pressures, aiding further tuning and catalyst design[177]. Single crystal studies showed that adorned metal clusters gain a negative charge at the metal-support interface, indicating charge transfer from TiO₂ to nanocluster active sites[178]. TiO₂ surfaces have also shown a specific affinity for Au adornment, with Au shown to be capable of completely wetting TiO₂ surfaces producing promising catalytic results[179].

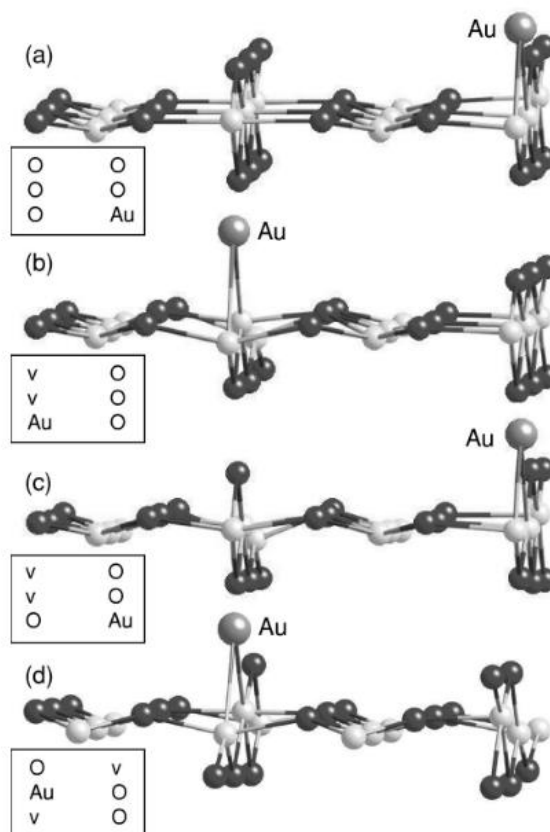


Figure 1-10 Simulated interactions between Au and a reduced 3x2 TiO₂ surface with vacancy sites. The inset boxes represent a top view of the system, with O denoting an bridging oxygen site and v denoting a vacancy. Au binding to vacancies is presented for (a) single vacancy system, (b),(c) and (d): three arrangements of multi-vacancy systems [180].

Optimising the Metal-Support interaction for properties like nanocluster stability, charge transfer, and catalytic efficiency is key to exploiting the properties of promising supports like TiO₂. Au clusters have been shown on rutile surfaces to diffuse easily on unreduced surfaces while binding strongly at defect sites, especially vacant oxygen bridging sites[180]. Au clusters have also shown some of the most significant stabilities and activity on defect-rich TiO₂[181]. Simulated models of reduced TiO₂ surfaces with bridging oxygen vacancies, such as those seen in

Figure 1-10 show the affinity between Au and reduced TiO₂. As the TiO₂ defects offer good stability and utility in combination with Au nanoclusters, alternative types of Titania have been explored to increase catalytic performance, chiefly nanoparticle TiO₂. Synthesis of mesoporous, nanoparticulate TiO₂ suitable for nanocluster attachment is possible through a range of synthetic pathways, including Sol-Gel fabrication[166]which can produce mixed-phase results when post-treated correctly[172]. RF[169, 171, 182] and DC[183] magnetron sputtering are also viable methods of nanoparticulate TiO₂ synthesis. These methods can produce different particle size, porosity and even band gap tuning[27] through post-synthetic annealing[169] processes providing a modifiable photocatalytic substrate.

The efficiency of charge transfer from support to metal nanocluster has been investigated and shown to be highly dependent on the DOS of the molecule-like nanocluster[184, 185]. Theoretical and experimental work done on HOPG using metal clusters supports this idea, showing the size and structure of d-band metal clusters (including Au) can undergo charge transfer due to valence electron structures[186]. These results suggest optimising the nanoclusters DOS into a 'goldilocks zone' where multi-step processes occur as the negative charges step-down from the support conduction band to the unoccupied clusters. These nanocluster-surface interactions are critical in unlocking the potential in heterogeneous photocatalytic systems[187, 188]. Control and characterisation of the DOS of attached nanoclusters and their stability on TiO₂ nano-particles are crucial to further photocatalytic efforts and will require further investigation.

1.3 Structural and electronic characterisation of clusters

The size, structure and electronic states of a nanocluster have all been firmly established as crucial to homogenous catalytic performance. Determining these characteristics is essential in exploring and developing homogenous catalytic systems. The techniques to reliably observe these factors have varied over time and between the different nanocluster/support systems, making comprehensive study and characterisation an involved and complex process utilising various techniques.

1.3.1 Structural characterisation

Determining the geometric configuration and arrangement of nanoclusters after synthesis is crucial in gas-phase and chemical synthetic methods. X-Ray Diffraction (XRD) has been highly useful in characterising the structure and phase state of both clusters[57, 189, 190] and their supports[25, 150, 191, 192]. XRD Au spectra can differentiate between atomic dispersions of gold and their bulk counterpart. Au/Fe₂O₃, after heating (400°C) under XRD showed characteristic diffraction peaks attributed to bulk/agglomerated Au[193]. Other studies have identified XRD line broadening in spectra of chemically synthesised clusters as denoting reductions in nanocluster size[57].

Pairing powder XRD with DFT calculations provides clearer pictures of synthesised particle size and structure with the detection of LSPR bands and structural shifts such as face-centred cubic (fcc) to non-fcc structures[117]. Similar work was done on metal nano-oxides, revealing a trigonal unit cell and the correlation of high DOS in the valence band with bond lengths between the Y, Bi, Cd and O s- and -orbitals[194]. As part of multi-experimental studies along with DFT predictions, XRD is also useful for the evolution of crystal phase and size under changing conditions for Cu nano-particles [195]. These developments have also allowed for precise determination and

confirmation of nanocluster size in size-selected synthetic products along with Nuclear Magnetic Resonance (NMR) and mass spectrometry[185, 196], providing mass size and resonance peaks for result confirmation.

No single technique is adequate for complete nanocluster characterisation. Various surface-sensitive techniques such as atomic force microscopy (AFM), transmission electron microscopy (TEM), scanning tunnelling electron microscopy (STEM), and a variety of spectroscopic X-ray techniques have investigated the homogenous interactions of metal-support catalysts[38, 197]. These techniques are often paired with theoretical calculations to check and refine nanocluster growth and activity models to propose mechanisms and characterise systems.

Scanning-style techniques such as AFM, TEM, STM and STEM have proven increasingly useful in imaging sub-nanometre and even atomic resolution nanoclusters on supports. AFM has found broad usage in its ability to give approximations of particle size on flat, ordered surfaces providing information on surface coverage, dispersion and particle size[183]. It is also useful in revealing the effects on size and dispersion after ligand removal processes [58]. However, the error in size determination is limited by tip resolution and surface aberrations, limiting its usefulness in commercially-minded, defect-rich systems. TEM is also useful for nanocluster size determination, perhaps more so as it shows a more accurate representation of nanocluster size limited only by device resolution and appropriate sample preparation. Size distributions using TEM have been used in a range of systems[198], [199] and can give good approximations of sample uniformity[35].

Scanning tunnelling microscopy (STM) can track and image small nanoclusters on surfaces but is also limited by the substrate and particle thickness. Early studies into metal clusters using STM focused on the technique's ability to image and characterise nanostructures[200]. These studies focussed on size characterisation through topographical imaging[200]. STM tips have also proved useful for depositing and then characterising single clusters from STM tips onto prepared surfaces. Bias pulses from the STM tip have shown the ability to deposit Nano structures down to 3nm in size, with pulse intensity and polarity contributing to changes in nanocluster type[201]. Clusters deposited in this method can also have properties such as their kinetic and thermodynamic stability investigated through STM-specific measurements[202].

STM has also proved particularly effective in tracking nanocluster agglomeration processes[203] on Au[204] and Pd[203, 205] particles. As the supporting surface's morphology, properties and defects are all crucial to these processes, STM's ability to detect features such as point defects on a surface allows the measurement and characterisation of such sites[206]. Formations of nanocluster thin films are also readily investigated with this technique. Surfaces prepared with defects[207] or ordered lattice-like structures[208] can be mapped before and after nanocluster deposition to reveal structural phenomena and electronic changes in the films.

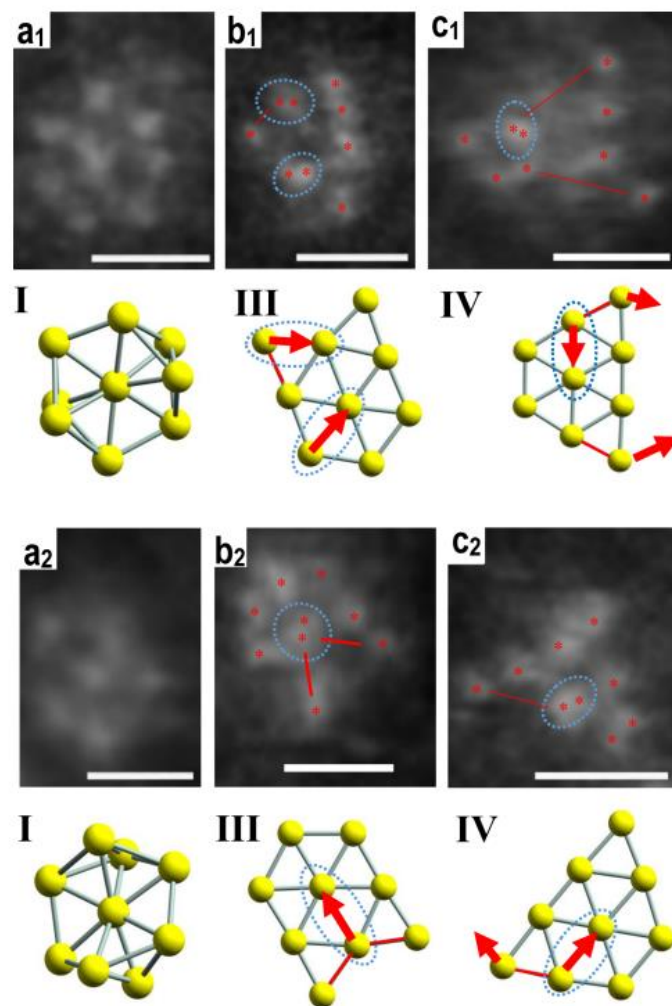


Figure 1-11 High resolution, aberration corrected HAADF-STEM images of Au₉ nanoclusters on TiO₂ nanosheets alongside DFT models of the same nanocluster showing the variety of nanocluster geometric structures observable in experimental depositions [196].

Scanning tunnelling spectroscopy (STS) also allows for observing quantised energy states on surface clusters similar to those seen in Ultra-violet Photoelectron Spectroscopy (UPS)[209]. This technique has proved useful for elucidating supported nanocluster electronic states across various nanoclusters[210-212]. These investigations allow fundamental insight into nanocluster ripening and agglomeration processes, offering insight into efforts to mitigate nanocluster size dispersion.

Scanning Transmission Electron Microscopy (STEM) has proved useful for studies on the dispersion and structure of nanoclusters once deposited onto supports. The ability for STEM down to image metal clusters and their particular morphologies to atomic resolution[213] allows for the correlation of DFT structures to experimentally observed images. This technique has proved effective in analysing metal clusters supported on oxide thin films[214].

Dispersion of the metal nanostructures and size-specificity can also be checked through STEM observations[215, 216]. Studies of Au nanostructures on thin carbon films revealed the Au's tendency to move and agglomerate on the surface under electron beam probes while binding strongly at defects[217]. The effects of agglomeration and electron-beam influence were observed

to be greatest for particles over 2nm in size. Surface functionalisation, such as sulphur-washed graphene supports, has been observed through STEM for these treatments' ability to bind Au clusters, preventing lateral displacement; however, nanocluster agglomeration can still occur in such systems[218].

Recent advances in Scanning Transmission Electron Microscopy (STEM) have allowed some of the first atomic-resolution images of Au₉:PR clusters on ALD TiO₂ surfaces[196]. Similar techniques have been used for Au on carbon supports[217, 218]. 3-D structures capable of distinguishing different nanocluster geometries have also been achieved using similar methods[174]. The interactions with clusters of low stability and the electron beam have been shown to influence nanocluster states and mobility[219]. These results have only been made possible by modifications to STEM instruments to correct for these electron aberrations, allowing for sub-angstrom resolutions[220]. These achievements in resolved imaging allow for true comparison between DFT-calculated nanocluster morphologies and real, observed structures interacting with supports. This kind of technique is useful for the characterisation of larger clusters as well as clusters with different supporting ligands[221].

1.3.2 Electronic Characterisation

Some of the primary techniques to examine the electronic states of clusters and their supports have been based on X-ray spectroscopy. Variants of X-ray characterisation techniques such as Grazing-incidence small-angle X-ray scattering (GISAXS), X-ray absorption fine structure (XAFS) and XPS are all widely reported for characterising different features. XAFS can give localised geometric information and the identities and number of neighbouring atoms[222]. XAFS has been used in studies of chemically synthesised clusters to determine interatomic coordination as well as electron orbital band analysis, providing insight into ligand-supported Au₂₅ and the role of the ligand in electronic structure for catalysis[223]. The internal structure and influence of supports on bi-metallic clusters have also been investigated through XAFS techniques, revealing the influence of synthetic methods and nanocluster-support interaction on the final structure[224, 225].

The sub-technique of Atomic-XAFS, where the outgoing electron scatters due to the electron cloud of the absorbing atom, has proven its ability to observe electronic changes in ionisation potential and electronic structure[226]. XAFS has also become specialised for catalytic analysis over the last 15 years, allowing in situ time-resolved measurements to observe charge transfer and redox structural changes during catalytic processes[226, 227]. Experimental progress at synchrotron beamlines, such as the photon factory, has also enabled XAFS to observe surfaces at near atmospheric pressures (NAP)[228]. This progress allows for the investigation of hetero and homogenous under near-working conditions and applies to NAP XPS measurements.

STM also contributes to electronic investigations, with the electronic interactions at the tunnelling tip of an STM providing strong, measurable interactions. Semiconductor surfaces are well suited for such measurements, which has allowed the measurement of electronic interactions in small metal clusters and semi-conductor supports[229]. The interaction of tunnelling electrons and clusters has proven capable of inducing photon emission, with observations at specific sites and sizes of nanoclusters pointing to quantum size effects[212, 230]. These effects have been linked to the size and structure of clusters, such as in the case of Au on TiO₂[231], suggesting that the electronic characteristics of heterogeneous photocatalytic systems could be investigated in this manner.

XPS has been useful in catalysis for determining the elemental composition of various treatments, oxidation states and even nanocluster size effects. XPS spectra of Au clusters have been performed since the 70s, with XPS sensitivity to atomic variation useful in establishing oxidation states of synthesised clusters[232]. Oxidation state observation is also important in heterogeneous nanocluster catalysis as understanding the role of defect sites in binding clusters improves. XPS has been extended to determining surface concentrations such as oxide surface hydroxyl groups[233] and reduced titania surface sites[234]. However, the XPS scans receive information from below the sample's absolute surface, where nanoclusters are deposited, and must therefore represent some sub-surface structure.

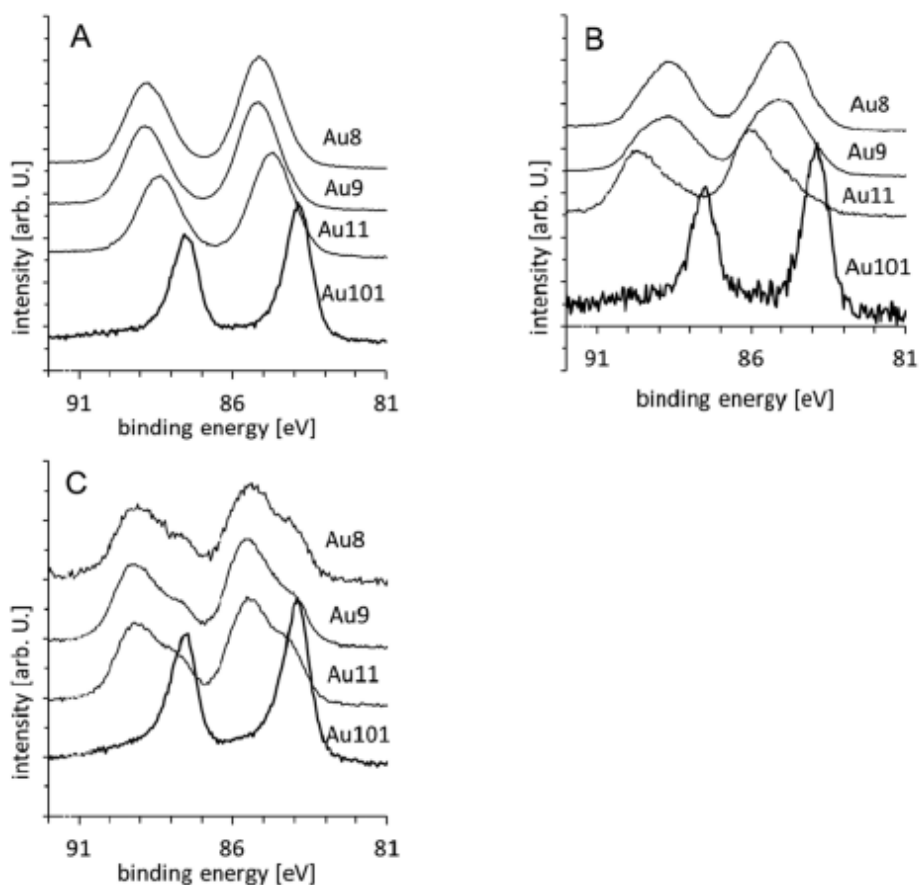


Figure 1-12 Synchrotron XPS spectra of chemically synthesised, atomically precise Au₈, Au₉, Au₁₁ and Au₁₀₁ nanoclusters in (A) untreated, (B) acid-washed and (C) calcined states, showing the distinct shifts in Au 4f peak binding energy with change in nanocluster size. The ~1.1 eV difference in binding energy observed for Au₁₀₁ indicates the onset of metallic properties associated with Bulk Au at that nanocluster size [235].

Defect characterisation is more suitable for XPS as it does not have to be quantitative. XPS on nano-particle TiO₂ (anatase) was able to identify Ti³⁺ defects' location and quantity with the help of electron paramagnetic resonance[236]. By identifying the defects' location as sub-surface, these supports, and their defects could offer pathways for improving photocatalytic performance or nanocluster attachment. Other defect studies on engineered TiO₂ nano-particles also used XPS defect identification and shifts in characteristic peaks to help explain changes in the band gaps of said nano-particles [27]. The defects in ZnO surfaces have also been characterised through XPS scans in conjunction with SEM and XRD[237].

Quantum size effects can also be quantified through XPS measurements, as clusters show characteristic binding energy shifts to higher energies as nanocluster size is reduced, as seen in Figure 1-12. Such observations in gas [238] and chemically synthesised nanocluster species[44] have been made using synchrotron XPS sources. The understanding for Au clusters is that clusters less than Au₁₀₁ in size have a +0.8-1.0eV shift in the 4f region, allowing for the identification of agglomeration effects on ultra-fine clusters. Similar XPS investigations of the growth and diffusion of Au clusters on polystyrene have shown the ability to track changes in the

clusters during different growth stages, excluding the need for potentially destructive analysis from AFM and scanning electron microscopy (SEM)[239]. Similar results have been seen for Ru nanocluster characterisation[240].

XPS investigations have confirmed through comparative measurements on pristine and reduced rutile TiO₂ surfaces that charge transfer from the reduced surfaces to the nanocluster is detectable [241]. Synchrotron XPS measurements have also been used to investigate the effects of ligand removal on clusters showing that phosphine-capped clusters on various treatments of anatase TiO₂ display differing levels of agglomeration and ligand removal dependant on the treatments pre and post-deposition on the support[189]. Proposals for time-resolved investigations in working conditions would allow observation of changing oxidation states and charge transfers throughout catalysis and further understanding of agglomeration [228].

While XPS is a useful surface-sensitive technique in UHV conditions, it is not *surface-exclusive*. Some signals originate from bulk materials within particles and beneath the homogenous interface[242]. A technique such as Metastable Induced Electron Spectroscopy (MIES) is necessary for investigations of surface-dependant structures like homogenous catalysts. MIES gives similar information on DOS to established techniques such as UPS, but due to a meta-stable ion beam used as the probe as opposed to a photon does not penetrate beyond a few Angstrom of the surface, stimulating an electron from the valence band of the surface species to provide DOS at the surface only[243]. This technique has been recently used to establish chemically synthesised, size-specific Au₉ nanocluster DOS on TiO₂ nano-particle support[185]. The kind of investigation performed here shows great potential in being useful for a range of homogenous catalysts with DOS-determined activity.

From the multiple surface analytical techniques presented, no one technique can be relied upon for a complete understanding of the structural composition and electronic structure of heterogeneous nanocluster catalysts. In structural studies, the speed and simple requirements for SEM and AFM allow rapid imaging of catalyst surfaces. Still, they require conducting (or coated) samples or relatively smooth substrate surfaces, respectively, to produce useful and easily interpretable results. STM and its close cousin STS have proved very useful in structural and electronic studies, and their surface sensitivity is very good for nanocluster investigations.

Of the electronic techniques, XPS is very useful across a range of metal clusters for determining nanocluster size. However, these effects have not yet been observed in all metals of interest and are not precise enough to determine the exact number of atomic constituents. As such, it should primarily only be considered as a mechanism to validate, and understand shifts in the effects of nanocluster size and to assist in interpreting other techniques. It is more broadly useful for characterising support surfaces and defect sites for deposition. XAFS, with its more flexible vacuum requirements and ability to probe electron orbital states, may be useful for charge transfer

observations and can operate in real-time, allowing for the observation of catalytic processes as they occur, something not yet done in many heterogeneous systems. The drawback of such a system, in addition to its complex and specialised equipment requirements, is common among x-ray techniques in that signal received is excited from both the surface and the near-surface bulk layers.

Bulk signal contributions do not allow surface-only phenomena to be easily separated from bulk interactions. Surface-exclusive techniques such as MIES are capable techniques that, with well-designed experiments, can reveal much about surface DOS. However, the requirement for extremely clean, well-characterised surfaces and UHV conditions can make MIES experimental design and analysis challenging. The findings of MIES require careful experimental design and sample preparation to give the greatest information regarding the electronic structure of surface electronic structures.

1.4 Conclusion

There are many factors to consider in creating heterogeneous catalytic systems using metal clusters. While early developments in inverse micellar synthesis and micro emulsions have produced some effective clusters, the intrinsic limitations on those systems limit the options for creating and utilising new clusters. The relative plethora of options in reducing agents, capping species and metal reactants available in the technique of chemical reduction of metal salts in the presence of stabilisers make it a far more flexible synthetic pathway. The wide range of metal clusters synthesised and characterised this way provides options for catalysis from <1-100nm in size. The properties and controls over nanocluster synthesis are being further revealed with promising options such as thiol ligand length and bi-dentate ligands offering greater customisation of size and stability.

Theoretical calculations have provided tremendous insights into the source of stability in small metal clusters. The work on “magic clusters” and the changes in nanocluster stability due to atomic constituent numbers have helped reveal the previously unexpected properties in catalytic results. The closed-shells of magic clusters provide reference points for nanocluster design. At the same time, theoretical calculations reveal the vastly different electronic states possible within different conformations of clusters, even at the same atomic size. The unique nature of these energy DOS point towards the potential of clusters as catalysts that could be tailored for specific reactions.

By supporting these clusters on appropriate surfaces, the specific sizes, conformations and electronic properties they bear can be preserved and potentially enhanced. While inert supports such as SiO₂ and, to some degree MgO have proved effective for certain types of clusters and

certain reactions, one of the most promising areas for nanocluster catalysis is paired with photocatalytic semi-conductors such as TiO_2 . The potential for precisely selected clusters deposited on TiO_2 to catalyse fuel-producing reactions would provide pathways to storing solar energy and transitioning away from traditional carbon fuels. Early results in this area are promising, but as with all nanocluster catalysts reported, preserving the nanocluster properties through effective immobilisation and charge transfer is crucial. Defect sites and surface functionalisation are both effective pathways to this goal, but neither is complete in understanding the final effects on nanocluster activity.

In order to understand and refine these systems the analytical methods used must be appropriate. With the wide range of surface-sensitive techniques available to investigate nanocluster structure, electronic state and the bonding between nanocluster and support, there are now established methods to characterise nanocluster's behaviour on supports. With new techniques offering the ability to determine specific DOS in heterogeneous systems, the correlation between simulated theory and practical reality can be bridged. While techniques must be carefully chosen and designed to be suitable for these delicate systems, the tools and methods required to determine the potential of nanocluster catalysis can be focussed on building systems that deposit, characterise, and preserve the specific properties of nanoclusters.

1.5 Aims and Scope

Metal nanoclusters have shown promise in delivering novel avenues in renewable, catalytically-driven energy conversion and storage. Size-specific cluster properties have become apparent that are determined by the nanocluster size and morphology. Chemically synthesised, ligand-supported nanoclusters have been shown to offer highly effective size control through the synthetic process and a high degree of stability while ligated. The chemical synthesis of nanoclusters also has the advantage of being highly scalable. It offers many synthetic pathways, both in nanocluster core elements and in capping ligand types. However, nanoclusters often require the removal of ligands to facilitate their catalytic activity and the retention of nanocluster size-specific properties after ligand removal has been a challenge. Modifying substrates before nanocluster deposition has been proposed as a potential solution to improve substrate-nanocluster interactions.

The materials discussed in this dissertation are: TiO_2 as a photocatalytic semiconductor substrate and both Au and Ru species of chemically synthesised nanoclusters. This project aimed to synthesise and characterise systems of modified TiO_2 substrates deposited with nanocluster species to determine the nanocluster size, dispersion, chemical state and electronic structure before and after the deposition and de-ligation of nanoclusters. The characterisation of these systems will assist in informing and optimising investigations into Au and Ru nanocluster

photocatalytic performance, which is determined by the nanocluster co-catalysts electronic structure and interaction with its photocatalyst support. However, certain challenges need to be overcome to allow for investigation into the impact of such treatments on nanocluster/substrate systems' electronic and physical properties.

The scope of this work focused on several specific challenges to surface-sensitive measurements used to characterise nanocluster properties. Firstly, existing methods of TiO₂ preparation, such as doctor-blading, drop and spin-casting of TiO₂ thin films, proved to be fragile and unreliable in adequately eliminating substrate signal from Si and C species in commonly used substrates, which was capable of dwarfing Au signal and DOS in XPS and UPS/MIES measurements respectively. A more robust method of coating TiO₂ thin films, which reduced or eliminated unwanted elemental intensities, was sought. The desirable characteristics of any candidate method included nanoparticulate TiO₂ structure and the ability to tune the TiO₂ crystal phase structure proportions. The preparation of such films through the development of radio frequency plasma sputtering techniques was seen to have the potential to deliver the desired characteristics and was investigated through synthesising a range of TiO₂ film deposition methods. A full characterisation of the elemental composition, film integrity and crystallinity of the TiO₂ films produced was sought.

Secondly, the challenge of investigating the changes and final states of electronic structures and interactions between chemically synthesised nanoclusters and TiO₂ semiconductor supports requires a new system for depositing nanoclusters onto modified semiconductor supports. Legacy techniques for such depositions require the removal of samples from the vacuum between surface treatments and the nanocluster deposition, which requires sample immersion in solvated clusters. This can introduce atmospheric and environmental contamination and potentially alter the surface treatment condition before a measurement. *In-situ* deposition of solvated nanoclusters is a pathway that would allow for the effects of modification on semiconductor substrates and their interaction with subsequently deposited nanoclusters to be isolated and examined by highly sensitive, surface-specific techniques without introducing contaminating species or agglomerating nanoclusters during deposition.

This thesis is structured in the following manner:

The synthetic process, compositional and morphological analysis, and electronic structure of a method of depositing thin, nanoparticulate TiO₂ films using an RF-sputtering technique are described. The desirable conditions for preparing such films are determined, and possible modifications to film composition, crystallinity and electronic structure are explored. (It should be noted that this chapter is a re-formatted version of a paper published by this author)

A novel method for depositing solvated, chemically synthesised Au nanoclusters under high vacuum (HV) conditions onto various substrates is explored. It is demonstrated that this method,

named pulsed nanocluster deposition (PNCD), can use ultrasonic pulses of solvated Au nanoclusters to produce sub-monolayer nanocluster films on a substrate surface. The effects of this method on cluster agglomeration, morphology and electronic properties are explored. (It should be noted that this chapter is a re-formatted version of a paper published by this author)

A comparative study between immersion and PNCD Au nanocluster deposition methods onto modified TiO₂ substrates is discussed. Results from an investigation into each method's respective impact on substrate treatments, elemental composition, levels of nanocluster agglomeration, and electronic structure are presented along with respective XPS and UPS/MIES results. This comparison is undertaken from measurements taken at three stages of sample preparation: After substrate modification, after nanocluster deposition and after the removal of nanocluster ligands. (This chapter has been prepared for submission for publication and, as such, is a modified version of that manuscript)

A case study is presented, which describes the design, investigations and results for a system for co-deposition of Au and Ru nanoclusters *in-situ* in HV conditions. This investigation was designed to probe the impacts of depositing two nanocluster species independently and through distinct *in-situ* methods onto a modified TiO₂ substrate. The DOS of the system was probed at each stage of sample preparation to determine whether the co-deposition of multiple nanoclusters on modified substrates would interact. Such interactions may provide a pathway for tuning photocatalytic system electronic structure and DOS. However, challenges with co-deposition methods and surprising Ru nanocluster behaviour mean that the chapter serves as a proof-of-concept for *in-situ* HV co-deposition of chemically synthesised nanoclusters. (As this chapter is the only chapter not published or prepared for publication, it should be noted that the structure of the chapter may contrast previous results chapters)

2 EXPERIMENTAL METHODS

2.1 Electron Spectroscopy

2.1.1 Photoelectron Overview

Photoelectron spectroscopy covers the range of techniques which rely on the ejection of electrons from a target surface due to electromagnetic excitation. The kinetic energy of the ejected electron can be described using Einstein's photoelectric equation,

$$E_{kinetic} = E_{photon} - (\phi_{spectrometer} + E_{binding}) \quad \text{Equation 2-1}$$

Where E_{photon} is the energy of the incident photon, $E_{binding}$ is the binding energy of the electrons from the surface and ϕ_{spec} is the work function of the spectrometer. By knowing the energy of emitted photons and the spectrometer's work function and measuring the kinetic energy of the ejected electrons, the binding energy of electrons can be determined. Depending on the incident energy of the photons, and the valence or core orbital energy levels of the target material, electrons can be ejected, as seen in Figure 2-1, allowing detection. The chemical species, electronic state and oxidation state of an electron's origin element can all be determined. The incident photon's energy will determine whether a target valence or core electrons will be ejected and therefore detected. Valence electrons exist in outer orbital shells and can be excited past the fermi level with lower energy. Core electrons exist closer to the nucleus and, due to increased forces, require more energy from incident photons to achieve ejection.

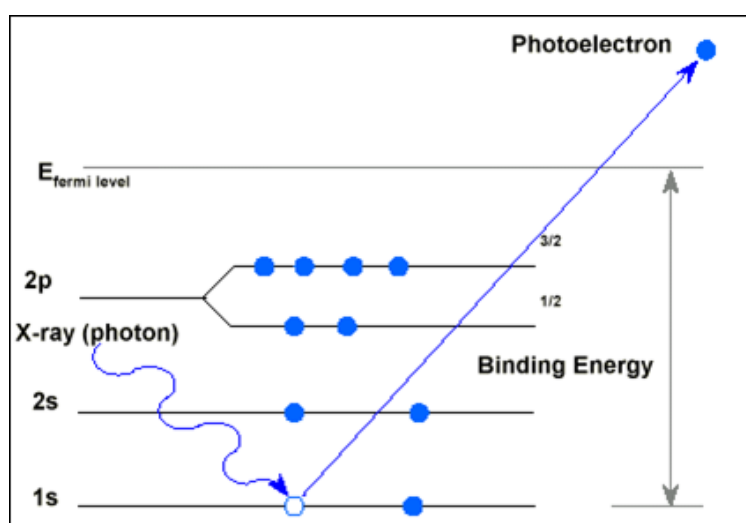


Figure 2-1 Diagram illustrating the excitation of core-level electrons through X-Ray illumination.

Photoelectron spectroscopy is considered a surface-sensitive analysis technique due to the emitted electrons' inelastic mean free path (IMFP). This IMFP is the average distance an electron will travel before interacting with surrounding electrons or atoms. For an electron between 10-1500eV energy, the IMFP is between 1-10nm. The intensity of an electron as it penetrates through a given material is described by:

$$I(d, E) = I_0 \exp\left(-\frac{x}{\lambda(E)}\right) \quad \text{Equation 2-2}$$

Where I is the measured intensity, I_0 is the initial electron energy, x is the electron's total displacement, and λ is the experimentally determined path length of an electron, which varies at different energies. For typical measurements with XPS, electrons will have binding energies below 800 eV. At the same time, ultra-violet spectroscopy (UPS) will generally focus on electrons with binding energies of less than 15 eV. Using photoelectron spectroscopy; useful information is gained solely from the surface and near-surface regions.

2.1.1.1 X-Ray Photoelectron Spectroscopy (XPS)

The core electrons emitted by XPS will carry the information of their parent atoms' energy levels, depending on chemical and bonding state, unless they undergo some secondary interaction before reaching the detector. This is useful for identifying the elemental composition of samples, as each orbital has a characteristic binding energy (see fig 10). The X-Rays used to excite these electrons are from either Al K_{α} ($E_{\text{photon}} = 1486.6\text{eV}$) or Mg K_{α} ($E_{\text{photon}} = 1253.6\text{eV}$) source anodes, K_{α} denotes the transition used to produce X-Rays.

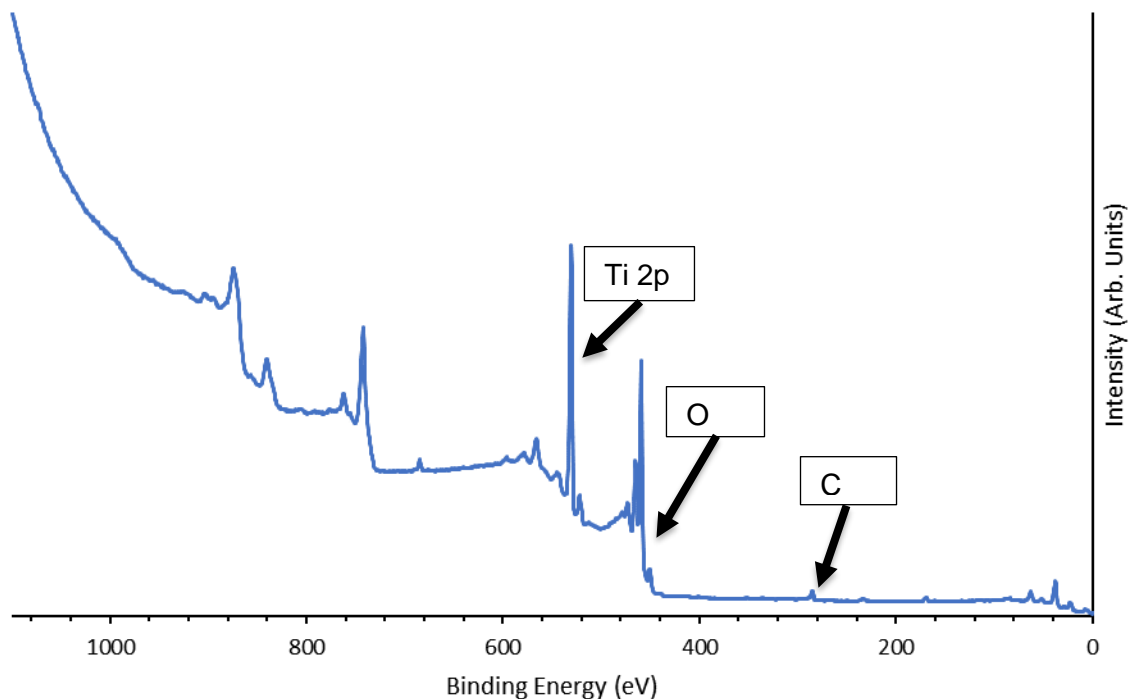


Figure 2-2 XPS scan trace recorded from a sample of TiO₂ indicating the characteristic peak positions for Ti 2p, O 1s and C 1s orbitals

Two possible processes can occur when using X-rays to excite electrons: Photoelectron emission and Auger electron emission. The photoelectrons are the product of direct energy transfer from the photon to the electron resulting in emission, and binding energies from this process are found at defined energy levels with sharp peaks, as seen in. These photoelectrons are the primary interest of XPS in general and this study. Auger electrons occur as the result of electron relaxations within the core of the irradiated atoms. The hole left behind by a photoelectron emission is filled by an electron from a higher energy level relaxing into the lower state. The excess energy from this process is either emitted as a photon or transferred to another electron which will subsequently eject from the sample. These auger peaks do not have a fixed binding energy, so they can appear relatively rounded and occur at different positions depending on the X-Ray source used.

Finally, non-monochromatic X-Ray sources (such as the one used in this work) exhibit some minor X-Ray components at higher photon energies. These components cause "Satellite" peaks with intensities and spacing determined by the characteristics of the anode material[244], see Table 2-1.

Table 2-1 X-Ray satellite energies and intensities for Mg and Al X-Ray Sources [244]

	$\alpha_{1,2}$	α_3	α_4	α_5	α_6	β
Mg displacement, eV	0	8.4	10.1	17.6	20.6	48.7
Relative height	100	8.0	4.1	0.6	0.5	0.5
Al displacement, eV	0	9.8	11.8	20.1	23.4	69.7
Relative Height	100	6.4	3.2	0.4	0.3	0.6

2.1.1.2 XPS Analysis

Key information gained from XPS is the binding energy position, full-width half maximum (FWHM) and the peak intensity, inferred from the peak area. These values can be compared to literature reference data[244], allowing the composition of a sample can be identified. Observed shifts in peak energy can indicate chemical changes as electron distribution is altered. The peak intensities are calculated using *Equation 2-3*;

$$Intensity = \frac{Peak\ area\ of\ Component}{S=f\sigma\theta y\lambda AT\ (Atomic\ Sensitivity\ Factor\ of\ Element)} \quad Equation\ 2-3$$

Where the atomic sensitivity factor is expressed as $S = f\sigma\theta y\lambda AT$ with f being x-ray flux (photons/cm²sec), σ being the photoelectric cross-section of the orbital being examined (cm²), θ being a constant determined by the measuring instruments angle between photon and electron paths, y being photoelectron formation efficiency, λ being electron mean free path, A being the area of sample from which detection occurs and T is the detection efficiency of emitted electrons from the sample. Peak positions and peak areas were calculated using a custom-made Excel spreadsheet to fit Gaussian peaks using known peak separation from the XPS reference handbook and NIST XPS Database. For Au 4f peaks, peak separation was set to $\Delta 1.4eV$ per literature values. All peaks were calibrated against the C 1s peak known to appear at 284.8eV in the XPS setup. Atomic sensitivity factors were taken from the XPS handbook for an analyser angle of 54.7°, summarised in Table 2-2, which matches the angular arrangement of the experimental setup used in these studies. Once peaks had been assigned an elemental species and peak fit, giving position and peak area, the composition can be determined using *Percentage Composition*=

$$\frac{Specific\ Intensity}{Total\ Intensity} \times 100 \quad Equation\ 2-4;$$

$$\text{Percentage Composition} = \frac{\text{Specific Intensity}}{\text{Total Intensity}} \times 100$$

Equation 2-4

Table 2-2 Atomic Sensitivity Factors for X-Ray Sources at 54.7°[244]

Element	Atomic Sensitivity Factor (54.7°)
Carbon 1s	0.296
Oxygen 1s	0.711
Silicon 2p	0.339
Titanium 2p	2.001
Gold 4f	6.250
Ruthenium 3d	4.273
Phosphorus 2p	0.486

Doublet peaks are also accounted for in peak fitting. These sets of 2 peaks form the same elemental orbital that are similar in shape but different in peak position and intensity. They exist due to the quantum multiplicity of states; $2j + 1$ where j is the quantum number $j = l + 1/2$ where l is the azimuthal quantum number. For Au 4f $l = 3$ and the intensity ratio between the doublet

p
e
a
k
s

$$2 \left(l - \frac{1}{2} \right) + 1 : 2 \left(l + \frac{1}{2} \right) + 1$$

Equation 2-5

The XPS apparatus employed for these experiments used an Xr50 X-Ray source. All measurements were performed on the Mg anode, with 12kV accelerating potential and 200W of anode power. The Hemispherical analyser used was a PHOIBOS HAS 150. Wide angle lens settings gave a beam diameter of 5mm. Survey spectra were done at a pass energy of 40eV, and high-resolution scans were performed at 10eV pass energy. All scans were done with a detector voltage of 3200V. Higher numbers of scans were performed on areas of particular interest, such as

c
a

Au 4f and P 2p regions (120 & 40 scans, respectively, were generally used for these regions). During the same scan, species of lower intensity (including C, Ti, O) underwent a 20-scan regime. All data was collected using Specs Lab 2 before exporting into CasaXPS for peak fitting and then relevant peak information was exported into Excel for analysis.

2.1.2 Density of States and the Fermi Level

Some definitions of terms and characteristics are useful when interpreting electron spectroscopy from systems comprised of photocatalytic semiconductors and nanoclusters. As these systems involve semiconductors, the properties of valence bands, conduction bands and band gaps are crucial, as is the definition of the Fermi level and the electronic DOS.

The band theory of solids describes a bulk material's upper available energy states as being arranged into energy bands instead of discrete energy levels as found in single-atom systems. The bands of interest here are the Valence band, and the Conduction band. In a conducting material, these bands overlap so that some electrons can move or conduct through the material. Insulators have conduction and valence bands separated by such large energy (band gap) that the excitation of electrons into the conduction band is very difficult. Semiconductors have relatively low band gaps to insulators but no overlap of bands as in conductors. For a semiconductor, the Fermi Energy lies somewhere between the valence and conduction bands, normally halfway between the two as seen in Figure 2-3.

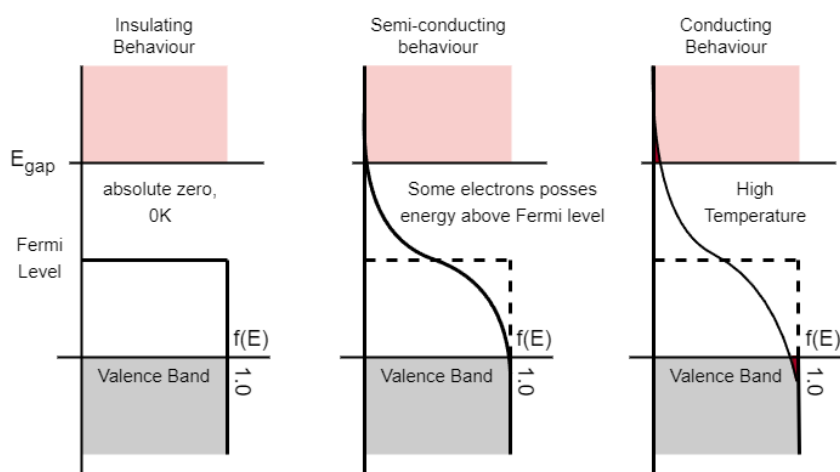


Figure 2-3 The changing conditions of the Fermi function within a semiconductor over a range of temperatures, note the small but noticeable probability for conduction band electrons in the third case (high temp.)

The Fermi level is a term, originating from Fermi-Dirac statistics describing the case where electrons, as fermions cannot occupy identical energy states due to the Pauli Exclusion Principle.

This means that at 0°K the electrons will fill all lowest available energy states, the Fermi level is then defined as the energy level above which no electron will be found at this temperature. As temperature increases the possibility for some electrons to rise above the Fermi level appears, obeying the Fermi function

$$f(E) = \frac{1}{e^{(E-E_f)/kT} + 1} \quad \text{Equation 2-6}$$

Where E_f is the Fermi level (in the range of eV for semiconductors), E is some arbitrary energy, and kT is the thermal energy. For most materials $f(E) \sim 1$ until the Fermi level, after which it rapidly approaches 0. This function is, therefore an expression of the probability that an energy state will be occupied for a given temperature. This can be seen in Figure 2-3, however it should be noted that while the fermi function expresses some finite value within the band gap region, no electrons will be found at these energies. The lack of electrons in this region is due to there being no DOS for them to occupy, hence the terminology of band *gap*.

The DOS is linked to the Fermi function in that while the function gives a probability of an electron being found at a given energy level the density of states, the electron cannot occupy a state unless one exists. The density of states is an expression of density per unit volume and energy of the solutions to Schrödinger's equation, or simply the number of available energy states in the material. The following equation expresses this:

$$N_{interval} = \rho_{energy}(E)dE \quad \text{Equation 2-7}$$

With $N_{interval}$ represents the number of available states in the energy range, dE , while $\rho_{energy}(E)$ is the density of states function, the bulk solution to the Schrödinger equation. Once the number of available energy states is found, it can be used in conjunction with the Fermi functions probability to describe the actual electron population at some specific energy.

$$f(E) \times N_{interval} = \text{Electron Population of the Interval} \quad \text{Equation 2-8}$$

2.1.2.1 Ultraviolet Photoelectron Spectroscopy

Ultraviolet (UV) light can excite electrons from within the valence band of a chemical species and cause them to be ejected as photoelectrons. This phenomenon underpins the ultraviolet photoelectron spectroscopy (UPS) technique, which involves analysing the kinetic energies of these ejected photoelectrons. The UV light source which excited the electrons in this work was generated from a helium discharge lamp, resulting in UV photons with 21.2 eV of energy, corresponding to He I discharge. Any photoelectrons which were ejected from a sample after

irradiation travelled through UHV to the same PHOIBOS hemispherical detector described in Chapter 2.1.1.2, with a -10V bias applied between the sample surface and the detector.

The -10V bias ensures that secondary electrons can be collected by increasing their kinetic energy. Such secondary electrons can be used to examine where the secondary electron cut-off appears and can provide insight into a material's work function Φ . Detectors in these systems bin detected electrons according to their measured kinetic energy, which includes the -10 eV, allowing for the calculation of binding energy through the following equation:

$$E_{binding} = 21.2 \text{ eV} - (E_{kinetic} + 10 \text{ eV}) - \Phi_{spectrometer} \quad \text{XPS Analysis Equation 2-9}$$

Therefore, the measured UPS spectrum of valence electrons represents the density of states for the measured sample, as described in Section 2.1.2. The spectra presented in this thesis are intrinsic semiconductors, meaning that their energy levels align in a way that means the Fermi level is at 0 eV [245]. The general structure of the spectrum is determined by the DOS of the surface species as described above. Some other features of the UPS spectrum are commonly shared with MIES scans and are therefore described below.

2.1.2.2 Meta-stable Induced Electron Spectroscopy

MIES is another electron spectroscopy technique with different use cases and excitation mechanisms. MIES' greatest attribute is its ability to gain information from the valence band electrons of the outermost layer of the surface of a sample. This exceptional surface sensitivity is possible through meta-stable helium ions (denoted He*) as the incident species instead of photons for XPS and UPS measurements.

The helium used in this process is in the He* 3s1 state, with an excitation energy of 19.8eV and is achieved through precisely controlled electrical discharge; this energy is sufficient to ionise valence electrons. With a lifetime of ~4000s under Ultra-high Vacuum (10^{-9} mbar) due to the $\Delta l = 0$ dipole transition characteristic. Quantum mechanical selection rules state that dipole transitions must have $\Delta l = \pm 1$ to be allowed. Instead, the He* can relax through a pathway that becomes available within a few Å of the target surface. Surface-exclusive sensitivity is achieved due to the extremely high cross-section for de-excitation of He* within the Å range of the surface.

The de-excitation process occurs through either Auger de-excitation (AD) or resonance ionisation (RI) with a subsequent Auger neutralisation (AN) [185]. These three possible processes are illustrated in Figure 2-4 and Figure 2-5. For an RI process, if the surface has an unoccupied state, Φ_p , then the He* can ionise as the electron in the He χ_b orbital tunnels into the sample surface,

leaving a He⁺ ion behind. A subsequent AN process will then occur to neutralise the He⁺; this occurs when an electron from the surface sheds energy and fills the vacant χ_a orbital in the He⁺, neutralising it to a He atom and causing the surface to absorb the lost energy and subsequently eject an electron. The ejected electron has kinetic energy E_k , while combinations of the Φ_i and Φ_j energy levels in the surface can lead to a broadening of detected features for an RI/AN spectrum.

In a surface without the unoccupied Φ_p state, RI is unfavourable, with AD processes instead allowing for a surface electron to transfer from the surface Φ_i state to fill the χ_a vacancy in the He^{*}. This interaction causes the He^{*} to eject the electron from its outer orbital χ_b with energy;

$$E_k = E'_i - E_{binding} \quad \text{Equation 2-10}$$

Of the two available pathways, Auger de-excitation (see Figure 2-5) dominates for the sample types in use here, including semiconductors, organic molecules and small metal clusters. The prevalence of AD is an advantage as the second process can make the interpretation of results much more ambiguous due to intrinsic complexities. The resulting ejected electrons are plotted as count rate/intensity vs binding energy, and the spectrum they form indicates the overall surface DOS.

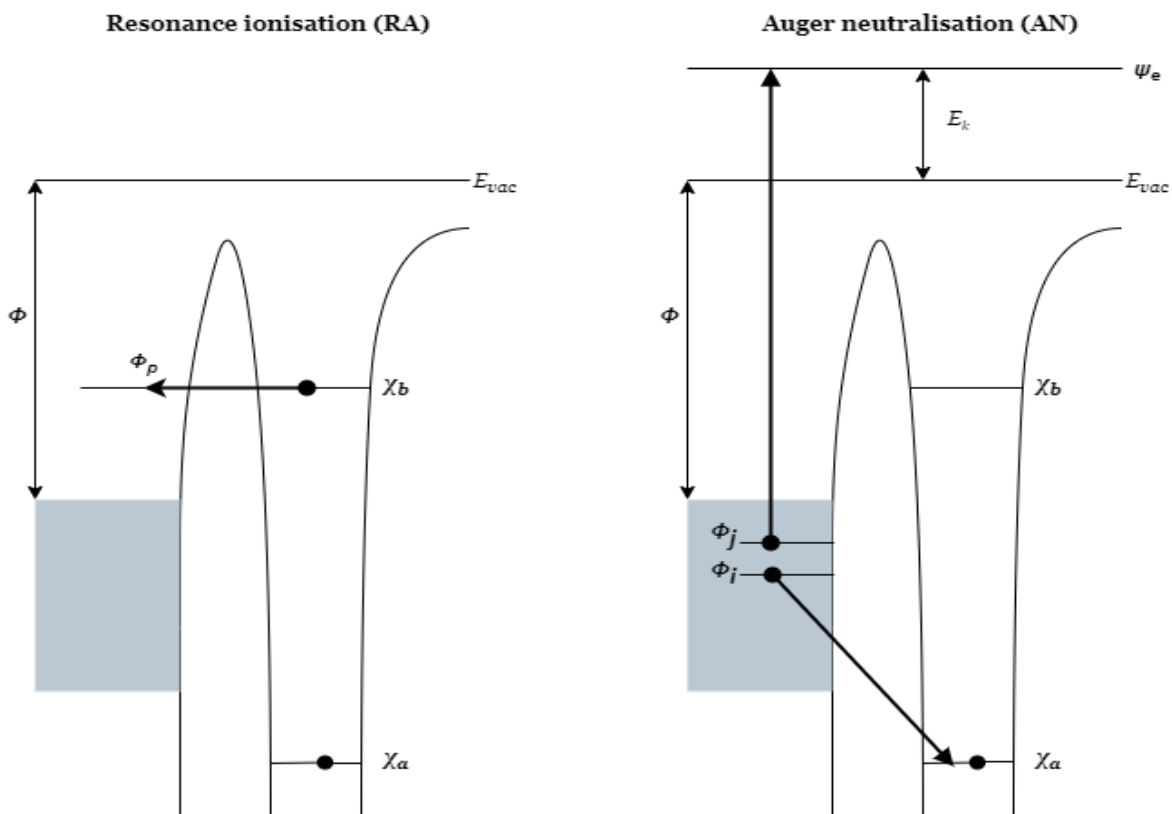


Figure 2-4 Representative diagrams of resonance ionisation and Auger neutralisation processes, modified from Harada et al.[246]

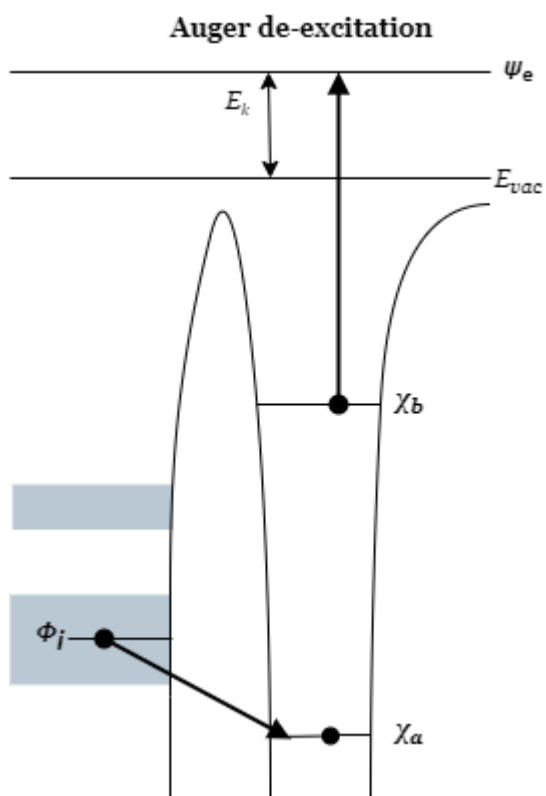


Figure 2-5 Schematic illustrating the process of Auger De-excitation (AD), the dominant process for He⁺ neutralisation in this study, modified from [246]

The MIES source used in this study was purpose-built by MFM Analytical systems (TU Clausthal) and used the same hemispherical analyser as for XPS and UPS. A 10V bias is applied to all tested samples to offset the spectrum and determine the exact point of secondary electron cut-off, which was accounted for in the analysis. The pass energy for these experiments was 10eV, with a dwell time of 0.1s and 3200 V detector voltage. Multiple scans were taken of each sample to check for variance and possible charging, with no charging observed. Multiple scans also reduced error and enhanced the signal-to-noise ratio.

2.1.2.3 MIES/UPS Analysis – Single Value Decomposition

Analysis was conducted in a custom-built Excel spreadsheet optimised for a process called Singular Value Decomposition (SVD). A set of MIES spectra measured under similar conditions can be considered a linear combination of reference spectra, each representing a common component throughout the series. If these reference spectra are well known, then specific features can be identified directly; however, often, they are not. For ambiguous spectra, the SVD algorithm determines how many base spectra are required to reconstruct the measured spectra. These base spectra have mathematical meaning; however, as they can have negative intensity, they do not necessarily have physical meaning. In the analysis technique developed by Morgner [247, 248], the required base spectra construct a matrix which is then multiplied by an ($n \times n$) matrix, with n being the number of base spectra. The elements of the ($n \times n$) matrix are then modelled with

criteria such that all reference spectra must be positive (and therefore physically meaningful) and that measured spectra must be reasonably fit with a linear combination of reference spectra as described by $I_{total} = \alpha \cdot I_{\alpha} + \beta \cdot I_{\beta} + \gamma \cdot I_{\gamma}$ Equation 2-11, which describes the requirement for a three-reference spectra system;

$$I_{total} = \alpha \cdot I_{\alpha} + \beta \cdot I_{\beta} + \gamma \cdot I_{\gamma} \quad \text{Equation 2-11}$$

Where α, β and γ are weighting factors while I_{α}, I_{β} and I_{γ} are the reference spectra. I_{total} must be equal to unity within the bounds of experimental error. Correlation with XPS data to identify likely DOS source elements is also useful and has been used in similar studies [185, 249]. The resulting spectra, once identified, provide insight into the DOS for the species of interest.

2.2 Surface Microscopy

2.2.1 Electron Microscopy Techniques

2.2.1.1 Scanning Electron Microscopy

Scanning electron microscopy (SEM) is a technique that uses focussed electron beams, as opposed to photons in optical microscopy, to scan rasterised patterns across a sample surface to build up an image from both backscattered and secondary electrons. The electron beam also produces Auger electrons and X-Ray fluorescence photons, although techniques using those signals are not explored in this work. The type of interaction caused by the electron beam with the sample surface affects the achieved images. The secondary electron intensity provides information regarding the topography of the surface. In contrast, the backscattered electron intensity can provide information regarding the atomic weights of the constituent elements in the sample. The intensities of these electrons are recorded for each location in the rasterised scan trace.

Electrons are accelerated to energies between 1-30 keV before passing through a series of magnetic condensers, objective lenses and electromagnetic deflectors (see Figure 2-6) for the x and y-direction to achieve a raster scan pattern. The electron beams used for SEM are focused by electromagnets in an objective lens, capable of tuning the beams' cross-section or 'spot size' to a diameter of 2-10 nm. The spot size directly determines the resolution of an SEM scan with spatial resolutions of 50-100nm possible in conventional equipment[250]. Magnifications of between 10x - 100,000x are possible. These secondary electrons are produced from a region that corresponds roughly to the diameter of the electron beam focussed on the sample surface[250].

2.2.1.2 Transmission Electron Microscopy

Transmission electron microscopy (TEM) also uses a beam of accelerated electrons focused directly on a sample to produce a magnified, detailed image of that sample. The sample being imaged needs to be specially prepared and of appropriate characteristics to allow the electron beam to *transmit through* the sample. The sample scatters incident electrons from the electron source as they transmit, and too dense a sample will block transmission completely. Maximum sample thickness usually falls in the range of 100-200 nm [251]. Scattered electrons are subsequently focused through a series of magnetic lenses and apertures, forming a magnified image on a detector surface that records the scan result.

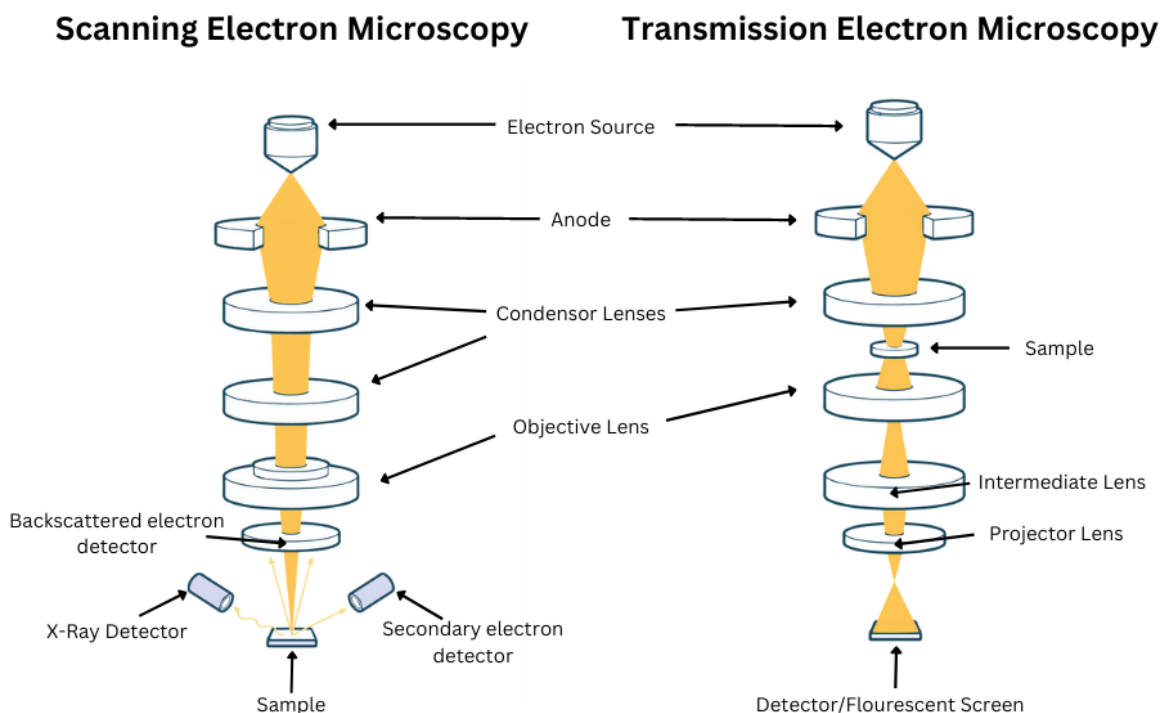


Figure 2-6 A simplified cartoon cross-section showing the similarities and differences between SEM and TEM experimental apparatus and lens and sample arrangements. Note the position of the sample and detector(s) in each technique.

Scans are controlled using techniques similar to SEM, with magnetic fields produced by magnets and coils providing electron beam control as seen in Figure 2-6. In contrast to SEM's surface imagery and morphology, TEM can provide topographical, morphological, compositional and crystalline information. TEM allows for the visualisation and analysis of samples in the realm of microns (10^{-6} m) down to nanometres (10^{-9} m) with resolutions of below 1nm and magnifications of 1,000,000X possible in modern equipment [251, 252]. The resolution of a TEM can be calculated using Abbe's equation, shown in:

$$d = \frac{0.61\lambda}{n \sin a} \quad \text{Equation 2-12}$$

Where d is the minimum resolvable distance for an instrument, λ is the wavelength of the electron beam, n is the refractive index of the medium, and a is the aperture angle of the TEM. The calculation for λ is done via the equation:

$$\lambda = \frac{h}{\sqrt{2meV}} \approx \lambda = \sqrt{\frac{1.5}{V}} \quad \text{Equation 2-13}$$

Where h is Planck's constant (6.626×10^{-34} js), m is the mass of an electron (9.109×10^{-31} kg), e is the charge of an electron (1.6×10^{-19} C) and V is the accelerating voltage. From the approximate

form seen on the right-hand side of $\lambda = \frac{h}{\sqrt{2meV}} \approx \lambda = \sqrt{\frac{1.5}{V}}$ Equation

2-13, it can be seen that higher accelerating voltages result in smaller values for λ (nm) and, therefore, a higher possible resolution for the resultant scan.

TEM offers distinct advantages over SEM for nano-scale systems: high resolution at high magnification, microanalysis of elemental composition at higher resolutions and crystalline information. However, the technique has some drawbacks, mainly relating to the requirements for the intended sample's properties and preparation. As samples need to be thin enough to allow electron transmission, they often require affixation as thin layers, slices or other specialised techniques to thin, delicate grids, which are only around 3 mm in diameter. These processes can be laborious and time-consuming, as well as have the potential to introduce artifacts into scan results. TEM scans are also highly vulnerable to electromagnetic or seismic interference, and care must be taken to isolate equipment from potential interference sources. The electron beam can also damage some samples due to the impacts of ionising radiation, so careful tuning of scan parameters and dwell time is advised to minimise these effects.

2.2.2 Scanning Probe & Atomic Force Microscopy

Atomic force microscopy (AFM) is a technique in which a probe with a very sharp tip, down to 2 nm tip diameter in some cases [253], is used to scan over a sample surface of interest. The interaction between the probe's tip and the sample surface is measured through conversion into an electronic signal. This signal can then be analysed and interpreted through conversion into a topographical image. In addition to these topographical images, modern AFMs can often provide information regarding the interaction of the probe with the sample surface as it scans, including frictional forces, adhesion, and elasticity. Some specialised tips can even measure interactions caused by chemical, magnetic or electrostatic forces [254].

In AFM, the probing tips are located at the end of a cantilevered arm, which is raster-scanned across the sample surface. A laser source is focused onto the back of the cantilever, and as it scans the surface topography and reacts to changes, the cantilever will deflect, shifting the laser position. A detector is positioned to collect the reflected photons and can measure the deflection of the beam in the x, and y-directions to produce a record of the surface. The sample is mounted onto a piezoelectric stage, allowing positional control in the z-direction in the order of a few nanometers. The detector and the piezoelectric stage are linked so that the instrument can maintain constant force or height between the probe tip and the sample surface, depending on the experimental setup.

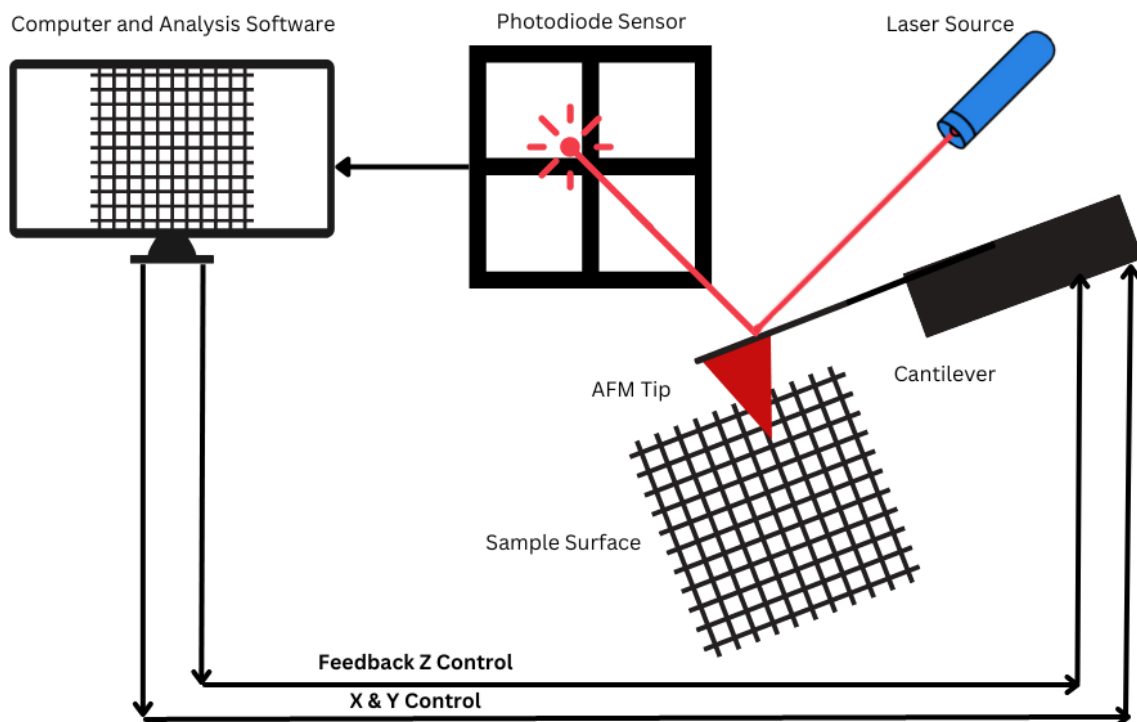


Figure 2-7 Diagram showing the basic principles of AFM measurement control. The movement or deflection of the tip and cantilever is recorded through a reflected laser source onto a photodiode sensor or similar. This signal is interpreted by computer analysis software, and signals to direct the cantilever in x, y, and z-planes are fed back to the scanning probe.

Three modes are commonly used for AFM measurements: Contact mode, tapping mode and non-contact mode. The contact mode maintains a constant deflection, or height, between the tip and sample surface. By keeping the force between the tip and surface constant through the detector-piezo feedback loop, the cantilever movement in the z-direction can be mapped to produce a 3D image. Cantilevers used for this technique generally have spring constants within the range of 0.01-1.0 Nm^{-1} [254]. Contact mode can inflict large lateral and normal forces on the probe tip, accelerating the dulling of tips and introducing artifacts into scan results.

Tapping mode AFM scans oscillate the cantilever arm at or near the resonant frequency of the cantilever, with amplitudes between 20 and 100nm possible. This oscillation causes the probe to

lightly touch or 'tap' the sample surface at the trough of each oscillation cycle. Any changes in the cantilever's vibration frequency are recorded, and the feedback loop maintains a constant oscillation amplitude. Targeting a constant oscillation makes a constant tip-sample interaction through the scan achievable.

Non-contact mode is similar to tapping mode in that an oscillation is applied to the cantilever while scanning. However, the probe tip is set higher from the surface, such that it does not contact the sample throughout the scan but instead interacts with surface forces. These attractive forces include van der Waals and magnetic and electrostatic forces, allowing for their quantification and analysis.

2.3 X-Ray Diffraction

X-Ray diffraction is a technique commonly used to investigate or determine a sample's elemental composition and crystalline structures. XRD is useful for determining the atomic structure of larger samples, and for smaller samples, such as powders and nanostructures, XRD is used for compositional information and sample crystallinity.

X-rays are used in this technique as their wavelength λ is similar to the inter-atom spacing d , commonly seen in crystalline structures, between 1-100 Å. This similarity ensures that diffraction effects are maximised and can therefore be observed from the photon-sample interaction.

X-ray photons will penetrate a sample upon irradiation, only changing their path after interacting with atomic orbitals in the sample. These interactions change the X-ray direction by some angle θ , called the angle of diffraction. This result occurs through an elastic scattering mechanism, leading to destructive interference in most cases. However, waves travelling in specific directions will constructively interfere, as determined by Bragg's law, where n is any integer:

$$n\lambda = 2d \sin\theta \qquad \text{Equation 2-14}$$

Using measured θ values, it's then possible to determine compositional and crystalline characteristics from the sample through a comparison of d with known distances between atomic planes for a given element and phase. This analysis is done by comparing spectral peaks on a 2θ scale to literature values for peak positions and taking factors such as spectral peak intensity and peak width into account.

3 COMPOSITION AND PROPERTIES OF RF-SPUTTER DEPOSITED TITANIUM DIOXIDE THIN FILMS

This chapter is a reformatted version of the paper published in:

Nanoscale Advances 2021 Vol. 3 Issue 4 Pages 1077-1086.

Author Contribution:

Jesse Daughtry: Designed and performed experiments, analysed data, prepared figures and manuscript.

Abdulrahman Alotabi: Assisted with some sample preparation, SEM and XRD measurements, provided measurement details, revision of manuscript.

Liam Howard-Fabretto: Sample preparation, UPS measurements on single crystal TiO₂, provided sample and measurement details for manuscript, revision of manuscript.

Gunther Andersson: Intellectual contribution in conceptualising experiments, data interpretation and revision of manuscript.

3.1 Abstract

The photocatalytic properties of titania (TiO_2) have prompted research utilising its useful ability to convert solar energy into electron-hole pairs to drive novel chemistry. The aim of the present work is to examine the properties required for a synthetic method capable of producing thin TiO_2 films, with well defined, easily modifiable characteristics. Presented here is a method of synthesis of TiO_2 nanoparticulate thin films generated using RF plasma capable of homogenous depositions with known elemental composition and modifiable properties at a far lower cost than single-crystal TiO_2 . Multiple depositions regimes were examined for their effect on overall chemical composition and to minimise the unwanted contaminant, carbon, from the final film. The resulting TiO_2 films can be easily modified through heating to further to induce defects and change the electronic structure, crystallinity, surface morphology and roughness of the deposited thin film.

3.2 Introduction:

Titania (TiO_2) has been a major area of research since the discovery of its photocatalytic properties in 1972 [23]. Since then, TiO_2 has been one of the most widely studied semiconductors, driven largely due to its non-toxic nature, low cost, stability, and varied methods of synthesis and property control [255-257]. The broad range of possible applications stems from its versatile photocatalytic properties. The activity of this material under UV light has led to its inclusion in many sun protection applications [258], sensors [255], integrated optical devices [171], photo-oxidation of pollutants and dangerous chemicals [259], and photocatalytic processes for energy storage [147]. All of these applications utilise TiO_2 in the form of nanoparticulate coatings [260], making scalable, affordable synthesis of such coatings valuable, especially if they can be modified for specific properties.

The synthesis of TiO_2 amorphous films, thin layers of nanoparticle sized TiO_2 has been achieved through a variety of techniques such as chemical vapour deposition (CVD) [261], sol-gel processing [172, 262] atomic layer deposition [263] and direct current (DC) and radio frequency (RF) magnetron sputtering processes [170, 183]. These final two sputtering methods have been widely explored due to their stability, reproducibility, ease of use and deposition control over a variety of substrates. The films deposited through this method are commonly dense, closed layers of nanoparticulate TiO_2 . Nanoparticle Titania has shown particular promise across the range of possible applications and also offers a level of control over characteristics such as particle size [182], phase-type [190, 264] and stoichiometry [190].

The use of well-understood TiO₂ nanoparticle thin films is especially useful for surface science studies utilising photoelectron spectroscopy. Several valuable techniques for probing electronic structure such as X-ray photoelectron spectroscopy (XPS) and ultraviolet photoelectron spectroscopy (UPS) require precision knowledge of a sample's elemental composition and electronic structure to yield meaningful results [44, 189]. Many photocatalytic systems require a robust substrate-catalyst electronic interaction to prevent changes in the performance of the catalyst due to agglomeration; one method proposed to achieve this is defect rich surfaces [179, 265]. Ti³⁺ defects have been explored as promising binding sites for heterogeneous catalysts that offer strong electronic interaction to prevent agglomeration [266, 267].

The topography, crystallinity and particulate characteristics have been well established in sputtered thin films using atomic force microscopy (AFM) [171, 268], scanning electron microscopy (SEM) [264, 269] and X-ray diffraction (XRD) [171, 182, 264]. However, the elemental composition of the final coating is relatively unexplored for RF sputtered TiO₂. Carbon-containing substances like hydrocarbons are considered as a contaminant for many methods of electron spectroscopy and is present in considerable quantities for many commonly used methods of TiO₂ synthesis. Hence, an RF sputtered deposition procedure resulting in low carbon percentage is desirable. Single crystal TiO₂ is also capable of addressing the issue of contamination but is prohibitively expensive for applications on a larger scale.

TiO₂ can be either amorphous or has one of three crystalline forms: Anatase, Brookite or Rutile. Layers or films of titania can be either pure or mixtures of these forms with synthetic methods often influencing the structure of the coating through control of factors such as deposition temperature [269], or by post-deposition treatments [171] [270]. The surface morphology and crystal phase composition of TiO₂ films are also modifiable through post-deposition calcination and have been shown to influence and improve the photocatalytic properties of deposited films [271].

The present study demonstrates a method of depositing RF sputtered TiO₂ thin films onto Si(110) substrates, with a range of target pre-treatments, deposition lengths and annealing as post-treatment. Systematic studies into elemental composition, morphology, crystallinity and chemical state of the nanoparticulate TiO₂ were conducted to determine their composition, contaminants and ease of surface modification with Ti³⁺ defects. The results indicate that one method, in particular, produced a TiO₂ nanoparticulate film capable of low-cost scalability, minimal carbon contamination in the final film and simple modification of surface defects, crystallinity and surface morphology.

3.3 Experimental Details

3.3.1 Preparation of TiO₂ Thin Films

TiO₂ thin films used in this work were prepared at room temperature using an RF magnetron sputtering system. High purity 2-inch (99.9%) TiO₂ targets were used to deposit TiO₂ nanoparticles onto 4-inch diameter Si(110) substrates. 2 TiO₂ targets were used, one having been used for several months, the other being brand new, to determine how target ageing affects the resultant deposition quality. The substrates were cleaned with ethanol and acetone for 15 min in an ultrasonic bath. The substrates were then dried under nitrogen. The deposition was done three times, with differing chamber/target conditions. Firstly after 1.5 hours of pre-sputtering to clean the target and chamber (designated 90m-RF), secondly after 30 min of pre-sputtering for cleaning (designated 30m-RF) and finally with an unused TiO₂ target after 30 mins pre-sputtering (designated FT-RF). The sputter deposition was performed in all cases with a chamber pressure of at least 2×10⁻⁵mbar, with 5ccm pure argon flowing, 500W magnetron power and a working distance of 14cm. These conditions provided a deposition rate of approximately 180nm/hr. The deposition took place at room temperature with no substrate heating.

All samples were cut into 1×1cm squares using a diamond-tipped silicon cutter to minimise surface contact and contamination. Particulate dust from cutting was removed with pressurised dry nitrogen. Samples were then mounted to Molybdenum sample holders and inserted into the Ultra-High Vacuum chamber (9.2-6×10⁻¹⁰ mbar). The samples were characterised in this unaltered condition (designated by the As-made tag next to sample name) before the samples were heated through filament emission heating to 500C and held there for 10 minutes in an attempt to reduce film contaminants. XPS scans marked "Heated" were taken almost immediately after heating.

Samples from all deposition methods were measured in As-made condition as well as after heating to 500°C in UHV. Further, post-deposition heating was performed on a single sample prepared from the FT-RF method in vacuum at 300°C, 500°C and 700°C in succession with photoelectron measurements taken after 30 minutes of heating at a given temperature before increasing the temperature. The sample designated “300°C and Ar Sputtered” was heated to 300° as described previously and then immediately exposed to an Argon ion sputter beam, exposing the sample surface with a dose of 6×10¹⁴ ions, controlled through exposure time dependant on ion current (see Table 3-2). FT-RF samples were also heated up to 1100°C in atmospheric conditions for crystal phase structure investigations.

Table 3-1 Sample series for comparison of deposition methods (measured As-made and heated 500°C in vacuum) and vacuum heated series using an FT-RF sample.

Deposition Methods	FT-RF TiO ₂ – Vacuum Heated Series, treatment
--------------------	--

FT-RF	300°C
30m-RF	500°C
90m-RF	700°C

Table 3-2 Sputter dose calculations for a range of argon ion currents, determining the required exposure time to receive the specified sputter dose.

current	current/1.6	area (cm ²)	dose	time (seconds)	Time (minutes)
1.30E-07	8.13E+11	1	6.00E+14	7.38E+02	12.31
1.40E-07	8.75E+11	1	6.00E+14	6.86E+02	11.43
1.50E-07	9.38E+11	1	6.00E+14	6.40E+02	10.67
1.60E-07	1.00E+12	1	6.00E+14	6.00E+02	10.00
1.70E-07	1.06E+12	1	6.00E+14	5.65E+02	9.41
1.80E-07	1.13E+12	1	6.00E+14	5.33E+02	8.89
1.90E-07	1.19E+12	1	6.00E+14	5.05E+02	8.42
2.00E-07	1.25E+12	1	6.00E+14	4.80E+02	8.00
2.10E-07	1.31E+12	1	6.00E+14	4.57E+02	7.62

Additionally, electron spectroscopy measurements were taken from rutile (110) single crystal (SC). The SC TiO₂ was pre-treated at 877 C (1150 K) *ex-situ* to induce bulk defects, making the sample conductive and useful for electron spectroscopy. The SC TiO₂ again was heated to 625°C *in-situ* immediately before photoelectron measurements to produce surface defects, the XPS relative elemental composition of SC TiO₂ can be seen in Table 3-3.

Table 3-3 Analysis XPS taken from a sample of Single Crystal (SC) Rutile TiO₂ after argon sputtering and heating to 625°C under vacuum. This sample served as an ideal TiO₂ reference.

Species Name	Peak Position (Calibrated)	Area	Relative Concentration (%)
Carbon 1s	285	985.1	1.2
Carbon 1s	286.7	256.9	0.3
Carbon 1s	289.2	112.9	0.1
Titanium 2p 4+	459.2	86766.1	22.4
Titanium 2p 3+	457.5	3846.3	1.0
Titanium 2p 2+	456.5	1192.3	0.34
Oxygen 1s	530.5	133731	66.64
Oxygen 1s	532.0	15410.2	7.7
SiO 2p	102.1	3846.3	0.4
		Total	100

3.3.2 Spectroscopy

3.3.2.1 X-Ray Photoelectron Spectroscopy (XPS) & Ultraviolet Photoelectron Spectroscopy (UPS)

Chemical composition of the prepared samples was undertaken using x-ray photoelectron spectroscopy (XPS). These measurements were taken with an X-ray source producing 1253.6 eV (Mg K α radiation) and 200W power using a SPECS PHOIBOS-HSA300 hemispherical analyser (Berlin, Germany). Survey scans were taken at 40 eV pass energy and high-resolution scans were taken at 10eV pass energy. The main adventitious Carbon peak was used as an energy reference for all other species and set to 285 eV. All XP spectra were analysed with Casa XPS using a Shirley background and a hybrid Gaussian (30%) and Lorentzian (70%) function to fit all peaks in a method described previously [235]. Elemental sensitivity factors for an X-Ray source at 54.7° were used in the analysis process [272]. Sample heating was performed either under Ultra-High Vacuum (UHV) conditions or in an air-atmosphere furnace, as specified in the results. UPS measurements were performed in the same UHV chamber and with the same SPECS hemispherical analyser.

The probe source used is a two-stage cold cathode gas discharge source from MFS (Clausthal-Zellerfeld, Germany) capable of generating He I line UV photons and metastable He atoms.

3.3.2.2 X-Ray Diffraction (XRD)

XRD was performed on a range of samples in as-made and heated (both in-vacuum and atmospheric) condition to determine the crystallinity of the deposited TiO₂ nanoparticle films. These measurements were performed using a Bruker D8 Endeavor instrument with a Cobalt X-Ray source at 1.78896 nm. Results were compared to TiO₂ anatase and rutile spectra calculated using materialsproject.org crystal toolkit for TiO₂ [273, 274]

3.3.2.3 Microscopy

Once the levels of unwanted contaminants were determined, and the best candidate surface (FT-RF) was selected, further analysis of the morphological characteristics of the film was performed using AFM and SEM techniques. Samples were prepared by identical cutting and cleaning procedures, with selected samples being heated in an air-atmosphere furnace at the required temperature before mounting onto flat or vertical SEM stubs as necessary. All SEM measurements were performed on the samples as they are.

3.3.2.4 Atomic Force Microscopy (AFM)

AFM scans were performed utilising a Multimode 8 AFM with Nanoscope V controller at scan sizes of 1×1µm and 3×3µm on both as-made and heated (500C) samples to investigate surface roughness and morphological characteristics. The analysis was performed using Bruker's Nanoscope Analysis package to extract surface roughness values to determine changes in the nanoparticle size and surface roughness after post-deposition heating. The surface roughness was measured using R_q, the root-mean-square roughness and R_a, the mean height deviation across a line profile.

3.3.2.5 Scanning Electron Microscopy (SEM)

SEM scans were performed using an FEI Inspect F50 instrument with 30kV on 0.5x1cm TiO₂ samples mounted onto either a vertical SEM mount to determine the deposited film thickness or horizontally-mounted for morphological investigation. Thickness measurements were taken at several sites along the sample edge and averaged.

3.4 Results and Discussion

3.4.1 Chemical composition

XP spectra were taken at the C 1s, O 2s, Ti 2p, Si 2p, F 1s and Na 1s regions for all samples. The breakdown of peak positions found in each region is presented in detail in Figure 3-1 and in Table 3-4 Analysis of an XP Spectra from FT-RF TiO₂ in as made condition, showing the energy peak

positions, FWHM and intensities found in each region scanned (No Na was found in this sample). These values are typical for such a sample..

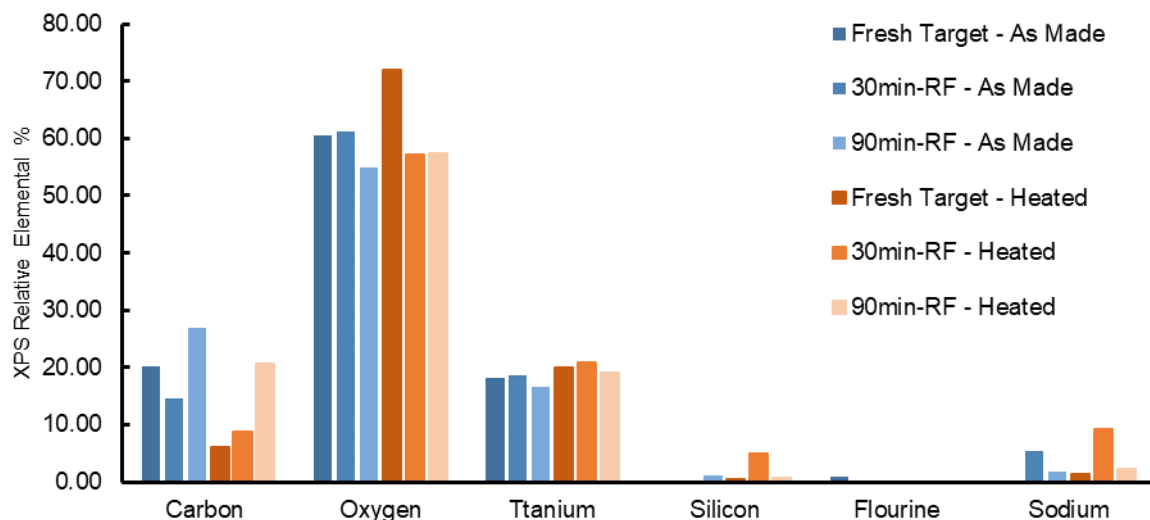


Figure 3-1 XPS relative elemental composition comparison between the as-prepared and heated RF sputter samples

Table 3-4 Analysis of an XP Spectra from FT-RF TiO₂ in as made condition, showing the energy peak positions, FWHM and intensities found in each region scanned (No Na was found in this sample). These values are typical for such a sample.

Name	Peak Position (Calibrated)	Area	Relative Concentration (%)
Carbon 1s	285	28823.9	21.5
Carbon 1s	286.7	4304.2	3.2
Carbon 1s	288.9	1795.8	1.3
Oxygen 1s	530.3	147337.8	45.7
Oxygen 1s	531.7	22609.5	7.0
Oxygen 1s	532.6	6667.5	2.1
SiO ₂ 2p	101.4	486.6	0.3
SiO ₂ 2p	102.4	321.2	0.2
Titanium 2p 4+	458.8	111379.5	12.3

Titanium 2p 3+	464.5	53309.8	5.9
Flourine	684.6	3177.4	0.7
		Total	100

The carbon in the sample is mostly attributed to adventitious hydrocarbons, and the C1s peak is assigned to 285 eV. This peak is very consistent in its energy position and therefore, suitable for use in calibration [275]. The oxygen signal is attributed mostly to titanium dioxide (530.3 ± 01 eV) with some minimal contribution from silicon dioxide (532.3 ± 0.1 eV), the high relative percentage of oxygen is discussed later in this text. The titanium signal is exclusively due to the nanoparticle thin film, and the dominant species (Ti^{4+}) is assigned to 459.3 ± 0.1 eV with titanium defects induced through sample treatments (Ti^{3+}) assigned to 457.6 ± 0.1 eV. The silicon signal is due to SiO_2 from the silicon wafer used as a substrate and is found at 102.4 ± 0.1 eV. Both sodium (1071.2 ± 0.1 eV) and fluorine (685.4 ± 0.1 eV) were contaminants of unknown origin with fluorine only found in one sample, while Sodium appeared in varying concentrations in all but FT-RF - As-Made and is likely due to sample handling prior to the XPS measurements.

Table 3-5: XPS relative elemental compositions of TiO_2 samples prepared with 90 min pre-sputtering (90m-RF), 30 min pre-sputtering (30m-RF) and 30 min pre-sputtering and a fresh TiO_2 target (FT-RF). Samples designated As-made has received no further treatment after deposition. Samples designated – Heated, have been heated to 500°C in UHV Conditions before measurement.

XPS Relative Elemental Composition %						
	Carbon	Oxygen	Titanium	Silicon	Fluorine	Sodium
FT-RF - As-made	20.2±0.1	60.4±0.1	18.2±0.1	0.2±0.1	0.9±0.1	0.00
30m-RF - As-made	14.6±0.1	61.3±0.1	18.5±0.1	0.1±0.1	0.00	5.5±0.1
90m-RF - As-made	26.8±0.1	54.8±0.1	16.7±0.1	1.1±0.1	0.00	1.7±0.1
FT-RF – Heated	5.9±0.1	72.1±0.1	20.1±0.1	0.5±0.1	0.00	1.5±0.1
30m-RF – Heated	8.7±0.1	57.1±0.1	20.8±0.1	5.0±0.1	0.00	9.2±0.1
90m-RF – Heated	20.5±0.1	57.4±0.1	19.1±0.1	0.6±0.1	0.00	2.3±0.1

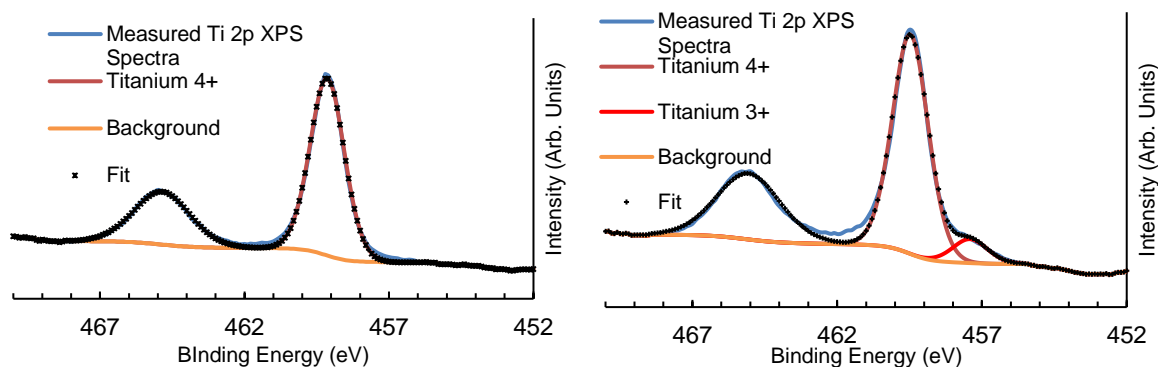


Figure 3-2: XPS high-resolution scan fitting for Vacuum Heated Ti 2p region showing As-made (left) and 500C heated (right) with Ti 3+ defect showing in the heated sample at around 457eV binding energy

The XPS scans of these samples, seen in Figure 3-2, with relative elemental composition fit seen in Table 3-5, revealed several trends and characteristics. Across all samples, the ratio of Ti 2p orbital signature to O 1s is around 3.1:1 (O: Ti) with O accounting for an average of 60% of the measured signal while Ti accounts for approximately 20%. These values, while not stoichiometrically expected, are both consistent between the three prepared surfaces as well as comparisons to previously measured P-25 and Atomic Layer Deposited TiO₂ surfaces measured using the same experimental equipment [185] and as such are seen as representative of TiO₂. One possible reason for non-stoichiometric O concentration is adsorbed O species such as OH and H₂O. Another possible reason is an inaccuracy in the sensitivity factor applied for the O 1s XPS intensity.

Surface contaminants, a particular concern when using synthesised thin films for surface-sensitive measurements, were also determined through their characteristic XPS orbital signatures summarised in Table 3-6. Carbon (1s) was the most apparent contaminant with every sample showing some noticeable percentage of carbon (between 6-26%) mainly due to adventitious carbon [276]. The highest levels of C 1s signal were found in as-made samples which had been exposed to the atmosphere after deposition and before undergoing heating, as would be expected. The 90m-RF sample was particularly carbonaceous in both as-made and post-heated form, indicating that a longer pre-cleaning time increases the carbon content within the final film, counter to the processes intent. The surface prepared through the fresh TiO₂ target (FT-RF) was the least carbonaceous of the three methods.

Silicon signal was below 1.1% for all samples; this elemental presence may be at least partly attributable to an intermixing of Ti and Si during the RF deposition. The only exception was for the 30m-RF-As-made, which showed approx. 5% Si after heating, probably due to film spallation [169] revealing some bare Si. This, coupled with the observation that while in previous studies on TiO₂ film depositions Si 2p were detected at a binding energy of 99.8±0.3 eV [185], all Si signal from these samples is observed at 102.3±0.3 eV. This binding energy points towards the presence of

organic silicon compounds. The RF-sputter deposition process likely results in the formation of small amounts of silicate species [277] or a Si-O-Ti compound formed during deposition.

Previous spectroscopic studies on systems utilising TiO₂ have had issues with Si and C signal interfering with sensitive data collection and analysis [185]. These contaminant species are found to be present in all samples prepared through RF sputter deposition. However, the sample prepared from the fresh target of TiO₂ showed negligible Si 2p signal and a very low concentration of C 1s, further lessened through heating in vacuum, making it the best candidate for sensitive surface spectroscopic studies.

Table 3-6 XPS Relative elemental compositions from an FT-RF sample, heated under UHV conditions to increasing temperatures to determine the change in C contribution through sequential heating. It can be seen that the level of C contribution in an As-made sample is significantly reduced by 300°C, decrease through 500°C and show a slight increase at 700°C. Sputtering an FT-RF sample with Ar ions at a set dose after heating to 300°C shows a reduction in C contribution over solely heating, as well as an increase in Ti³⁺ defects.

FT-RF: Vacuum Heated Series	Carbon	Oxygen	Titanium	Ti ³⁺ Defect	Silicon	Fluorine
As-made	26.0±0.1	54.7±0.1	18.1±0.1	0.00	0.5±0.1	0.7±0.1
300C	5.1±0.1	72.1±0.1	21.4±0.1	1.2±0.1	0.6±0.1	0.7±0.1
500C	4.8±0.1	71.6±0.1	22.8±0.1	1.7±0.1	0.8±0.1	0.00
700c	5.6±0.1	70.3±0.1	22.5±0.1	1.6±0.1	1.6±0.1	0.00
300C + Ar Sputtered	4.4±0.1	68.8±0.1	26.1±0.1	4.5±0.1	0.8±0.1	0.00

Table 3-7 Ti3+ defects as a proportion of total Ti 2p signal

Vacuum Heated FT-RF	
300°C	5.4%
500°C	7.5%
700°C	6.9%
300°C + Ar Sputtered	17.1%

Other contaminants were minimal. Fluorine (1s) was observed in the Fresh Target sample before heating at 1% of the surface signal. However, heating removed this signal to below detectable amounts. Sodium (1s) was also detected although the variability of Na in samples from the same deposition proves suggests this contamination is due to sample processing. However, after heating, all sodium-containing samples had their sodium content increase, raising the possibility that some sub-surface Na may be drawn to the surface through heating processes. This interpretation would be consistent with the observed low surface energy of Na, causing it to migrate towards the surface of metal oxides during heating processes and electron beam exposure [278, 279].

Samples from the FT-RF: Vacuum Heated Series were heated under UHV conditions to analyse any compositional/electronic changes that might be induced. Calcination of FT-RF samples was performed over a range of temperatures under UHV conditions (Table 3-6). It can be seen that calcination as low as 300°C was able to produce a significant reduction in C XPS signal, with a further slight C reduction at 500°C before an increase in C contribution was observed for heating at 700°C. The increase in C at 700°C was accompanied by an increased Si contribution, pointing toward the onset of film spallation at this temperature, consistent with previous reports on TiO₂ thin films [169]. This process exposes small regions of the Si substrate through cracks in the film, simultaneously exposing C impregnated in the bulk of the TiO₂ film. To further explore this, an FT-RF sample was heated to 300°C before being exposed to a dose of sputtering Ar ions. Sputter treatment should preferentially remove any C present at the surface of the film, while bulk C signal is unaffected. The 300°C + Ar sputter treatment As can be seen (Table 3-6) to result in the lowest C contribution compared to a purely heated sample at 4.4±0.1% of XPS relative composition. The C signal in the 300°C + Ar sputter treatment is therefore assumed to be a baseline C contribution through RF sputtered deposition, as it would not be removable without compromising the integrity and coverage of the TiO₂ layer.

The XPS elemental relative concentrations seen in Table 3-6 show that heating under vacuum to higher temperatures induced Ti^{3+} defects at around 457.3 ± 0.1 eV binding energy (Figure 3-2). These defects increase as a relative proportion of total Ti 2p signal with heating, as seen in Table 3.7. The highest proportion of Ti^{3+} defects are seen in the 300°C and Ar sputtered sample, which registered 17.1 % of all Ti XPS signal as Ti^{3+} defect. The sputter treatment also decreased the overall O XPS signal in the sample, indicating that these defects were the result of oxygen vacancies induced through the sputter dose. Exposure to atmosphere quenched all previously measured Ti^{3+} signal. The relative ease with which such defects can be induced is a useful surface modification for use in studies of heterogeneous photocatalytic systems.

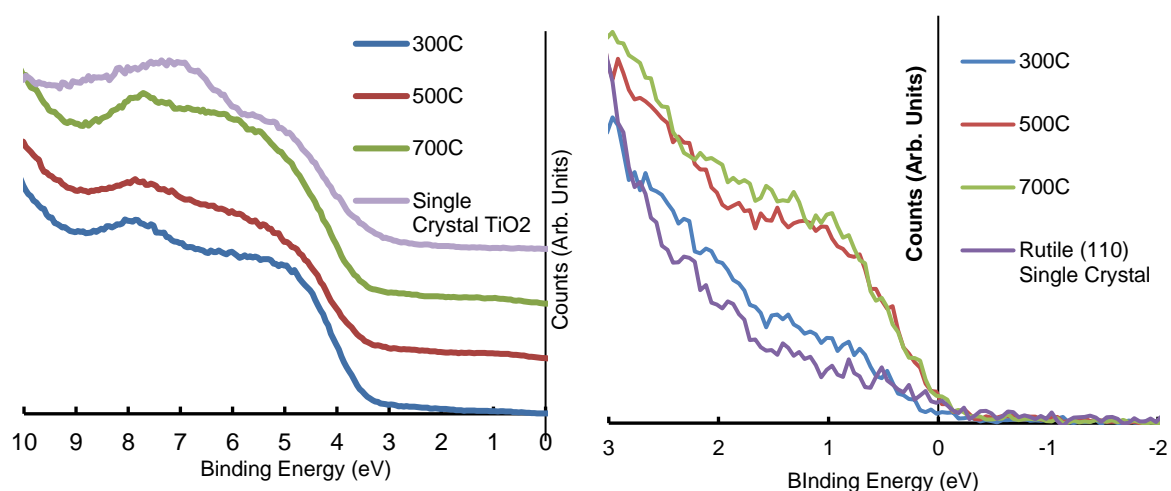


Figure 3-3 UPS scans from a range of heated FT-RF samples and rutile (110) single crystal TiO_2 showing broad range electronic structure on the left (series are offset in the y-axis) and the near-Fermi valence band on the right.

The UPS scans of the heated range reveal the changing electronic structure of the TiO_2 nanoparticles as they are heated, energies above 10eV are affected by secondary electrons and as such are not considered here. The electronic features seen in heated RF- TiO_2 in the region from 3-9eV are consistent with several previously reported studies examining the features found in DOS of modified TiO_2 and are reported to be from O(2p) species [280, 281].

Krischok et al. identify the peak around 4.5 eV as being associated with the ionisation of oxygen states in the upper valence band, mainly from bridging oxygen in the TiO_2 , it can be seen that all four spectra in Figure 2 share this peak's energy position. The visible decrease in the 4.5 eV peak over the heated range of samples corresponds with a loss of the bridging oxygen, giving rise to the observed increase in Ti^{3+} defects in Table 4.

The 8eV peak originates from oxygen species in the oxygen plane of the TiO_2 surface [282, 283]. While the single-crystal TiO_2 shares the 4.5eV peak with RF- TiO_2 samples, the single crystal displays a shifted oxygen plane energy peak at around 7 eV compared to the RF- TiO_2 which

appears at around 8 eV. This kind of variance in TiO₂ UPS spectra is not unexpected, as similar differences have previously been observed [284, 285]. One possible reason for such a shift could be attributed to the lower work function of the single crystal TiO₂ [282].

The near-Fermi region shows a clear peak centred at 1eV is attributed to the Ti³⁺ defect and shows an apparent increase at higher temperatures for the RF-sputtered films, in agreement with XPS observations. The UPS spectra of the RF sputtered TiO₂ shows higher signal around 1eV, attributed to Ti³⁺ defects, when compared to single-crystal TiO₂ showing its suitability for surface modification, even at lower calcination temperatures.

3.4.2 Morphological Characterisations

Figure 3-6 shows the uniformly distributed nature of the nanoparticulate film deposited through RF-TiO₂ deposition. SEM on a vertically mounted sample is shown in Figure 3-4, illustrating the deposited TiO₂ film having a thickness of 150 ± 5 nm across the film's cross-section.

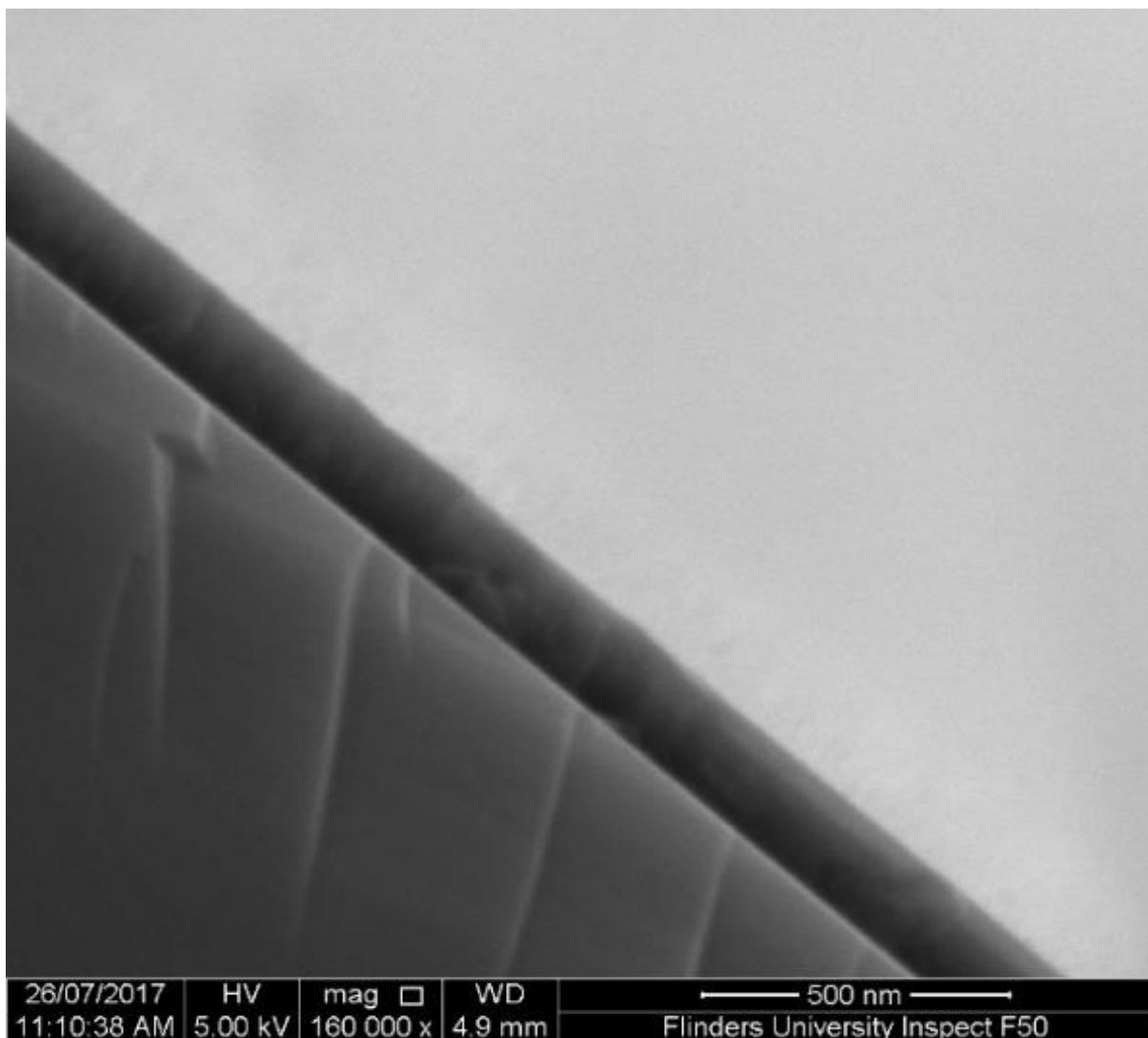


Figure 3-4 SEM image of 90min-RF-As Made Sample, the arrow indicates TiO₂ film thickness of approximately 153nm.

Comparison between Figure 3-6, A-D shows differences between the as-made and vacuum heated samples. The relatively smooth, close-packed nature of the film was observed across the sample surface, and in as-made condition consists of roughly spherical particles approximately 25-45 nm in diameter (Figure 3-6, A). While the sample heated to 500°C appears to show a lack of spherical particles and the appearance of larger particles of arbitrary shape, possibly through the ripening of the TiO₂ under vacuum heating conditions. The 3µm scans (Figure 3-6, C & D) show more significant regions separated by boundaries on the surface of increased height in both the as-made and vacuum heated samples. Again, the vacuum heated sample displays less defined particles and a noticeable flattening of the film surface when compared to the as-made sample viewed at the same magnification.

The roughness parameters (R_q root-mean-squared average roughness, R_a mean surface roughness) values for the heated samples have also decreased from the as-made samples to the heated samples (see Table 3-8). This change confirms that the RF-TiO₂ deposited film has undergone some level of rearrangement from the as-made, nanoparticulate form into a flatter, more aligned surface. High-resolution images seen in Figure 3-5 High magnification SEM scans on RF-TiO₂ after different heat treatments, clockwise from top left: As made, 300°C, 500°C, 700°C showing the transition from smaller, spherical particles on the film surface into aggregation and alignment into larger TiO₂ gshow that these spherical particles grow to larger sizes after heating to higher temperatures. Previous work has attributed these changes to an increase in crystallinity of TiO₂ and smaller particles' ripening' into larger ones [168, 171, 182].

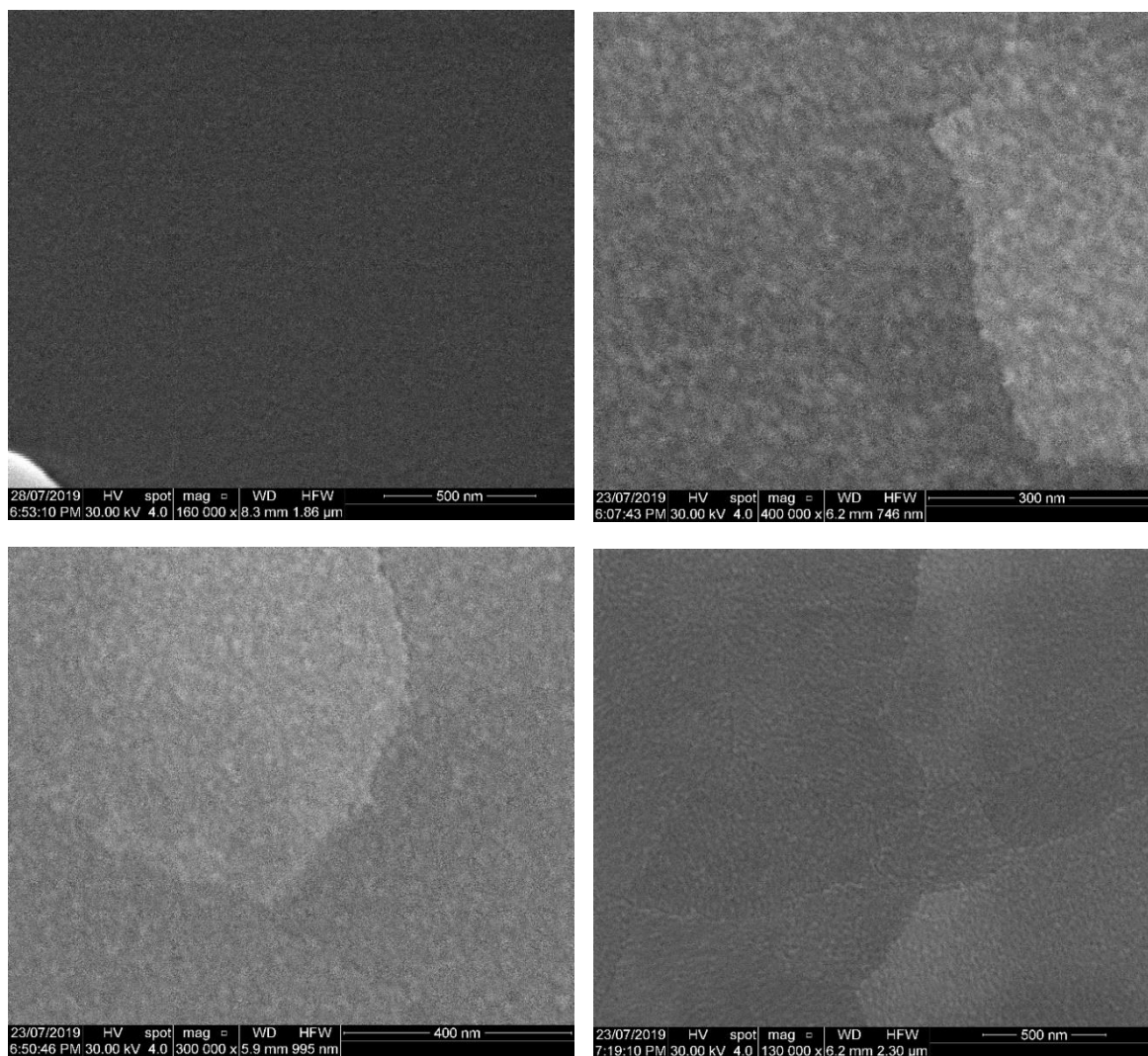


Figure 3-5 High magnification SEM scans on RF-TiO₂ after different heat treatments, clockwise from top left: As made, 300°C, 500°C, 700°C showing the transition from smaller, spherical particles on the film surface into aggregation and alignment into larger TiO₂ grains

The large aggregations of particles seen in Figure 3-6 C appear to have transitioned into the raised lines visible in Figure 3-6 D that divide the film into rough regions. These same phenomena can be observed in Figure 3-7; once calcination temperatures reached >900°C the resultant condition of the coating was that of well-defined grain boundaries containing regions of varying size. At 1100°C, some of these regions showed a visibly distinct texture with increased roughness, potentially related to a crystal phase transition observed in samples heated to this temperature.

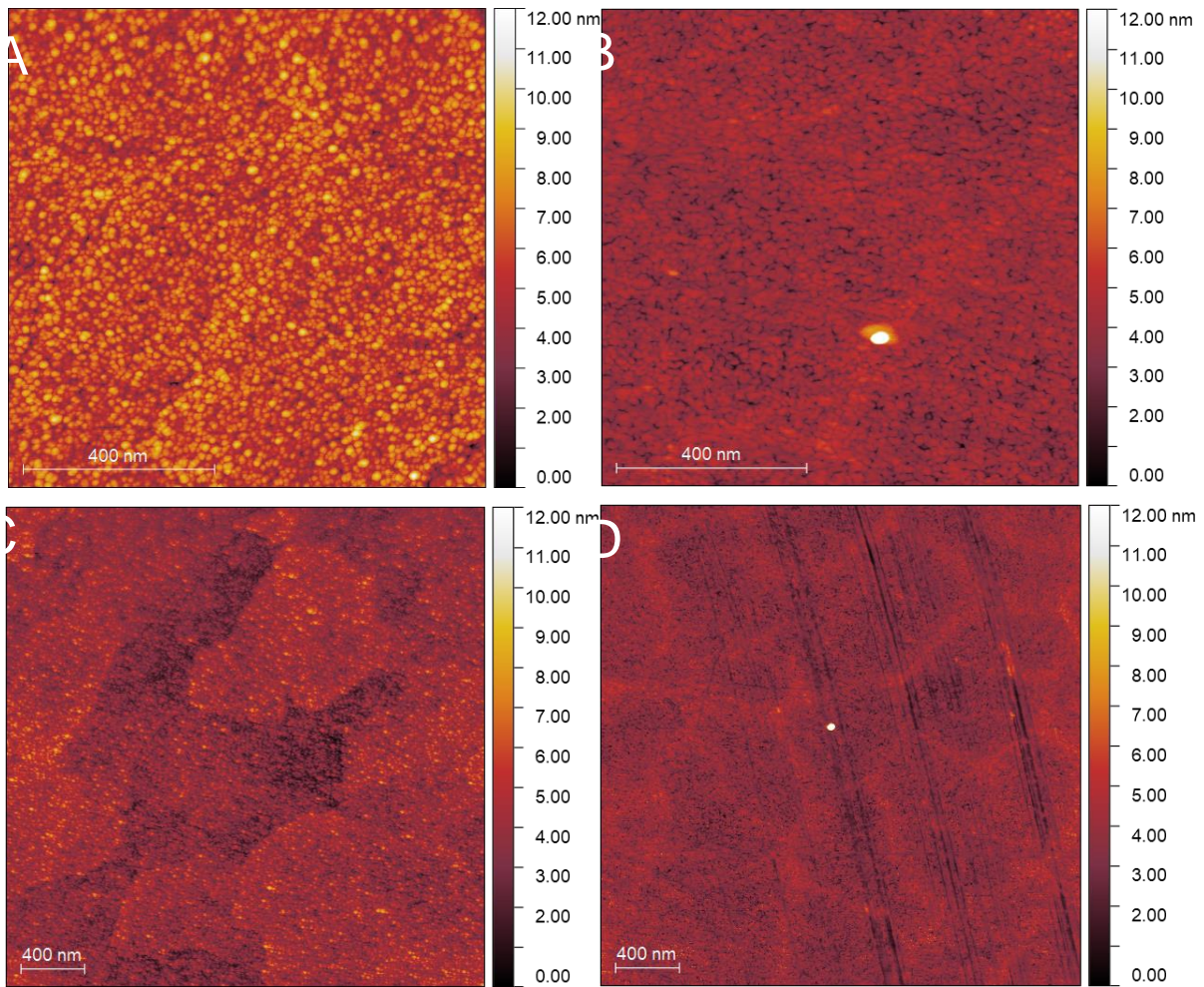


Figure 3-6 AFM scans on a) As-made, 1x1µm b) 500C Vacuum Heated, 1x1µm c) As-made, 3x3µm d) 500C Vacuum Heated, 3x3µm

Table 3-8 Average roughness characteristics from as-made and 500C heated sputtered TiO₂ samples

Roughness Parameters	500°C Vacuum Heated (nm)	As-made (nm)
R _q	0.76 ± 0.01	1.06 ± 0.12
R _a	0.60 ± 0.03	0.84 ± 0.08

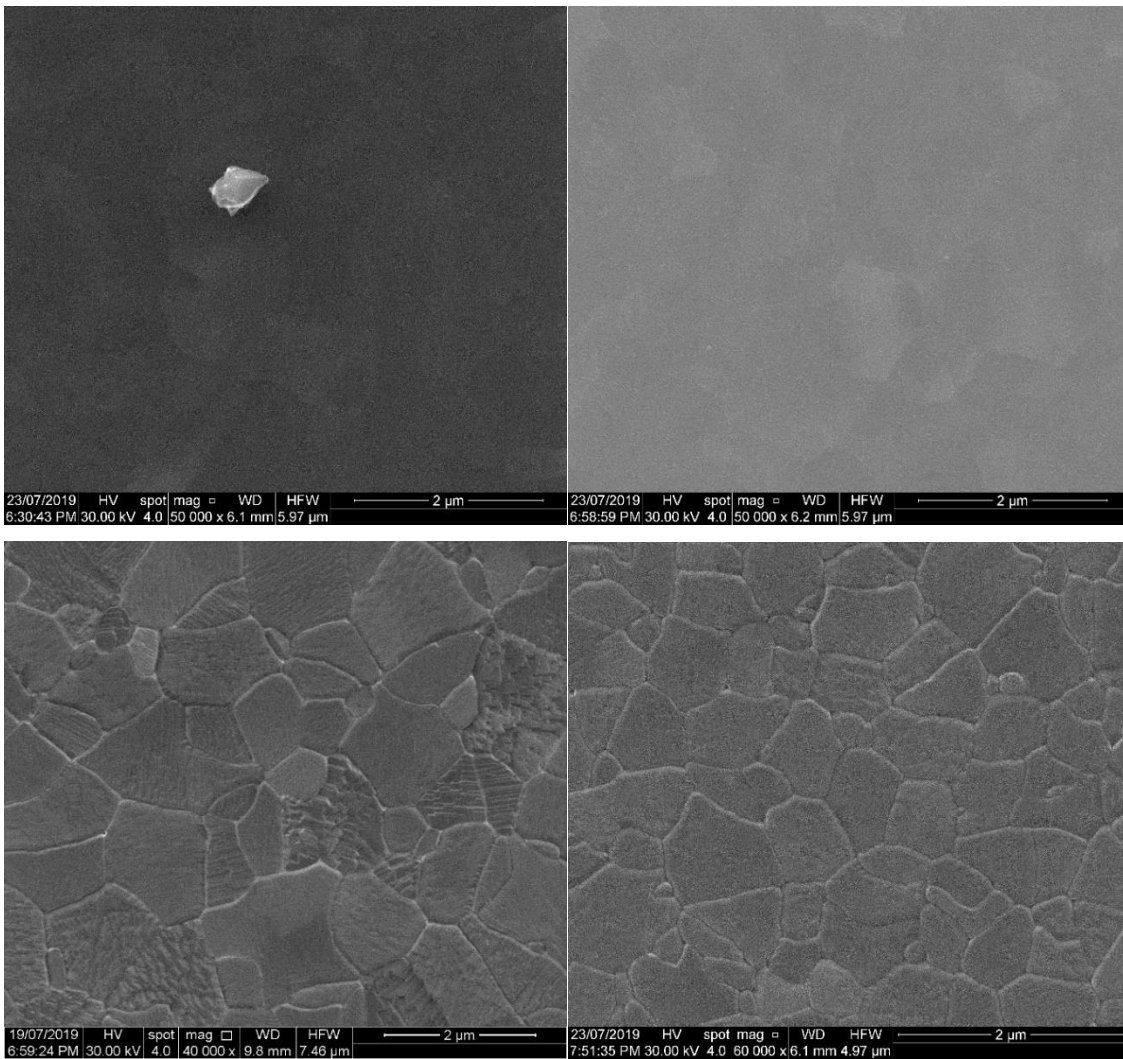


Figure 3-7 SEM scans showing the morphological changes to FT-RF sputtered TiO₂ films as they are heated, clockwise from top left, 500°C 1h, 600°C 1h, 900°C 1h, 1100°C 24h. The particle shown in the 500°C image was included to aid focussing of the measurement.

3.4.3 Crystal Structure

Samples measured with XRD are shown with offset intensities in Figure 3-8 and spanned a range from i) Si, ii) as-made RF-TiO₂, iii) as-made atomic layer deposition TiO₂, iv) 500°C atmosphere heated RF-TiO₂ (1h), v) 600°C atmosphere heated RF-TiO₂ (1h), vi) 900°C atmosphere heated RF-TiO₂ (3h) and vii) 1100°C atmosphere heated RF-TiO₂ (24h). The reference spectra for Anatase and Rutile TiO₂ calculated using the materials project are displayed in Figure 3-8, showing the reference peaks for the respective TiO₂ phases.

The change in crystallinity in systems such as reactively sputtered TiO₂ films and sol-gel crystallised TiO₂ have previously found the phase transition to rutile phase to occur at around 600°C with film thickness and temperature being critical factors in the phase transition [190, 277]. The system studied here shows markedly different crystallisation behaviour. We see in Figure 3-8 that the onset of anatase phase TiO₂ appears in ALD TiO₂ (ii) in its as-made state, but does not appear in RF-TiO₂ until the 500°C heated samples remaining up to 900°C with no corresponding Rutile phase emerging. The emergence of Rutile crystal peaks in the XRD is seen only in 1100°C samples heated for > 18 hours. This high temperature required produced samples with distinct, peaks for Anatase and Rutile phases, with an approximate 1:1 ratio in the peak areas.

The time-dependence and the elevated temperature necessary to attain Rutile TiO₂ are distinct from critical factors reported in phase transitions for other TiO₂ synthetic methods. The significant differences in crystallisation temperatures for Anatase and Rutile phases offer the potential of controlling substrates for required phases type and ratio with post-deposition treatments.

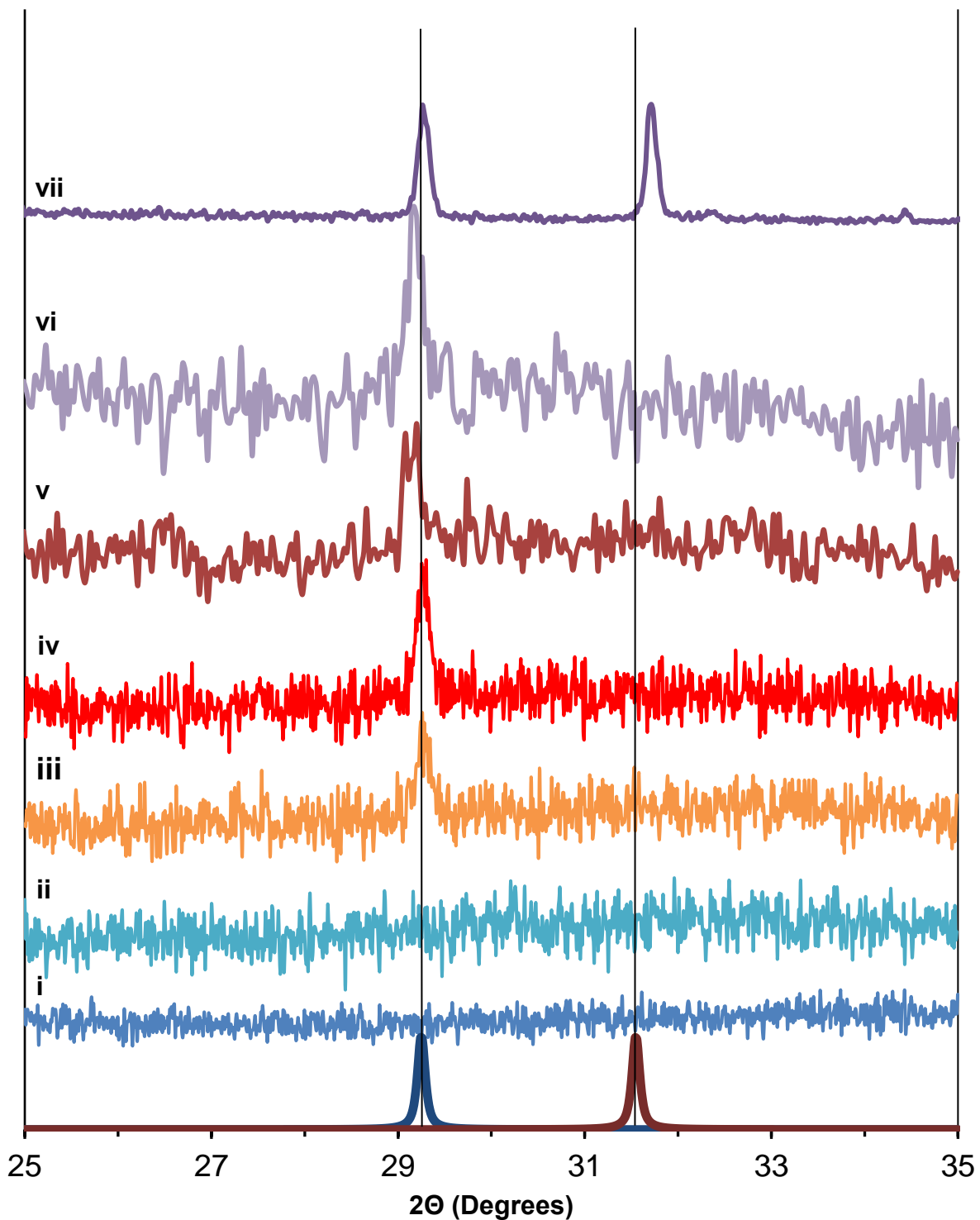


Figure 3-8 offset XRD scans on as-made and heated samples showing the transition from amorphous TiO₂ towards anatase phase. Rutile phase formation was detected only within the 1100C heated sample. Anatase and Rutile main XRD peaks shown on the x-axis, in blue and orange respectively. XRD spectra shown are i) Si, ii) as-made RF-TiO₂, iii) as-made atomic layer deposition TiO₂, iv) 500°C atmosphere heated RF-TiO₂ (1h), v) 600°C atmosphere heated RF-TiO₂ (1h), vi) 900°C atmosphere heated RF-TiO₂ (3h) and vii) 1100°C atmosphere heated RF-TiO₂ (24h)

3.5 Conclusions

This paper details the successful deposition of RF-sputtered TiO₂ films onto Si (110) substrates from TiO₂ targets with a range of deposition processes. The chemical composition, particularly with regards to the presence of contaminant species undesirable in surface-sensitive photoelectron studies was determined for a range of different deposition conditions. The results of these studies indicated that for minimal contaminant surface species the use of 30 minutes of pre-cleaning of the sputter target and the use of a new, pristine TiO₂ target produced the surface with lowest concentrations of Si (<1%) and C (6%) achieved through heating to 500C under vacuum. These films are capable of modification through heating to induce Ti³⁺ defect sites. Morphological studies revealed that these films consisted of close-packed, films of circular nanoparticles 20-30nm in size. Heating of the films increased the surface roughness and particle size of the TiO₂. The crystallinity of the substrate is capable of being tuned for anatase or an anatase/rutile mixture with heating between 500-1100°C for extended periods (18-24h)

4 SUB-MONOLAYER AU9 NANOCUSTER FILM FORMATION VIA PULSED NOZZLE CLUSTER DEPOSITION

This chapter is a reformatted version of the paper published in:

Nanoscale Advances 2020 Vol. 2 Issue 9 Pages 4051-4061

Author Contributions:

Jesse Daughtry: Designed and performed experiments, analysed data, prepared figures and manuscript.

Gunther Andersson: Intellectual contribution in conceptualising experiments, data interpretation and revision of manuscript.

Gregory Metha: Intellectual contribution in conceptualising experiments, provided pulse nozzle expertise, and revision of manuscript.

Siriluck Tesana: Chemical synthesis of Au nanoclusters, provided experimental details for manuscript.

Tomonobu Nakayama: Intellectual contribution in conceptualising experiments, AFM and pulse nozzle experimental expertise, and revision of manuscript.

4.1 Abstract

Sub-monolayer coverages of chemically synthesised triphenylphosphine-protected Au₉ clusters on mica and TiO₂ substrates were achieved through the development of a Pulsed Nozzle Cluster Deposition (PNCD) technique under high vacuum conditions. This method offers the deposition of pre-prepared, solvated clusters directly onto modified substrates in a vacuum without the potential for contamination from atmosphere. AFM and TEM were used to investigate the rate of gold nanocluster deposition as a function of nanocluster solution concentration and the number of pulses, with pulse number showing the most effective control of the final deposition conditions. TEM and XPS were used to determine that the clusters retained their unique properties through the deposition process. Methanol solvent deposited in the PNCD process has been shown to be removable through post-deposition treatments. A physical model describing the vapour behaviour and solvent evaporation in a vacuum is also developed and presented.

4.2 Introduction:

The properties of atomically precise gold nanoclusters have been found to have novel properties distinct from those found in bulk Au and gold nanoclusters. Gold nanoclusters can be defined by their small size (<2nm) and consist of fewer than 246-279 Au atoms[286] with clusters below this threshold exhibiting properties that are highly dependent on the number of atoms constituting the nanocluster[40, 286-288]. These properties have proven to be associated with their unique electronic density of states[115, 181]. Utilising the properties of atomically precise clusters for use in catalysis, for example, in water-splitting[289, 290] and CO oxidation,[291, 292] has become a promising field of research. The interactions between atomically precise nanoclusters and substrates have been shown to be crucial to stabilising and retaining nanocluster properties and can also enhance catalysis[38, 147, 185].

Metal nanoclusters can also be generated in gas phase nanocluster sources and deposited on substrates; however, they must be used immediately and cannot be stored for any period of time. While vacuum generated nanoclusters can be deposited directly onto treated substrates for further analysis,[293, 294] chemically synthesised nanoclusters are able to be assembled in the liquid phase with near total homogeneity¹ and, after recrystallization have traditionally required any deposition to take place outside of vacuum, thus introducing contamination and potentially affecting any surface treatments made in vacuum[266, 295]. Thus, a method of depositing pre-prepared, chemically synthesised nanoclusters directly onto a treated substrate under vacuum conditions would be advantageous in examining the substrate-nanocluster interaction.

The usefulness of pulsed vapour depositions to achieve controlled thin film growth have been demonstrated in surface coating systems, particularly metal oxides utilising ultrasonically vibrated

vacuum pulse nozzles to inject packets of the solvated precursor from high pressure to vacuum[261, 296, 297].

These reports raised the question of whether a similar technique utilising pulsed valves could achieve the desired characteristics for deposition of metal nanoclusters through the injection of solvated nanoclusters into high vacuum. Injection over a large pressure differential in such a manner means liquid would undergo a supersonic expansion, evaporating the solvent and allowing deposition of nanoclusters. Such a deposition would ideally have the following characteristics:

- Being able to deposit only fractions of a monolayer of clusters onto the substrate surface
- Distribution of clusters should be as homogeneous as possible
- Deposition of individual clusters and avoiding agglomeration of clusters or droplets of solvent
- Retaining the nanocluster properties and characteristics
- Verifiable decrease in solvent deposited compared to known deposition methods.

High vacuum pulse valves offer control of deposition conditions through the valve opening time (pulse width), the time between pulses (pulse frequency), solution concentration and the pressure differential between vacuum and backing pressure of the valve. In this paper, we present the operation and design of a pulsed nanocluster vacuum deposition system for ligand-protected, atomically-precise gold nanoclusters, specifically $[\text{Au}_9(\text{PPh}_3)_8]^{3+}$, from a methanol solution. Optimisation of the system was investigated for several deposition parameters towards the desired nanocluster deposition conditions stated previously. Atomic force microscopy (AFM), X-ray photoelectron spectroscopy (XPS) and transmission electron microscopy (TEM) have been used to characterise the surfaces after pulsed nozzle deposition of the gold clusters.

4.2.1 Experimental Methodology

To investigate the usefulness of Pulsed Nozzle Cluster Deposition (PNCD) for chemically synthesised nanoclusters, a representative nanocluster was selected for the study, $[\text{Au}_9(\text{PPh}_3)_8]^{3+}$ (hereafter referred to as Au_9). Chemically-synthesised, atomically-precise gold clusters were synthesised and purified as reported previously,[186, 298] before recrystallisation and the use of nuclear magnetic resonance spectroscopy, mass spectrometry and X-ray crystallography to confirm the size specificity of the clusters[235]. Au_9 was stored at -17°C in the dark before use in the deposition process. For PNCD, the Au_9 was weighed before dissolution in ultra-pure methanol (HPLC grade, Scharlau) to the desired concentration. The concentration range used was 1 mM, 0.5 mM, 0.25 mM, 0.125 mM, 0.063 mM.

This solution was placed into the liquid reservoir of the pulse nozzle in 0.5 mL aliquots before being flushed with and then back pressured by argon to 2 bar. The Au_9 was deposited onto (i) mica (grade V-4 Muscovite, SPI supplies) for atomic force microscopy (AFM) measurements, (ii) lacey

carbon film TEM microgrid (# 10-1003 RO-C15, Okenshoji) for transmission electron microscopy (TEM), and (iii) RF sputtered, nanoparticulate TiO₂ for x-ray photoelectron spectroscopy (XPS). While the substrates differ in chemical makeup and surface roughness, they are not expected to alter the deposited cluster's properties without further treatment such as heating (*vide infra*).

While the chosen substrates have different surface properties, the interaction of ligated gold clusters with mica and TiO₂ is known to be similarly weak. Therefore, it is assumed that examining particle size and pulsed deposition topography with mica through AFM and elemental composition and chemical properties with TiO₂ through XPS is a reasonable approach. The mica was freshly cleaved along the [001] plane before deposition, with both mica and clean nanoparticulate TiO₂ cut into 10x10 mm samples and mounted to sample holders. TEM microgrids were held by a custom sample holder.

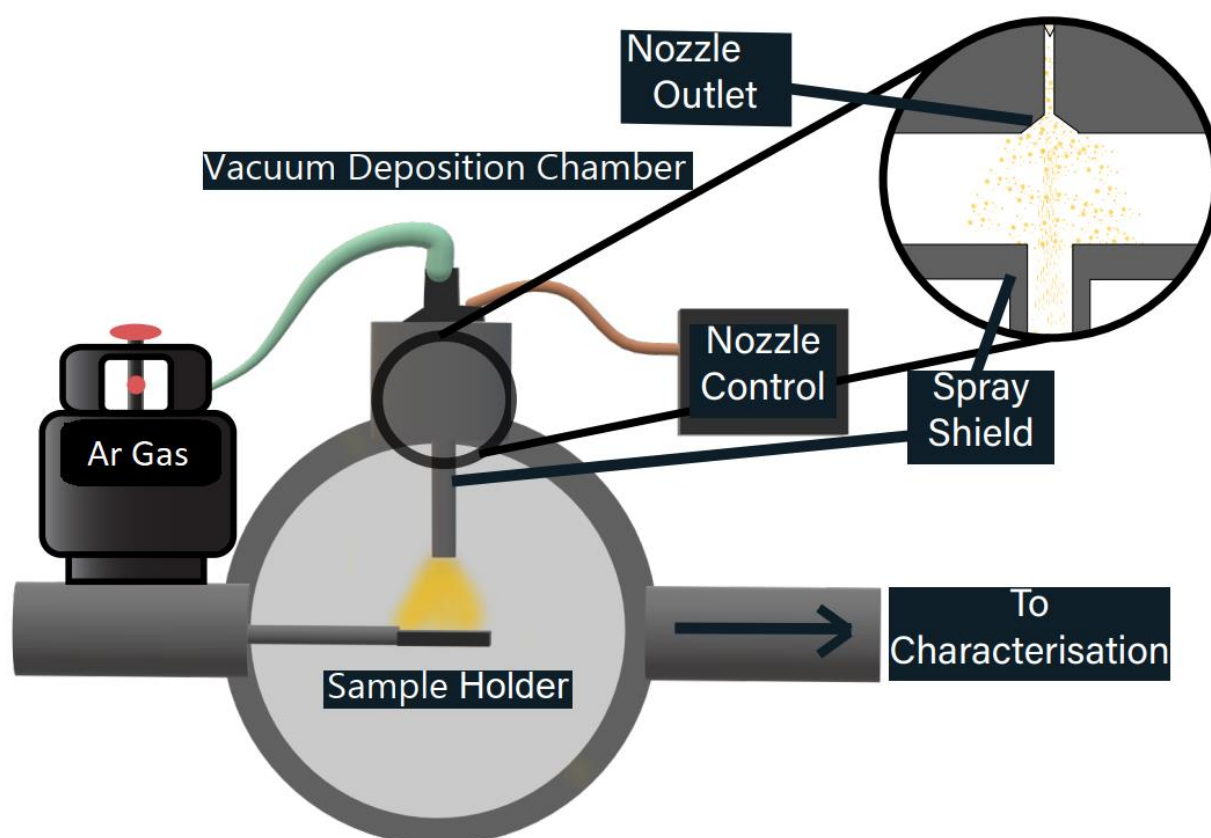


Figure 4-1 Representation of the PNCD system, mounted to a high vacuum load lock (cutaway). Au₉ is loaded into the liquid reservoir and then backed with argon to 2 bar of pressure. The pulse nozzle control unit was operated with a programmed frequency to drive the opening/closing of the solenoid valve. Inside the vacuum chamber, a fabricated metal channel allows the pulsed vapour to reach the sample via line of sight while collecting the more dispersed vapour. The sample is held in a sample manipulator in the path of the vapour pulse and once deposited, can be inserted into the ultra-high vacuum for XPS measurement. AFM measurement requires removal to atmosphere.

After mounting, all substrates were placed into a high vacuum sample load lock and were pumped to 10^{-6} mbar over 6-8 hrs. Each sample was deposited with a set number of pulses of equal pulse length (250 μ s, unless otherwise stated). After waiting for the 'settling time', the system can be pulsed again to inject further material until the desired amount has been injected. For gold clusters, the ideal case is that a certain amount of pulses delivers specific coverage in a controllable manner. The desired depositions for this process would be capable of producing a controllable, sub-monolayer coverage. Up to 2 samples could be prepared in the load lock chamber at the same time, allowing for identical deposition conditions across different substrates. The PNCD system design is schematically represented in Figure 4-1.

The pulse vapour deposition system is comprised of three main components:

- High vacuum pulsed valve
- Pulsed valve control unit
- Cold-wall vacuum chamber with sample manipulator

The high vacuum pulse valve used is a miniature high-speed, high vacuum dispense solenoid valve (Parker Hannifin, USA) with a 0.51 mm orifice, cone-shaped outlet flange and polytetrafluoroethylene (PTFE) poppet. The valve has an internal 3 mL reservoir and is fitted for a gas line for providing backing pressure. This valve is mounted such that it is in a vertical orientation, pulsing vertically downwards. The nozzle is not a ultrasonic vibrational nozzle. The latter is probably not suitable for the deposition of clusters because the ultrasound could lead to disintegration of the clusters.

The pulse valve control unit (Iota One valve driver, Parker Hannifin, USA) used at NIMS was specifically designed for operating high-speed solenoid valves. Depositions performed at Flinders utilised a custom-built pulse driver to control identical high-speed solenoid valves. The control unit allows the selection of pulse width (nozzle open time) to the microsecond range as well as the ability to make single pulses or automatically triggered pulse sequences at determined intervals. A successful pulse would register an audible click from the high-speed vacuum valve followed by a rapid increase in observed pressure, peaking in the high 10^{-5} to low 10^{-4} mbar. The pressure would return to the starting value within approximately 30 seconds, and after a further 30 seconds, the next pulse was injected, giving a 60-second pulse interval.

The load lock used for deposition is attached to a separate UHV chamber, allowing deposited samples to be easily introduced, or removed to atmosphere for further analysis. A custom-designed vapour shielding channel (see Fig 1) was used in the load lock to restrict the path of injected vapour, allowing only those nanoclusters with a line of sight to the substrate to reach it, it was then removed for cleaning in between depositions.

4.2.2 AFM

All AFM measurements presented were performed at NIMS. Mica substrates were selected for AFM measurements due to their low surface roughness to easily distinguish the sub-nanometer deposited species[267, 299]. These samples were removed from vacuum and transferred directly to a vibrationally isolated AFM (SPA400, Seiko Instruments, Japan) and scanned with tapping mode (SI-DF20 cantilevers, Hitachi, Japan) rated at 42 K(N/m), 250-390 kHz with 125 μm cantilever length. Scans were run in atmospheric conditions at multiple sites across the surface of a sample. Scans were made from 10x10 μm down to 200x200 nm.

AFM imaging allows plotting of the distribution of deposited particles as well as their height for analysis. AFM tip curvature means that surface species smaller than the AFM resolution cannot be accurately resolved laterally but their height measurements are unaffected by tip curvature and remain accurate. Raw topography scan data was processed with the Gwyddion software package. Once the scan was levelled, deposited particles were masked using the mask by watershed feature, with each watershed region containing approximately one particle. The masked particles were then filtered to remove any particles larger than known nanocluster size, as well as to have a minimum height cut-off to remove substrate regions with a roughness that had been incorrectly marked as particles. The maximum and mean particle heights could then be extracted through the in-built grain analysis package.

4.2.3 XPS

All XPS measurements were performed at Flinders University (FU) under UHV conditions. While mica substrate was found to be suitable for AFM measurements, test samples used in XPS showed charging effects that interfered with elemental identification. TiO_2 has been shown to be appropriate support material for electron spectroscopy[300]. Therefore, all samples deposited onto mica for AFM were simultaneously deposited onto TiO_2 for XPS measurements to identify the chemical composition of the sample surface. Samples prepared at NIMS (Series A & B) were transported to Flinders for measurement using XPS. These samples were transported in individual light-blocking sample holders and stored at -17°C when not in transit. XPS was performed as soon as possible to avoid unnecessary sample degradation. Samples for the investigation of solvent removal were deposited and investigated at FU under UHV conditions without exposure to atmosphere.

X-ray spectra were recorded at 1253.6 eV (Mg K_α radiation) using a SPECS PHOIBOS-HSA300 hemispherical analyser as previously described[301]. Due to the limited mean free path of the electrons, only the top $\sim 5 - 10$ nm of the sample is probed. These measurement conditions have been shown not to damage samples of this type[266].

High-resolution XP spectra of the C 1s, O 1s, P 2p, Ti 2p and Au 4f regions were collected at 10 eV pass energy. All XP spectra were analysed with Casa XPS using a Shirley background and a hybrid Gaussian (30%) and Lorentzian (70%) function to fit all peaks in a method described previously[235]. Elemental sensitivity factors for an X-Ray source at 54.7° were used in the analysis process. The adventitious carbon peak found at 285 eV binding energy was used as the calibration peak for all samples[272].

4.2.4 TEM

TEM measurements were undertaken at NIMS on samples prepared using lacey, amorphous carbon film TEM grids that were subsequently dried under vacuum for several days prior to measurement. Measurements were performed on a JEOL JEM-2100F instrument with a 200 kV accelerating voltage in both dark and light field modes. Energy dispersive X-ray (EDX) measurements were also taken on specific samples for elemental analysis. Recorded images were processed using the DigitalMicrograph (Gatan) software package to determine particle sizes. It is worthwhile noting that initial testing on TiO₂ nanosheet microgrids showed that pulse deposition could destroy the nanosheet integrity, making measurement difficult or impossible. Subsequently 6 nm amorphous carbon microgrids were used for deposition and were far more resistant to damage by the deposition process.

4.3 Results

4.3.1 Controlling and Optimising Deposition:

Initial attempts to deposit gold clusters using a differing number of pulses at a range of pulse widths resulted in either very heavy coverages or no discernible change in sample surface as viewed in AFM. This was attributed initially to the pulse length as pulses around 150 μs resulted in inconsistent pressure increases, and longer pulses (>300 μs) showed clear circular features assigned to the impact of a droplet of particles on the substrate, similar investigations using ultrasonically vibrated nozzles had reported imperfect pulse conditions lead to large droplet formation[261]. From AFM, it was clear that the depositions were higher than a monolayer coverage and therefore undesirable (Figure 4-2). This range shows depositions from high pulse numbers that produce very high coverage and appearance of surface structures attributed to droplet impacts on the surface, even with low pulse width (opening time). This was attributed to continued pulsing allowing larger droplets to form and reach the substrate before vaporisation.

Improved dispersion and reduced droplet-like features were observed with the use of larger pulse width and lower pulse numbers. Pulse time was determined through iteration, 100μs was observed to be too short for observable pressure increases on pulsing. Increased in 50μs steps until stable pressure increases were observed. The pulse width was optimised to produce consistent peak

pressures (10^{-5} mbar) and reduction of circular features at an open time of 250 μ s was used for all final measurements.

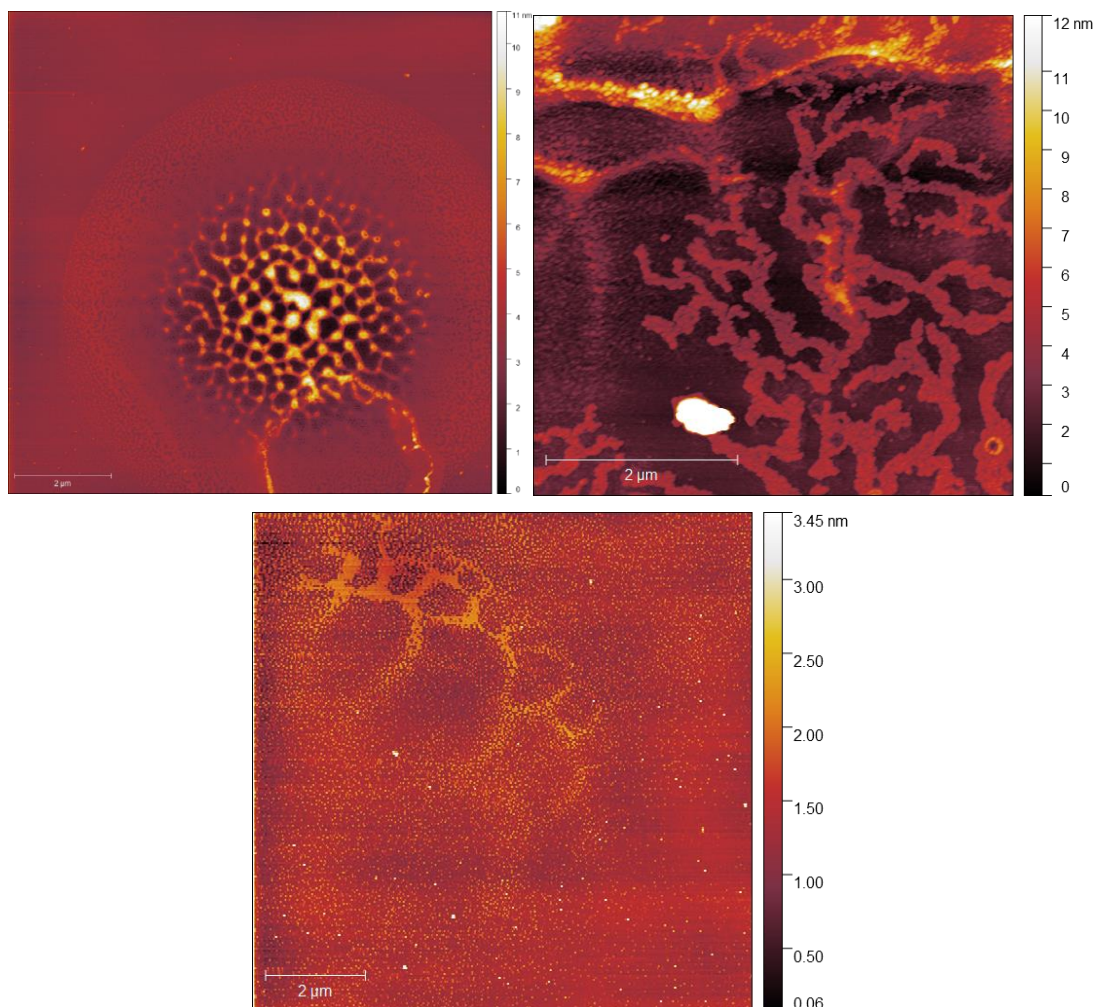


Figure 4-2 AFM measurements displaying non-optimal regions from PNCD on mica surfaces, displaying droplet impacts (top left, 0.125mM Au₉/methanol, 30x pulses, 250 μ s, B4) multi-layer coverages (top right, 0.125mM Au₉/methanol, 100x pulses, 250 μ s) and nanocluster aggregations (bottom, 0.04 mM Au₉/methanol, 10x pulses, 150 μ s)

Control depositions were performed using only methanol in a freshly cleaned pulse nozzle set-up. These depositions were performed onto freshly cleaved mica using 250 μ s pulse width, 50x pulses at 60 seconds intervals allowing deposition chamber pressure to recover to low 10^{-7} mbar pressure between pulses. The mica used for deposition was measured in AFM directly after cleaving and then again straight after removal from the deposition chamber. The AFM scans of the before and after deposition conditions can be seen in Figure 4-3. The mica before a pulsed deposition can be seen to have a reasonably homogenous coverage of 2-3 nm high particles. Similar features have been found in previous studies on mica cleavage and assigned to crystallite growth from surface contaminants[299].

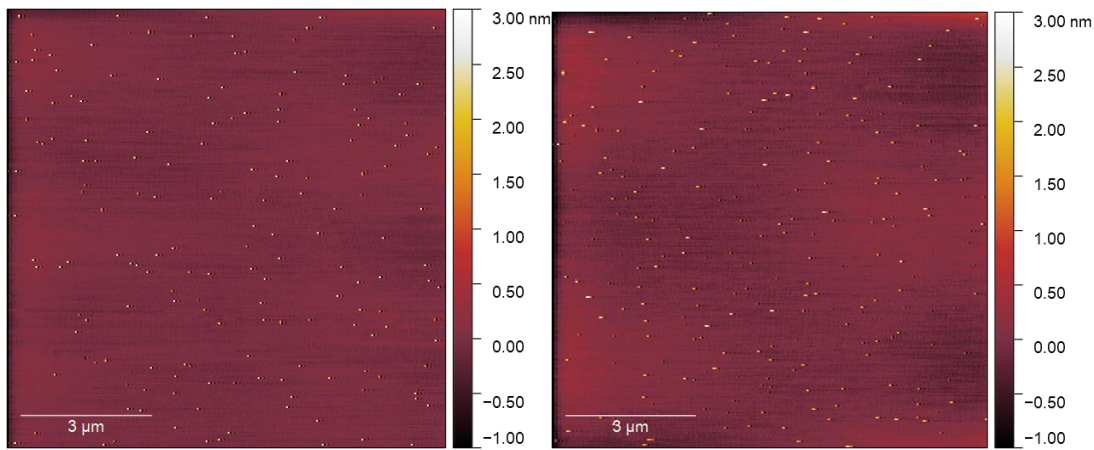


Figure 4-3 (left) AFM scan on freshly cleaved mica, (right) AFM scan on mica after 50 pulses of methanol, some larger features are clipped out of scale range.

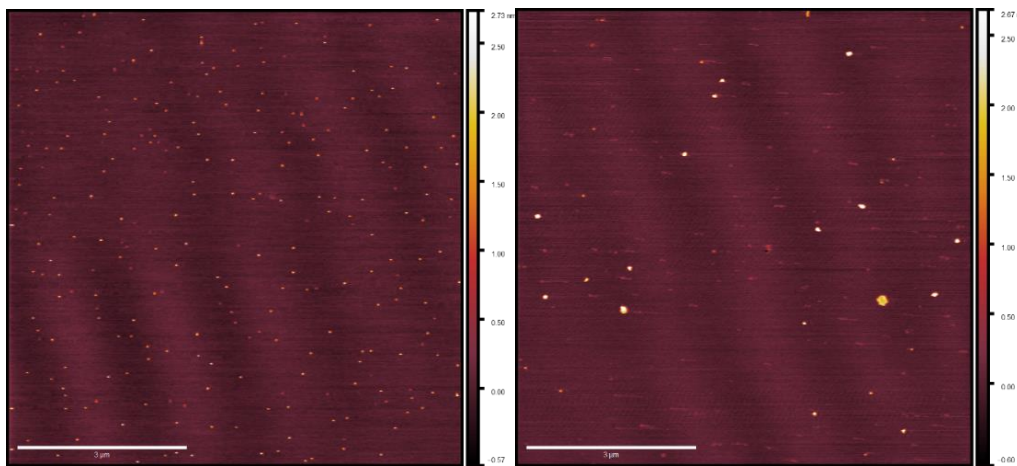


Figure 4-4 AFM scans of mica control images showing a methanol-only (no nanocluster) deposition (left) resulting in partial removal of the particles seen in fresh cleaved mica samples and some larger particles/residue (approx. 10-20 nm high) across the surface (right). This was only for the one sample presented and was attributed to sub-optimal deposition conditions.

AFM scans of post-deposition methanol exhibited the continued observation of the 2-3 nm features, with a small number of larger features in the 3-5 nm range being introduced, with an exceptional case showing larger features presented in Figure 4-4. As both prior and post-deposition scans show large regions of picometer roughness (attributed to flat mica) with observable features being of a size range easily distinguishable from deposited gold clusters (0.75-1.25 nm)[196, 302], the use of PNCD on mica was determined to be appropriate for the study of Au₉ nanoclusters. As such, a series of measurements were undertaken to investigate the effect of PNCD solution concentration and pulse number (see Table 2-1) onto mica and TiO₂ placed side by side in the load-lock.

Table 4-1 Deposition series for concentration change (A) and pulse number change (B). Series A were all deposited for 30x pulses. Series B used 0.125 mM Au₉ in methanol solution. All samples were simultaneously deposited onto both mica and TiO₂ substrates for AFM

Deposition Series A		Deposition Series B	
A1	1 mM	B1	100x
A2	0.5 mM	B2	50x
A3	0.25 mM	B3	40x
A4	0.125 mM	B4	30x
A5	0.061 mM	B5	20x
		B6	10x
		B7	1x
Sample A4 & B4 come from the same deposition			

4.3.2 XPS results and analysis

The amount of gold nanocluster deposited for each sample was determined through quantification with XPS. It has been determined through previous studies that ligated Au₉ clusters have a 4f_{7/2} peak with characteristic binding energy (BE) at 84.9 ± 0.3 eV contrasting with the same peak for agglomerated clusters found at the binding energy for bulk gold at 84 ± 0.2 eV[235, 266]. For samples A4-5, B2-5, agglomeration is consistent at around 70/30 nanocluster/bulk, as shown in Figure 4-5 for sample A4. All other samples showed no signs of agglomeration, as shown in Figure 4-6 for sample B6, suggesting that agglomeration in the other samples may have been caused by transport or sample handling.

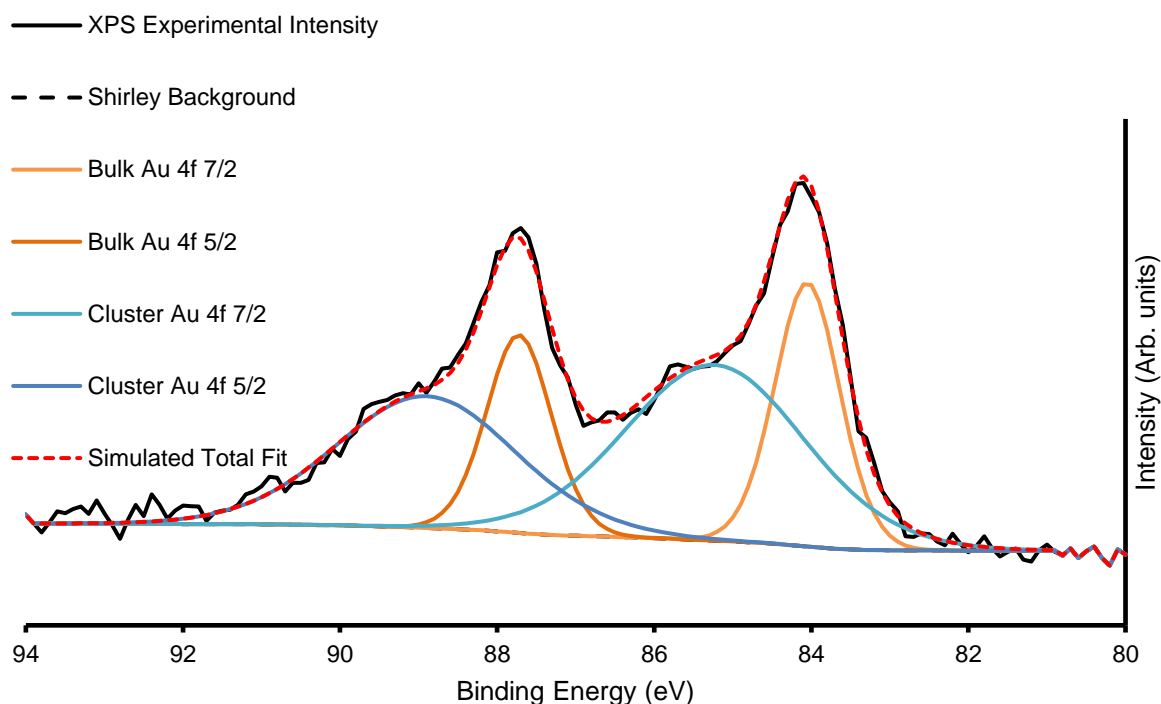


Figure 4-5 High resolution XPS scan at the Au 4f region. 2 distinct species are evident with gold cluster 4f7/2 Au peak at 85 eV while bulk Au peak can be seen at 84.2 eV showing that some cluster agglomeration has occurred.

The P 2p region was also investigated, but no discernible peaks were found, probably due to partial ligand loss during the multiple vacuum pumping events, as found by us previously[196]. The results of the analysis can be seen for all species in Table 4-2, with the trends of gold nanocluster deposition across series A and B shown in Figure 4-7.

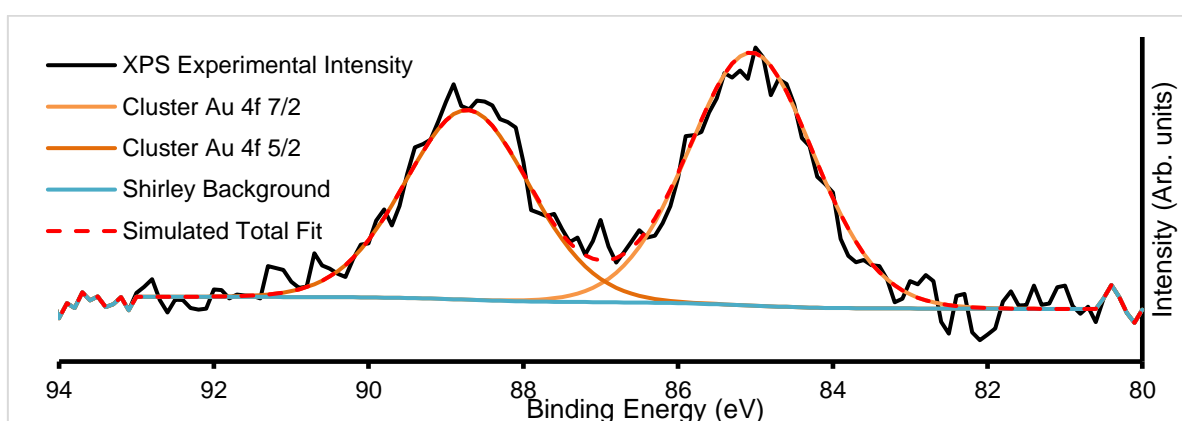


Figure 4-6 Example XP spectra of sample B6 showing Au 4f region, with the characteristic nanocluster Au 4f_{7/2} peak at 85.2 eV.

Table 4-2 XPS relative elemental contributions for series A & B across C 1s, O 1s, Ti 2p and Au 4f regions.

	C (285 eV)	O (530.5 ± 0.2 eV)	Ti (459 ± 0.2 eV)	Au (nanocluster, 85 ± 0.2 eV)	Au (Bulk, 84 ± 0.2 eV)
A1	22.4±0.1	57.6±0.1	19.9±0.1	0.1±0.01	-
A2	23.8±0.1	57.6±0.1	19.9±0.1	0.3±0.01	-
A3	33.8±0.1	49.0±0.1	16.3±0.1	0.8±0.01	-
A4	17.6±0.1	61.0±0.1	21.2±0.1	0.07±0.01	0.03±0.01
A5	19.2±0.1	60.1±0.1	20.5±0.1	0.07±0.01	0.03±0.01
B1	24.0±0.1	56.6±0.1	19.1±0.1	0.2±0.01	-
B2	25.2±0.1	56.3±0.1	18.4±0.1	0.11±0.01	0.03±0.01
B3	23.9±0.1	57.1±0.1	18.9±0.1	0.8±0.01	0.06±0.01
B4	17.6±0.1	61.1±0.1	21.2±0.1	0.07±0.01	0.03±0.01
B5	25.7±0.1	56.0±0.1	18.2±0.1	0.034±0.01	0.016±0.01
B6	21.1±0.1	58.7±0.1	20.2±0.1	0.02±0.01	-
b7	17.2±0.1	58.5±0.1	24.3±0.1	0.014±0.01	-

It can be seen that the carbon contribution across all samples is very high, as would be expected for samples having been exposed to the atmosphere. Cleaning of the samples with heating/sputtering was not undertaken as it has been shown to affect Au₉ stability, causing agglomeration. Sample A3 had unexplained, particularly high carbon contribution (10% higher) and concomitantly lower Ti and O contribution. Otherwise, the samples were quite similar with the exception of gold nanocluster contribution, which showed marked differences depending on deposition conditions. Across series A, the amount of gold nanocluster deposited seemed to follow no discernible trend for different solution concentrations, with the highest concentration of gold

nanocluster in methanol, A1 giving the lowest gold coverage overall. The 0.25 mM sample A3 meanwhile had the highest gold contribution of any measured sample.

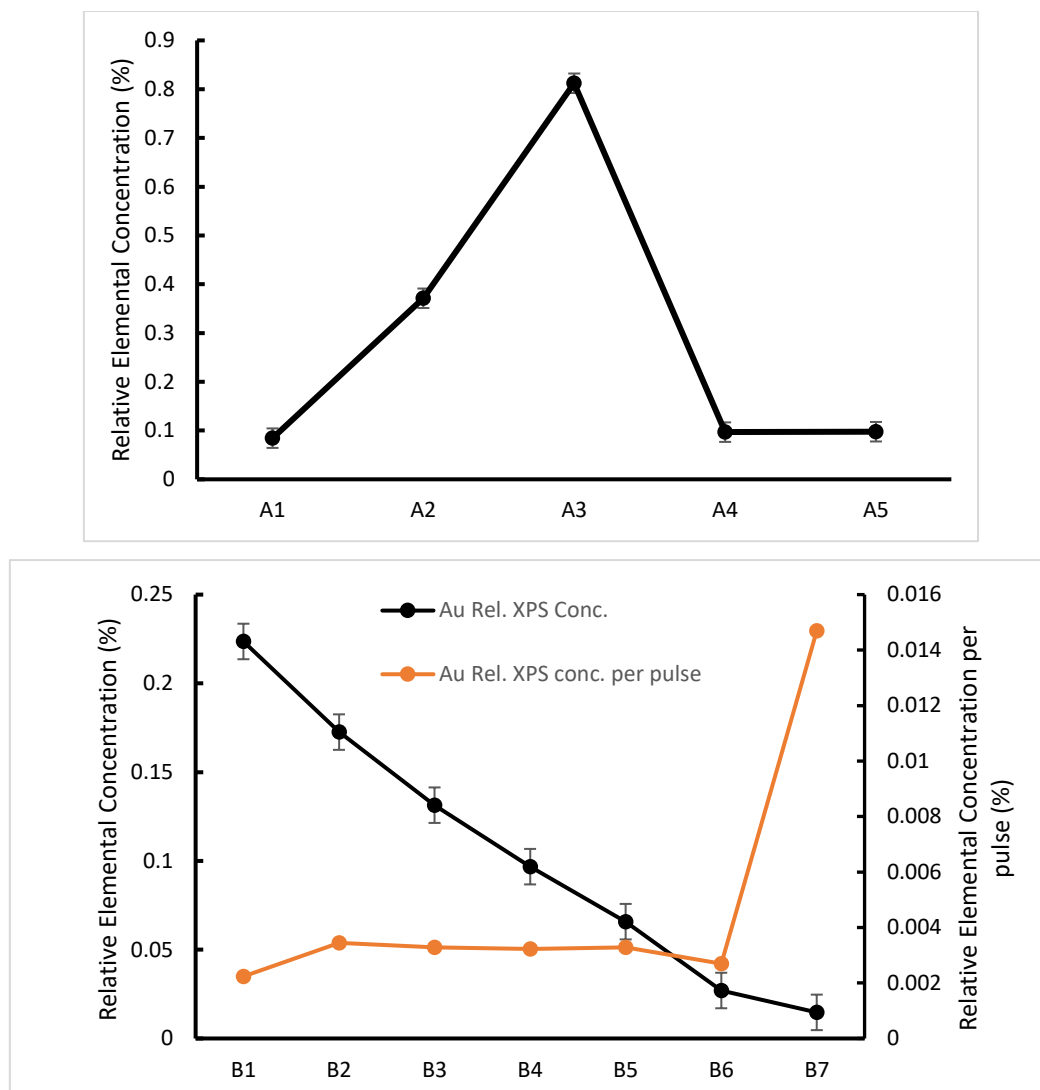


Figure 4-7 Relative elemental concentration of Au₉ clusters from XPS analysis across series A (concentration change) and series B (pulse number change). No trend is evident in series A, whereas series B shows a clear reduction in gold nanocluster conc. with lower pulse no. and, when normalised per pulse, reveals that the initial pulse deposits far more Au than subsequent pulses.

4.3.3 AFM Results and Analysis

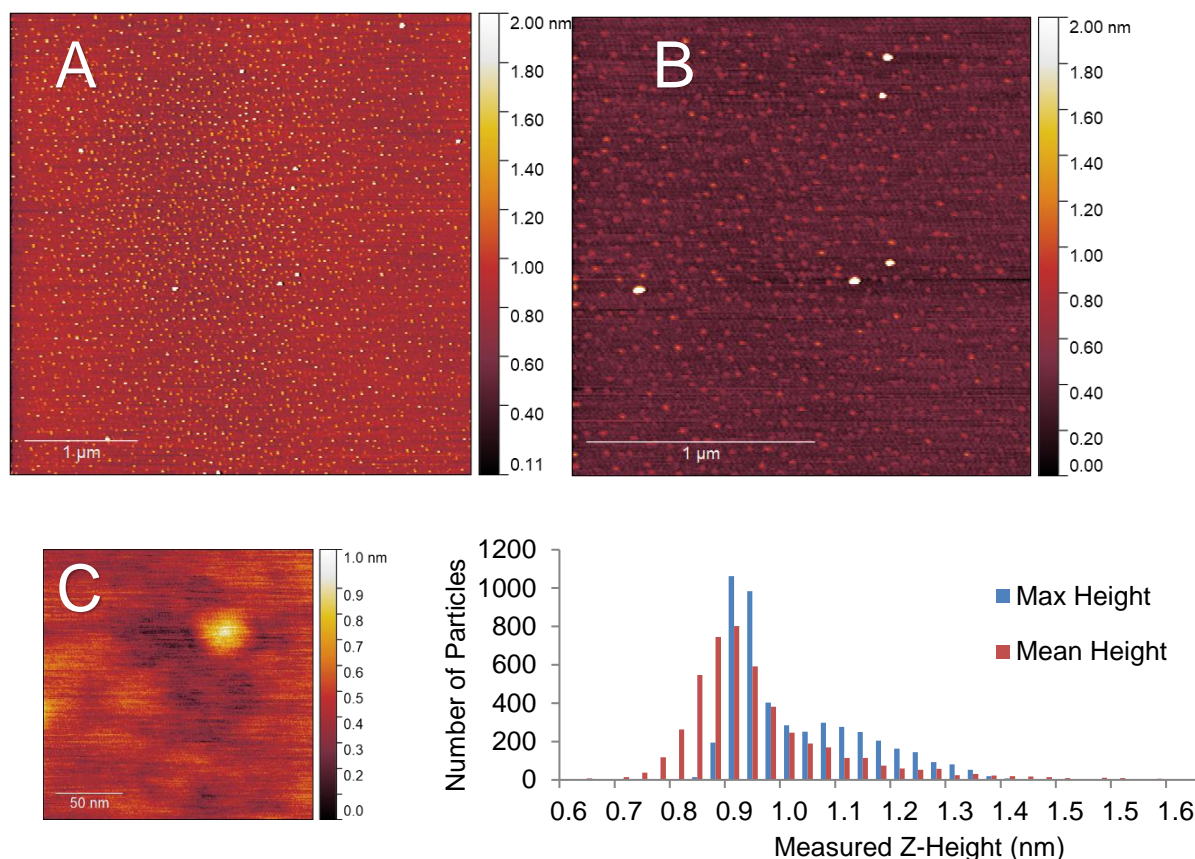


Figure 4-8 Top - A: 0.125mM Au₉/Methanol single pulse (sample B7) on mica. B: higher magnification scan of A C: High magnification scan on a single nanocluster-sized object found on the same sample. Particle height distribution for 5 μm² scan of 0.125 mM from one pulse. Some larger particles are clipped out of scale range.

AFM scans on series A samples showed highly variable coverages with many circular, droplet-like features (see Figure 4-2). These results suggest that solution concentration, at least over multiple pulse regimes are not an effective method of controlling sub-monolayer depositions of gold clusters.

In series B, while the elemental concentration of Au does not scale in a perfectly linear fashion with the number of pulses applied, the response in Au relative XPS contribution results in a near-linear decrease with decrease in pulse number. However, when the relative Au XPS contribution per pulse is examined (orange line in Figure 4-7 B), the amount of Au deposited per pulse is almost constant, except for the sample B7. This single pulsed sample shows nearly 5 times the amount of Au deposited per pulse. The reasons for this are not fully understood but as the first pulse is injected into a vacuum achieved through hours of pumping it undergoes the greatest pressure differential, which may also explain why the most dispersed, homogenous depositions were achieved from such depositions. The first pulse could change the local pressure at the nozzle, or the seal of the nozzle poppet, affecting how much material is drawn through in subsequent pulses.

While the amount of gold nanocluster deposited is a key criterion for assessing PNCD, another is the dispersion and coverage of a sample with Au₉ clusters. Especially given that size-specific clusters are observed to agglomerate more readily in concentrated depositions from solution. The AFM images of samples B1-5 show patchy areas of very high coverage resembling features of closely packed small particles along with some much larger particles (2-4 nm) dispersed throughout (see Figure 4-2). Scans of the samples B6 & B7 showed many more isolated, nanocluster-like features and very few regions of closely packed clusters. An AFM scan from series B7 can be seen in the top half of Figure 4-8 displaying the types of coverages seen in a 1x pulsed deposition. No highly concentrated regions were detected in the scanned areas; instead, disperse particulate coverage exist across the scan, with much less variation in particle concentration. The particle height distribution for the scans on sample B7 can also be seen in Figure 4-8. The particle size analysis revealed a distribution of maximum particle heights peaking between 0.85-0.98 nm while taking the mean particle height gave the largest number of particles at 0.90 nm with a broader overall distribution.

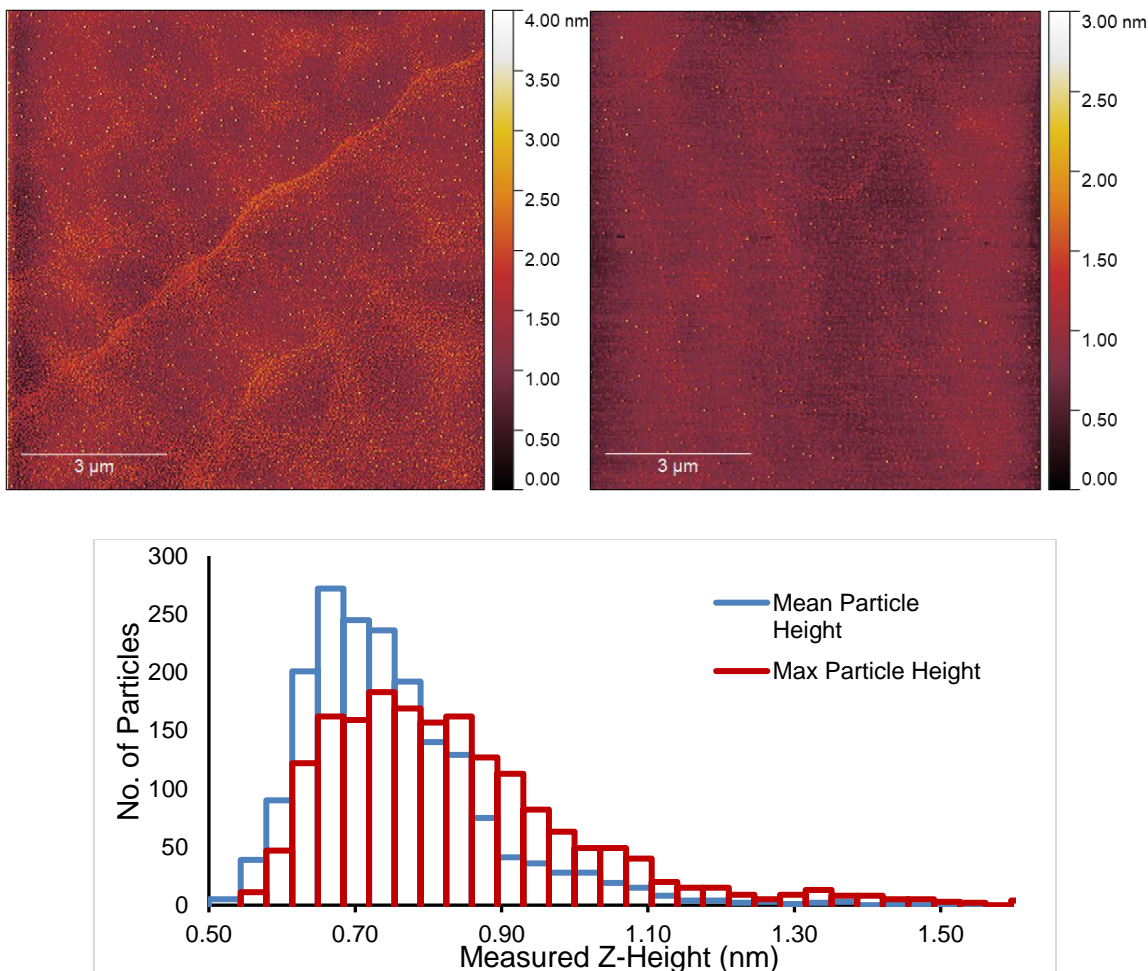


Figure 4-9 AFM scans of sample B6 (on mica) at different locations showing largely homogenous depositions of cluster sized particles with no droplet-like features. Bottom - Particle height distribution for 10 μm scan of sample B6 show the weighting of maximum and mean particle heights for each scan, with the distributions for both in agreement for large numbers of sub-nanometer (gold cluster sized) particles.

AFM analysis was undertaken on sample B6 pulse as this sample also produced dispersed coverages with a large fraction of single nanocluster sized objects. The AFM results for this deposition can be seen in Figure 4-9 along with the particle size analysis of the $5 \mu\text{m}^2$ scan. The maximum and mean height distributions show maxima both between 0.65-0.91 nm. Both samples B6 and B7 measurements also showed that particle max height analysis contained a small fraction of larger particles across the sample surface.

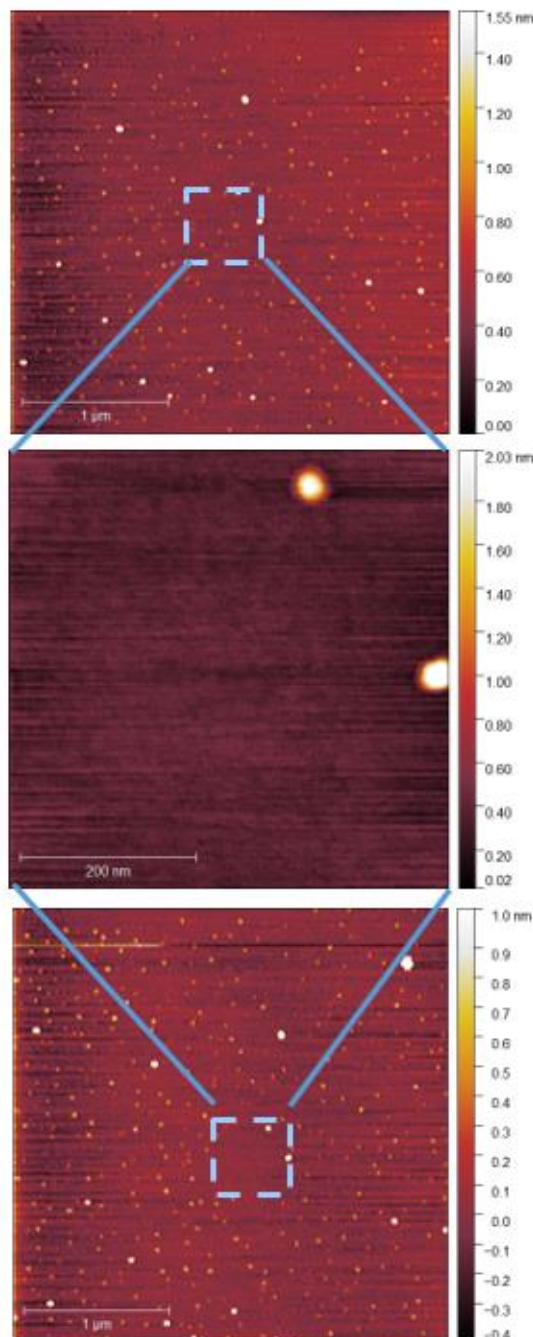


Figure 4-10 AFM scans of pulsed vapour deposited Au_9 onto Mica. All scans were performed at the same location with top and bottom being $3\mu\text{m}^2$ and middle being 500nm^2 . The blue frame indicates common scan regions. The top and bottom images are $3\mu\text{m}^2$ AFM scans taken before (top) and after (bottom) the central 500nm^2 scan.

Particle sizes of 0.65-0.98 nm are in good agreement with results previously reported by Al Qahtani *et al.* from AFM of the same gold clusters on TiO₂ nanosheets deposited through immersion, where they showed the average z-height of deposited clusters was 0.75 nm[302] albeit on a rougher substrate. Previous DFT modelling of ligated gold clusters proposed larger sizes between 1.47-1.66 nm when ligated but did not take into account the change in nanocluster orientation and arrangement, as seen in high-resolution STEM, gold clusters are capable of 'laying flat' when interacting with surfaces[196], or after the loss of some ligands in a vacuum environment, as is suggested to have occurred in this case, through XPS results. Thus, it can be assumed that particle sizes of 0.65-0.98 nm correspond to the height of single Au₉ clusters on mica.

Further AFM measurements on the single pulsed sample showed that under certain scan conditions, the gold clusters could be moved by AFM tip contact (see Figure 4-10) as has been previously observed for gold nanocluster depositions on TiO₂ nanosheets[267]. The cluster sized objects in the top scan are not evident in the centre scan and once the large scan was repeated in the bottom scan it was evident these clusters had been pushed to the frame edge by the AFM tip.

4.3.4 TEM Results and analysis

Samples for TEM measurements were prepared only under conditions closely resembling samples B3-B6 (i.e. conditions similar to series A were not examined with TEM). This involved depositing the samples with 0.125 mM Au₉/methanol, at 250 μs pulse time for 40-10 pulses at 60-second intervals. The samples were imaged using darkfield TEM. Several sites were chosen for imaging across each sample. The TEM scans from a 10-pulse deposited microgrid can be seen in Figure 4-11. The well-dispersed bright spots indicate individual gold clusters on the carbon substrate. The coverage observed is homogenous, and while there is a variety of particles sizes evident, the TEM intensity line profile (Figure 6) clearly shows that lateral particle size is in good agreement with complementary AFM height measurements for gold clusters at 0.8-0.95 nm. Several larger particles appear to be irregular in shape and may indicate a grouping of multiple deposited gold clusters. EDX was used to attempt identification of the metallic species but due to low sensitivity was only effective on heavily deposited samples, as seen in Figure 4-12, where it identified Au as present.

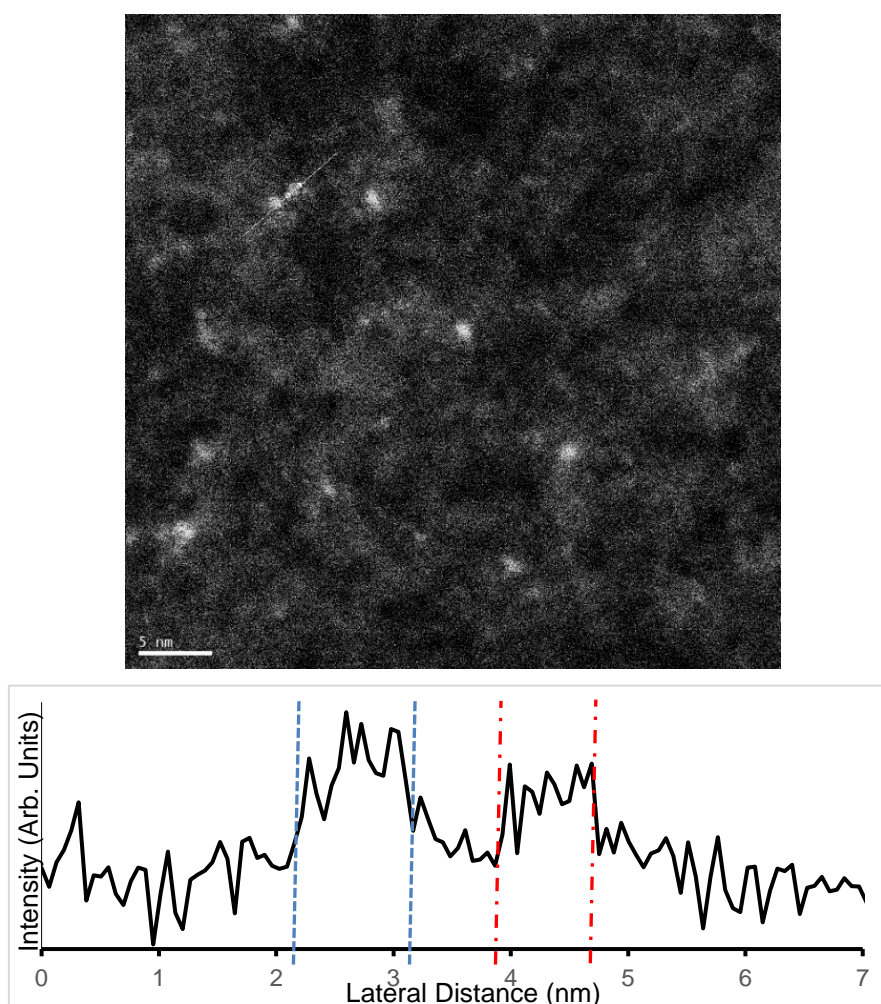


Figure 4-11. Above - Darkfield TEM of microgrids deposited with 10 pulses of 0.125 mM Au₉/methanol solution. Below – intensity profile along the white trace of the image

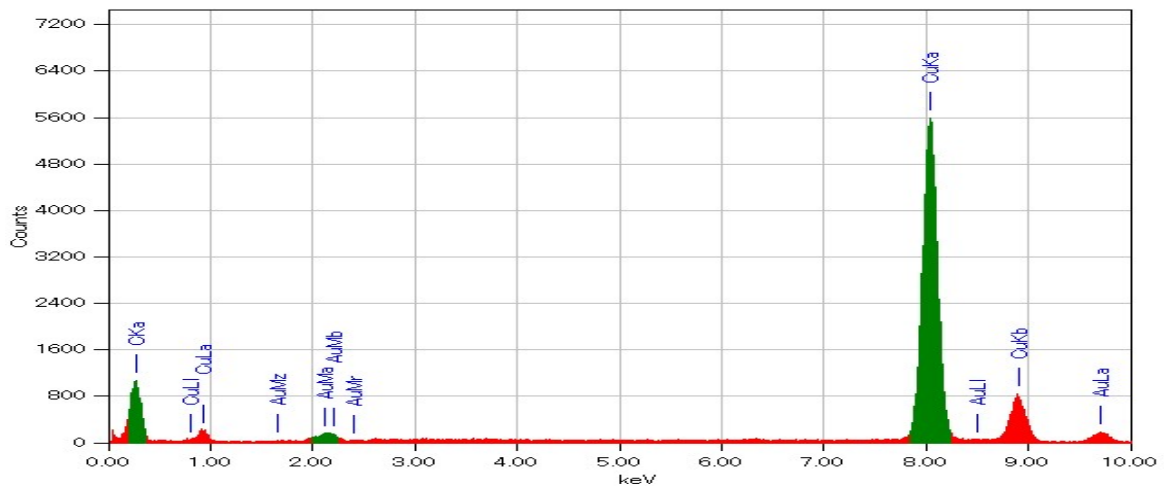
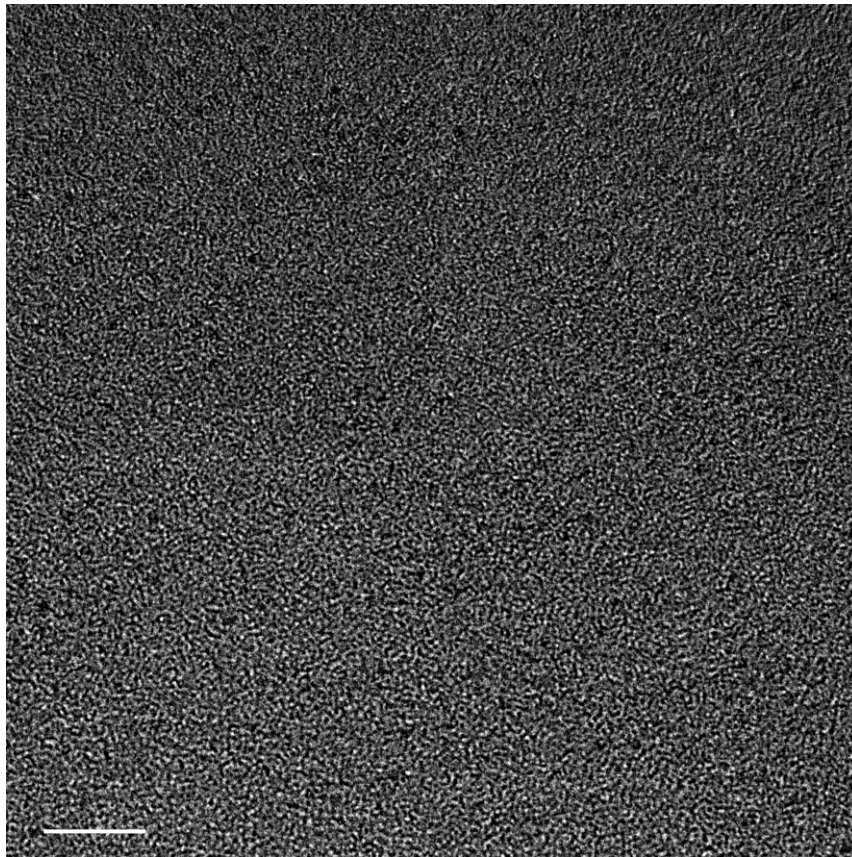


Figure 4-12 TEM scan on a 40x pulse deposited 0.125mM Au₉/Methanol sample using amorphous carbon microgrid. The top part shows a TEM scan of a PNCD deposition on to carbon microgrid with a region of dense coverage of metallic species. The bottom part shows the EDX result. Au was found (~ 2.1 keV) on this sample. In other TEM samples the Au concentration was below the threshold for detection using EDX. Cu signal seen in the EDX comes from the microgrid structure.

4.3.5 Solvent Removal – Effect of heating

In order to determine the presence of solvent from the PNCD process on the samples, the system detailed in the experimental section was set up on a load lock with direct access to XPS measurements. The TiO₂ substrate was inserted into the vacuum and cleaned of adventitious carbon and other contaminants through heating to 300°C and sputtering with Ar. It was then deposited with 3 pulses of gold nanocluster/methanol solution (0.125 mM) before being heated to 200 °C all while remaining in at least 10⁻⁷ mbar vacuum.

It was observed that by measuring the high-resolution C 1s region in XPS between every step of the vacuum deposition the growth of the carbon peak at 286.7±0.1eV binding energy appears after the pulses are deposited onto the sample and correspond to C-O bonds from methanol. This peak is nearly entirely removed through the final heating step, and Table 4-3 shows the increase and decrease in relative XPS percentage from C 1s. The lowest relative percentage of carbon in the 200°C heated sample is justified as with the addition of Au the relative proportions of each species are lowered. These measurements confirm that pulse deposition is a method of depositing gold nanocluster with low-contamination with solvent. Carbon contamination introduced through PNCD is nearly entirely removable.

Sample Process	Relative XPS % (C 1s)
Heated 300°C, Ar Sputtered	3.9±0.2
Pulsed w/ Au ₉ /methanol	6.4±0.2
Heated 200°C	3.0±0.2

Table 4-3 Carbon 1s XPS percentages for the 3 measured steps, cleaning, deposition, and decontamination of a PNCD preparation of gold clusters

The procedure described above mirrors that undertaken for previously reported attachment of gold nanocluster to TiO₂ through liquid immersion[266]. The critical distinction being that deposition through liquid immersion requires the vacuum treated sample to be removed into atmosphere, introducing and increasing the probability of sample contamination, and altering its treated state, including any surface treatments.

4.4 Pulsed Nozzle Cluster Deposition Modelling

The PNCD process involves the injection of a pulsed ‘packet’ of gold clusters/solvent into the chamber. This packet undergoes a supersonic expansion in a pressure differential which causes prompt solvent evaporation. Removal of vapour through surface deposition and constant pumping returns the vacuum chamber to its initial pressure after ~30 seconds.

The evaporation rate of the solvent upon supersonic expansion is important to determine the distance a solvent droplet can survive before vaporisation in the vacuum. Versteeg et al. proposed a model for a droplet of given radius to evaporate utilising partial pressure from a droplet of solvent combined with a curvature of the solvent surface (assuming a round droplet)[261] as well as the resulting monolayers deposited per pulse and velocity of the injected pulse. Their modelling was for an ultrasonically active nozzle but was adapted for the nozzle used in these investigations.

$t_{evaporation} = B \int_{r_{initial}}^{r_{final}} e^{\frac{-A}{r}}$ Equation 4-1 integrates the time to evaporate a methanol droplet from an initial radius ($r_{initial}$ taken as radius of the nozzle bore) to a final radius of a single nanocluster (i.e.an isolated nanocluster).

$$t_{evaporation} = B \int_{r_{initial}}^{r_{final}} e^{\frac{-A}{r}} \quad \text{Equation 4-1}$$

$$\text{where } A = \frac{2\gamma\Omega}{kT}, B = \frac{\sqrt{(2\pi mkT)}}{\Omega p_0} \quad \text{Equation 4-2}$$

Table 4-4 Values for modelling methanol droplet evaporation after pulsing

γ	2.25E-2	Surface tension of the solvent (N/m)
Ω	1.76E-28	Molecular volume (cm ³)
k	1.38E-23	Boltzmann’s constant
T	293.15	Temperature (K)
m	1.53E-25	Mass of evaporated particle (kg)
p_0	1.89E4	Vapour Pressure (Pa)[303]
r_{final}	4.00E-9	Final droplet radius (m)
$r_{initial}$	5.10E-4	Initial droplet radius (nozzle radius) (m)

E
v
a

luating $t_{evaporation} = B \int_{r_{initial}}^{r_{final}} e^{\frac{-A}{r}}$ Equation 4-1 and **where** $A =$

☒
☒

Monolayers deposited per pulse are calculated with the parameters defined in Table 4-4 and the

u
s
e

$$N_{monolayers} = \frac{m^{1/6}c}{\rho_{mo}^{2/3}\sqrt{2\pi kT}} \left[\Delta p_{max} \tau \left(1 - e^{-\frac{t_w}{\tau}} \right) \right] \quad \text{Equation 4-3}$$

This model is drawn from kinetic gas theory coupled with the assumption that a pulse causes an infinitely fast rise time in chamber pressure at pulse injection followed by exponential decay until the chamber returns to its base pressure. Infinitely fast means here in comparison with the time characteristics of the pulse. This model then gives a pressure curve that can be integrated over the time from 1st to 2nd pulsing to give the fraction of monolayers per pulse deposited by the valve.

Coupling this with the assumption that the partial pressure of the gold nanocluster is proportional to its concentration in solution and that the growth of monolayer is proportional to adsorbed molecular

area, approximated as a cube allows for $t_{evaporation} = B \int_{r_{initial}}^{r_{final}} e^{-\frac{A}{r}}$ Equation

4-1 to be expanded to estimate coverage for a single pulse at a given waiting time.

i

n Table 4-5 values used to model the number of monolayers deposited per pulse using Equation 4-1

a

t_w	60	Inter-pulse waiting time (s)
T	275	Temperature (K)
k	1.38E-23	Boltzmann's constant
ρ_{mo}	19.3	the density of gold (g/m ³)[304]
τ	1.58E-4	decay constant (s ⁻¹ , experimentally determined)
Δp	4.32E-4	Pressure Maximum (mbar)
m	3870.9828	Mass of nanocluster (g/mol)
c	0.125	nanocluster concentration (mM)

t

i

o

n

o

f

R

E

F

–

Using equation $N_{monolayers} = \frac{m^{1/6}c}{\rho_{mo}^{2/3}\sqrt{2\pi kT}} \left[\Delta p_{max} \tau \left(1 - e^{-\frac{t_w}{\tau}} \right) \right]$ Equation 4-3 and the

values from Table 4-5 gives $N_{monolayers} = 0.003$ per pulse. This value, while relying on some

f

1

2

8

approximations, is approximately in agreement with gold XPS measured for sample B6 (10 pulses) giving 0.02 monolayers and could provide a framework for achieving specific sub-monolayer coverages.

Estimating the velocity of the solution on injection assumes the pressure drop and resulting acceleration occur entirely within the nozzle bore. Modelling for this can be done using the formula for head loss in a circular pipe, assuming a turbulent flow. This injection velocity, h_f , can be determined from $h_f = \frac{\Delta P}{\rho} = f \frac{L \bar{v}}{d 2g}$ Equation 4-4:

$$h_f = \frac{\Delta P}{\rho} = f \frac{L \bar{v}}{d 2g} \quad \text{Equation 4-4}$$

Table 4-6 values for use with equation 4-4 to estimate pulsed packet velocity on exiting nozzle bore.

ρ	791	Density of methanol kg.m ⁻³
ΔP	2.0x10 ⁵	Pressure drop from nozzle head to chamber, Pa
d	0.51	Nozzle diameter, mm
L	1.25	Nozzle orifice length, mm
f	0.035	Friction factor, drawn steel, 0.0015mm roughness, Reynolds number > 10 ⁴
g	9.8	Acceleration due to gravity, ms ⁻²

Equation 4-4 evaluated using values from Table 4-6 gives 30 ms⁻¹ as the final velocity on entering the vacuum chamber, combining this value with the lifetime of a 10 μm droplet evaluated from (1) gives droplet evaporation within 5.7x10⁻³ m from the nozzle bore. Given the evaporation chamber has dimension 8x10⁻² m from the nozzle to sample, only (methanol) vapour will reach the sample surface. Thus, deposition of solvent onto the substrate only occurs from the gas phase. The total amount of solvent attaching to the surface through the deposition method thus is significantly less than when depositing clusters by dipping the substrate into solution[185, 266]. The circular feature identified on some heavily deposited surfaces in AFM (Figure 4-2) may be accounted for by vacuum degradation over lengthy depositions affecting the solvent evaporation rate. Alternatively, in some pulsed CVD modelling[297, 305] it has been proposed that particles can aggregate in a vacuum as the solvent droplets containing the particles evaporate and contract, clumping solvated contents into more concentrated groups. The Mathematica code used for this model can be found in Figure 4-13.

It is worth noting that while the conditions for this model are relevant for a single pulse, and that the predicted monolayer coverage per pulse aligns well with samples B1-6; the observed coverage on sample B7, a single pulsed sample is in worse agreement. For B1-6, this model's predictions are within a factor of 2 of observed monolayer coverages. For B7 it is more like a factor of 5. While this

is still a useful result, it does reinforce the idea that the conditions of the first pulse may interact in a manner not wholly captured in this model.

```

In[ ]:= f =  $\frac{-A}{e^r}$  ;

In[ ]:=  $\gamma = .0225$ ; (*surface tension*)
 $\Omega = 1.76 \times 10^{-28}$ ; (*molecular volume*)
 $k = 1.38 \times 10^{-23}$ ; (*Boltzmann's Const.*)
 $T = 300$ ; (*Temperature*)
 $m = 1.53 \times 10^{-25}$ ; (*molecular mass (evap. particle)*)
 $p = 18870$ ; (*partial pressure of flat surface*)
 $A = \frac{2 * \gamma * \Omega}{k * T}$  ;
 $B = \frac{\sqrt{2 * \pi * m * k * T}}{\Omega * p}$  ;
 $r_f = 3.5 \times 10^{-10}$ ;
 $r_o = 0.00001$ ;

In[ ]:=  $tev = B * (Integrate[f, \{r, r_f, r_o\}])$ 
Out[ ]:= 0.000189629

In[ ]:= ScientificForm[tev]
Out[ ]//ScientificForm=
 $1.89629 \times 10^{-4}$ 

In[ ]:= NumberForm[0.000189629]
Out[ ]//NumberForm=
0.000189629

In[ ]:= ClearAll[ $\rho$ ,  $\Delta P$ ,  $d$ ,  $L$ ,  $F$ ,  $g$ ,  $v$ ,  $x$ ]

In[ ]:=  $\rho = 791 \text{ kg/m}^3$  ; (*density of Methanol, kg/m^3*)
 $\Delta P = \text{UnitConvert}[202700 \text{ Pa}]$  ; (*pressure drop from nozzle head to chamber, Pa*)
 $\frac{\Delta P}{\rho}$ 
 $d = 0.51 \text{ mm}$ ; (*nozzle diameter, meters*)
 $L = \text{UnitConvert}[1.25 \text{ mm}]$  ; (*nozzle orifice length, meters*)
 $F = 0.035$ ; (* reynolds number  $10^4$ , drawn steel,
stainless steel roughness 0.0015mm roughness,
https://www.nuclear-power.net/nuclear-engineering/fluid-dynamics/major-head-loss-friction-loss/friction-factor-turbulent-flow-colebrook/,
http://www.calctool.org/CALC/eng/civil/friction\_factor*)
 $F * \frac{L}{d}$ 
 $g = 9.8 \text{ m/s}^2$  ; (*gravitational constant, newton square meters per kilogram squared*)

Out[ ]:=  $\frac{202700}{791} \text{ m}^2/\text{s}^2$ 

Out[ ]:= 0.0857843

In[ ]:=  $\text{Sqrt}\left[\frac{\Delta P}{\rho} / F * \frac{L}{d} * \frac{1}{2g}\right]$ 

Out[ ]:=  $30.2584 \sqrt{\text{m}}$ 

In[ ]:=  $30.258 \text{ m/s} * 0.000189629 \text{ s}$ 

Out[ ]:= 0.00573779 m

```

Figure 4-13 Mathematica code used to model the PNCD evaporation time and velocity

4.5 Conclusions

Au₉ clusters were deposited onto mica and titania substrates via pulsed nozzle cluster deposition (PNCD) using a variety of nanocluster concentrations and pulse conditions and the surfaces analysed with AFM, XPS and TEM. AFM allowed for analysing the height distribution of the clusters on the surfaces and thus a measure for the degree of agglomeration. Through XPS, it was possible to determine the degree of agglomeration via the Au binding energy. It was found that the conditions for the deposition affect the dispersion of the clusters over the substrate surface. Change in Au₉ concentration was found not to be a suitable method for controlling the number of deposited clusters. Varying the number of pulses at an Au₉ concentration investigated (0.125 mM) resulted in effective control over the concentration of clusters deposited.

Under conditions of homogeneous dispersion of the Au₉ clusters over the surface, it was found that the vast majority of features found with AFM had a height corresponding to the size of a single Au₉ nanocluster. Additionally, TEM images show Au particles whose lateral size is consistent with single Au₉ clusters. XPS showed that most of the Au is at a BE of 85.0±0.3 eV, giving evidence that nanocluster agglomeration is largely suppressed through the deposition process. XPS also showed that the minimal addition of hydrocarbons from the solvent used in the process (i.e. methanol) to the sample could be almost completely removed through applying heating of the samples under vacuum up to 200 °C.

In summary, PNCD with single pulse deposition at low concentrations is a suitable method for depositing ligand protected clusters onto substrates at fractions of a monolayer be deposited and produces deposited clusters that are distributed as individual and isolated clusters over the surface.

4.5.1 Acknowledgements

The author thanks A/Prof Vladimir Golovko (Canterbury University) for providing access to the Au₉(PPh₃)₈(NO₃)₃ clusters.

5 SPECTROSCOPIC COMPARISON OF ELECTRONIC STRUCTURE VIA GOLD METAL NANOCUSTER IMMERSION AND PULSE NOZZLE CLUSTER DEPOSITIONS ON DEFECT RICH TITANIA

5.1 Abstract

Au Nanoclusters (NC) show a range of novel properties due to their size-specific electronic structure, which can be negatively impacted by NC instability and agglomeration. Spectroscopic investigations of Au NCs on reduced photocatalytic TiO₂ substrates under ultra-high vacuum conditions, using X-Ray Photoelectron Spectroscopy (XPS) and Metastable Ion Electron Spectroscopy (MIES), allow for comparison of *in-situ* Pulsed Nozzle Cluster Deposition (PNCD) and *ex-situ* immersion deposition methods with regards to substrate treatments, surface contaminants and electronic structure. It is shown that the PNCD process results in greatly reduced concentrations of surface carbon compared to immersion deposition. PNCD also differs from immersion deposition by allowing for the retention of sputter induced Ti³⁺ defects through the NC deposition process. MIES spectra analysis show that the two deposition methods result in key differences in the NC electronic density of states (DOS), indicating that differences in surface conditions on otherwise identical substrates can result in changes to NC DOS, likely due to NC/surface interactions.

5.2 Introduction

Atomically precise, metal NCs, typically consisting of two to a couple of hundred atoms and up to 2 nm in diameter[32] have become an area of quickly growing interest owing to their ultrasmall size, discrete energy levels,[306] and their tuneability through size and elemental-specific properties offering rich technological potential. Investigations into harnessing these properties towards fields such as sensing, bioimaging and catalysis have been well documented[307].

Small changes in the size, geometry and local environment of metal NCs have been observed to cause significant differences in their catalytic ability[308, 309]. These changes have been attributed to the small size of the metal NCs, which allow for the quantisation of energy levels within the NC, unlike the continuous energy bands found in nanoparticles or bulk structures[307]. These properties can also differ through other factors, including the synthesis pathway of the NC.

One major synthetic route for results in 'bare' NCs, produced in the gas phase using techniques such as laser ablation and sputtering before mass selection is applied to deposit size-selected NCs or metal ions[310]. Many experimental studies to date have used bare metal NCs, including Au, deposited *in-situ* from laser vaporised[311, 312] or sputtered cluster sources[313], enabling the study of NCs model surfaces and their interactions with the substrate. Gas-phase synthesised Au NCs have proven helpful in examining the size-specific properties of the NCs, as well as the interactions between substrate surfaces and metal NCs deposited onto them. However, these synthetic methods are more useful as model systems and catalysts and are not as scalable as chemically synthesised metal NC techniques.

Recent years have seen a range of chemical synthesis techniques developed to allow for metallic precursor salts to undergo reactions before being 'capped' at specific sizes through the use of ligands, such as CO[314] or Phosphine[309] groups to produce highly homogenous size distributions. These techniques result in scalable, reproducible NCs with size-uniformity and flexibility to change NC size, and therefore properties through varying the reactants, ligands, or reaction conditions.

As the properties of a NC depend on its size and geometry, it is critical to retain the size of the clusters when depositing onto solid substrates and avoid the agglomeration of the deposited clusters in cases when the surface of a substrate shall be modified such that a narrow range of new and additional specific electronic states shall be established at the surface through the NCs. Theoretical calculations have shown that the specific geometries of a ligated Au NC are highly dependent on the cluster-ligand interface[315]. Investigations into chemically synthesised NCs have repeatedly encountered that calcination, radiation exposure and other ligand-removing treatments post-deposition of the clusters can induce polydisperse cluster growth[316]. The agglomeration that results from these events has led to observed losses of desirable properties of the NCs such as catalytic activity. To control NC agglomeration, surface treatments such as acid-washing[298] and sputtered defect sites[267] have been explored to improve NC stability through stronger surface interactions.

Given the nature of metal NCs, their size specific properties can easily be affected not only by agglomeration into larger clusters and particles, but also by their interaction with the supporting substrate that they are deposited onto[317, 318] even though such cluster-support interactions have been observed as helpful in stabilising NCs and providing improvements to catalytic and photocatalytic performance[108]. Surface treatments and modifications to oxide substrates such as TiO₂ have been shown to influence the properties of NCs deposited onto these surfaces. Increased catalytic efficiency has been achieved through routes such as photo deposition of Pd NCs_[319] and depositions of Au catalysts onto reducible metal oxides[320]

such as TiO₂. While experimental Scanning Tunnelling Electron Microscopy has shown that, once partially de-ligated, chemically-synthesised Au NCs can be seen to have one of several possible geometries, influenced by the interaction of the NC core with a TiO₂ substrate[196].

However, the exact nature of the interaction between Au NCs and reduced TiO₂ is still undetermined. On reduced TiO₂ substrates, Ti³⁺ surface defects, in the form of bridging oxygen vacancies and interstitial Ti[321], are thought to combine in a stabilising cluster-support interaction with metal NCs leading to a decrease in agglomeration and improving catalytic performance. It has also been shown that Au NCs bind weakly to a pristine TiO₂ surface while oxygen vacancies, and Ti³⁺ defect sites have been observed to bind and stabilise the same NCs readily[322]. Several previous experimental studies using chemically-synthesised, ligated Au NCs have focussed on the production of Ti³⁺ defects from nanoparticulate TiO₂ in the presence of Au NCs[295] as well as the stabilising effects of Ti³⁺ defects in atomic layer deposited (ALD) titania on the size-specific electronic structure of Au NCs[266, 323]. The techniques used to deposit such NCs onto substrates generally involve *ex-situ* immersion of a treated substrate into a cluster-containing solution. Therefore, they require the substrate's exposure to atmospheric conditions, potentially affecting the substrate surface conditions by quenching defect sites and introducing contaminants in a non-quantifiable manner before deposition takes place.

Pulsed NC Deposition (PNCD) is a deposition technique that allows for the *in-situ* deposition of chemically synthesised, size-specific ligated NCs through injecting small pulses of NC solution into a high vacuum chamber, allowing for a highly disperse, sub-monolayer coverage of a target substrate to be achieved, and has been previously demonstrated using Au NCs[324]. This deposition method allows a treated substrate to undergo deposition without exposure to atmosphere, allowing for a defect-rich surface created through pre-treatment to be retained in vacuum until Au NCs are deposited through PNCD, something that previous immersion deposition studies have not been able to show[323]. Ensuring the presence of Ti³⁺ defects when Au NCs are deposited allows for examining the impact of any NC-defect interaction on the stabilisation and prevention of agglomeration. This technique also allows substrate-NC systems free from atmospheric and carbonaceous contamination present in immersion techniques. Ligated Au NCs deposited through PNCD, therefore, will be able to access pristine, vacuum-treated substrate surfaces and their defect sites in a manner similar to bare NCs synthesised in the gas phase.

Radiofrequency (RF) deposited TiO₂ was used as the substrate in this study as it produces a dense, uniform layer of TiO₂ that can be easily fabricated and readily modified with Ti³⁺ defects[325]. RF-deposited TiO₂ is polycrystalline and therefore is better representation of real

catalysts than the single crystal TiO_2 often used in model studies of cluster-substrate interactions.

The interaction of Au NCs with Ti^{3+} defect sites can be thoroughly examined through a combination of electron spectroscopy techniques. Meta-stable induced electron spectroscopy (MIES) is a technique that possesses an extreme surface sensitivity, with the probing meta-stable He atoms (He^*) only interacting with the outmost valence electron density of a sample surface[326]. This makes MIES a valuable tool for probing nano-sized objects and investigating their electronic density of states (DOS). Through the comparison of MIE spectra with the chemical composition of the surface from X-ray photoelectron spectroscopy (XPS), any differences in DOS found for *ex-situ* immersion depositions and *in-situ* PNCD can be correlated with the relative concentrations of Au NCs and Ti^{3+} surface defect density.

The aim of this study is to compare the differences in DOS from NCs deposited through both immersion and PNCD deposition techniques onto prepared titania substrates. Chemically synthesised, atomically precise $\text{Au}_9(\text{PPh}_3)_8$ NCs have been used for deposition onto RF sputter-deposited TiO_2 , treated under UHV conditions to induce Ti^{3+} defects. The ability of PNCD deposition to restrict surface carbon concentration, while retaining surface treatments such as Ti^{3+} defects provide a contrasting surface environment to immersion deposition on an identically prepared substrate. The chosen deposition techniques therefore allow for the correlation of observable differences in NC electronic structure, obtained through MIES, with Ti^{3+} defect-rich surface interactions, as well as the impact of defect-rich titania on the stabilisation of NC agglomeration.

5.3 Experimental Methodology

5.3.1 Chemically Synthesised, Atomically Precise NC Materials and Preparation

The following investigation was performed using a well-characterised representative NC, $[\text{Au}_9(\text{PPh}_3)_8]^{3+}$. These clusters were synthesised and purified in a previously reported process[327, 328]. They were subsequently recrystallised and characterised using nuclear magnetic resonance spectroscopy, mass spectrometry and X-ray crystallography to confirm the size and uniformity of the NCs[44]. Au_9 was stored at a temperature of -17°C and in sealed, covered containers to minimise exposure to sunlight.

Preparation of the deposition solutions for immersion and PNCD was identically for all solutions. Au_9 was weighed, then dissolved in ultra-pure methanol (HPLC grade, Scharlau) to the required concentration. For the immersion deposited samples the $\text{Au}_9/\text{Methanol}$ concentrations used were 0.01mM, 0.001mM, .0006mM, 0.0001mM and 0.00006mM. For the

PNCD depositions, the small amount of material injected with each PNCD pulse required higher concentrations of the solution, with the concentrations of 0.01mM, 0.006mM, 0.001mM, 0.0006mM, 0.0001mM used. PNCD depositions were prepared using the same process described elsewhere[324].

5.3.2 Substrate Selection, Surface Treatment and Deposition Techniques

The substrate chosen for both deposition techniques was nanoparticulate, RF-sputter deposited TiO₂ thin film prepared and characterised using Scanning Electron Microscopy (SEM), Atomic Force Microscopy (AFM), X-Ray Diffraction (XRD) and XPS as previously reported[325]. In addition, all substrates used in control, PNCD and immersion deposition samples underwent treatment under ultra-high vacuum to induce surface Ti³⁺ defects. This step was performed by heating to 300°C for 10 minutes before being exposed to a fixed dose of 6x10¹⁴Ions/cm Argon sputtering ions at 10eV.

Immersion deposition was performed by removing a prepared, surface-modified substrate from a high vacuum (HV) load lock, immediately removing the substrate from the sample mount and immersing the sample completely into 5mL of pre-prepared Au₉/Methanol solution of a known concentration. Immersion was maintained for 30 minutes before the sample was removed, gently dried under nitrogen and re-mounted for insertion into the HV load lock and subsequently the UHV chamber for measurement.

The method for PNCD deposited samples followed the same process described elsewhere[324]. PNCD in this case was used in a single-pulse regime, whereby a small volume of pressurised Au₉/Methanol solution was injected into the HV load lock through a controlled pulse nozzle (Iota One valve, Parker Hannifin USA) set to open for 200µs. This single opening allowed the injected pulse to enter the vacuum, undergoing ultrasonic expansion and droplet evaporation before depositing the Au NCs onto surface modified TiO₂ under vacuum conditions at < 10⁻⁷ mbar. The substrate for PNCD samples was therefore never removed from vacuum after modification, allowing the pre-prepared atomically precise NCs to access the as prepared, defect rich TiO₂ surface without atmospheric exposure and contamination which could result in quenching the defects generated through the surface treatment. Au for both immersion and PNCD depositions, a post-deposition heating procedure was applied to both remove any H₂O adsorbed to the sample, and to partially de-ligate NCs for further surface-sensitive spectroscopy. This procedure was identical for both sample preparations, and involved heating the NC-deposited sample using an *in-situ* resistive filament heating mechanism to heat the Mo sample holder and sample from underneath by increasing the filament current. Heating occurred at a rate of 20°C per minute under UHV conditions until

200°C was achieved. The sample was maintained at 200°C temperature for 10 minutes, then cooled at the same rate as the heating step.

5.3.3 X-Ray Photoelectron Spectroscopy (XPS)

XPS was applied using Mg K α radiation at 1253.6eV to determine the elemental composition and the chemical states of all components. Under the condition chosen, XPS has a probing depth of less than 10nm, depending on the electron mean free path^[329], and have previously been shown not to damage samples of this type[266]. The apparatus was built by SPECS (Berlin, Germany) with a non-monochromatic X-ray source and has a base pressure of a few 10⁻¹⁰ mbar with the details described in [301]. The angle between the X-ray source and the SPEC PHOIBOS-HSA300 hemispherical analyser is 54.7 °. At a pass energy of 10 eV the FWHM of the Ag 3d_{5/2} peak is < 1 eV. The uncertainty of the peak positions is typically 0.2 eV. High-resolution scans were recorded at a step size of 0.1 eV for Carbon (C), Oxygen (O), Phosphorus (P), Titanium (Ti), Silicon (Si) and Gold (Au) at a pass energy of 10 eV. XPS measurements were taken after all substrate treatments were complete, before deposition; after deposited samples were returned to the UHV environment; and after samples underwent heating to remove surface carbon and PPh₃ ligands.

Analysis and quantification of the subsequent spectra were performed in Casa XPS (SPECS lab) using a hybrid Gaussian (30%) and Lorentzian (70%) peak and a Shirley background to fit the recorded peaks as previously described[235]. In addition, elemental sensitivity factors for an X-Ray source at 54.7° were used for analysis[244] with the C 1s peak; associated with C-C sp³ bonds, set to 285eV, for calibrating the XPS energy scale. Using this calibration, it was found that the Ti⁴⁺ peak binding energy was stable within \pm 0.2 eV confirming that the energy calibration described above does not lead to artefacts in the binding energy of other peaks in the XP spectra.

5.3.4 Metastable Impact Electron Spectroscopy (MIES) and Ultraviolet Photoelectron Spectroscopy (UPS)

All MIES and UPS measurements were performed using a cold cathode two-stage discharge source (MFS, Clausthal-Zellerfeld, Germany) for generating metastable helium (He*) and Hel UV photons. The He* and UV photons are separated into packets through a mechanical chopper. A 10V bias was applied to the sample stage. The Hel excitation energy is 21.218 eV and results in a UP spectrum collected from approximately 3nm into the sample surface. The MIES excitation energy is 19.218 eV and is a perfectly surface-sensitive technique, with the metastable He ions interacting with the surface's outermost valence electrons, reference^[330, 331]. To further understand the nature of the Au₉ NCs deposited through immersion and PNCD,

MIES/UPS spectra were recorded from the samples after they had been heated for ligand removal.

The individual measured UP, and MIE spectra can be viewed as linear combinations of the characteristic electronic spectra from the constituent species on the sample surface. Individual sample measurements are first normalised against a known, stable and well-characterised polymer surface to adjust the intensity variations of the MIES source over the course of the experiments which were undertaken over several days due to the length of sample preparation. The input spectra were analysed up to a binding energy of 10eV to reduce the interference from the secondary electron contributions at lower kinetic energies (i.e. higher binding energies). Subsequently, a process known as singular value decomposition (SVD) was applied to analyse, separate, and identify the constituent reference spectra. This process, described in detail elsewhere[243], generates a series of reference spectra and assigns a weighting factor to each reference spectrum, the sum of which should be unity. The reference spectra determined through the SVD analysis of a MIES/UPS spectra represent the electronic structure of the various components (chemical species) forming the surface. By comparing the reference spectra and their weighting factors with relative concentration as determined by XPS, changes in elemental concentrations can be correlated with changes in reference spectra weighting to associate specific reference spectra and the electronic structure they describe to a particular surface species.

5.4 Results and Discussion

We will first discuss the influence of the deposition method on the presence of hydrocarbons on the sample surface and then present the analysis of the clusters deposited onto the substrates.

5.4.1 Carbon contamination from PNCD – Effect of heating

In order to determine the amount of carbon deposited during the PNCD process and whether deposited carbon can be removed via post-PNCD heating, XPS was applied.

The C1s spectrum in Figure 5-1 A from a heated and sputter cleaned TiO₂ substrate shows one discernible carbon peak at 285 eV. The peak centred around $285\text{eV} \pm 0.1\text{eV}$ is assigned to C-C sp³ bonds from adventitious carbon[332], a common presence even under UHV conditions.

Figure 5-1 B shows two carbon peaks, one peak at 285 eV and one peak at $286.7 \pm 0.1\text{eV}$. The carbon peak at $286.7 \pm 0.1\text{eV}$ appears after PNCD deposition onto the sample and correspond to C-O bonds from methanol[333].

This peak is nearly entirely removed through the final heating step as can be seen in Figure 5-1 C.

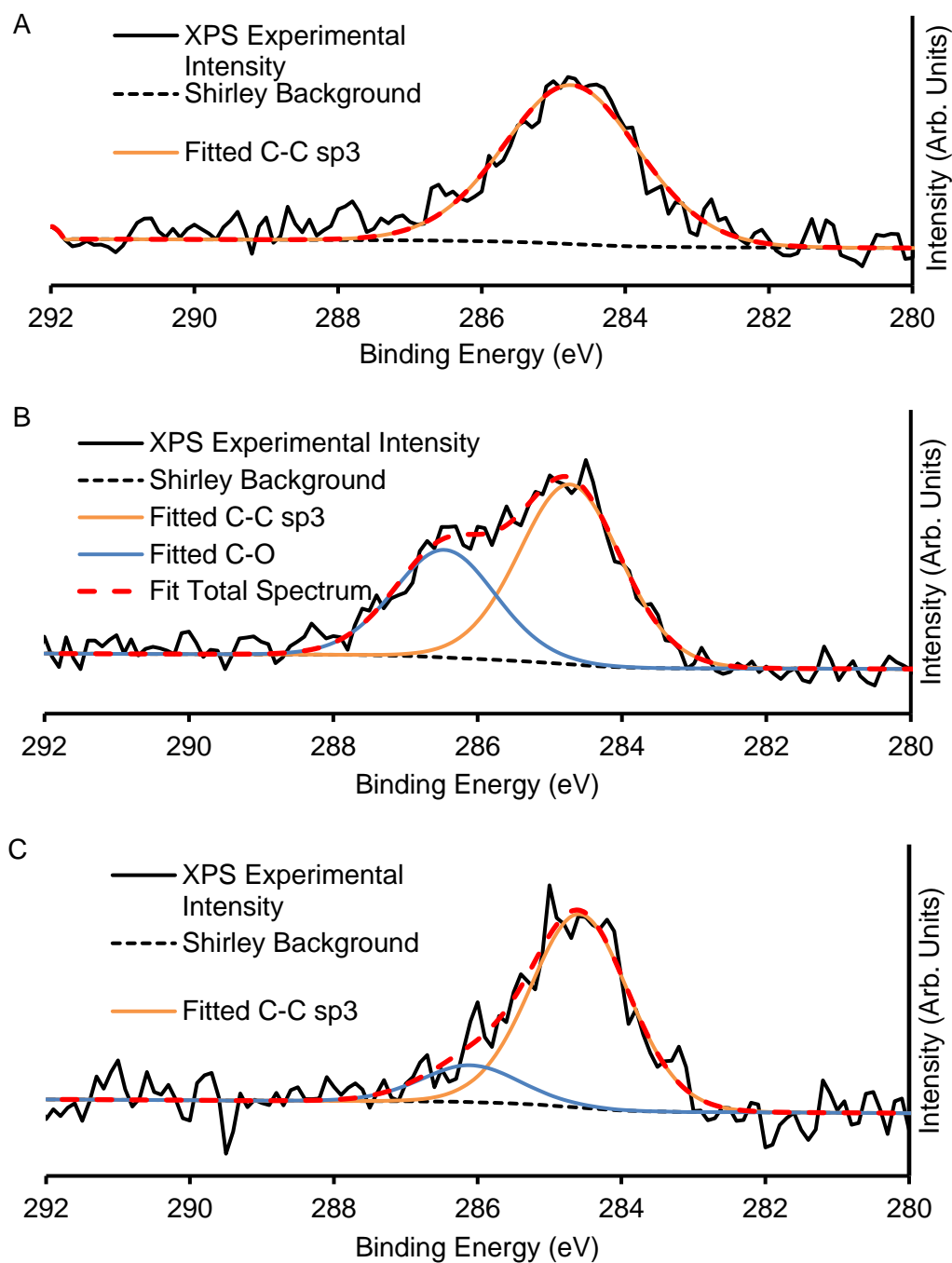


Figure 5-1 High-resolution XPS spectra of the C 1s region showing the change in C-C sp³ and C-O fitted peaks across a heated and sputtered TiO₂ surface (A), the same surface after PNCD deposition (B), and after post-deposition heating to 200°C (C). The change in the C-O peak through this range illustrates the removable nature of the low levels of carbon introduced through PNCD.

Table 5-1 shows the increase and decrease in relative XPS intensity from C 1s and corresponds to the fitted C 1s XP spectra shown in Figure 5-1. These measurements show that PNCD is a method capable of depositing NCs whereby any increase in carbonaceous

species (e.g. solvents) introduced through deposition is nearly entirely removable through heating to temperatures which can remove supporting ligands without leading to overall NC agglomeration.

Table 5-1 Carbon 1s XPS relative intensities for the three measured steps displayed in Figure 1, substrate cleaning (A), deposition (B), and decontamination (C) of a single PNCD preparation of Au NCs.

Sample Process	Relative XPS %		
	C 1s Total	C-O	C-C sp ³
Heated 300°C, Ar Sputtered	3.9 ± 0.2	-	3.9 ± 0.2
Pulsed w/ Au ₃ /methanol	6.4 ± 0.2	2.4 ± 0.2	4.0 ± 0.2
Heated 200°C	3.0 ± 0.2	0.5 ± 0.2	2.5 ± 0.2

The carbon content across samples is distinctly different between the two deposition methods employed. PNCD in NC deposition resulted in up to 2.5 times lower surface carbon species concentration than the immersion deposited samples. Table 5-2 clearly shows that the immersion deposited samples showing not only the highest individual carbon relative percentage (0.0001mM) but an average of 8.2 ± 0.1% carbon, compared to a calculated average of 3.7 ± 0.1% for the PNCD sample series. It will be described below that in applying MIES and UPS, surface carbon is an unwanted element, as it can block TiO₂ and Au NCs from ion impact and, therefore, observation. The difference in C contamination between the PNCD and the samples prepared by solution immersion is that PNCD occurs under vacuum and uses only a small amount of solvent. In contrast, the immersed samples are exposed to air as well as the entire surface to a solvent, resulting in the adsorption of adventitious hydrocarbons from the atmosphere and of solvent.

5.4.2 Surface Treatment and Elemental Composition of Immersion and PNCD deposited TiO₂

The measurements of XPS relative concentrations are shown in Table 5-3 across both the immersion and PNCD series. XPS measurements from nanocluster deposition can be seen in Figure 5-2 & Figure 5-3. Carbon overall signal consists of two detectable peaks, assigned to adventitious carbon (mainly C-C and C-H bonds) at 285 ± 0.2eV[332], and C-O bonds at 286 ± 0.2eV as seen in Figure 5-1. The oxygen 1s region shows two clear peaks, which can

be seen in Figure 5-2, one at $530.6 \pm 0.2\text{eV}$ associated with metal oxides, TiO_2 in this case[334], and another at $532.2 \pm 0.2\text{eV}$ likely from organic C=O bonds[332].

Table 5-2 XPS relative concentrations (At%) measured directly after nanocluster deposition via PNCD (P1-6) and immersion deposition (I1-6)

Sample Number	Solution Concentration Au_9	C	O	Si	Ti^{4+}	Ti^{3+} (Defect)	Au (Total)
<i>P1</i>	0.01mM	14.7 ± 0.1	60.2 ± 0.1	0.9 ± 0.1	23.8 ± 0.1	4.6 ± 0.1	0.8 ± 0.01
<i>P2</i>	0.006mM	8.4 ± 0.1	65.3 ± 0.1	0.9 ± 0.1	25.2 ± 0.1	4.8 ± 0.1	0.2 ± 0.01
<i>P3</i>	0.001mM	13.0 ± 0.1	62.5 ± 0.1	1.0 ± 0.1	23.5 ± 0.1	3.7 ± 0.1	0.2 ± 0.01
<i>P4</i>	0.0006mM	7.3 ± 0.1	66.0 ± 0.1	0.8 ± 0.1	26.0 ± 0.1	4.3 ± 0.1	0.1 ± 0.01
<i>P5</i>	0.0001mM	6.8 ± 0.1	66.3 ± 0.1	1.0 ± 0.1	25.8 ± 0.1	4.5 ± 0.1	0.03 ± 0.01
<i>P6</i>	Blank	6.4 ± 0.1	67.1 ± 0.1	1.1 ± 0.1	25.5 ± 0.1	5.1 ± 0.1	-

Sample Number	Solution Concentration Au_9	C	O	Si	Ti^{4+}	Ti^{3+} (Defect)	Au (Total)
<i>I1</i>	0.01mM	25.6 ± 0.1	51.6 ± 0.1	0.9 ± 0.01	19.6 ± 0.1	-	0.76 ± 0.01
<i>I2</i>	0.001mM	15.4 ± 0.1	59.1 ± 0.1	0.5 ± 0.01	22.8 ± 0.1	-	0.12 ± 0.01
<i>I3</i>	0.0006mM	11.7 ± 0.1	61.8 ± 0.1	0.5 ± 0.01	23.5 ± 0.1	-	0.12 ± 0.01
<i>I4</i>	0.0001mM	14.0 ± 0.1	59.6 ± 0.1	0.4 ± 0.01	22.8 ± 0.1	-	0.06 ± 0.01
<i>I5</i>	0.00006mM	11.9 ± 0.1	62.5 ± 0.1	0.7 ± 0.01	23.4 ± 0.1	-	0.03 ± 0.01
<i>I6</i>	Blank	11.3 ± 0.1	63.9 ± 0.1	-	24.7 ± 0.1	-	0

Each column in Table 5-3 is representative for a XPS peak with a specific binding energy and therefore for a specific chemical state: The Si 2p peak as seen in Figure 5-2, is found at $102.7 \pm 0.3\text{eV}$ and in very low relative concentrations of around $1.0 \pm 0.3\%$, consistent with SiO_2 originating from the silicon wafer, with some mixing with TiO_2 [335]. Phosphorus, which was only observed immediately after depositions, prior to the final heating step, displayed a low

intensity peak in the P 2p region with binding energy at $131.9 \pm 0.1\text{eV}$, attributed to Au NCs stabilised by PPh_3 ligands[336].

A typical example of Au peaks both before, and after heating can be seen in Figure 5-3. Au XPS data in Table 5-3 is displayed with the total Au relative percentage in Au (total), followed by the individual breakdowns of the Au High Binding Peak (HBP) associated with Au_9 NCs at $85.5 \pm 0.4\text{eV}$, seen in the orange trace in Figure 5-3 A & B. The Au Low Binding Peak (LBP) corresponding to bulk Au and agglomerated clusters is found at $84.1 \pm 0.4\text{eV}$. Analysis of the quantified elemental compositions in each sample illustrates several key points of comparison between the two methods of NC deposition.

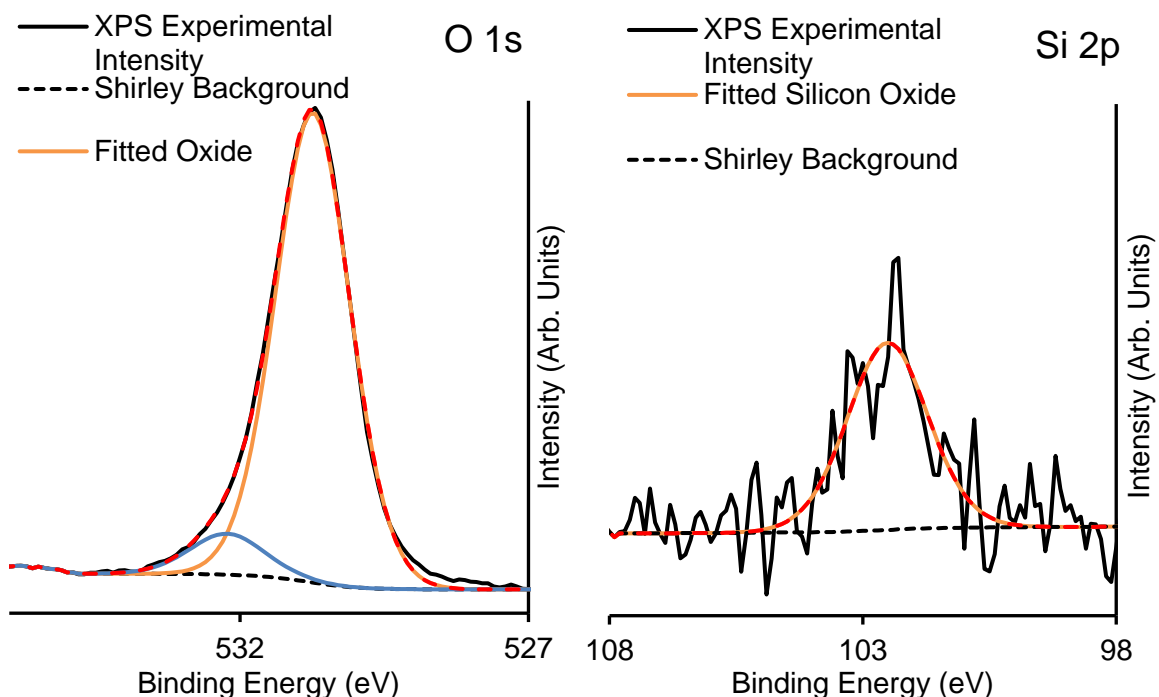


Figure 5-2 High resolution XPS scans showing typical spectra from the Oxygen 1s, and Silicon 2p regions

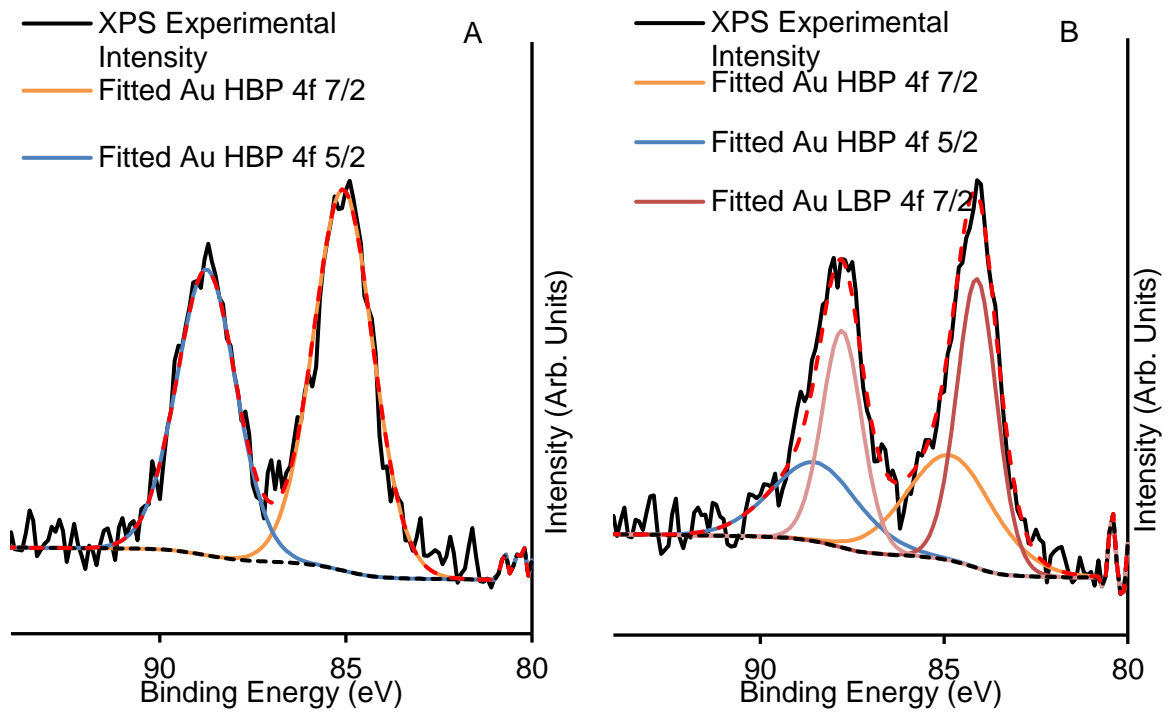


Figure 5-3 High resolution XPS scans on the Au 4f region of 0.006mM PNCD before (A) and after (B) post-deposition heating with peaks showing typical Au HBP and LBP fitting analysis.

Table 5-3 XPS relative concentrations for PNCD and Immersion depositions, all measurements presented here were recorded after deposition and post-deposition heating (@ 200°C, 10 mins) for surface carbon and ligand removal had occurred.

Pulse Nozzle Cluster Deposition – XPS Relative Percentage – Heated/Ligands Removed

<i>Sample Number</i>	Solution Concentration Au ₉	C (C-C & C-O)	O	Si	Ti ⁴⁺	Ti ³⁺ (Defect)	Au (Total)	Au High Binding Peak (HBP)	Au Low Binding Peak (LBP)
<i>P1</i>	0.01mM	5.9 ± 0.1	66.4 ± 0.1	0.89 ± 0.1	26.6 ± 0.1	5.4 ± 0.1	0.33 ± 0.1	0.11 ± 0.1	0.23 ± 0.1
<i>P2</i>	0.006mM	3.2 ± 0.1	68.2 ± 0.1	1.1 ± 0.1	27.2 ± 0.1	5.2 ± 0.1	0.25 ± 0.1	0.07 ± 0.1	0.2 ± 0.1
<i>P3</i>	0.001mM	6.7 ± 0.1	66.4 ± 0.1	1.2 ± 0.1	25.5 ± 0.1	6.7 ± 0.1	0.09 ± 0.1	0.04 ± 0.1	0.08 ± 0.1
<i>P4</i>	0.0006mM	2.7 ± 0.1	68.6 ± 0.1	1.0 ± 0.1	27.6 ± 0.1	4.6 ± 0.1	0.08 ± 0.1	0.05 ± 0.1	0.06 ± 0.1
<i>P5</i>	0.0001mM	2.9 ± 0.1	69.1 ± 0.1	0.99 ± 0.1	27.1 ± 0.1	4.6 ± 0.1	0.03 ± 0.1	0.03 ± 0.1	0.03 ± 0.1
<i>P6</i>	Blank	3.0 ± 0.1	68.5 ± 0.1	1.0 ± 0.1	27.5 ± 0.1	4.9 ± 0.1	0	0	0

Immersion Deposition - XPS Relative Percentage – After Deposition, Heated/Ligands Removed

<i>Sample Number</i>	Solution Concentration Au ₉	C (C-C & C-O)	O	Si	Ti ⁴⁺	Ti ³⁺ (Defect)	Au (Total)	Au HBP	Au LBP
<i>11</i>	0.01mM	12.8 ± 0.1	61.8 ± 0.1	0.89 ± 0.1	23.4 ± 0.1	0	0.76 ± 0.01	0.35 ± 0.01	0.41 ± 0.01
<i>12</i>	0.001mM	8.2 ± 0.1	64.7 ± 0.1	0.89 ± 0.1	25.9 ± 0.1	0	0.12 ± 0.01	0.05 ± 0.01	0.07 ± 0.01
<i>13</i>	0.0006mM	6.4 ± 0.1	66.8 ± 0.1	1.0 ± 0.1	25.6 ± 0.1	0	0.12 ± 0.01	0.12 ± 0.01	0
<i>14</i>	0.0001mM	9.5 ± 0.1	64.4 ± 0.1	0.46 ± 0.1	24.9 ± 0.1	0	0.06 ± 0.01	0.06 ± 0.01	0
<i>15</i>	0.00006mM	11.5 ± 0.1	62.1 ± 0.1	1.49 ± 0.1	25.5 ± 0.1	0	0.03 ± 0.01	0.03 ± 0.01	0
<i>16</i>	Blank	7.2 ± 0.1	66.0 ± 0.1	0.98 ± 0.1	24.2 ± 0.1	0	0	0	0

Titanium dioxide, from the substrate of these samples, displays itself in these XPS results as one of two Ti 2p doublet peaks. The first doublet was observed at a binding energy of around $459.6 \pm 0.2\text{eV}$, associated with Ti^{4+} from the bulk of the $\text{TiO}_{2[244]}$. The second, found as previously reported, at around $458 \pm 0.3\text{eV}$ was assigned to defects, with a state of Ti^{3+} [323]. An example of the fitting of these peaks to a high-resolution XPS scan from both the immersion and PNCD series can be seen in Figure 5-4. These scans were taken after TiO_2 samples had undergone a complete heating and sputtering cycle. To simulate the exposure to atmosphere on the presence of the Ti^{3+} defects during the immersion deposition process, a sample was measured before and after (Figure 5-4, A and B) being removed from the HV load lock and exposed to atmosphere for 15 seconds. This is approximately equivalent to the time it takes to remove a sample from the load lock and fully immerse it in a prepared NC solution for immersion depositions. Measurements of a sample before and after (Figure 5-4, C and D) being deposited with PNCD technique with no Au NCs in the pulsed methanol.

The difference is evident in comparing the impacts of these different methods on the proportion of Ti^{3+} defects retained after deposition. Samples exposed to the atmosphere, such as before immersion deposition, clearly show that any Ti^{3+} defect sites induced through the heating and sputtering of the sample are no longer observable in XPS after deposition. In contrast, samples prepared with NC-free PNCD show well-defined peaks at around $458 \pm 0.2\text{eV}$ in XPS before and after deposition. While a slight reduction in the peak intensity of the Ti^{3+} defect peak (yellow trace) can be seen between the scans, indicating a loss of some Ti^{3+} through the PNCD process, reviewing the Ti^{3+} defect percentages from Table 5-3 XPS relative concentrations for PNCD and Immersion depositions, all measurements presented here were recorded after deposition and post-deposition heating (@ 200°C , 10 mins) for surface carbon and ligand removal had occurred. shows that the final state of PNCD prepared samples retain an average of $5.1 \pm 0.6\%$ Ti^{3+} relative to other surface species. This indicates that samples deposited with Au NCs through PNCD can retain their defect sites through the deposition and ligand-removal steps, allowing for potential interactions between Au NCs and Ti^{3+} surface defects to occur. In comparison, it is shown that a vacuum-treated sample will have almost all measurable Ti^{3+} defects quenched within 15 seconds, the required time for manipulation prior to immersion into the NC-containing solution.

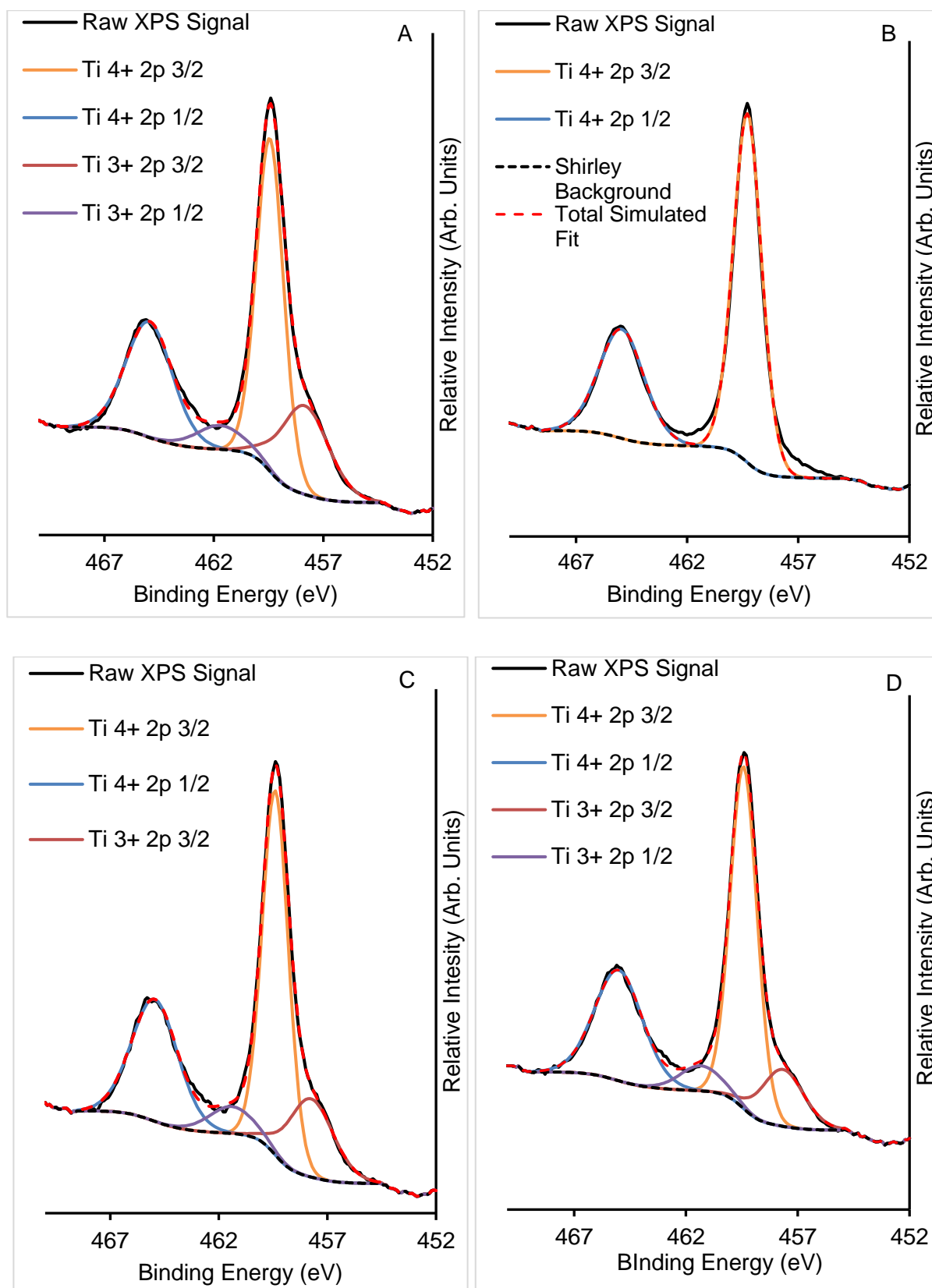


Figure 5-4 Ti high resolution XPS region before (A) and after (B) exposure to air as a form of immersion deposition simulation. Ti high res XPS region before (C) and after (D) PNCD in vacuum conditions.

For the PNCD samples P1-6, analysing the Ti^{3+} defects as a proportion of the total Ti XP signal indicates an $\text{Au}_9 \text{ NC-Ti}^{3+}$ defect interaction. As shown in Table 5-4 PNCD deposited sample Ti^{3+} defects as a proportion of total Ti signal (%) showing the changes in each sample through different

deposition steps., the measured intensity of Ti³⁺ defects introduced through heating to 300°C and Ar sputtering decreases for all samples after Au NC deposition through PNCD by an average 1.8%. After the deposited samples are heated to 200°C for ligand removal there is a general trend of an overall increase in Ti³⁺ proportion, with only the lowest Au₉ NC deposition (P6) and the control sample exhibiting a decrease in Ti³⁺ intensity on further heating. As shown in Figure 5-4, a large fraction of the Ti³⁺ defects are retained through PNCD, these defect sites would be available for interaction and potential stabilisation of atomically precise NCs after the ligand removal step.

Table 5-4 PNCD deposited sample Ti³⁺ defects as a proportion of total Ti signal (%) showing the changes in each sample through different deposition steps.

	<i>P1</i>	<i>P2</i>	<i>P3</i>	<i>P4</i>	<i>P5</i>	<i>P6</i>	
<i>PNCD Series</i>	0.01mM	0.006mM	0.001mM	0.0006mM	0.0001mM	Control	Average
<i>300C + Sputtered</i>	23.7	18.4	19.3	17.7	19.3	21.4	20.0
<i>Post PNCD</i>	19.3	18.0	17.6	16.5	17.6	20.2	18.2
<i>200C Ligand Removal</i>	20.4	19.2	26.2	16.7	16.9	17.9	19.6

The post-deposition calcination to 200° results in the thermal removal of PPh₃ ligands from the Au₉, allowing for contact between the AuAu NCs and the substrate. Similar ligand removal to facilitate substrate contact has been shown elsewhere to activate catalytic properties[337]. However, this process resulted in the XPS phosphorus signal being too weak to be reliably separated from the XPS background for all samples. While one interpretation of the lack of P XPS intensity is the complete removal of PPh₃ ligands from the NCs, as the Au HBP was clearly observed after heating and the loss of P signal, some sizable fraction of size-specific NCs were retained, an unlikely outcome if calcination had resulted in the total removal of stabilising P ligands. The lack of P XPS signal is thought therefore to be associated with the properties of the TiO₂ substrate, as identical processes in systems utilising an atomic layer deposited (ALD) TiO₂ substrate have previously recorded XPS spectra displaying P signal on immersion deposited NC samples after heating[266].

5.4.3 Au₉ NC De-Ligation and Agglomeration Effects

As seen in Figure 5-5, throughout the immersion deposition series, it was observed that the 0.01mM-0.0006mM fraction of the Au HBP peak position shifts from around 85.4 ± 0.2eV after deposition to an LBP around 84.6 ± 0.2eV after heating, indicating de-ligation and some subsequent agglomeration has occurred across all immersion samples. For the 0.001mM and 0.00006mM samples, only one Au 4f peak was resolved through analysis, interpreted as HBP, given their binding

energy position being greater than 85 eV. All samples with the exception of 0.0006mM showed around a 0.4eV reduction in the HBP measured after heating, as shown in Figure 5-5.

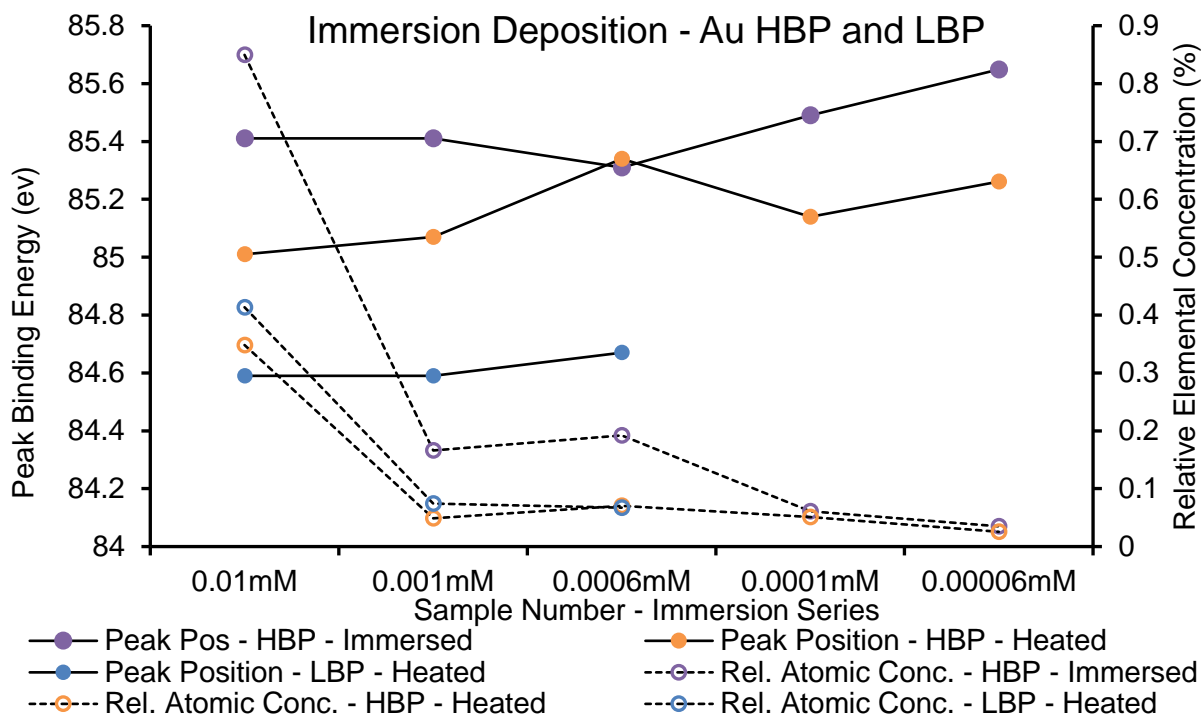


Figure 5-5 - Immersion deposited series Au₉ HBP peak position and relative elemental concentration post immersion and after heating to remove PPh₃ ligands showing the full range of concentrations in the immersion deposited samples. The control sample has been excluded as no Au was deposited or recorded on that sample. Any lower Au relative elemental concentration between Immersed and Heated values is mainly due to Au HBH agglomeration into the LBP state.

The AuAu NC binding energies observed in PNCD samples can be seen in Figure 5-6 to be noticeably shifted when compared to the binding energies seen in the immersion series in Figure 5-5. The Peak Position – HBP – PNCD trace in Figure 5-6 shows that before heating for ligand removal, the deposited clusters occur at a lower average HBP position at around 85eV ± 0.3eV, around 0.4eV lower on average compared to the immersion deposition series.

The differences in binding energy results are not the only notable difference in outcomes between cluster deposition methods. Across the entire PNCD sample range, the Au HBP increases from an as-deposited HBP range of between 84.8-85.3eV to between 85-85.8eV after heating. The HBP series after heating should be viewed as displaying three binding energy position groupings. These groupings consist of samples 0.01mM and 0.006mM showing HBPs at around 85.0 ± 0.1eV, sample 0.001mM at 85.5 ± 0.1eV and samples 0.0006mM and 0.0001mM displaying HBPs at 85.8 ± 0.1eV. This increase in the binding energy for de-ligated NCs indicates that as lower deposition concentrations are used, an increase in the fraction of NCs able to interact with available surface Ti³⁺ defects can lead to changes in the final state of NCs HBP.

The exact cause of the unexpected increase in post-heated HBP binding energy is unknown. It is possible that this energy shift is the result of Au transitioning towards an oxide state, such as

Au₂O₃[338], however previous investigations into Au interactions with reduced TiO₂ substrates have proposed that shifts of this type could be attributed to cluster surface interactions, likely between NCs and surface Ti³⁺ defect sites[322]. The retention of Ti³⁺ defects on the substrate surface at the time of PNC deposition are a key difference between the PNCD and immersion series, which was shown to have the same defects quenched by atmospheric exposure prior to sample immersion. Therefore the observed shift in HBP binding energy is assumed to be a direct result of the effects of Ti³⁺ defect interaction with PNCD Au₉ NCs.

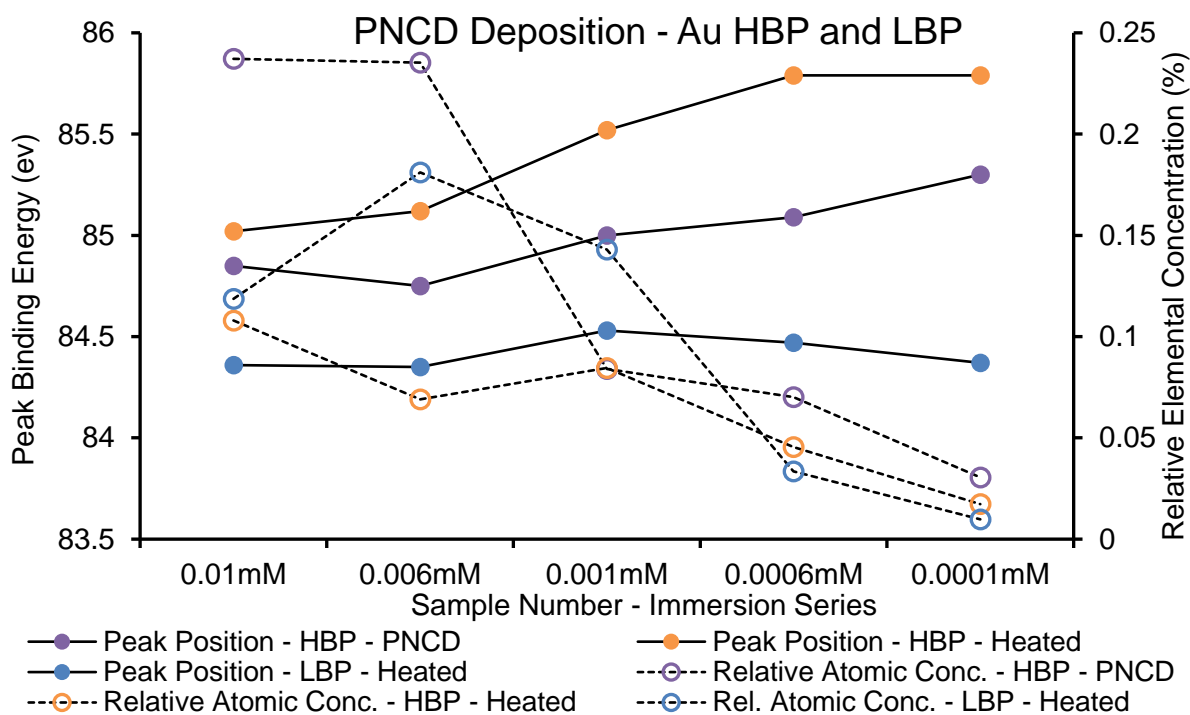


Figure 5-6 - PNC deposited series Au₉ HBP peak position and relative elemental concentration after PNCD and heating to remove PPh₃ ligands showing PNCD samples 0.01mM-0.0001mM; control sample was excluded as no Au was deposited or measured on that sample.

NC agglomeration, seen as a shift in intensity from the Au HBP to Au LBP after heating and ligand removal, is seen in all PNCD samples although the extent of that agglomeration differs as seen in Figure 5-7. For the higher concentration samples, 0.01mM-0.001mM, the post-deposition heating resulted in more LBP than HBP Au signal. While the 0.0006mM-0.0001mM samples show the majority of Au signal registering in the higher energy HBP range as can be seen in Figure 5-7. The PNCD LBP peak positions, and the (partially) agglomerated Au they represent in comparison, remain generally consistent at around 84.4 ± 0.1eV across the range of samples.

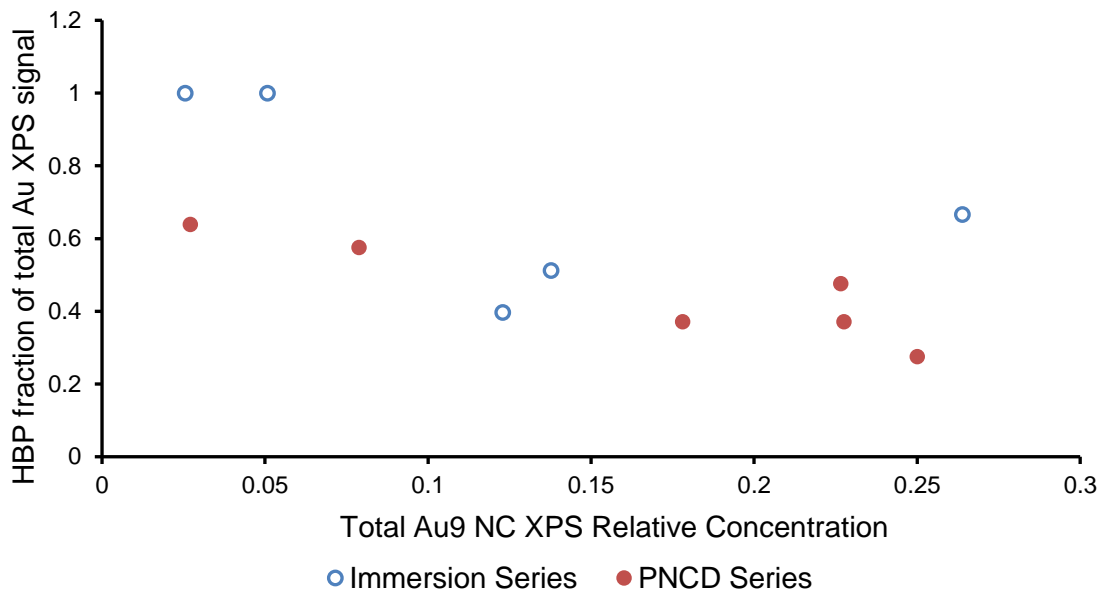


Figure 5-7 Plot of HBP fraction of total Au XPS signal against total Au XPS creative concentration. Both immersion and PNCD samples show lower HBP fractions at higher total Au concentrations.

5.4.4 MIES/UPS analysis and XPS correlation

UPS provides limited information when investigating surface-deposited NCs due to the UV photons penetrating the surface of a sample and returning information from the sub-surface region. The Au9 NCs are exclusively present at the sample surface in low concentrations, so their UPS signal is very low compared to bulk Ti, O, Si, and C species. The UPS for this series, seen in Figure 5-8, displayed characteristic features of a TiO₂ substrate similar to those seen in chapter 3.4.1 previously reported and discussed elsewhere[325].

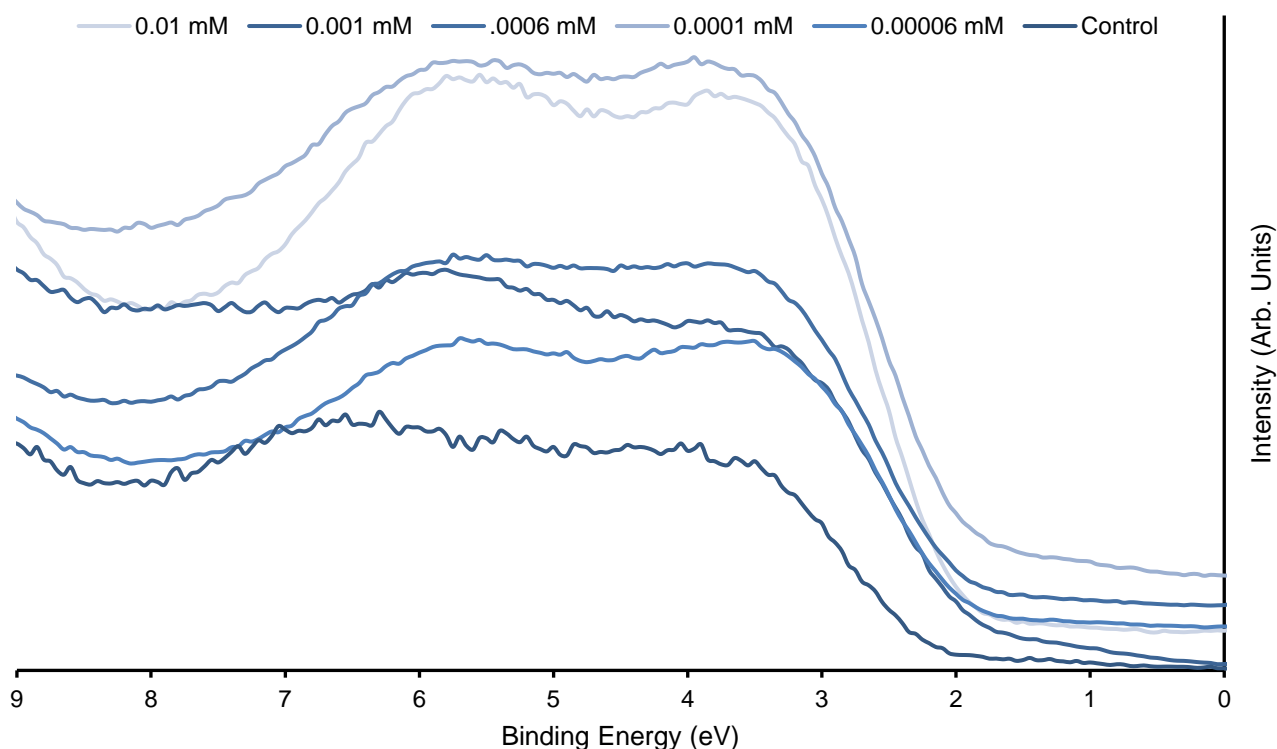


Figure 5-8 UPS scan traces from the I1-6 immersion deposition series, showing the characteristic doublet peak structure of TiO₂ between 2-8 eV.

5.4.4.1 Immersion Deposition

The MIES spectra recorded from the final, heated state of immersion samples I1-I6 were evaluated with SVD as detailed in the methods section and resulted in two reference spectra. Both reference spectra can be seen in Figure 5-9, labelled reference spectrum Alpha and reference spectra Beta. Each measured spectrum can be fitted as a linear combination of Alpha and Beta by giving each a weighting factor indicating its share in constituting the measured spectrum.

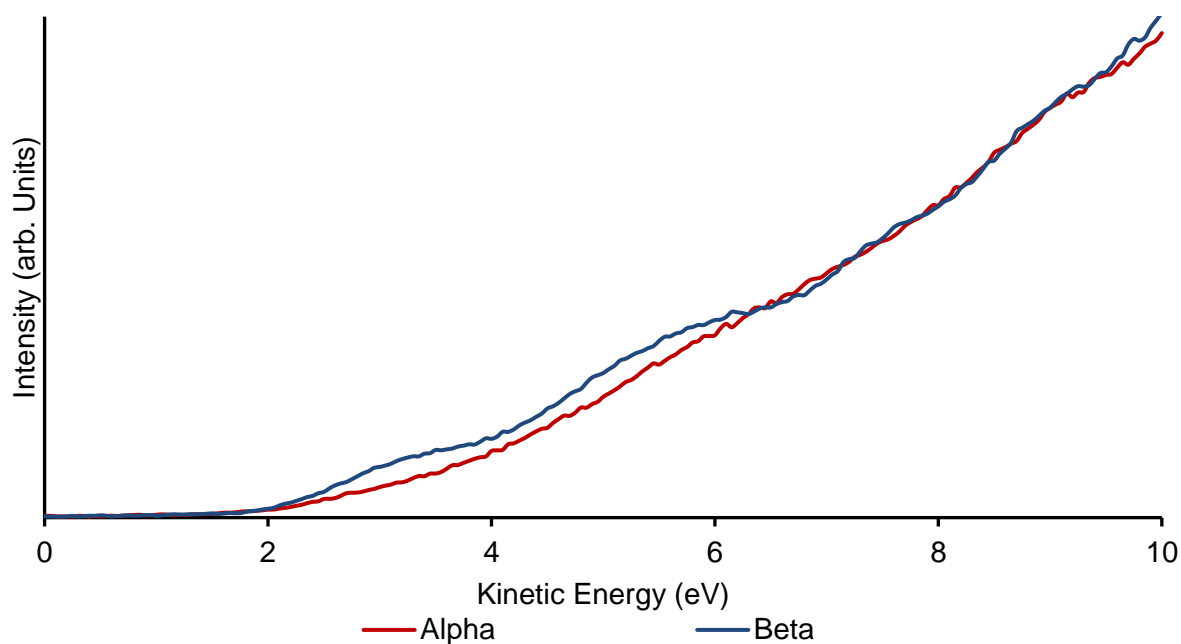


Figure 5-9: Immersion Series MIES SVD reference spectra. Through correlations with XPS relative elemental concentrations and binding energies, Alpha has been associated with the TiO₂ substrate, while Beta correlates to the Au₉ AuAu NCs.

As seen in the weighting factors in Figure 5-6; the control sample, I6, with a full deposition treatment but no Au₉ NCs included in the immersion solution, had an Alpha weighting factor of 0.97. The Alpha reference spectra, therefore, show a strong correlation to the final state of the TiO₂ substrate after deposition and treatment. I6's remaining 0.03 weighting factor for Beta is within experimental uncertainty. It is worth noting that bulk Au, such as those agglomerated species assigned to the Au LBP in XPS, do not display clear peaks in MIES[339]. Agglomerated Au is therefore assumed to be represented in the broadly featureless Alpha spectrum.

The Beta reference spectra therefore most likely originates from the unagglomerated Au₉ NC surface species which result in the XPS Au 4f HBP. In Figure 5-9 the relative intensity of Au HBP in XPS is compared with the weighting factors for the Beta reference spectrum of the immersion deposited sample series. The similarity in the graph traces for the Au₉ XPS relative concentration and reference spectrum Beta support the assumption that the reference spectrum Beta represents non-agglomerated Au₉ Au NCs.

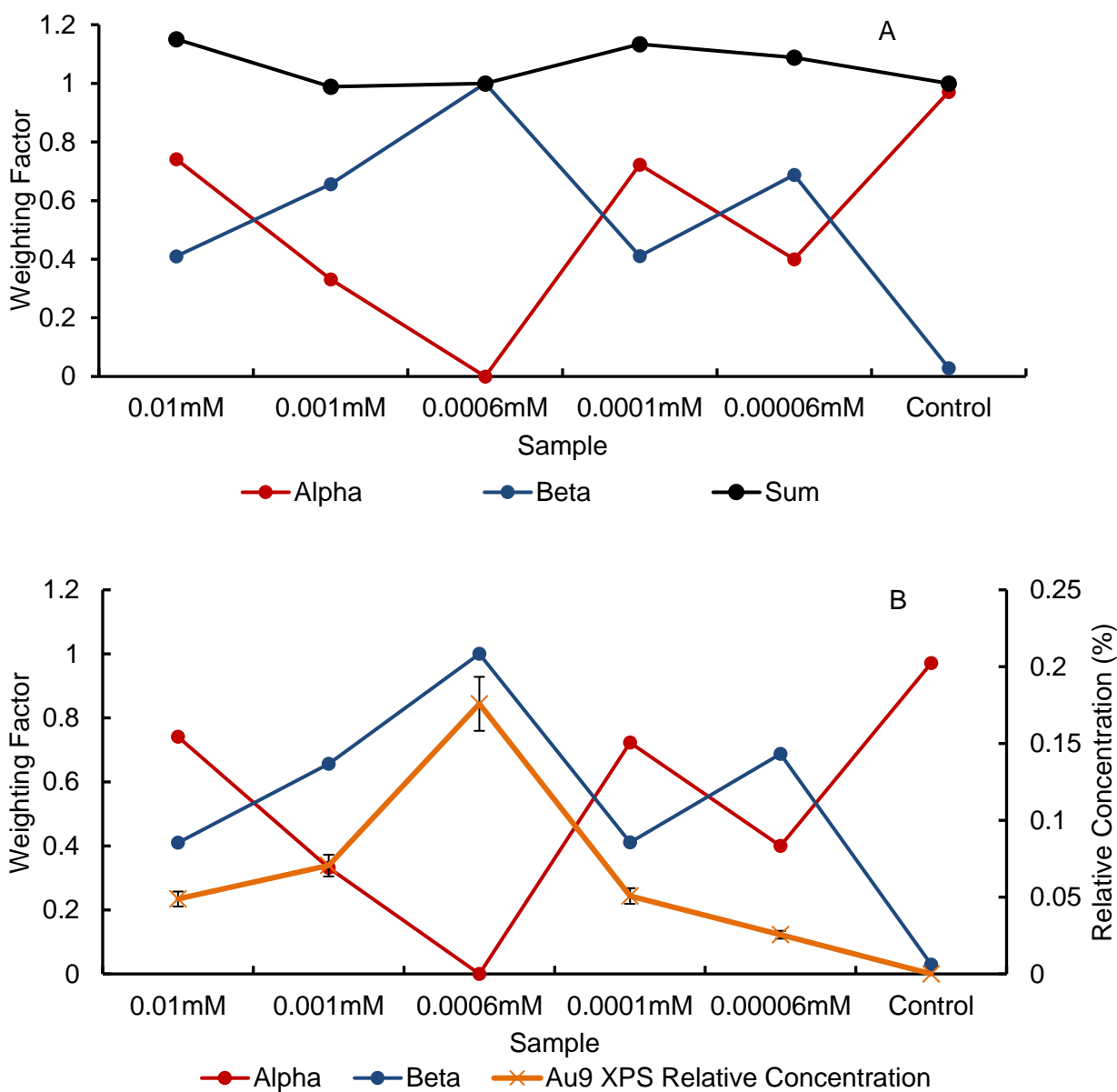


Figure 5-10 A- Immersion series MIES SVD weighting factors; B – MIES SVD weighting correlation with XPS Au9 HBP relative concentration, the near 100% correlation of 0.0006mM sample to the Beta reference spectrum corresponds to the highest concentration of non-agglomerated Au₉ NCs across the sample range. This indicates a strong correlation with the Beta electronic structure and un-agglomerated, size specific Au₉ NCs.

The Au HBP binding energy positions from XPS provide further support for correlating the Beta reference spectrum with Au₉ NCs. The 0.0006mM sample, correlated most strongly with reference spectra Beta, was also recorded as possessing an Au HBP XPS peak position of $85.3 \pm 0.1\text{eV}$. This observation closely aligns with the previously reported characteristic XPS peak position of stable Au₉ NCs, at $85.1 \pm 0.1\text{eV}$ [235], further strengthening the case for reference spectra Beta's correlation with Au₉ AuAu NCs. Across the immersion sample range, samples which show Au HBP binding energies at around 85 eV or higher, have higher Beta weighting factors. Therefore, the Beta spectrum is associated with non-agglomerated size-specific Au₉ NCs with binding energy at 85.1eV and above.

As the Beta reference spectra (Figure 5-9) correlates to Au₉ NCs, any peak features arise via Auger de-excitation of the NCs and are representative of the NC DOS, or electronic structure. This structure has two very clear peaks, the first evident at around 2 - 4 eV with a maximum localised at 3.2 ± 0.2 eV. The second peak is seen from 4.3-6.8eV with a maximum localised at $5.7\text{eV} \pm 0.2\text{eV}$. These peaks, while broad, are clearly defined from the relatively featureless Alpha reference spectra, and from Beta's background outside of these regions. These results point to the conclusion that immersion deposited Au₉ NCs on TiO₂ supports have clear, broad DOS peaks at around 2-4eV and 4.3-6.8eV.

Previous investigations into Au₉ NCs on atomic layer deposited TiO₂ substrate, have assigned MIES reference DOS spectra featuring peaks at 4.4eV, 7.3eV and 9.2eV to Au₉ NCs and phosphorous from their supporting ligands[323, 340]. While the peaks energies observed in this work are not in identical positions, the energy difference between the first and second peaks is similar at $2.5 \pm 0.3\text{eV}$ in the present study and $2.9 \pm 0.3\text{eV}$ in the work of Krishnan et al. The cause of these energy differences could partly be attributed to the difference in substrates, with prior studies performed on ALD Titania substrates. The differences in substrate could potentially result in NC-substrate dipole shifting, which may account for the peak energy position differences compared to the previous studies. The formation of dipoles at interfaces results in a shift of the spectrum of the respective species. The P signal, not detected in this study after the heating step for ligand removal, was clearly found in previous works using ALD titania. The lack of P in this study, may explain the 'missing' third DOS peak, which was observed in systems where P was detectable after the ligand removal step.

5.4.4.2 Pulsed Nozzle Cluster Deposition

The SVD process run on six PNCD spectra from sample range P1-6 resulted in two reference spectra being deconvoluted from the raw MIES data, reference spectra Alpha and reference spectra Beta, as shown in Figure 5-11A. The ratio of weighting factors for both reference spectra across the sample series showed a clear trend. The weighting factor for reference spectra Beta gradually increased through with increasing concentration of the solution for the pulsed nozzle deposition until accounting for 0.94 of the control sample. The broadly featureless Beta reference spectrum was therefore assigned to the TiO₂ substrate again.

The Alpha and Beta weightings were relatively even between 0.01mM-0.0006mM, before Beta increased while Alpha decreased to the 0.0001mM sample and to zero for the control sample. The Alpha reference weighting trend was compared to the relative elemental percentages of the chemical species detected in XPS, correlating weakly with every element except the Au₉ HBP. In the case of PNCD, the strongest correlation was shown between Alpha and the Au₉ HBP XPS relative concentration, as can be seen in Figure 5-10. Based on the strength of this correlation, the association of the Alpha reference spectra with PNC Deposited Au₉ NCs was determined to be the most reasonable conclusion. Reference spectrum Alpha has three peaks. The first peak is at around

2 - 4 eV and is rather weak, the second peak is at 4.3 - 6.8eV with a maximum localised at $5.7\text{eV} \pm 0.2\text{eV}$ and a third peak between 7 and 9 eV with the maximum at 8.2 ± 0.2 eV. The first two peaks are at the same positions as the the two peaks in the Alpha reference spectrum of the immersion deposition series.

The PNCD Alpha reference spectrum is of particular interest, given that of its peaks have different intensities compared to the immersion Alpha reference spectra, pointing to differences between the Au_9 electronic DOS for each deposition method. While the PNCD Alpha spectrum does have some information indicating a minor peak at around 3eV, it is noticeably less pronounced than the corresponding peak in the immersion Alpha reference spectra. The primary peaks instead appear at around 4-6.5eV and 7-9eV. The first of these broad peaks are equivalent to the immersion Alpha peak observed between 4.3-6.8eV and may indicate a standard DOS feature for Au_9 NCs.

The peak seen at 7-9eV in the alpha reference spectrum has no equivalent in the immersion series Au cluster reference spectrum and, given that the primary observed difference in surface chemistry between the two deposition methods is the retention of Ti^{3+} defects, this peak may be an outcome of the interactions between Au_9 NCs and Ti^{3+} defect sites. Wahlstrom et al. found, using scanning tunnelling microscopy, that bare Au clusters bind weakly with stoichiometric TiO_2 due to bond polarisation. In contrast, Au bonds with Ti^{3+} defects are covalent and were found to be the most stable configuration for single-atom Au clusters on TiO_2 substrates [322]. Recent density functional theory (DFT) investigations by Yoo et al. have probed the interactions between reduced titania surface defects (such as Ti^{3+}) and Au metal NCs, predicting a Au NC valence band maximum at around 4-5eV finding that surface defects indirectly interact with Au NCs, increasing the surface polarizability and inducing a charge redistribution at the localised TiO_2/NC interface[341]. These findings point to the possibility that Au NCs at a TiO_2 interface in proximity to Ti^{3+} defect sites can undergo charge transfer to the TiO_2 conduction band, resulting in a strong bond and positively charged Au NCs. These predictions align with the observed positive shifts seen in the PNCD series NC DOS features compared to the immersion NC DOS peak positions. .

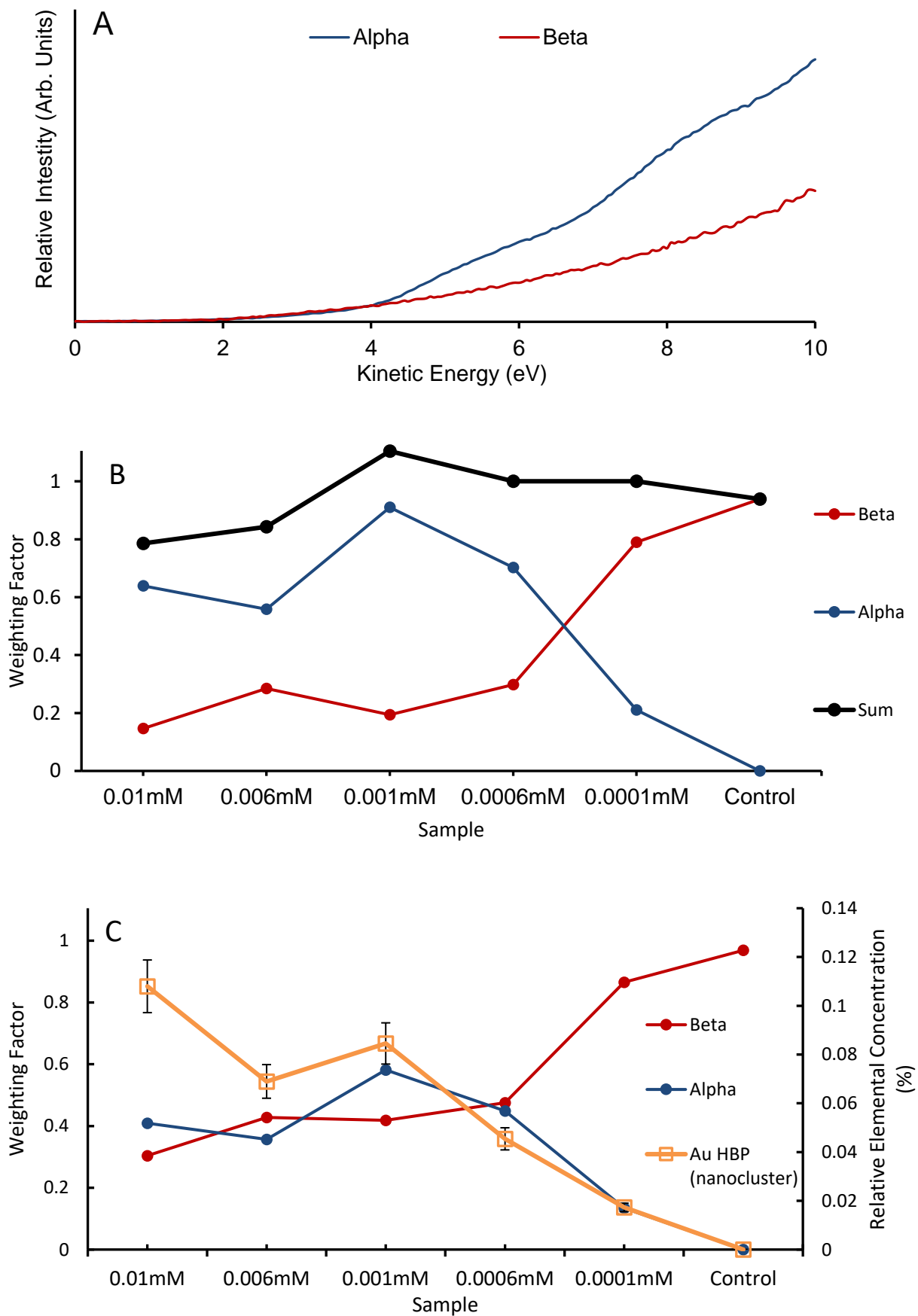


Figure 5-11 Top - Deconvoluted reference spectra from samples P1-P6 after undergoing MIES SVD analysis. Middle - The Alpha and Beta weighting factor breakdown for samples P1-P6. Bottom - Au₉ HBP overlaid on SVD weighting factors showing a strong correlation to the Alpha reference spectra.

The apparent differences in DOS between the same Au₉ NCs on identical substrates highlight that, through different deposition methods, the deposition to a TiO₂ surface with a low and high Ti³⁺ defect density on the sample surface can lead to marked differences in the final electronic DOS when depositing Au₉ NCs. These differences, along with the observed changes in NC agglomeration behaviour and binding energy, likely correspond to specific interactions between Au₉ NCs and the Ti³⁺ defect sites available at the surface of PNCD samples. The differences in the Au₉ bonds with a defect-rich surface may offer new methods to control, stabilise and tune the DOS and properties of atomically precise Au₉ NCs.

5.5 Conclusions

In comparing the effects and outcomes of immersion and PNCD deposition methods on the TiO₂ surface treatment, NC stability and electronic structure of the cluster/substrate system, several key differences have been observed. PNCD technique was shown to allow for NC depositions with far lower overall carbon contributions than similar samples prepared through immersion deposition; especially from the C-O bonds associated with methanol, the solvent used in both deposition methods, with most methanol deposited during PNCD proving to be removable through post-deposition heating. Reduced levels of surface carbon allow for deposited novel surface species to be more easily detected and analysed using extremely surface sensitive techniques such as MIES/UPS.

PNCD was also found to allow surface treatments such as Ti³⁺ defect inducement through heating and sputtering of nanoparticulate TiO₂ to survive the deposition process of ligand protected NCs, ensuring that deposited NCs could access surface defect sites. Ensuring that chemically synthesised NCs can access substrate treatments made under vacuum conditions has proved difficult in past studies and PNCD may allow a new pathway to probe NC-surface interactions.

Au₉ Au NC immersion deposition on RF-TiO₂ was associated with electronic DOS extracted from MIES SVD analysis and showed strong peaks between 2-4eV and 4.3-6.8eV, these peak positions differed from past DOS identified using same deposition method and NCs on ALD titania, however the similar inter-peak spacing suggests that the nature of the substrate used for deposition may play a larger role in the final NC electronic structure than previously understood.

Au₉ Au NC deposited via PNCD showed stronger correlations between surface NCs XPS relative percentages and MIES SVD reference spectra than for the immersion deposited samples, likely due to the reduced carbon content and lack of exposure to atmospheric conditions.

The Au₉ NC PNCD series displayed a changed electronic structure compared to the immersion series. Unique energy peak positions seen in PNCD Au NC DOS features are potentially caused by a charge transfer between cluster and substrate resulting in a positively charged cluster when

deposition and subsequent ligand removal are performed in the presence of Ti^{3+} defects. Overall, the characteristics and treatment of the TiO_2 substrate is seen to have a larger impact on Au NC electronic structure than previously assumed. The role and impact of Ti^{3+} defects on the NC DOS, is seen to result in significant shifts in electronic structure, consistent with stronger NC-surface bond formation on a Ti^{3+} -rich substrate, although without topographical mapping of DOS, the exact nature of the defect/NC interaction is still somewhat uncertain.

5.6 Acknowledgements

The work was supported by the US Army project FA5209-16-R-0017. This research was performed as part of the Australian Solar Thermal Research Institute (ASTRI), a project supported by the Australian Government, through the Australian Renewable Energy Agency (ARENA). This work was supported by Japan's National Institute of Material Science International Cooperative Graduate School Fellowship program. The authors acknowledge the facilities, and the scientific and technical assistance, of Microscopy Australia (formerly known as AMMRF) and the Australian National Fabrication Facility (ANFF) at Flinders University. The authors acknowledge Flinders Microscopy and Microanalysis and their expertise. The authors thank A/Prof Vladimir Golovko (Canterbury University) for providing access to the $\text{Au}_9(\text{PPh}_3)_8(\text{NO}_3)_3$ clusters.

6 INVESTIGATIONS INTO THE ELECTRONIC STRUCTURE AND INTERACTION OF *IN-SITU* VACUUM-DEPOSITED AU AND RU METAL NANOCCLUSERS ON TiO₂

6.1 Introduction

Given the pressing need of the world to transition away from CO₂-emitting fossil fuels, two primary goals must be met to achieve this. First is the transition to renewable, carbon-neutral energy sources; second is the optimisation of current high-energy processes to enable more energy-efficient and economic outcomes. One area of research that currently offers potential pathways towards solutions to both issues is nano-catalysis, with promising results and outlooks in areas such as ammonia production[342], industrial chemistry[343-345] and hydrogen production, especially through photocatalysis of hydrogen[346, 347]. The efficacy of a nanocatalyst is highly dependent on properties such as physical geometry or the specific number of atoms contained within the nanocatalyst, especially for the branch of nanocatalyst known as nanoclusters (NCs)[348-350]. Changing the size, shape, and composition of such NCs can dramatically impact their properties, resulting in NCs that behave radically differently from their related bulk materials and from individual atoms of the constituent elements[350, 351].

These qualities open the door to 'tuneable' catalytic systems designed and optimised to facilitate specific reactions. Simulated studies of the available energy states in a given nano-catalytic system have been used to find candidate catalytic and photocatalytic systems whose DOS aligns with the energy requirements of a given reaction[352-354]. These simulated results require physical experimentation and analysis to determine how real systems perform and react to changes in NCs and their local environments, given that even changes in NC structure or size in the order of a single atom or bond can result in markedly different performance[309, 355]. Various spectroscopic techniques have successfully been used to study these systems, including IR spectroscopy[309, 356], STEM and SEM[196, 267]. However, using extremely surface-sensitive spectroscopic techniques, MIES and UPS, have proven especially useful in revealing the electronic structures and DOS of metal nanoclusters deposited onto photocatalytic catalytic systems. These techniques, coupled with supporting methods, such as XPS and ab-initio simulations, have allowed for the identification of specific electronic DOS associated with homogenous nanoclusters, as well as shifts in these DOS due to modification of clusters and their supporting substrates[266, 267, 295, 323, 324, 340]

Such surface-sensitive spectroscopic techniques require ultra-high vacuum (UHV) conditions and consistent and reproducible sample preparations for best results. These requirements have led to the development of specialised TiO₂ substrates and studying their influence on the attachment and

agglomeration of NCs, especially Au and Ru NCs[267, 325, 331, 357-359]. The attachment of NCs to a substrate has been performed in many studies through the use of a solution-mediated technique outside of the UHV chamber, such as drop-casting[196, 360], immersion[266, 323, 356] or photo-deposition[125, 126]. These *ex-situ* techniques do not, however, guarantee the preservation of surface treatments such as defect sites and can result in the introduction of contaminants and excess surface C from the solvent. As such, the development of *in-situ* deposition techniques has been pioneered, with chemical vapour deposition (CVD) for Ru NCs[357, 358, 361, 362] and the pulsed nozzle cluster deposition (PNCD) technique[363]. These techniques open the door to depositing chemically-synthesised NCs onto prepared substrates while maintaining vacuum conditions, improving the experimental design space for investigations into the nature of cluster-substrate interactions.

While such *in-situ* techniques are promising in isolation, they offer further opportunities for use in concert to deposit multiple NC species onto prepared substrates. The possibility to deposit and analyse nanoclusters through complementary *in-situ* methods opens up the investigation and design of multi-catalyst systems. Each deposited NC could be tailored towards a single step of a complex, multi-step process in such a system. An experiment of this type would require understanding how candidate NCs would behave and change in relation to any co-deposited NCs and the substrate in use. One such system investigated in this study is the co-deposition of Ru₃(CO)₁₂ NCs, which have proved promising for oxygen evolution reactions alongside Au₉(PPh₃)₈ NCs, used for hydrogen evolution. By depositing both NCs onto a photocatalytic ALD TiO₂ substrate, the system can be considered a useful model for photocatalytic water-splitting. This investigation aims to present the first evidence for the suitability of co-depositions of Au and Ru NCs onto prepared, defect-rich TiO₂ substrates under vacuum conditions and examine the interactions and modifications to NC and substrate DOS in such a system.

6.2 Methods and Materials

6.2.1 Substrate Information

The substrate for all samples and measurements reported here was an atomic layer deposited (ALD) TiO₂ characterised by its highly smooth and uniform surface. A thin amorphous TiO₂ was deposited on P-type, boron-doped Si wafers with resistivity $\leq 0.005\Omega\cdot\text{cm}$ (MTI Corp., USA) via ALD. The typical thickness of the deposited film is around 10nm, with less than 1nm surface roughness. A detailed explanation of the method used to fabricate the ALD TiO₂ is described in detail by Walsh et al.[364]

This ALD TiO₂ was heated under UHV conditions to 300 °C for 10 minutes immediately before sputtering with Ar⁺ ions to a dose of 6×10^{14} ions/cm². This step was performed to induce Ti³⁺

defects at the substrate surface consistent with previous studies into the deposition and properties of chemically synthesised, atomically precise metal nanoclusters[266, 323, 365].

6.2.2 Vapour Pressure Deposition

Chemical vapour deposition (CVD) was performed in the same UHV load-lock chamber as for PNCD deposits. The apparatus, consisting of a manipulator arm capable of extending and retracting the CVD deposition vial and a vial-capping shield, is attached to the load-lock chamber described in previous chapters. As they possess a high vapour pressure, metal carbonyl clusters can vaporise at room temperature in environments in the range of 10^{-7} mbar[366]. Deposition testing within the Andersson group determined that pressures of 4×10^{-6} mbar (or lower) could produce reasonable deposition rates on a target substrate.

For each Ru_3 CV Deposition, $2\text{mg} \pm 0.05\text{mg}$ of $\text{Ru}_3(\text{CO})_{12}$ was weighed and loaded into a prepared vial before approximately 2mL of dichloromethane was added before the vial containing the solution was ultrasonicated for one minute. Dichloromethane was used as it did not degrade the cluster condition or result in cluster agglomeration during the deposition process. After ultrasonication, the exterior of the vial was cleaned with ethanol and placed in a fume hood to allow all remaining dichloromethane to evaporate for around 30 minutes. This process resulted in a thin film of ligated $\text{Ru}_3(\text{CO})_{12}$ coating the interior surface of the vial.

The vial was subsequently loaded into a vacuum chamber by placement into a retractable manipulator arm. This apparatus allowed for the vial to be placed such that a substrate for deposition was $<1\text{cm}$ from the vial's opening for depositions and allowed for the vial to be retracted such that the vial's opening was sheathed behind a physical screen, preventing further deposition. All samples were exposed to identically prepared vials for 30 minutes before undergoing spectroscopic measurements. After deposition, all Ru_3 CVD samples were heated under UHV conditions to 625K for 10 minutes, shown in previous studies as sufficient to partially remove CO ligands from Ru-CO binding sites[365]. All CVD depositions and subsequent measurements were performed *in situ*. The cluster vial and the substrate were both at room temperature for all results described here.

6.2.3 Pulsed Nozzle Cluster Deposition

The details regarding the equipment, sample preparation and process employed for PNCD of $\text{Au}_9(\text{PPh}_3)_8$ have been described in section 4.2.1, including details regarding the preparation of equipment, the process and materials used to prepare Au cluster solutions in methanol, and the effects of varying the number of pulses. The depositions described here were performed using a

single pulse PNCD regime with solutions concentrations varied between samples. Deposited samples were heated under UHV conditions to 473K for 10 minutes to remove the PPh₃ ligands.

6.2.4 XPS, UPS and MIES Instrumentation

Details of the UHV experimental apparatus, measurement techniques and data analysis for XPS and MIES/UPS are given in sections 2.1 and 5.3. All XPS measurements were performed using the XPS instrument at Flinders University. The Mg K α X-Ray anode was used for all measurements, with all spectra calibrated at the analysis step to the adventitious C 1s peak at 285.0eV. A detailed explanation of the XPS peak fitting procedure is given in section 3.3.2.1.

High-resolution XPS measurements were performed on each sample's Ti 2p, C 1s and O 1s regions after each substrate surface treatment to monitor the level of Ti 3⁺ defects induced via treatment and the sample's O and C content. Subsequent high-resolution XPS scans were taken after cluster depositions (CVD for Ru₃ and PNCD for Au₉) on the Ru 3d, Au 4f and P 2p regions in addition to the original Ti, C and O regions. The complete series of Ru, Au, P, Ti, O and C scan regions were measured again after the required *in-situ* de-ligation heating process was performed for each cluster.

MIES/UPS measurements were undertaken directly after the *in-situ* heating step for each deposition to probe the surface after supporting ligands were removed from the respective nanoclusters. All MIES/UPS spectra were normalised against a polymer sample known to have highly reproducible MIES spectra; this process was used to reduce the impact of differences in measurement intensity on the MIES/UPS SVD process.

6.3 Results and Discussion

6.3.1 X-Ray Photoelectron Spectroscopy

The discussion of XPS results and associated analysis is presented below in three sub-sections, ALD TiO₂ substrate treatment, Ru₃ cluster deposition and Au₉ cluster deposition, covering the three stages of each sample's preparation and analysis. Each sample was analysed using the same XPS analysis methods described in sections 2.1.1 and 4.2.3

6.3.1.1 ALD Titania Substrate Treatment

The elemental relative percentages, primary peak position and respective Ti³⁺/Ti⁴⁺ ratios for all prepared samples after identically applied surface treatment processes are presented in Table 6-1. These tables summarise the substrate's chemical state as prepared immediately before the Ru₃ NC deposition step.

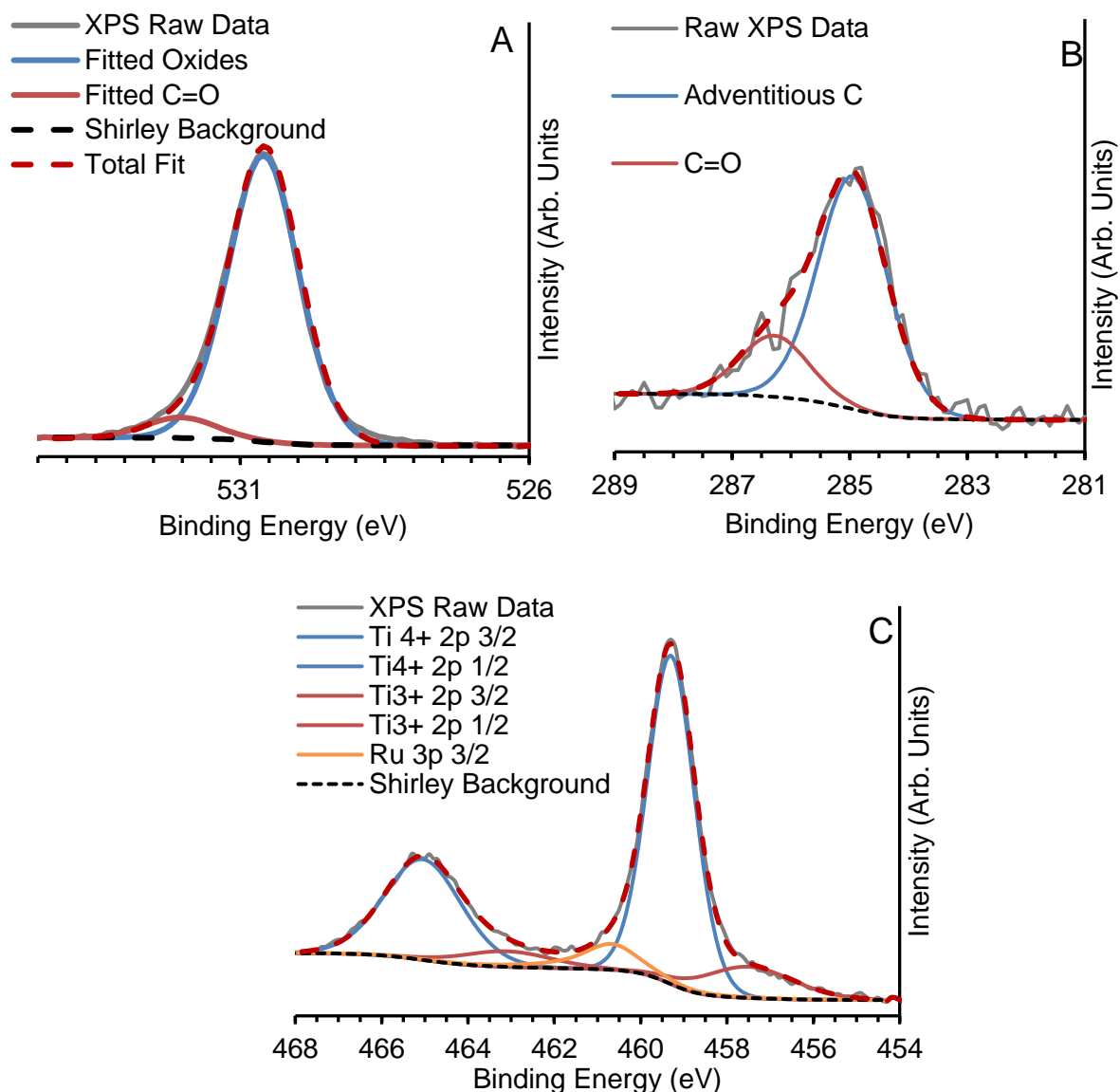


Figure 6-1 Example high resolution XPS scans exhibiting all fitted chemical species for (A) O 1s after heating and sputtering (B) C 1s after heating and sputtering, and (C) Ti 2p after heating sputtering and Ru₃ deposition

A typical O 1s spectra for ALD TiO₂ substrate after heating and Ar-sputtering is seen in Figure 6-1-A. For the O 1s region, two broad peaks were sufficient to model and fit the measured XPS data across the range of samples prepared. While some discrepancy between the total fit of the two O 1s species and the XPS raw data can be seen around 528-529 eV, the minimum number of peaks was used to fit all XPS analyses as the observed FWHM for these peaks was not unreasonably broad. The proposed XPS fittings for all samples do not preclude the potential presence of additional species of lower intensity within the sample, masked by the broader and more intense peaks already identified. The first of these peaks, with the higher intensity, corresponds to the metal oxide TiO₂ substrate, with a possible contribution from SiO₂ and can be seen at around

530.5 ± 0.1 eV[367]. The second, less intense peak at 532.1 ± 0.1 eV corresponds to the O component of single bonded C-containing species[368] and other adventitious species.

Table 6-1 Elemental relative concentrations and primary species binding energy positions were determined by fitting XPS data collected after ALD TiO₂ substrate treatment (Calcine @ 300°C, 10 mins & Ar sputtered). The ratio of Ti⁴⁺/Ti³⁺ defects is recorded as an indication of substrate treatment results.

Relative Elemental Ratio (At%)				
Sample No.	C Species (adventitious, C-O)	O Species (Oxides, C=O)	Ti Species (Ti ⁴⁺ , Ti ³⁺)	Si Species (SiO ₂)
1	7.0 ± 0.1	66.7 ± 0.1	25.6 ± 0.1	0.6 ± 0.01
2	2.9 ± 0.1	69.0 ± 0.1	27.4 ± 0.1	0.8 ± 0.01
3	4.9 ± 0.1	67.8 ± 0.1	26.6 ± 0.1	0.7 ± 0.01
4	6.8 ± 0.1	66.4 ± 0.1	26.3 ± 0.1	0.6 ± 0.01
5	3.1 ± 0.1	69.3 ± 0.1	27.7 ± 0.1	-
6	3.3 ± 0.1	68.8 ± 0.1	27.3 ± 0.1	0.7 ± 0.01
Control	3.9 ± 0.1	67.3 ± 0.1	27.3 ± 0.1	1.1 ± 0.01
Primary Peak Binding Energy (eV)				
Sample No.	C (Calibration Peak)	O	Ti	Si
1	285.0 ± 0.1	530.97 ± 0.1	459.69 ± 0.1	99.65 ± 0.1
2	285.0 ± 0.1	530.75 ± 0.1	459.47 ± 0.1	99.46 ± 0.1
3	285.0 ± 0.1	530.86 ± 0.1	459.59 ± 0.1	99.59 ± 0.1
4	285.0 ± 0.1	530.36 ± 0.1	459.12 ± 0.1	99.44 ± 0.1
5	285.0 ± 0.1	530.94 ± 0.1	459.66 ± 0.1	99.53 ± 0.1

6	285.0 ± 0.1	530.83 ± 0.1	459.55 ± 0.1	99.47 ± 0.1
Control	285.0 ± 0.1	530.94 ± 0.1	459.69 ± 0.1	99.42 ± 0.1

Sample No.	1	2	3	4	5	6	Control
Ratio - Ti ³⁺ /Ti ⁴⁺	0.1373	0.1220	0.13189	0.1513	0.1511	0.1104	0.2216

The C 1s region seen in Figure 6-1-B was fitted with two broad peaks after the complete heating, and sputtering surface treatment was applied. The first peak, centred at 285 eV, is attributed to adventitious C, mainly from C-C and C-H bonds. Adventitious C is detected at this binding energy with sufficient consistency to be used as a calibration peak for XPS analysis, including in this study. The second peak, found at 286.6 ± 0.1 eV is attributed to the C component of surface species, e.g. C-O. Previous studies have identified that surface C is reduced to a minimum after such treatments[266, 323]. However, some adventitious C is retained even after such treatment in UHV conditions. The C-O signal is assumed to originate mainly from contamination from carbonaceous species embedded into the bulk of the ALD substrate during synthesis[266, 267, 323].

The Ti 2p region for ALD TiO₂ displayed Ti species as a spin-split pairing of peaks, the 2p_{3/2} and 2p_{1/2} doublet pair. Doublets were identifiable for both the Ti⁴⁺ species commonly associated with crystalline TiO₂ and a Ti³⁺ doublet attributed to surface-induced defects due to the Ar sputtering treatment.

The primary Ti⁴⁺ 2p_{3/2} peak was identified at a binding energy of 459.7 ± 0.2 eV, while the binding energy of the Ti³⁺ 2p_{3/2} was 457.8 ± 0.2 eV. It is worth noting that the Ti³⁺ 2p_{3/2} peak seen in Figure 6-1C is at least partly due to the peak fitting in this region overlaying the gradient from the Shirley background in this region. To account for this, an approximation was made for the Ti³⁺ XPS Ti³⁺ At% values given in Table 6-1, whereby a peak was fitted for the 457.8 ± 0.2 eV region using the as-made ALD TiO₂ without defects induced. This peak intensity was then considered as an approximate 'background' for Ti³⁺ and was subtracted from the measured intensities for these peaks for all samples after defect-induction preparation step. The resultant ratio of Ti⁴⁺/ Ti³⁺ for each sample's substrate treatment is given in Table 6-1. The poor fitting seen in previous chapters for the region between the 2p_{3/2} and 2p_{1/2} Ti⁴⁺ peaks, attributed to a changing background signal between the primary Ti peaks[365], was also present in ALD TiO₂ substrates when only

considering the Ti^{3+} and Ti^{4+} species. However, after Ru_3 deposition, fitting a $Ru\ 3p_{3/2}$ peak in this region[367], resulted in the more consistent total fit seen in Figure 6-1-C.

Some trace amounts of Si presented in the Si 2p region were measured in all samples XPS scans, except for sample 5, which could not be reliably fit in the Si 2p region. The primary Si $2p_{3/2}$ was identified at 99 ± 0.5 eV for all samples and accounted for less than 1% of the relative XPS signal in each case. This trace Si signal originates from some intermixing of the SiO_2 substrate that the ALD TiO_2 was deposited onto during synthesis.

The spectroscopic summary of raw XPS traces from the as-made state, once heated and after Ar sputtering of the ALD substrate treatment, can be seen in the stacked graphs for the C, O and Ti high-resolution scan regions presented in Figure 6-2.

For the O 1s region, Figure 6-2-A, the most notable changes occur in the 534-531.5 eV binding energy region. The as-made XPS scan presents a significant shoulder in this region, which was fit with multiple peaks related to surface oxide species. After the heating step, this shoulder region shows a reduction in intensity between 532-534 eV, likely due to the removal of more volatile surface oxides. No great change is seen between the heated and sputtered XPS scans, retaining the primary and secondary peaks at around 530 eV and 532 eV, respectively.

In the C 1s region, seen in Figure 6-2B, the as-made sample displays a large shoulder at around 286 eV and a third distinct peak at around 289 eV in addition to the primary adventitious peak at 285 eV. The heating step can be seen to both reduce the 289 eV peak intensity significantly and slightly reduce the shoulder region at 287 eV. The post-sputtered scan shows a further decrease to the 287 eV peak such that it is almost completely eliminated with respect to the XPS noise and background. The final state of the treated ALD TiO_2 after sputtering also shows a significant lowering of C primary peak intensity, demonstrating the additional C removal applied through the sputtering process.

For the Ti 2p region, the primary doublet peak position and intensity are relatively unchanged through the heating and sputtering steps. The primary region altered through the surface treatment can be seen between 455-458 eV, where a shoulder increases in intensity through heating and sputtering treatments. This growth is consistent with the measured inducement of Ti^{3+} defects in the ALD TiO_2 .

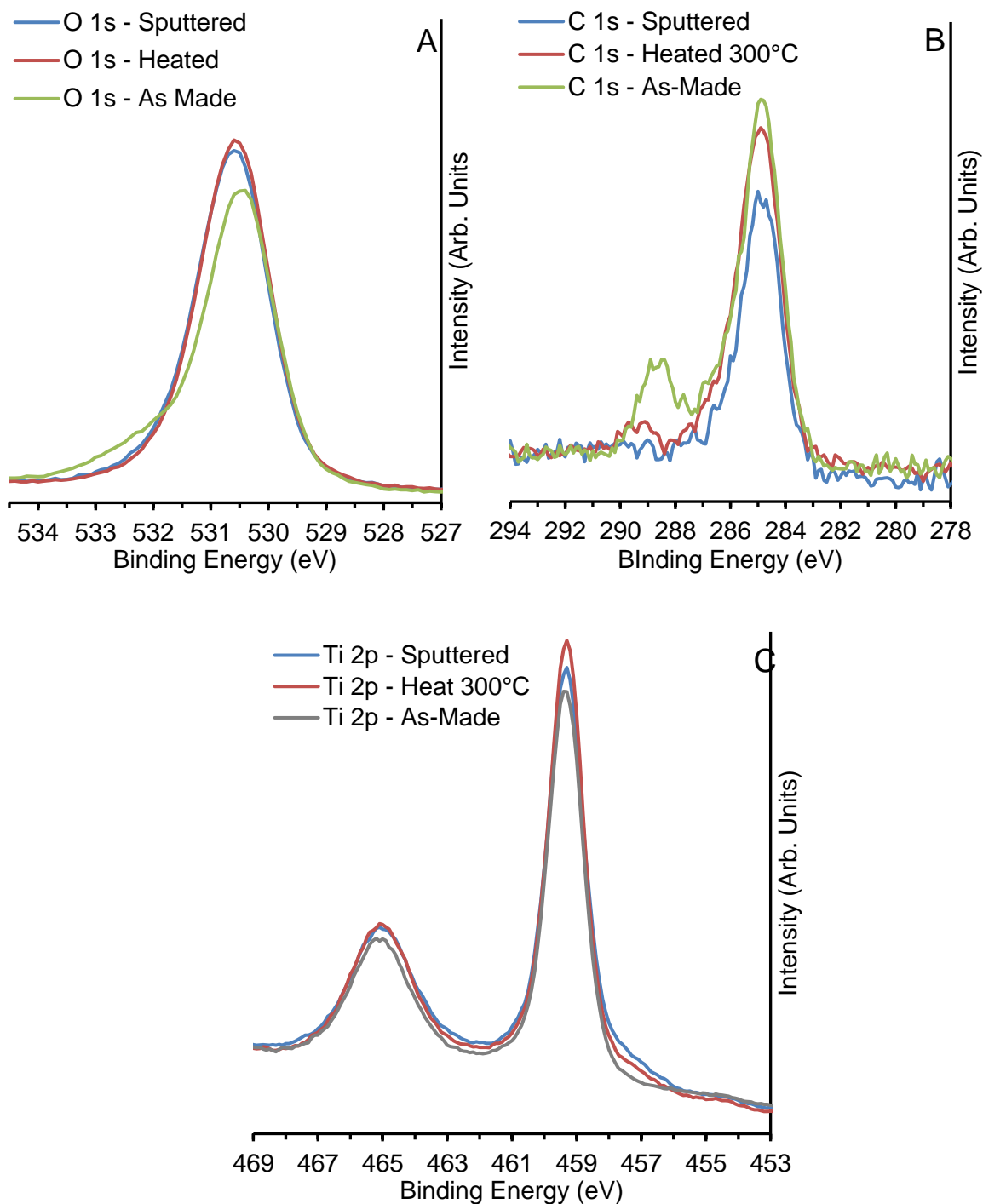


Figure 6-2 Stacked comparison between the XPS raw data of as made, heated (300°C) and sputtered stages of sample treatment on Sample 1. O 1s scans (A) show the reduction of the C=O peak at 532eV present in an as made sample, through sputtering and heating.

6.3.1.2 Ru₃ Nanocluster Chemical Vapor Deposition

As the Ru₃ vapour deposition was performed on the prepared samples described in the previous section, the primary changes to each sample's XPS observations were in the Ru 3d region. The Ru 3d region overlaps heavily with the C 1s region between 278-290 eV binding energy, complicating the fitting and analysis of both C and Ru species. An example fitted high-resolution XPS scan of

the C 1s/Ru 3d region can be seen in Figure 6-3, showing fitted peaks for the previously described adventitious C and C-O species as well as a third C peak, and a Ru 3d doublet.

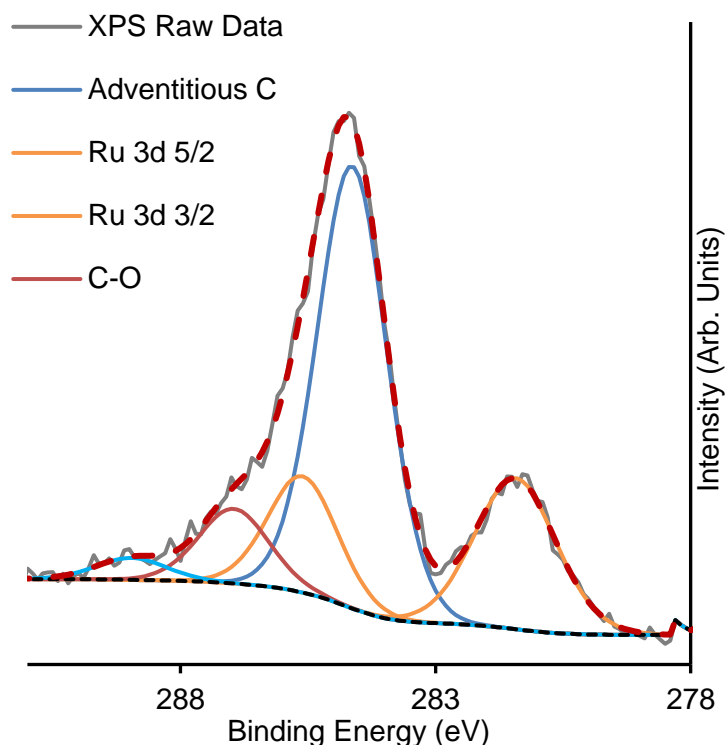


Figure 6-3 XPS high resolution scan of the C 1s/Ru 3d region after $\text{Ru}_3(\text{CO})_{12}$ vapour deposition processing

The third C peak, found at a binding energy of 289 ± 0.1 eV, is typically attributed to COOH functional groups associated with unwanted adventitious C, naturally occurring on sample surfaces. However, as shown in Figure 6-4, this COOH peak is almost removed through the heating process used for the de-ligation of the Ru_3 nanoclusters.

The Ru 3d doublet seen in Figure 6-3 represents the as-deposited chemical state of the $\text{Ru}_3(\text{CO})_{12}$ nanoclusters after chemical vapour deposition. The Ru 3d doublet in the post-deposition XPS scan was fitted using a Gaussian-Lorentzian GL(30) symmetrical peak shape for the pristine Ru_3 NC with a primary peak position of 281.3 ± 0.1 eV and a doublet peak separation of 4.17 eV. These characteristics are consistent with the studies of Howard-Fabretto et. Al. in their investigations on $\text{Ru}_3(\text{CO})_{12}$ NCs deposited onto RF-sputter deposited nanoparticulate TiO_2 films[347, 361]. This peak fitting was found to be appropriate for all as-deposited samples. However, once the samples were heated to partially remove CO ligands, the XPS fitting regime for Ru 3d required some revisions.

After the samples were heated as described in Vapour Pressure Deposition to induce partial de-ligation, a distinct shift was observed in the 282-286 eV binding energy region. A comparison example can be seen in Figure 6-4A, clearly showing the changed symmetry of the Ru 3d 5/2 peak, from its as-deposited symmetrical nature, to an asymmetrical peak shape with a tailing edge

toward higher binding energies as displayed in Figure 6-4B. The peak position has also shifted slightly to lower binding energy, from 281.3 ± 0.1 eV for as-deposited Ru₃ to 280.6 ± 0.2 eV for the heated, asymmetrical Ru 3d 5/2 peak. These observations are consistent with the work of Morgan and others[357, 369], who have investigated changes in Ru peak symmetry due to Ru's changing chemical state, showing that the shift from symmetric to asymmetric line shapes corresponded to the metallisation and increased conductivity of Ru. In this investigation, the line shapes used by Morgan for metallic Ru required a slight modification to reflect the experimentally observed line shape as the XPS resolution, dependant on the experimental equipment used, has been shown to influence the observed Ru asymmetry[369-371].

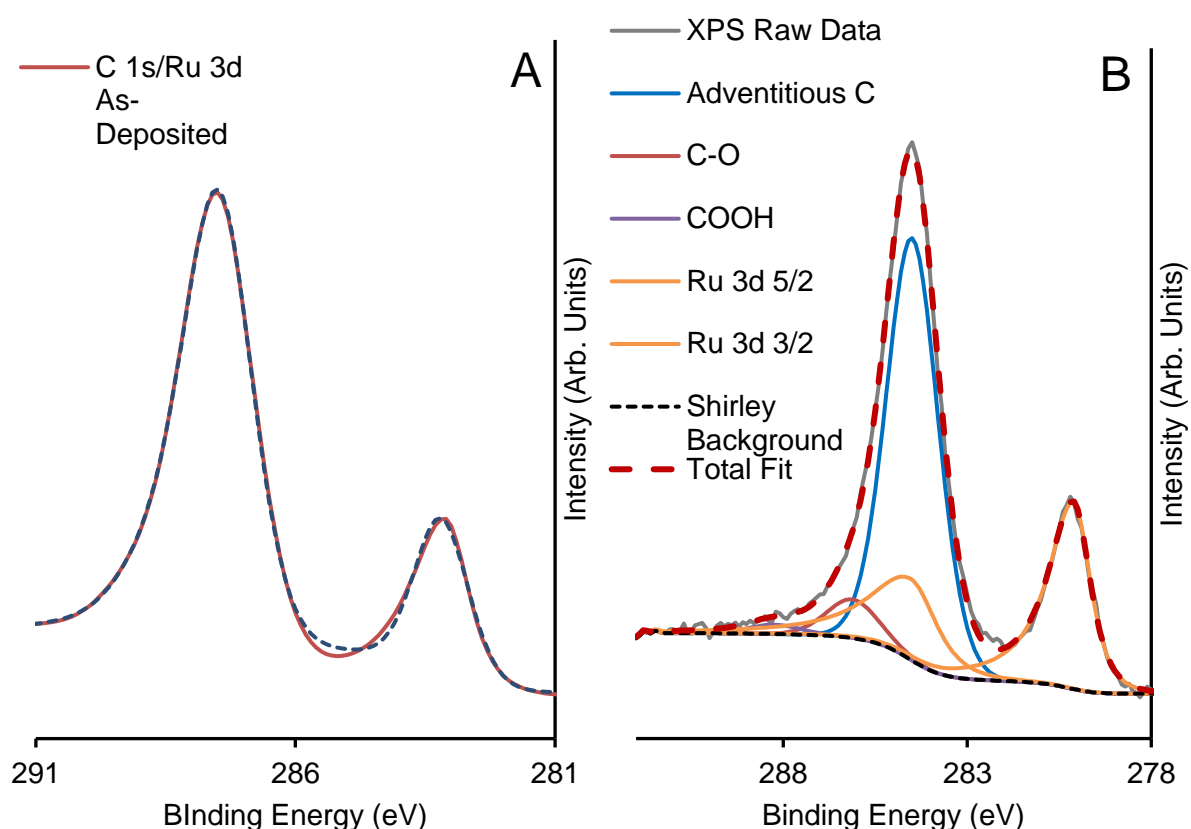


Figure 6-4 XPS high-resolution scans of the C 1s/Ru 3d region showing (A) the comparison between as-deposited and heated scan traces for sample 1, displaying a clear shift in Ru 3d 5/2 peak shape and position, and (B) the fitted scan for the same sample after heating.

The final XPS fits for this deposition process step could not fit an Ru 3d_{5/2} peak at the same binding energy observed for the as-deposited Ru peak position, 281.3 ± 0.1 eV. This was true across the sample series, indicating that the transition from symmetric to asymmetric Ru species is at or near total for deposited Ru₃ NCs after heating for deligation has been performed.

The fitted XPS relative At% for the heated Ru₃ NC deposited sample series can be seen in Table 6-2. All Ru 3d At% presented in this table is of the asymmetric, de-ligated chemical state. It should be noted that given the deposition process involved an identical pre-measured dose of Ru₃(CO)₁₂ NCs and underwent identical exposure periods, the analysed At% of Ru 3d recorded on each sample had a variety of outcomes, from 0.35%-0.93% of the total XPS signal for each sample. This

is indicative of a non-linear relationship between sample exposure time and deposition yields offered by this CVD method, as previously reported by Howard-Fabretto et. al. and assigned to Ru₃ NC [357]

Apart from the Ru species and the appearance and removal of a third C peak through CVD and heating, the major changes to surface chemical species are in the Si 2p, Na 1s and Ti 2p regions.

All deposited samples displayed an increase in their Si 2p At% after their vapour deposition and post-deposition heating processes were complete. While directly comparing At% values from the same sample at different stages of preparation does not take into account relative changes in other elements on the sample, the increase in the Si 2p signal after the addition of Ru species and a corresponding uptick in C At% on all samples does indicate that the post-deposition heating process may increase the amount of XPS-visible Si on the sample surface. Possible mechanisms for these observed changes include ALD film crystallisation or pin-holing effects[359, 372]. Given the low overall At% of Si even after the increase, the Si contribution is not assumed to have interfered with surface-sensitive measurements and interpretations described below.

The appearance of Na 1s peaks in select samples (see Table 6-2) with a clear 1s peak at 1071.0 ± 0.3 eV is not thought to be due to contamination, given that samples 4 & 5 only displayed these peaks after post-deposition heating. This peak is more likely to have been caused by the thermal cycling of the sample, previously mentioned in chapter 3.4.1 and attributed to Na mobility towards the surface due to low Na surface energy [278, 279].

Table 6-2 XPS relative At%, primary peak positions and Ti³⁺/Ti⁴⁺ ratio for the sample range after Ru₃(CO)₁₂ deposition and calcination at 450°C for 10 minutes.

Relative Elemental Ratio (At%)							
Sample No	C 1s	O 1s	Ti 2p	Ti ³⁺ 2p	Si 2p	Ru 3d	Na 1s
1	7.7 ± 0.1	65.6 ± 0.1	25.4 ± 0.1	5.1 ± 0.1	1.0 ± 0.1	0.35 ± 0.1	-
2	3.2 ± 0.1	67.6 ± 0.1	27.3 ± 0.1	6.7 ± 0.1	0.9 ± 0.1	0.93 ± 0.1	-
3	5.4 ± 0.1	66.2 ± 0.1	26.4 ± 0.1	5.4 ± 0.1	1.4 ± 0.1	0.55 ± 0.1	-
4	6.3 ± 0.1	64.6 ± 0.1	25.6 ± 0.1	5.9 ± 0.1	1.4 ± 0.1	0.45 ± 0.1	1.6 ± 0.1
5	4.3 ± 0.1	67.2 ± 0.1	26.3 ± 0.1	4.6 ± 0.1	0.8 ± 0.1	0.77 ± 0.1	0.7 ± 0.1
6	4.7 ± 0.1	67.4 ± 0.1	26.1 ± 0.1	2.9 ± 0.1	1.0 ± 0.1	0.76 ± 0.1	-

Control	3.1 ± 0.1	68.2 ± 0.1	27.2 ± 0.1	6.9 ± 0.1	0.9 ± 0.1	-	-
Peak Positon Binding Energy (eV)							
Sample No	C 1s	O 1s	Ti 2p	Ti ³⁺	Si 2p	Ru 3d	Na 1s
1	285	531.1 ± 0.1	459.9 ± 0.1	458.0 ± 0.1	99.8 ± 0.1	280.6 ± 0.1	-
2	285	531.2 ± 0.1	460.0 ± 0.1	458.2 ± 0.1	99.9 ± 0.1	280.7 ± 0.1	-
3	285	531 ± 0.1	459.8 ± 0.1	457.9 ± 0.1	99.7 ± 0.1	280.5 ± 0.1	-
4	285	531.0 ± 0.1	459.7 ± 0.1	457.9 ± 0.1	99.9 ± 0.1	280.5 ± 0.1	1072.7 ± 0.1
5	285	531.0 ± 0.1	459.7 ± 0.1	457.9 ± 0.1	99.5 ± 0.1	280.5 ± 0.1	1073.3 ± 0.1
6	285	530.8 ± 0.1	459.6 ± 0.1	457.8 ± 0.1	99.5 ± 0.1	280.5 ± 0.1	-
Control	285	531.2 ± 0.1	460.0 ± 0.1	458.2 ± 0.1	99.9 ± 0.1	-	-

The shift observed in the peak shape and position of Ru NCs through the de-ligation process indicates that after the de-ligation heat treatment, a chemical change is induced in the deposited Ru₃ NCs resulting in an altered Ru state, with some metallic characteristics as has been described elsewhere[357]. Investigations by Miyajima et al. investigating Ru NCs with carbonyl supports have found that Ru₃(CO)₇ compounds have the highest thermal stability at temperatures of 650°K/376.85°C [373]. Similarly, previous work using electron ionisation produced large fractions of Ru₃(CO)₇⁺ as fragment ions[374]. While this investigation provides no further insight into the effects of de-ligation on the number of carbonyl ligands retained on the deposited Ru NCs, the temperatures samples were exposed to were too low for complete thermal decomposition or removal of all ligands, found to occur above 650°K and reaching total decomposition by 1000°K[373, 375]. Considering these observations, Ru₃(CO)₇ is proposed as the most likely state of Ru NCs retained on samples after heat treatment for le-ligation.

6.3.1.3 Au₉ Pulsed Nozzle Cluster Deposition

The final stage of sample preparation and analysis was completed with the deposition of Au₉ NCs via PNCD onto the same sample series already having undergone surface treatment and Ru₃(CO)₁₂ deposition and ligand removal. The deposition of Au NCs and subsequent de-ligation treatment completed the intended *in-situ* dual-deposition process. The XPS AT% and primary peak positions for each region measured directly after PNCD deposition can be seen in Table 6-3.

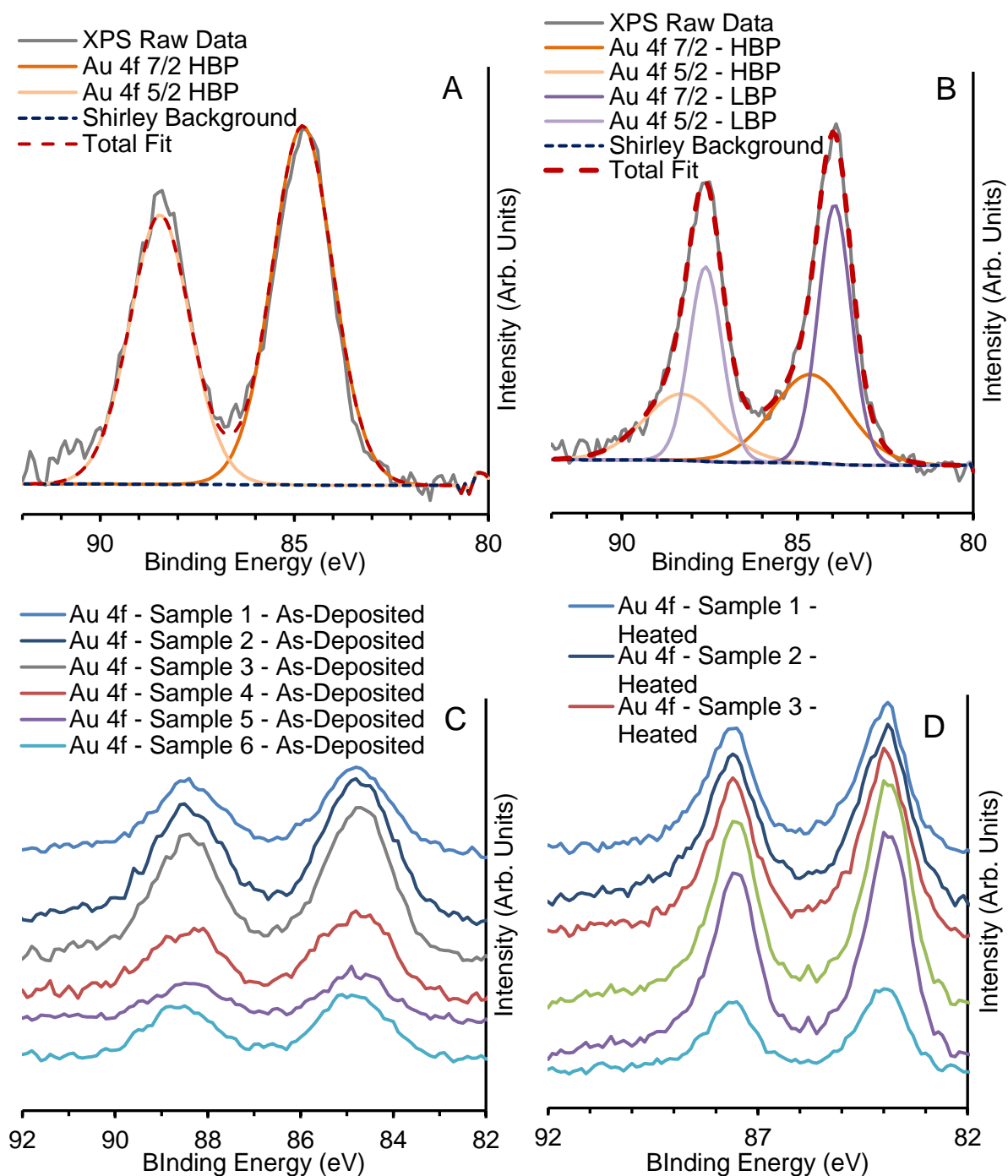


Figure 6-5 Au 4f high resolution XPS scans showing (A) An example of the fitted Au 4f region for post-PNCD, as-made Au NC species doublets as measured for Sample 1. (B) The fitted Au 4f region for heated, partially de-ligated Au NCs from Sample 1, showing the presence of characteristic HBP and LBP Au doublets associated with Au NCs and agglomerated Au respectively. (C) the stacked traces of all co-deposited samples after PNCD Au NC deposition and (D) the stacked traces of the same samples after heating, showing the partial Au NC agglomeration across the series.

Variance in the substrate species, namely C, O, Ti and Na (where applicable) was minor overall. The observed At% for C markedly increased across all samples after PNCD completion. However, the calcination step performed for de-ligation removed the majority of deposited C species. O species were largely unchanged through this step, with observed differences in At% attributed to relative changes in other species more directly affected by deposition and calcination processes. Ti^{3+} defect At% generally decreased at each stage of the Ru NC de-ligation to the final state after

Au NC deposition and calcination. This decrease is consistent with observations made in chapter 5.4.2 when Ti^{3+} surface treatments were associated with Au NC binding sites. Na species observed in select samples during earlier steps also increased in At% after calcination, as would be expected from NA contamination caused by surface migration effects.

As the PNCD process introduced Au species to the sample surface, XPS high-resolution scans were added to the existing high-res scan regions observed in the Ru_3 NC CVD step for the Au 4f region, as well as the P 2p region, to account for the PPh_3 ligand species which encapsulate the Au_9 NCs. The P species associated with these PPh_3 ligand structures were observed both in the post-PNCD sample range (see Table 6-3) and calcined, partially de-ligated samples (see Table 6-4). The P At% ranges from 0.3-0.9% across the sample range before heating, with decreasing At% detected for all samples after calcination. The primary peak position after calcination shifts from as-deposited at 131.4-132.3 eV to lower binding energies at 130.0-130.6 eV. These results are distinct from investigations using RF- TiO_2 , on which P is no longer detectable after the calcination step, as in Chapter 5.4.3. The retention of measurable P on the sample surface is consistent with previous investigations into Au NCs on ALD TiO_2 [266, 323].

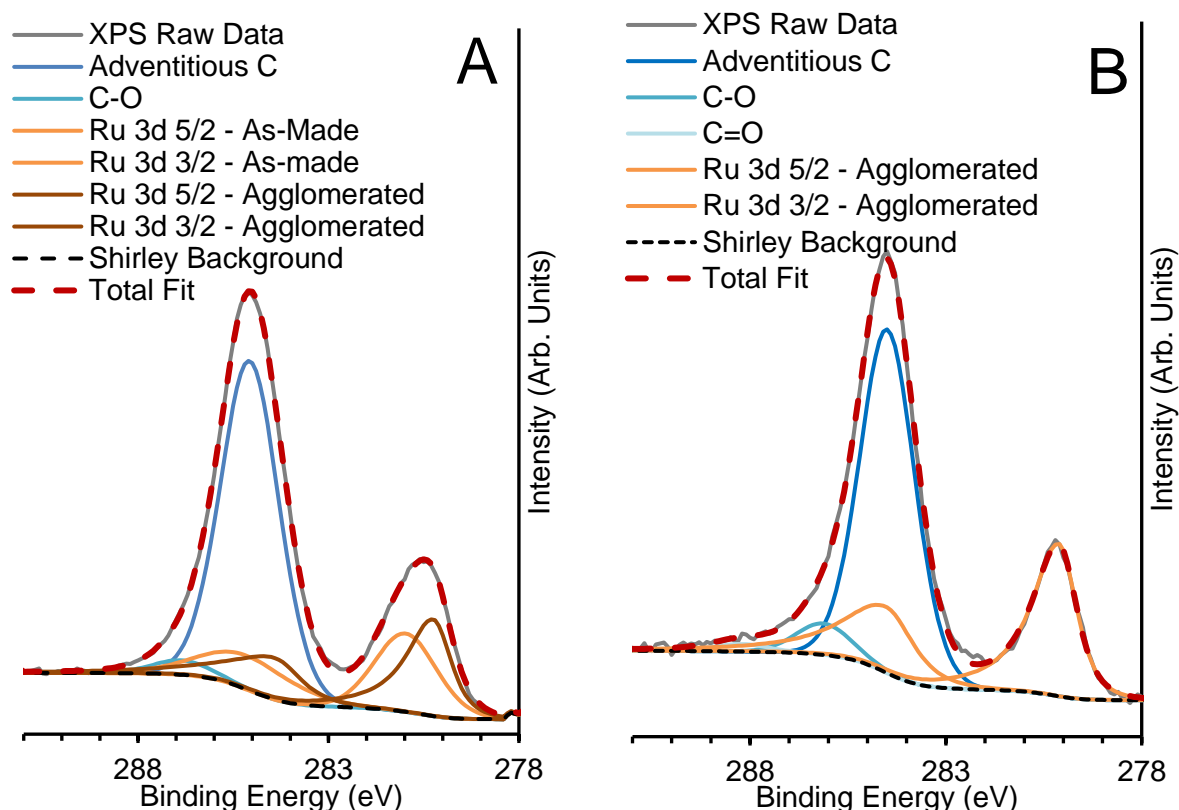


Figure 6-6 Fitted high-resolution XPS scan traces on Sample 1, showing the C 1s/Ru 3d region both immediately after Au NC PNCD deposition (A) and after subsequent heat treatment to 200C in order to partially de-ligate Au NCs (B) it can be seen that the post-PNCD scan shows the presence of Ru NCs correlating to an as-made chemical state in addition to the already deposited Ru species. This suggests that the PNCD process resulted in the deposition of residual Ru NCs onto the sample surface. The subsequent fitting after heating suggests that these Ru NCs undergo some level of agglomeration through the subsequent heating process.

The high-resolution XPS scans for the Au 4f region for the as-deposited PNCD sample series can be seen in Figure 6-5. The PNCD process for Au NC deposition was again successful in depositing Au NCs onto the sample surfaces which retained their characteristic Au 4f doublet with high binding peak energy (HBP) as discussed previously in chapter 5.4.3 and can be seen in Figure 6-5-A. As expected, the stacked traces for the as-deposited PNCD sample range in Figure 6-5-C show that this characteristic HBP position was retained for all depositions at around 85 eV.

Table 6-3-i Relative atomic percentages (At%) as determined through fitting XPS scans on the sample series directly after Au₉ NCs through PNCD. Ru 3d I corresponds to the symmetrical Ru peak doublet, as measured for as-made Ru₃ clusters. Ru 3d II corresponds to the asymmetric Ru doublet peak observed after Ru₃ NCs are heated and delegation occurs. Au 4f – HBP is the high binding energy position of Au observed in Au₉ NC samples which originates from ligated Au₉PPh₃ nanoclusters.

Relative Elemental Ratio (At%)										
Sample No	C 1s	O 1s	Ti 2p	Ti ³⁺ 2p	Si 2p	Ru 3d I	Ru 3d II	Na 1s	Au 4f - HBP	P 2p
1	17.7 ± 0.1	57.5 ± 0.1	22.2 ± 0.1	3.1 ± 0.1	0.6 ± 0.1	1.1 ± 0.1	0.6 ± 0.1	-	0.4 ± 0.1	0.5 ± 0.1
2	18.2 ± 0.1	56.1 ± 0.1	22.3 ± 0.1	3.7 ± 0.1	0.8 ± 0.1	1.8 ± 0.1	0.9 ± 0.1	-	0.5 ± 0.1	0.3 ± 0.1
3	22.1 ± 0.1	53.7 ± 0.1	20.7 ± 0.1	3.4 ± 0.1	0.9 ± 0.1	1.4 ± 0.1	0.5 ± 0.1	-	0.6 ± 0.1	0.6 ± 0.1
4	8.0 ± 0.1	60.1 ± 0.1	24.8 ± 0.1	5.7 ± 0.1	1.3 ± 0.1	0.4 ± 0.1	0.9 ± 0.1	2.6 ± 0.1	1.0 ± 0.1	0.9 ± 0.1
5	16.3 ± 0.1	57.5 ± 0.1	22.9 ± 0.1	2.8 ± 0.1	0.9 ± 0.1	1.3 ± 0.1	0.8 ± 0.1	0.5 ± 0.1	0.6 ± 0.1	0.5 ± 0.1
6	16.7 ± 0.1	56.9 ± 0.1	22.2 ± 0.1	2.4 ± 0.1	1.6 ± 0.1	1.4 ± 0.1	0.9 ± 0.1	-	0.6 ± 0.1	0.5 ± 0.1
Control	9.09 ± 0.1	64.2 ± 0.1	23.4 ± 0.1	5.7 ± 0.1	1.1 ± 0.1	-	-	-	-	-

Table 6-3-ii

Peak Position Binding Energy (eV)										
Sample No	C 1s	O 1s	Ti 2p	Ti ³⁺	Si 2p	Ru 3d I	Ru 3d II	Na 1s	Au 4f - HBP	P 2p
1	285	530.5 ± 0.1	459.2 ± 0.1	457.4 ± 0.1	99.3 ± 0.1	280.9 ± 0.1	280.1 ± 0.1	-	84.7 ± 0.1	131.9 ± 0.1
2	285	530.5 ± 0.1	459.2 ± 0.1	457.5 ± 0.1	99.2 ± 0.1	280.7 ± 0.1	280.0 ± 0.1	-	84.7 ± 0.1	131.6 ± 0.1
3	285	530.4 ± 0.1	459.1 ± 0.1	457.4 ± 0.1	99.2 ± 0.1	280.6 ± 0.1	280.0 ± 0.1	-	84.6 ± 0.1	131.5 ± 0.1
4	285	531.1 ± 0.2	459.8 ± 0.2	458.1 ± 0.2	99.9 ± 0.2	281.5 ± 0.2	280.7 ± 0.2	1072.7 ± 0.2	85.5 ± 0.2	132.3 ± 0.2
5	285	530.4 ± 0.1	459.1 ± 0.1	457.3 ± 0.1	99.3 ± 0.1	281 ± 0.1	280.1 ± 0.1	1073.3 ± 0.1	84.6 ± 0.1	131.8 ± 0.1
6	285	530.3 ± 0.1	459.1 ± 0.1	457.3 ± 0.1	99.5 ± 0.1	281 ± 0.1	280.2 ± 0.1	-	84.7 ± 0.1	131.4 ± 0.1
Control	285	530.5 ± 0.1	459.2 ± 0.1	457.4 ± 0.1	99.1 ± 0.1	-	-	-	-	-

Once the PNCD samples underwent heating, the effects of partial de-ligation of the Au NCs, as discussed in previous chapters, also became apparent in this series. The partially de-ligated samples displayed a corresponding partial agglomeration evidenced by the appearance of an Au 4f doublet peak at the lower binding energy (LBP), associated with bulk Au. In Figure 6-5-B it can be seen that fitting the heated PNCD XPS scan supports an interpretation similar to that of heated PNCD Au nanoclusters on RF-TiO₂ as seen in Chapter 5.4.3 whereby the Au 4f HBP and LBP can reasonably be fit in tandem, confirming the retention of some fraction of HBP Au NC after heating on ALD TiO₂ substrates. This asymmetry can be seen to be true for the entire sample series, as Figure 6-5-D displays the stacked CPS for each samples Au 4f region, with each sample's trace

displaying a broad shoulder at higher binding energy for the primary doublet peaks and providing a good fit for both LBP and HBP species.

Table 6-4-i Relative atomic percentages (At%) as determined through fitting XPS scans measured directly after calcination of the dual Au and Ru NC deposited sample series at 473 K for 10 minutes. Compared to Table 3, some species observed after PNCD have changed. Only Ru 3d II was detected after calcination, and two Au species, the Au HBP seen in the previous step and Au LBP associated with agglomerated Au NCs, were detected.

Relative Elemental Ratio (At%)										
Sample No	C 1s	O 1s	Ti 2p	Ti ³⁺ 2p	Si 2p	Ru 3d II	Na 1s	Au 4f - HBP	Au 4f - LBP	P 2p
1	9.2 ± 0.1	64.4 ± 0.1	24.6 ± 0.1	3.2 ± 0.1	-	1.0 ± 0.1	-	0.2 ± 0.1	0.5 ± 0.1	0.2 ± 0.1
2	8.6 ± 0.1	62.6 ± 0.1	25.0 ± 0.1	4.08 ± 0.1	0.9 ± 0.1	1.9 ± 0.1	-	0.3 ± 0.1	0.6 ± 0.1	0.3 ± 0.1
3	10.1 ± 0.1	61.8 ± 0.1	24.8 ± 0.1	3.3 ± 0.1	1.1 ± 0.1	1.3 ± 0.1	-	0.4 ± 0.1	0.5 ± 0.1	0.2 ± 0.1
4	11.4 ± 0.1	58.1 ± 0.1	23.7 ± 0.1	5.2 ± 0.1	0.34 ± 0.1	1.3 ± 0.1	3.2 ± 0.1	1.1 ± 0.1	1.5 ± 0.1	0.4 ± 0.1
5	7.9 ± 0.1	64.0 ± 0.1	24.6 ± 0.1	3.0 ± 0.1	0.5 ± 0.1	1.2 ± 0.1	0.7 ± 0.1	0.4 ± 0.1	0.6 ± 0.1	0.4 ± 0.1
6	9.0 ± 0.1	63.0 ± 0.1	24.9 ± 0.1	2.9 ± 0.1	0.82 ± 0.1	1.4 ± 0.1	-	0.4 ± 0.1	0.6 ± 0.1	0.2 ± 0.1
Control	9.1 ± 0.1	67.4 ± 0.1	27.3 ± 0.1	6.0 ± 0.1	1.1 ± 0.1	-	-	-	-	-

Table 6-4-ii

Peak Position Binding Energy (eV)										
Sample No	C 1s	O 1s	Ti 2p	Ti ³⁺	Si 2p	Ru 3d II	Na 1s	Au 4f - HBP	Au 4f - LBP	P 2p
1	285	531.2 ± 0.1	460.0 ± 0.1	458.1 ± 0.1	99.9 ± 0.1	280.7 ± 0.1	-	85.2 ± 0.1	84.6 ± 0.2	130.6 ± 0.1
2	285	531.2 ± 0.1	459.9 ± 0.1	458.1 ± 0.1	99.9 ± 0.1	280.6 ± 0.1	-	84.8 ± 0.1	84.5 ± 0.2	130.2 ± 0.1
3	285	531.3 ± 0.1	460.1 ± 0.1	458.3 ± 0.1	100.0 ± 0.1	280.8 ± 0.1	-	84.9 ± 0.1	84.6 ± 0.2	130.3 ± 0.1
4	285	530.9 ± 0.2	459.7 ± 0.2	458.0 ± 0.2	99.8 ± 0.2	280.5 ± 0.2	1072.2 ± 0.2	85.5 ± 0.2	84.3 ± 0.2	130.0 ± 0.2
5	285	530.9 ± 0.1	459.6 ± 0.1	457.9 ± 0.1	99.8 ± 0.1	280.5 ± 0.1	1073.1 ± 0.1	85.2 ± 0.1	84.3 ± 0.1	130.3 ± 0.1
6	285	530.8 ± 0.1	459.5 ± 0.1	457.7 ± 0.1	99.2 ± 0.1	280.4 ± 0.1	-	84.8 ± 0.1	84.2 ± 0.1	130.4 ± 0.1
Control	285	530.9 ± 0.1	459.7 ± 0.1	457.9 ± 0.1	99.6 ± 0.1	-	-	-	-	-

An additional chemical species observed at this stage of the sample series was found in the C 1s/Ru 3d XPS region. In fitting this region, the Ru peak structure appeared distinct from the previously observed as-deposited and heated Ru₃ sample preparation stages. An example of a fitted C 1s/Ru 3d XPS region recorded from Sample 1 can be seen in Figure 6-6-A showing that two distinct Ru species could be fit after PNCD was used to deposit Au₉ NCs. The first Ru doublet's primary 5/2 peak appears centred at around 280 ± 0.2 eV, with a symmetric peak shape. The second Ru doublet's 5/2 peak is centred at around 280.4 ± 0.2 eV with an asymmetric peak shape, made using identical parameters to the Ru peaks seen after heat treatment of deposited Ru₃ NCs. The Ru relative atomic percentage for each sample increases across the sample range in comparing Ru 3d At% between Table 6-2 and Table 6-3. As such, the lower BE Ru doublet referred to as Ru 3d I was attributed to Ru₃ Ncs in their as-made, ligated state. The asymmetric Ru

doublet, referred to as Ru 3d II, was attributed Ru NCs retained on the sample surface after the initial Ru₃ vapour deposition and heating process described in the previous section.

The detection of an Ru species corresponding to as-made, ligated Ru₃ NCs after the PNCD process was completed, while unexpected, is not without explanation. The most likely pathway for a second, unplanned deposition of Ru NCs onto the sample series is proposed to be caused by the rapid change in pressure on the injection of the PNCD pulse. As per the description of PNCD given in Chapter 4.2.1, the pressure within the deposition chamber is observed to spike on the PNCD pulse injection, nominally into the range of 1×10^{-3} mbar, however given the pressure gauges in use on the vacuum chamber were only able to be read manually, it's possible that the true peak of the resultant pressure spike is even higher.

The nature and localised effects of the resultant pressure wave on the deposition chamber are also not understood, however it is proposed that the pressure spike and its effects on the chamber are responsible for the second, Ru deposition and its associated Ru 3d I doublet peak. While the vapour deposition is undertaken with the sample surface near the Ru NC crucible, and the crucible is stored behind a line-of-sight shield when not in use, the nature of vapor deposition means that the Ru NCs are likely able to vaporise and deposit over chamber surfaces at some low rate. The appearance of the Ru 3d I peak after initial Ru vapor deposition was found to only occur in measurable quantities after the injection of a PNCD pulse. It is proposed then, that either changes to the localised pressure around the PNCD nozzle at the time of pulse injection, or the resultant pressure wave as the pulse travels through the deposition chamber re-vaporise some fraction of chamber-deposited Ru NCs. This would allow these Ru species to travel to the sample surface, either carried with the PNCD pulse, or under their own momentum resulting in the observed deposition and appearance of two Ru doublet peaks.

6.3.2 MIES Results and Discussion

The final state of both NC deposition processes investigated in this work, Ru nanoclusters via CVD and Au nanoclusters via PNCD, results in a TiO_2 surface rich with Ti^{3+} defects, co-deposited with both Ru_3 and Au_9 NCs in states of partial de-ligation. Such a surface is ideal for investigation by extremely surface-sensitive spectroscopy such as MIES and UPS. These measurements were conducted after the de-ligation step for Ru_3 CVD and again after the Au_9 NC PNCD deposition calcination step to compare electronic structures' differences with different surface states. Throughout this analysis, the analysis and interpretation of UPS and MIES results are presented for this system, firstly using spectra recorded after Ru_3 CVD and heating have taken place and secondly after subsequent Au_9 PNCD and heating were completed.

6.3.2.1 Ru_3 Nanocluster MIES results and analysis

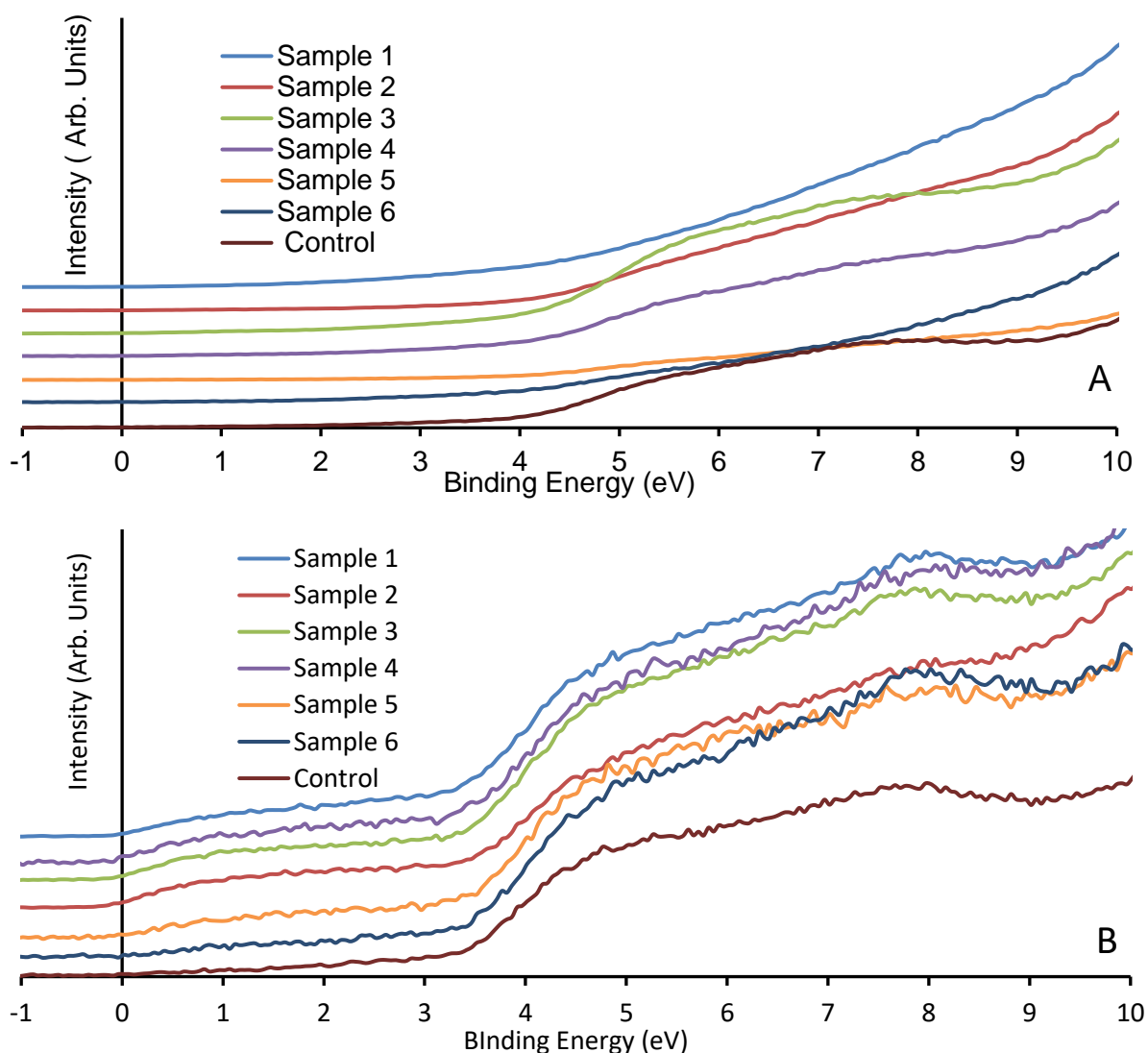


Figure 6-7 Stacked, normalised MIES (A) and UPS (B) raw scan data measured from the sample series directly after Ru NC de-ligation was completed. Each trace has been offset on the vertical axis to display differences in the electronic structure more clearly between samples. MIES scans display some variation between samples in the 4-9 eV region, and no clear difference to ALD TiO_2 in the 0-3

eV region. UPS scans display a clear increase in electronic structure in the 0-3 eV region, while some variation in intensity is seen between samples in the peak located at around 8 eV.

The sample series was first investigated using MIES/UPS immediately after the Ru₃ NC de-ligation treatment to examine the electronic DOS associated with the Ru NCs on treated ALD TiO₂ defect-rich substrates. The collected raw MIES spectra are presented in a stacked offset overlay in Figure 6-7A.

MIES scans on these samples display significant inter-sample variance, mainly in the 4-9 eV range, with clear peaks evident in the scan traces of the control ALD TiO₂, samples 3, 4, and to a lesser extent, Sample 5. This feature appears in the control sample and a previous report by Krischok et. Al observes TiO₂ structures in the 4-9 eV range[283], it's reasonable that this feature can be associated with ALD TiO₂. Although the corresponding XPS species At% data does not clearly indicate the exact nature of which surface species this feature corresponds to most strongly. This uncertainty is reflected in the inter-sample variance seen for weighting factor sums presented in this analysis, representing the sum of deconvoluted reference spectra for each sample with a result of unity achieved for a perfectly deconvoluted spectrum. By achieving a sum under or over unity, some uncertainty in the assignment of surface spectra is assumed.

Compared to the control sample, all Ru₃ CVD samples UPS scans display an increase in electronic structure between 0-3 eV and a slight extension of electronic structure past 0 eV. This increase in the near-fermi DOS for Ru CVD onto TiO₂ surfaces is consistent with investigations by Howard-Fabretto finding similar changes in electronic structure when depositing Ru₃ NCs onto RF-Sputtered TiO₂ substrates[357].

The SVD process of the MIES data from these samples suggested that attempting an SVD using three basis spectra would be appropriate. The results of this process are displayed in Figure 6-8. The deconvoluted reference spectra across Alpha A, Beta B and Gamma C (alphabetical labels are used to distinguish Alpha, Beta and Gamma reference spectra between analyses) provided three visually distinct reference spectra, each with key peaks found at distinct binding energy positions.

Alpha-A displays a minor peak at 3 eV, with broader peak structures also evident at around 5.5 eV and 8 eV. Alpha's weighting factors are at a maximum for Sample 1, with a generally decreasing trend through the sample series, falling to approximately zero in the control sample. When considered alongside XPS results, this weighting factor trend suggests a correlation from Alpha A with de-ligated Ru NC surface species.

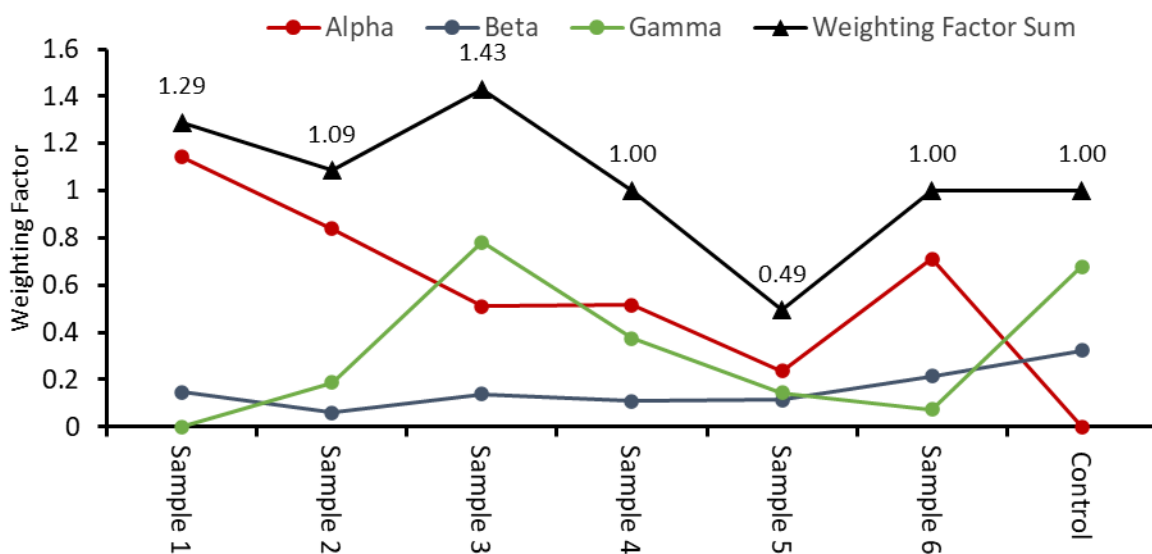
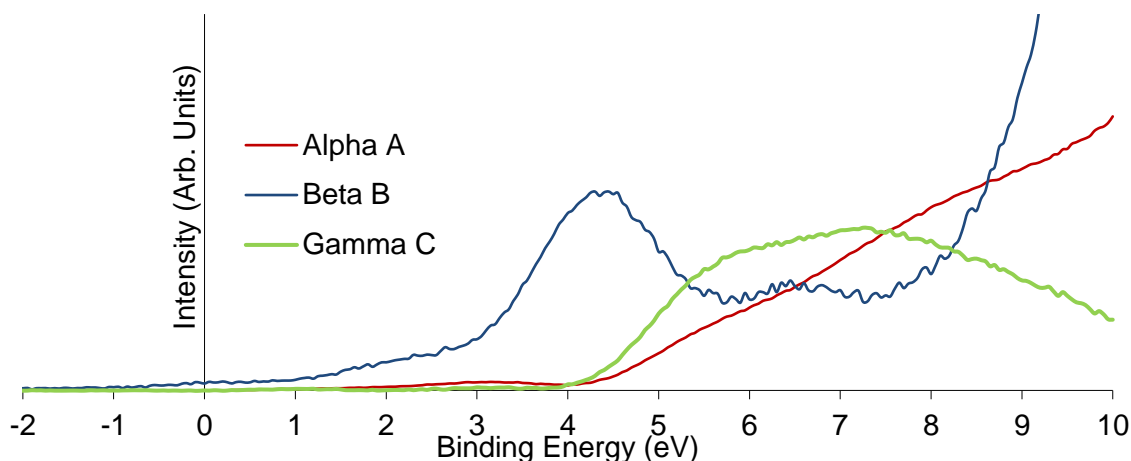


Figure 6-8 The MIES reference spectra determined through SVD using three basis spectra (top) resulted in clearly differentiated Alpha, Beta and Gamma spectra, each with defining DOS features at 3 eV, 4.5 eV and 5-8 eV, respectively. The relevant weighting factors for each sample are presented (bottom), showing the respective trends throughout the sample series and the sum of weighting factors for each sample as determined by SVD.

Beta B is distinguished by its clear energy peak at around 4.4 eV, a subsequent smaller, broader peak at around 6.5 eV and an increase in electronic DOS in the sub-3 eV region, extending into negative binding energies until around -1 eV. Beta weighting factors stay consistently low, below 0.3, for the full sample range, with a maximum weighting factor occurring in the control sample. This trend suggests that Beta B correlates with substrate species, such as Ti, O, C, Si, or some combination. In that case, the distinct electronic structures seen in Beta B compared to those seen in chapter MIES/UPS analysis and XPS correlation could be partly assigned to the use of ALD TiO₂ instead of the RF-sputtered variety but also could point to the influence of the Ru₃ nanoclusters on the substrate's DOS.

Gamma C displays almost no information below 4 eV, with what appears to be two close-lying peaks appearing at around 5.7 eV and 7.3 eV. Gamma C weighting factors vary throughout the sample range, with a strong contribution in Sample 3, Sample 5 and the Control sample. Lower

weighting factors are seen throughout the rest of the sample series without a clear trend. The majority weighting of Gamma C in the control sample points towards a substrate species, distinctly from that seen in Beta B, being primarily responsible for Gamma C. However, the reference spectra observed here do differ from the MIES reference spectra associated with RF-TiO₂, as seen in chapter MIES/UPS analysis and XPS correlation. The observed peak positions in Gamma C do display some similarities with the TiO₂ UPS peak structures seen in scans on these same samples, as well as those described in a study by Krishcok et al. [331].

The sum of weighting factors between the three reference spectra is not at unity in several samples, with Sample 3 and Sample 5 unable to achieve weighting factor sums within ± 0.4 of unity. These fitting issues may be due to various factors, such as changes in the MIES sensitivity, depending on the sample's overall composition. While not unreasonable, the variance in these fitting results, with only three samples outside of the 0.9-1.1 range normally taken to indicate a successful fit, suggests that the overall outcome of this three-basis analysis may not consider all possible surface conditions or species.

6.3.2.2 Ru₃ nanocluster UPS results and analysis

UPS measurements, by nature, are taken simultaneously with MIES but allow for measurement and analysis of the sub-surface substrate regions. The stacked scan traces for the sample range can be seen in Figure 6-7 and display increased uniformity between samples compared to the MIES scan range. All scans show a significant region between 3.5-9 eV, previously discussed as representative of TiO₂ surface and near-surface states for bridging and in-plane O species. For all samples except Control, there is also an increase in electronic DOS in the low energy region from around 3 eV down to approximately -0.2 eV. The modification and extension of the DOS seen here have previously been observed in similar experiments conducted using CVD of Ru₃ onto RF-TiO₂ substrates[357].

Given the collected data, the UPS analysis through SVD suggested that only the two-basis SVD process would be appropriate. The resultant deconvoluted reference spectra, Alpha D and Beta E are presented in Figure 6-9 and display distinct energy profiles between the two reference spectra. The UPS reference spectra do not contain such clear peaks as for those found in the MIES results for the same samples, instead being characterised by broader energy features across specific regions of the binding energy scale.

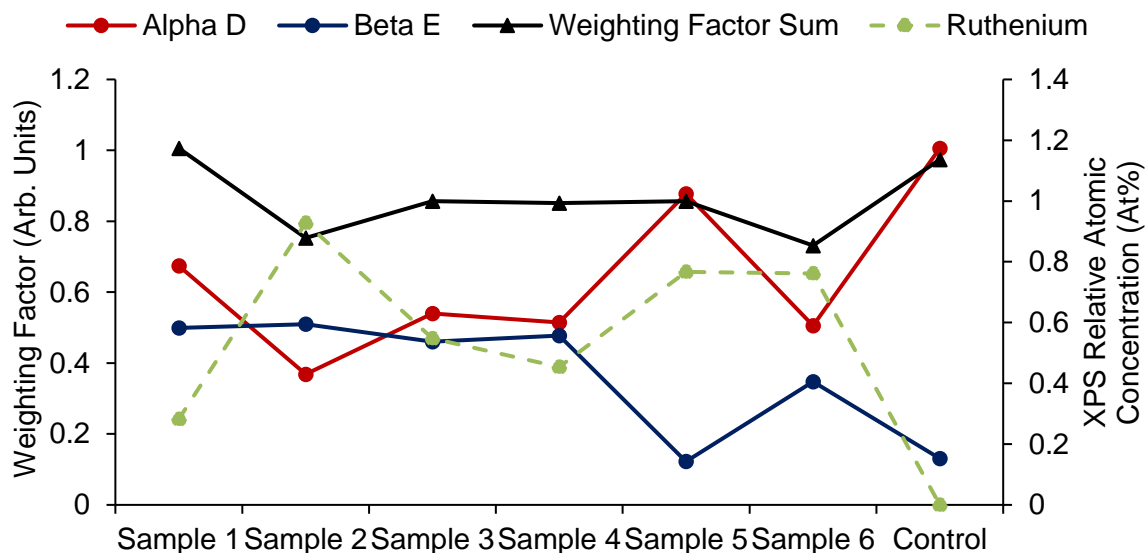
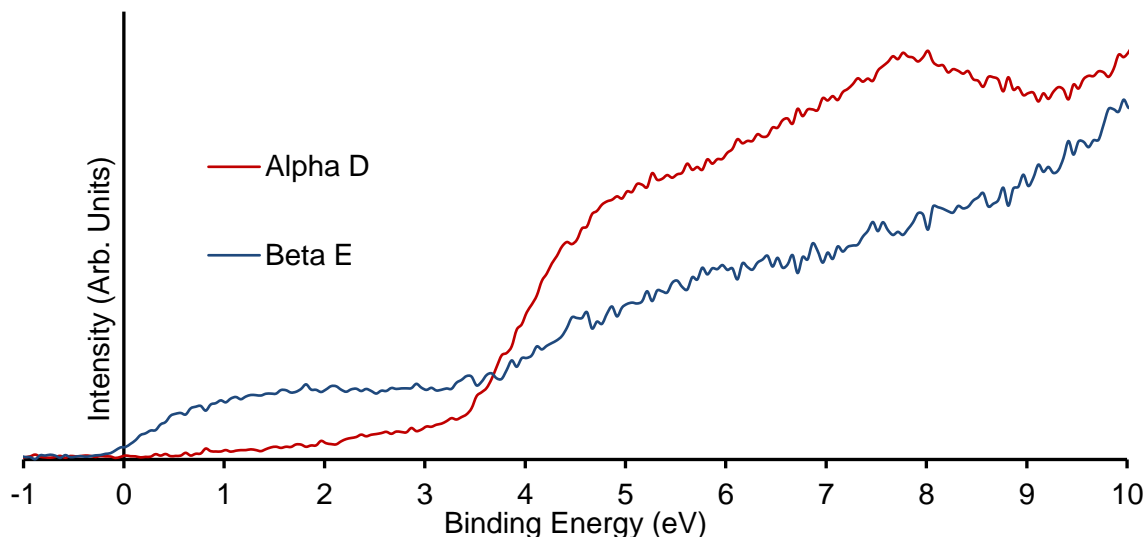


Figure 6-9 Resultant reference spectra, Alpha D & Beta E, produced from SVD of the Ru₃ sample series UPS scans (top), with Alpha D associated with typical Ti UPS features and Beta E associated with Ru NC DOS, the resultant weighting factors and their sum for each sample is seen below.

Alpha D shows very little information below 3.5 eV. The major feature for Alpha D is a broad region between 3.5 – 9 eV, which contains at least two local peaks, at 4.5 eV and 7.7 eV, with only a minor decrease in energy in the intermediate region. These structures align with key DOS features in that same 4-9 eV range from previously reported UPS spectra using TiO₂ substrate[331, 357]. Alpha D's weighting factor trend can be seen in Figure 6-9 and shows a general increase through the sample series, resulting in a 1.00 contribution for the Control sample, with this correlation to TiO₂ substrate reinforcing its association with Ti species.

Beta E shows, in contrast to Alpha D, its primary features below 3.5 eV, where a broadly raised region of the DOS is up to the fermi level of 0 eV. Although increased intensity is observed until around -0.2 eV, this is an artifact of the energy resolution of the MIES/UPS instrument. The features of the Beta E reference spectra above 3.5 eV do not show much in the way of distinct

peak structures but rather a consistent increase in intensity over this energy range. The weighting factor contribution of Beta E throughout the sample series is consistent at around 0.5 through Samples 1-4, before a decreasing trend in Samples 5, and 6 and a relative minimum, a non-zero contribution for the Control sample. As seen in Figure 6-9, the correlation between Beta E and RU XPS At% across the sample range follows the same general trend, with a particularly strong correlation in those samples, which achieved an overall weighting factor sum of 1.00 ± 0.01 , corresponding to successful SVD processes.

The overall sum of the two reference spectra weighting factors across the sample range can be seen in Figure 6-9 to resolve to within 1.00 ± 0.17 across the sample range, which is not far outside the $1.00 \pm$. Samples 3, 4, and 5 achieved a weighted unity sum between the two spectra. Samples 2 and 6 cannot achieve unity, with lower-than-expected weighting factor sums, although at different Alpha D/Beta E contributions. Sample 1 and Control are overfitted with a resulting weighting factor sum above unity. For the Control sample in particular, the Alpha D contribution was 1.00, but the assignment of a 0.14 contribution for Beta E is the cause of the unexpectedly high weighting factor sum. These fit outcomes may point towards some regions of the Beta E reference spectra retaining some contributions from TiO₂ substrate species even after SVD. Overall, the weighting factor sum totals observed trends in weighting through the sample series. The distinct association of Alpha E with the control sample provides strong evidence of the proposed reference spectra and correlations to surface species.

The success of a two-basis SVD process, using UPS spectra collected from these samples after Ru₃ nanocluster CVD and de-ligation, points towards two possible conclusions. Firstly, the modification of an ALD TiO₂ substrate through the CVD of Ru₃ and subsequent heat treatment for de-ligation appears to result in detectable sub-surface alterations to the electronic DOS. The UPS results and their contribution from sub-surface bulk species point directly towards a possible bulk DOS alteration through Ru₃ NC deposition, as previously observed in other similar investigations[357, 358]. Secondly, the changes to DOS induced by Ru₃ NCs seem to affect the sub 3.5 eV energy range primarily, extend the DOS past the fermi level, and into the negative eV region. These results and interpretations align well with recent studies on CVD deposition of Ru₃ nanoclusters onto RF-sputtered TiO₂, where it was found that Ru nanoclusters did not have strong MIES features but were associated with electronic structures observed in UPS[357].

6.3.2.3 Co-deposited Au₉ & Ru₃ nanocluster MIES results and analysis

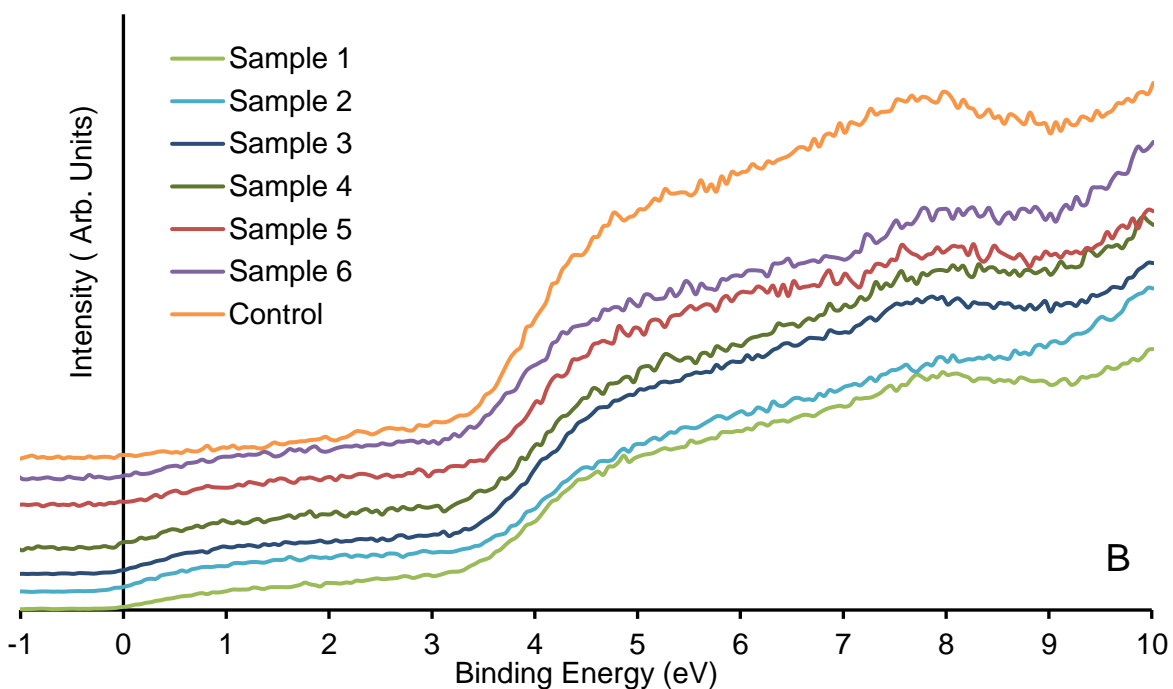
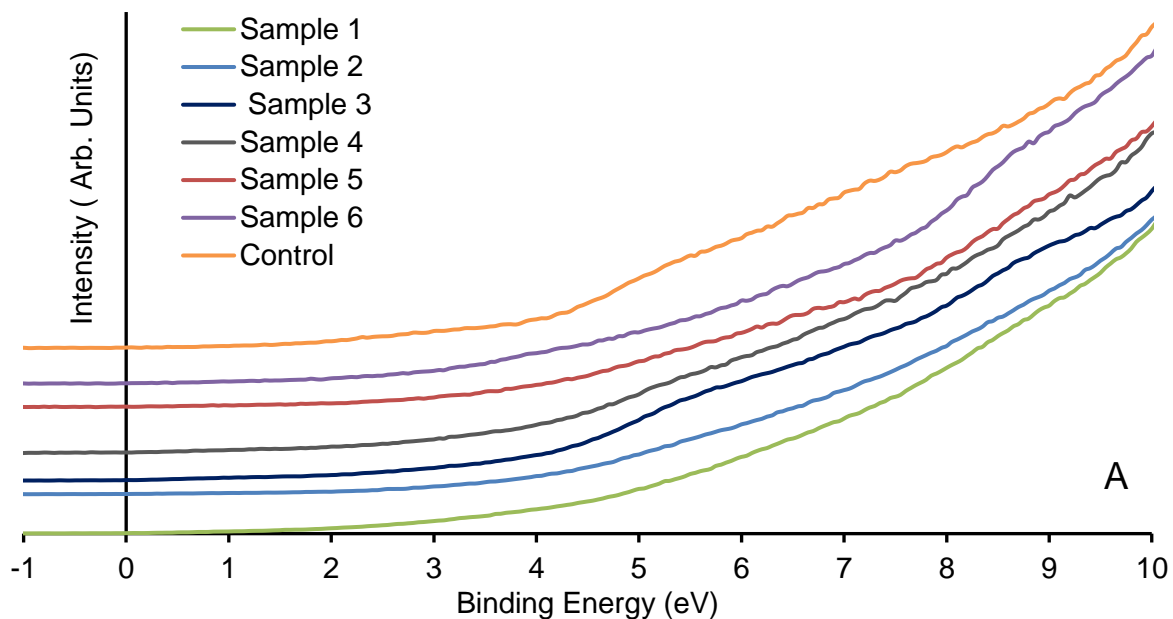


Figure 6-10 normalised and stacked UPS (A) and MIES(B) scan traces from across the sample range as measured after the Au₉ NC calcination step. UPS scans display increased DOS in the sub-3.5 eV region and slightly suppressed intensities in the 4-9 eV range. MIES Scans display a distinct shoulder peak at around 5 eV in the control, and some NC deposited samples, with smaller peaks at various lower energy positions. The UPS scan results display visibly increased uniformity between samples compared to the MIES scans, indicating higher variability of surface species DOS compared to combined surface & bulk DOS.

MIES/UPS scans were again taken on the sample series directly after the calcination step once Ru₃ and Au₉ NCs were deposited and heated on the sample surface. As results collected at this stage indicated the final state of the samples, the electronic structure measured should reveal any notable changes, modifications or interactions between the multiple surface species and substrate.

The stacked MIES scans seen in Figure 6-10-A show that the variance between samples MIES spectra, seen in the Ru₃ NC deposited MIES scans, is also evident for this Au/Ru NC series. The control sample for the co-deposited series is consistent with the MIES scan seen in Figure 6-7-A for the control sample, with a broad region of increased intensity between 4-9 eV. Samples 3, 4 and 6 also show increased intensity in this region. However, the only common feature between these three samples is a peak at around 8.5 eV. Samples 3 and 4 both show small peak structures around 5.5 eV. These scans show key differences to MIES results from the previous deposition step and point toward changes to surface DOS once co-deposition and de-ligation of Ru and Au NCs are achieved.

As in the UPS results seen previously in Figure 6-7, the UPS scans at this stage show higher inter-sample consistency than the MIES results. The key features present on Ru₃ NC deposited samples are also largely present in these results. Primarily, the prominent double peak structure between 3.5 and 9 eV, associated with TiO₂ species, is also evident in all dual-deposited sample scans. The entire sample range also shows increased intensity in the 0-3.5 eV range compared to the control sample. This region is perhaps more pronounced in this sample series than for those UPS scans presented earlier for the CVD Ru₃ nanoclusters. The DOS is again observed throughout the dual-deposited sample range to have some intensity up to -0.2 eV, indicative of states at the Fermi level.

In using SVD analysis on this sample series MIES results, a three-basis SVD process was conducted. The results of the three basis decomposition were compared against weighting factor sum convergence to unity and XPS At% data.

The three-basis SVD analysis was performed on the same MIES data and produced three distinct reference spectra, Alpha F, Beta G and Gamma H, seen in Figure 6-11. Alpha F broadly increases through the binding energy range and contains two broad distinct peaks centred at around 3 eV and around 5 eV with no other significant peak features. These peak positions correlate to the Alpha A spectrum associated with the Ru NCs in Figure 6-8. However, the intensity of these peaks in Alpha F is somewhat lower, and the peaks appear broader than those seen in Alpha A.

While distinct, the Beta G reference spectra is quite similar in general structure to Beta B, with an increased DOS in the lower binding energies < 4eV. The key peak features in Beta G present as a broad doublet peak observed between 4.3 eV – 7.9 eV, the lower centred around 5.45 eV, and the higher at around 7.2 eV. The onset of this region of increased intensity increases sharply between 4-5 eV for both Beta B and Beta G, and both reference spectra show dominant weightings in the control sample. These factors suggest that the assignment of Beta B to TiO₂ substrate species can be reasonably carried over for Beta G.

Gamma H, on the other hand, is more indicative of Au nanocluster correlation. Gamma H has two primary peak features, the first and most prominent at 4.2 eV. A second, broader peak can be seen higher up the energy scale, centred at 8.7 eV. There was also some indication that a smaller, broader peak at around 6.6 eV could be distinguished from the background intensity. Gamma H's weighting through the sample series started at 0.48 for Sample 1 before dropping to 0.11 for Sample 2, then displayed a generally increasing trend through the remaining sample series to achieve its highest weighting factor in Sample 6 at 0.85. Gamma H also contributed to the overall fit of the control sample with a weighting factor of 0.19, an unexpected analysis that suggests that SVD retained some Ti, O or C species energy features across all three reference spectra.

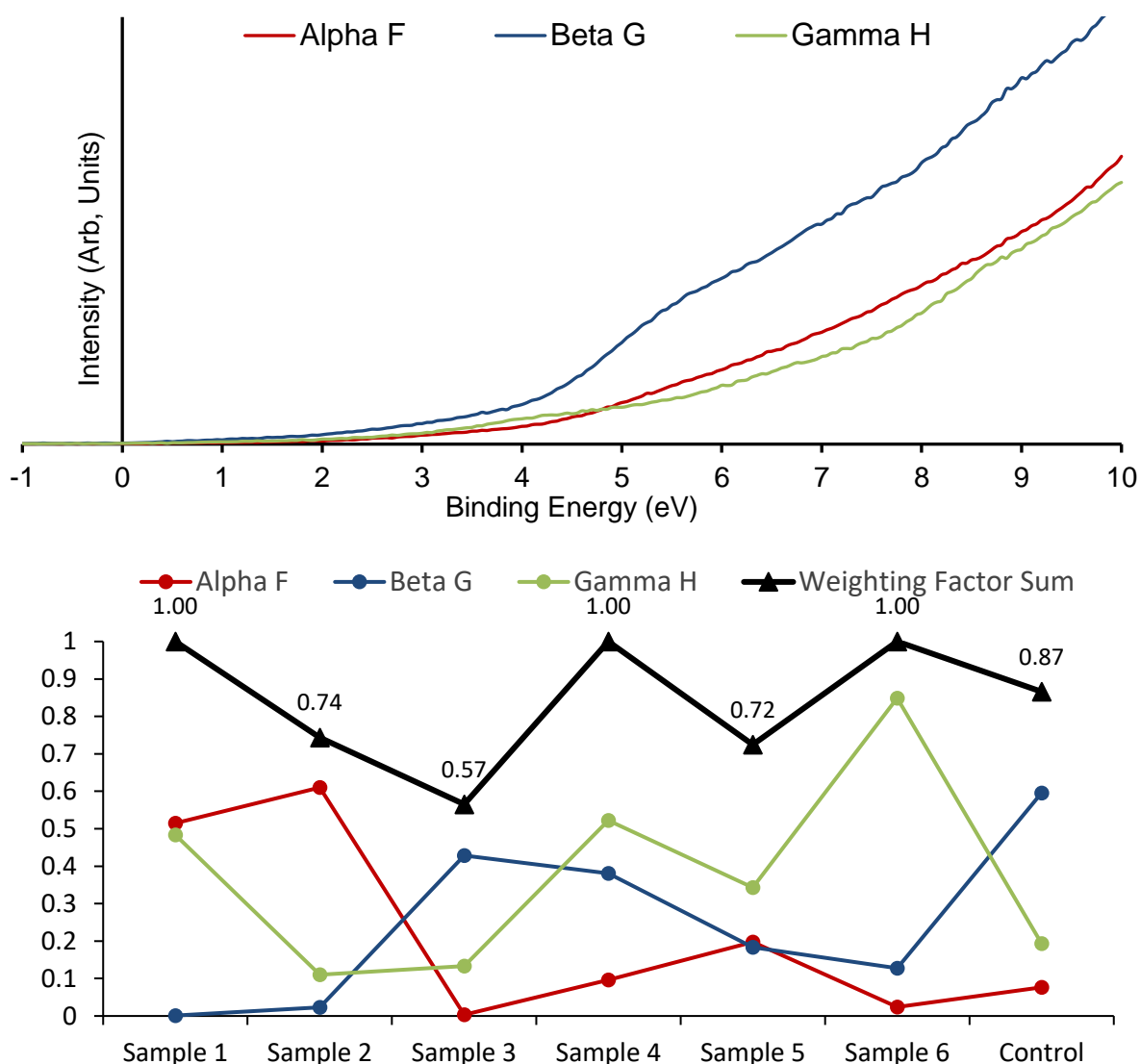


Figure 6-11 Three-basis SVD analysis results from co-deposited and calcined Au₉ and Ru₃ NC MIES scans. Distinct reference spectra (top) are Alpha F, Beta G and Gamma H. The per-sample weighting factors for each reference spectra are shown (below), along with each sample's overall weighting factor sum. This three-basis system still struggles to achieve series-wide convergence of weighting factor sums to unity. The control sample contains residual weightings of all three reference spectra, suggesting that even a three-basis interpretation may not account for the variety of final surface species.

Regardless, the position of Gamma H's key energy features and weighting factor trend correlates with similar DOS peak positions observed in past studies of Au₉ NCs on ALD TiO₂, strengthening this reference spectra assignment[323]. While Gamma H does share some features with Au nanocluster-associated DOS seen in chapter 5.4.4.2, at 4-6.5eV and 7-9eV, the key peaks observed in this Gamma H are shifted compared to those energies. Outside of the differences in the substrate for each case, these shifts may point toward the first evidence of electronic interactions between Ru₃ and Au₉ nanoclusters on the surface, which can alter the DOS of co-deposited nanoclusters.

Analysing the weighting factor sums for this series shows that even the three-basis SVD could not produce reference spectra fitting for each sample to unity across the entire series. Samples 1, 4 and 6 achieved unity, with all these spectra containing at least 0.48 weighting factors from Gamma H. The Control sample, while dominated by Beta G, contained notable contributions from Alpha F and Gamma H and could only converge on a weighting factor sum of 0.87. Samples 2 and 5 achieved 0.74 and 0.72, respectively, a relatively poor fitting result. While Sample 3, as in the two-basis SVD, was a very poor fitting result, only able to be fitted to 0.57. While the overall weighting factor sum for the three-basis SVD analysis improved the two-basis SVD, the improvement was only marginal. It did not necessarily provide convincing evidence that for such a co-deposited NC surface, three-basis SVD was the more appropriate choice.

6.3.2.4 Co-deposited Au₉ / Ru₃ NC UPS results and analysis

Similar to the post-Ru₃ deposition results and analysis, UPS, as a less surface-sensitive technique, can be seen in Figure 6-10B to have highly consistent scan traces across this sample series. Similar to the UPS results on Ru₃ NCs, the primary region of variance is in the -0.2-3.5 eV range, with increased electronic DOS seen for co-deposited NC samples in this region. The small extension of the DOS into negative energies is retained through the co-deposition process. There also appears to be a minor suppression in the intensity of the double peak structure associated with TiO₂, observed between 4-9 eV, compared to the control sample.

SVD analysis for this UPS series was undertaken using a two-basis process, which provided two deconvoluted reference spectra, referred to as Alpha I and Beta J, as shown in Figure 6-12. These two reference spectra are reminiscent of Alpha D and Beta E, as seen in the post-Ru₃ UPS presented previously, although they do present key differences.

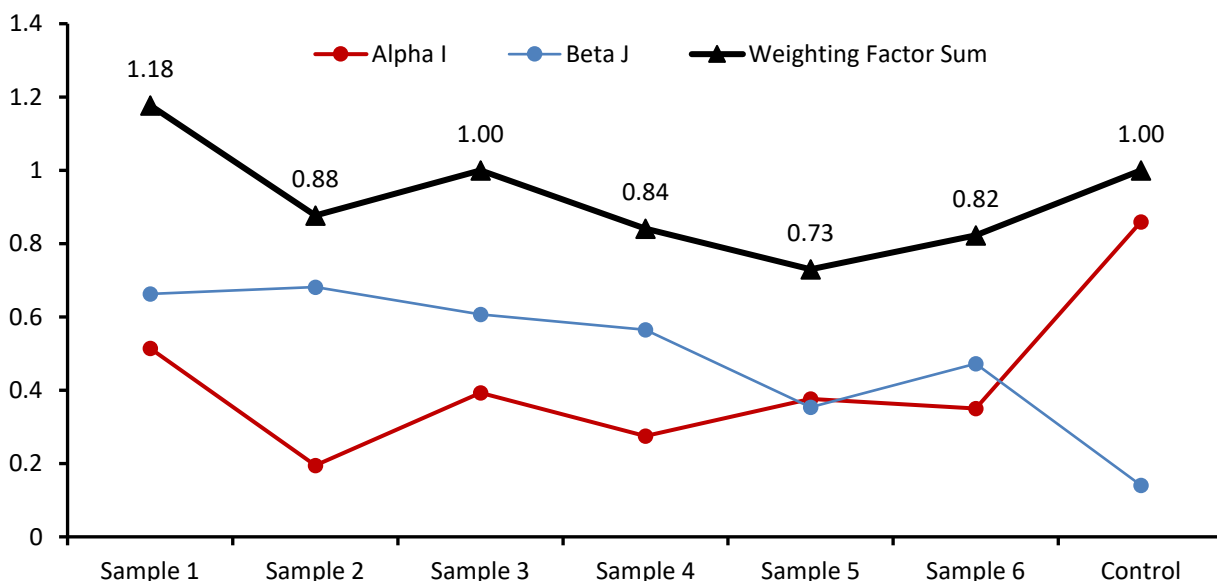
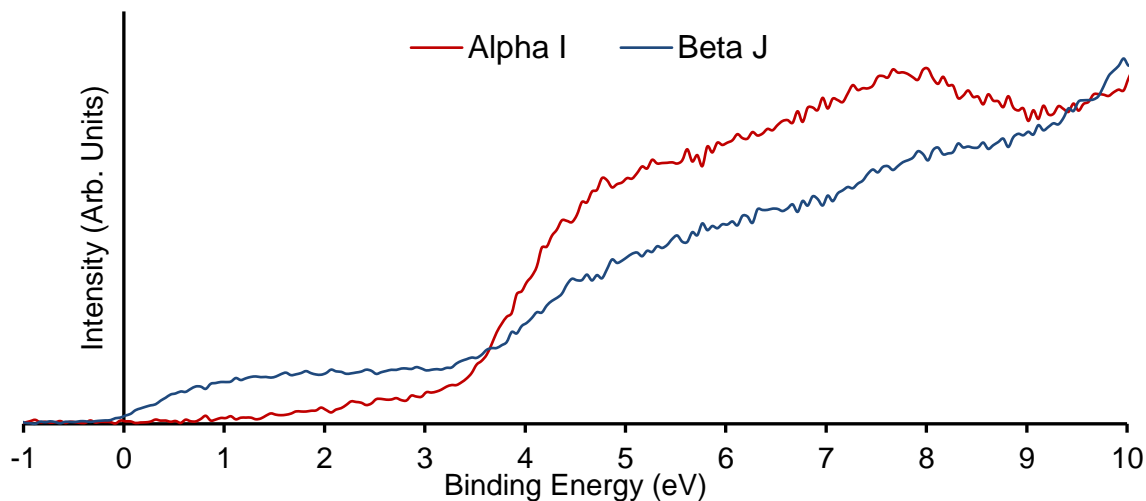


Figure 6-12 Two-basis SVD analysis results from co-deposited and calcined Au₉ and Ru₃ NC UPS scans. Two distinct reference spectra have been deconvoluted and can be seen (top) in the form of Alpha I, and Beta J. Per-sample weighting factors for each reference spectra and the sum of factors are presented (below). While there is some deviation from unity in the weighting factor sums across the sample series, convergence is improved from MIES results and within reasonable bounds when considering the complex co-deposited surface conditions.

Alpha I shows almost no intensity below 1 eV, and very low intensity between 1-3.5 eV before the primary features appear above around 4 eV. As for previously discussed UPS features on TiO₂ substrates, the distinctive double peak structure between 4-9 eV is again strongly evident in this UPS analysis. The weighting factor contribution from Alpha I remains at a reasonably steady fraction through the sample series at around 0.35 ± 0.15 before spiking to contribute a factor of 0.86 to the control sample. These energy features and the strong correlation between Alpha I and the NC-free control sample again provide strong evidence for associating this reference spectrum primarily with the ALD TiO₂ substrate.

For Beta J, the most distinctive energy features can be seen in the region of increased intensity between around -0.2 – 3.5 eV. In Epsilon B, the near-fermi region of increased intensity was

associated with an increase and extension in the DOS through the interaction of Ru₃ with the substrate. For the co-deposited sample, this also appears to hold. While there has been no further extension of the DOS into negative energies by the deposition of Au NCs, the intensity of the DOS in the -0.2-3.5 eV region does appear to have increased.

A shoulder appears in the Beta J reference spectra at 4.5 eV, which overlaps with the primary peak seen in Alpha I before Beta J increased gradually to 10 eV, the energy cut-off for analysis. The overlap of these peak shoulders and the increasing intensity in Beta J past 5 eV suggest that this SVD analysis did not fully achieve the deconvolution process. Further support for this conclusion is found by the appearance of a 0.14 Beta J weighting factor in the weighting factor sum for control when complete deconvolution would entail a weighting factor of 0.

Across the sample series, the weighting factor sum seen in Figure 6-12B displayed an increase in overall convergence to unity and more consistent fits compared to the MIES analysis from this same series. Both sample 3 and control achieved fits unity, while samples 2, 4, 5, and 6 all resulted in below unity fits, the lowest being Sample 5 with a sum of 0.73. Sample 1 resulted in a sole overshoot, with a fit of 1.18. The level of deviation seen in this series is reasonable and suggests that the SVD analysis was moderately successful in deconvolution and fitting weighting factors to describe the surface species DOS.

In correlating these reference spectra with surface species detected through XPS measurements, general trends in XPS At% for each surface species were compared to the weighting factor trends across the sample range. A correlation between the At% and the weighting factor for a particular reference spectra was seen as further support for assigning a reference spectra's DOS to a particular surface species. The At% for both Ruthenium II and Au₉ NCs can be seen mapped against the reference spectra weighting sums for Alpha I and Beta J in Figure 6-13.

The At% trend for Ruthenium II can be seen in Figure 6-13 to display a strong correlation with the Beta J weighting factor trace across the sample range. While the increase or decrease in the Ru II signal does not map exactly to the inter-sample changes in Beta J, the general trend of both series is similar, with a slight decrease across the series before approaching zero in the control sample. UPS results from the Ru₃ CVD step, seen in Figure 6-9, also assisted in interpreting these results with the Beta E spectrum associated with Ru nanoclusters, which shares key features, especially in the 0-4 eV range with Beta J.

Any observable correlation between Au₉ NCs and the Beta J spectra is weaker than for Ru II, with Au₉ At% showing a slight increase in signal across the sample series before dropping to zero for the control sample. This is unsurprising, however, given that Au₉ NCs exist only at the substrate surface, and UPS collects signals from both the surface and the sub-surface bulk regions. Given that the previously mentioned investigation by the Andersson group have determined that Ru₃ has

been observed to encapsulate when heated on some TiO₂ substrates[358], it's plausible that Ruthenium II signal from the substrate bulk would also be represented in this analysis.

The anti-correlation between Alpha I and both Ru II and Au₉ NCs is expected, given that the key energy features of Alpha I correspond to known Ti and O surface species and the high weighing factor seen for Alpha I in the control sample. As such, the evidence to associate the Beta J with the Ruthenium II and Au₉ NC species DOS on the co-deposited surface is reasonable.

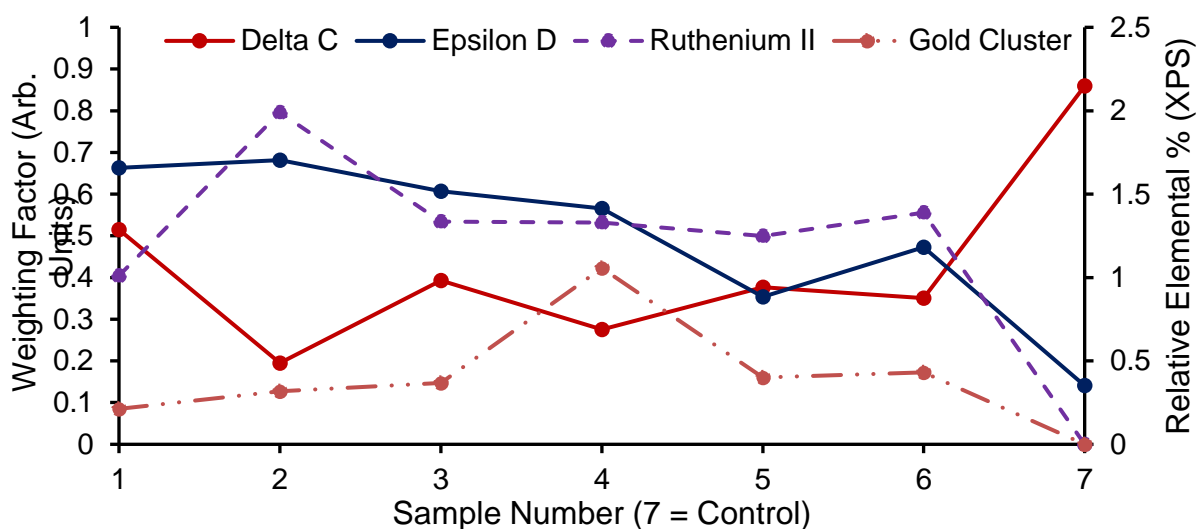


Figure 6-13 A comparison between the relative atomic percentages (At%) for both Ruthenium II and Au₉ NCs as determined by XPS against the respective weighting factors for Alpha I and Beta J across the sample series. It can be seen that a strong correlation in the trend of Beta J and Ruthenium II exists, while a weak correlation between the Au₉ species is also suggested.

Given the addition of Au₉ NCs between the initial UPS analysis on CVD Ru₃ nanoclusters and the results presented above, the influence and outcomes of this novel co-deposited system were analysed through the use of a difference spectrum. This involved the normalisation of the Epsilon B (CVD Ru₃) and Beta J (co-deposited Ru & Au NCs) reference spectrum, followed by determining the difference between the resultant spectral intensities. The results of this operation can be seen in Figure 6-14.

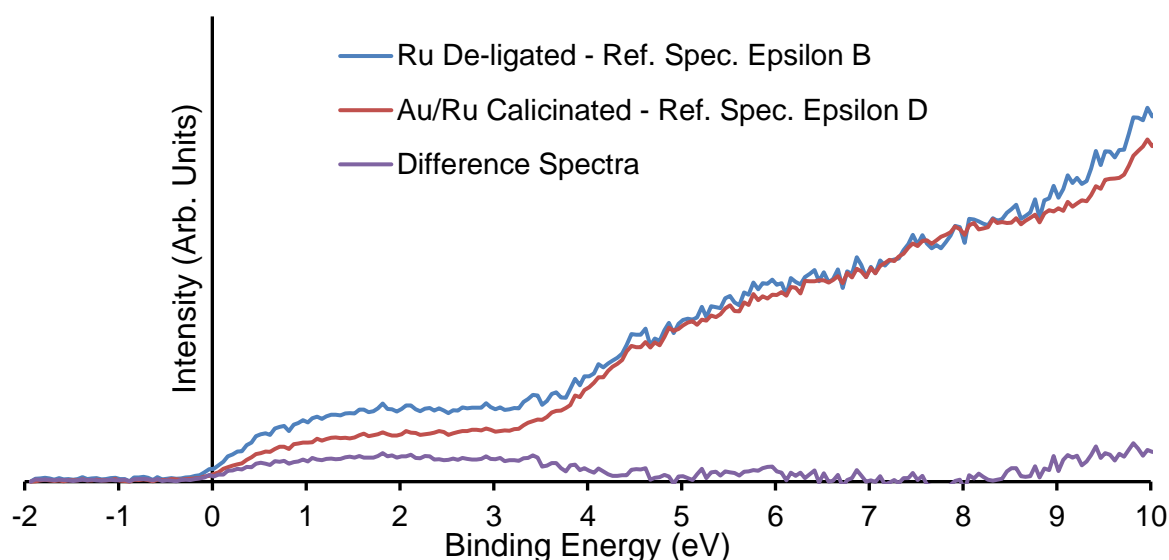


Figure 6-14 The reference spectra associated with Ru and Au NCs, Epsolin B and Beta J are presented here as normalised spectra, along with their difference spectra, produced through the subtraction of Beta J's intensity from Epsilon B. The difference spectrum highlights the changes in DOS between the Ru₃ CVD samples and the co-deposited Ru/Au₉ samples, seen to primarily express in the -0.2-4 eV range, with some other minor differences at higher energies

The difference spectrum produced highlights that the major difference between the DOS at the two measured stages of sample preparation is seen in the characteristic region associated in both cases with Ruthenium NCs most strongly, -0.2-4 eV. The co-deposited samples displayed a reduced intensity in this region compared to those CVD Ru₃ nanoclusters. This indicates that the interaction between Au₉ NCs and the Ru/TiO₂ system may suppress the low binding energy region of the DOS. Interestingly, the extension of the DOS into negative energies does not seem to be reduced by these interactions, with very little difference at the low and negative energy ranges.

The only other notable difference seen in Figure 6-14 occurs at around 9 eV, where it can be seen that the two Epsilon reference spectra differ again most clearly. Again, the Beta J reference spectra appear to have been suppressed in this region compared to Epsilon B. At around 5.9 eV, another minor difference can be seen. However, it is uncertain whether this reflects a true difference in DOS between the two sample series, given that it is only slightly higher than the background noise.

6.4 Conclusions

These vacuum deposition processes have shown their utility in allowing for the observation between cluster species and the prepared substrates onto which they are deposited. These chemically-synthesised, atomically precise NCs are shown to survive their respective deposition processes, landing on the prepared surfaces while maintaining their characteristic binding energies and ligand species. These *in-situ* vacuum depositions are also associated with reduced Ti³⁺

defects on the prepared substrates, pointing toward potential interactions between substrate modifications and deposited NCs.

Some unforeseen outcomes and unexpected findings were also presented in this work. Firstly, the impact of ligand removal steps for CVD Ru₃ nanoclusters on the Ru XPS peak shape was observed to shift to asymmetric fits after ligand removal, corresponding to at least partial metallisation of the Ru₃ NCs, and likely also indicating agglomeration. Similar effects have been observed in other systems exploring CVD for Ru₃ on TiO₂[357].

Secondly, the appearance of pristine Ru₃ NCs in XPS scans after the Au₉ PNCD sample preparation step was an unexpected variable in these depositions and resulted in additional Ru species on the surface. These unexpected Ru species did appear to metallicise after calcination, however given the different temperature treatments, it's uncertain that they result in the same final state as for Ru NCs which were vapour deposited and heated for ligand removal. The potential for differences in these Ru species may have contributed to the difficulty in fitting MIES SVD results, even with three-basis SVD processing. However it should be noted that the observation of Ru₃ vapor depositions taking places simultaneously to PNCD may offer opportunities for alternative methods of simultaneous co-deposition using these two techniques and could be further explored.

The MIES and UPS results obtained from the two post-deposition stage of sample preparation differed in their success. MIES results for both Ru₃ and co-deposited NC sample stages did not converge to easily interpretable reference spectra or weighting factor sums. For the post-Ru₃ vapor deposition samples a three-basis SVD distinguished three unique reference spectra. The three-basis pointed to two reference spectra, Beta B & Gamma C, corresponding to substrate species such as Ti and it's defects and O; while Alpha A, which showed three distinct energy peaks at 3 eV, 5.5 eV and 8 eV was most strongly correlated with Ru₃ surface species.

MIES proved even more complicated for the post-PNCD co-deposited samples to achieve easily interpretable SVD analysis. No one reference spectra produced from three-basis SVD analysis obtained a zero weighting factor contribution to control. The three-basis analysis, justifiable given the two NC species and substrate contributions, successfully produced observable correlations between the Gamma H reference spectra with Au XPS measurements. The energy peaks observed in Gamma H, at 4 eV, 6.5 eV and 8.5 eV, align reasonably with previously observed Au₉ NC DOS on ALD TiO₂. However, these peak positions are shifted from those observed from Au₉ nanoclusters on RF-sputtered TiO₂ presented in chapter 5, suggesting that the co-deposited nanoclusters may well result in first evidence of modification of electronic DOS in such a system. At the same time, the Alpha F reference spectra showed correlations to peak features of Alpha A, associated with Ru NC. These observations indicate that while the co-deposition of Au₉ and Ru₃ NCs with calcination may result in slight modifications to the electronic DOS of the subsequent surface, the exact origin of the observed shifts in surface DOS are not yet fully understood.

UPS results were generally more successful for both measurement series. However, their increased signal from sub-surface bulk regions means that substrate species are more highly represented than surface-deposited nanoclusters, which dominate in MIES results. For both the post-Ru₃ depositions and post-PNCD co-depositions, a two-basis SVD analysis produced two reference spectra corresponding in features and weighting factors with previously reported TiO₂ results. The second reference spectra, which in both cases showed an extension of the DOS into negative energies and a region of increased UPS intensity between -0.2-4 eV, also correlated strongly with Ru At% from XPS weakly correlated with Au At% in the co-deposited samples. The differences between these Ru-associated UPS reference spectra were analysed using a difference spectrum, which showed that the co-deposited UPS spectrum resulted in a comparative suppression of the -0.2-4 eV DOS region compared to the Ru-only depositions series.

These results collectively provide the first evidence for examining chemically synthesised, atomically precise nanoclusters undergoing co-deposition onto modified substrates under vacuum conditions. The potential to prepare, deposit and analyse the preparation through to the final state for multi-species depositions while also analysing changes in chemical species and electronic DOS has the potential to be applied not only in NC depositions with relevance for catalytic systems but could be expanded to any other system and material which proves appropriate for either CVD or PNCD. The versatility of these deposition methods, when coupled with surface spectroscopy techniques such as XPS, UPS and MIES, may prove, once optimised, to be the closest *in-situ* analytical comparison for investigations into co-deposited catalytic systems or other surface-dependant systems.

Given the issues presented by Ru₃ CVD deposits made simultaneously with PNCD, improvements to the experimental design of any future dual-deposition system could be made to avoid two separate Ru deposition events. Firstly, sealing the CVD apparatus behind a closeable gate valve would allow for a reduction in unplanned NC deposition onto deposition chamber surfaces, although unlikely to eliminate this issue. Alternatively, the observed effects of the PNCD pulse on Ru NCs could be harnessed to perform a truly simultaneous co-deposition. By exposing the CVD crucible only during the PNCD process, it seems likely that the resulting pressure spike would enable enough Ru NC to reach the sample surface along with the PNCD deposited NCs so that a simplification of sample preparation may be viable. These proposed improvements have not been further explored within this investigation but may point to future deposition pathways useful to surface-sensitive NC measurements under UHV conditions.

7 CONCLUSIONS

To understand, design and optimise photocatalytic systems using chemically-synthesised, ligand-supported nanoclusters, we must carefully characterise each component of these systems. The size-specific properties of nanoclusters may offer pathways toward tuning catalytic activity if their electronic structure is well-defined and their interactions with photocatalytic substrates, such as TiO₂, are known. To appropriately characterise these species, the challenge of making direct, quantitative measurements of the system surface at each stage of preparation must be met while distinguishing surface species and eliminating unwanted surface contributions.

Characterising these interactions and the electronic structures they result in required the development of novel TiO₂ substrates, methods for *in-situ* HV nanocluster deposition and careful comparison with legacy techniques. These developments have allowed for the investigation of nanocluster agglomeration, nanocluster-substrate interactions, and nanocluster-nanocluster interactions with highly surface-sensitive spectroscopic and topographic methods.

This thesis has focussed on such investigations through a heavy focus on developing appropriate materials, deposition, and treatment methods along with comparative measurements by using surface-sensitive spectroscopic techniques such as XPS, UPS and MIES for material properties and scanning probe and electron microscope techniques, including AFM, SEM and TEM, for topographical investigations. The following conclusions are related to the aims and scopes presented in the introduction chapter.

7.1 Composition and Properties of RF-Sputter Deposited Titanium Dioxide Thin Films

The development and characterisation of a novel process for the deposition of TiO₂ thin films onto Si(110) substrates using RF-sputter deposition are presented, capable of producing nanoparticulate TiO₂ films with minimal Si and C composition while also offering easily modifiable nanoparticle size, crystallinity and electronic structure. Multiple RF-sputter 'recipes' were prepared and compared through XPS elemental analysis, with a regime involving the use of a TiO₂ sputter target after 30 minutes of plasma cleaning produced films with <1% Si and 6% C after heating to 500°C. These films were determined through AFM and SEM investigations to consist of close-packed, amorphous TiO₂ nanoparticles between 20-30nm in size. Heating these films above 300°C under UHV conditions resulted in observable increases in Ti³⁺ defect states compared to Rutile (110) TiO₂ single crystal. Heating of films under atmospheric conditions to 500-1100°C for up to 24 hours revealed through XRD, the onset of Anatase TiO₂ above 500°C and a mixture of Anatase and Rutile TiO₂ when heated at 1100°C for 18+ hours.

7.2 Sub-monolayer Au₉ nanocluster film formation via pulsed nanocluster vapour deposition

A new technique for depositing solvated nanoclusters onto target surfaces through the pulsed injection of the nanocluster solution from a high-pressure environment into a deposition chamber under high vacuum conditions. These depositions were successfully performed on ultra-flat Mica [001] sheets, lacey carbon TEM microgrids and RF-sputtered nanoparticulate TiO₂.

AFM measurements on Mica revealed that under appropriate PNCD deposition conditions, dispersed, sub-monolayer coverage of the Mica surface was achievable. AFM measurements found that most post-PNCD surface features corresponded to the height of a single Au₉ nanocluster (1.1 nm). AFM also displayed the ability to move and manipulate deposited nanoclusters when using contact mode. TEM measurements on carbon microgrids correlated well with AFM, showing Au particles with a diameter of 0.8-1 nm dispersed across the TEM grid. XPS measurements on PNCD nanocluster-deposited TiO₂ samples show that at least 70% of the deposited nanoclusters correspond to the signal from size-specific Au₉ nanoclusters. For low nanocluster coverages, 100% of deposited nanoclusters were found to have survived the PNCD deposition process without agglomeration, showing that this method is useful for preserving nanocluster size-specificity.

By varying the nanocluster solution concentration and the number of pulses used in deposition, it was determined that solution concentration offered poor control over nanocluster coverage on the sample. Varying the number of pulses used in deposition offered high levels of control over deposition concentration, with deposition regimes using fewer pulses displaying evenly dispersed, sub-monolayer coverages. Successful depositions were also achieved using Au₅₅/dichloromethane solution, confirming the potential usefulness of PNCD to explore various nanocluster regimes.

A mathematical model for the evaporation of a drop of nanocluster solution after pulsed injection in HV is presented, describing solvent evaporation before an injected pulse reaches the sample surface. A second model is proposed for estimating the monolayer coverage from a single pulse of PNCD. This model predicts 0.02 monolayers per pulse are deposited for Au₉ nanoclusters in methanol, which agrees with XPS observations on the elemental composition of deposited samples. PNCD offers *in-situ* deposition of nanoclusters into HV environments while preserving nanocluster size and control over monolayer coverage.

7.3 Spectroscopic Comparison of Electronic Structure through Gold Metal NC Immersion and Pulse Nozzle Cluster Depositions on Defect-Rich Titania

A comparison is made between two deposition methods used to deposit nanoclusters onto photocatalytic semiconductor surfaces for spectroscopic measurements in a vacuum. Immersion

deposition, a legacy technique requiring atmospheric exposure of the prepared semiconductor and the newly developed PNCD method, which allows for *in-situ* depositions under HV conditions, were compared for unwanted elemental contributions, impact on semiconductor pre-treatment and resulting electronic structure of the Au₉/TiO₂ nanocluster-semiconductor system.

It is shown that PNCD depositions introduced less C onto the sample than immersion depositions and that C introduced by PNCD was largely removed by post-deposition heating. Given the extreme surface sensitivity of MIES, minimising surface C can result in improved measurements. PNCD was also shown to preserve Ti 3+ defect sites induced during pre-deposition treatments, ensuring Au₉ introduced via PNCD was deposited on a defect-rich surface. Immersion deposition methods almost completely remove induced defects before Au₉ deposition.

Series of Au₉/TiO₂ depositions prepared via the contrasting techniques are shown to express key differences in their respective electronic DOS, as measured by MIES and analysed with SVD. The differences in final DOS between two systems containing identical nanoclusters and semiconductor substrates are attributed to the impact of Ti 3+ pre-treatment, possibly through stronger Au₉/TiO₂ surface bond formation made possible on a defect-rich substrate. The exact nature of the Ti 3+ defects' influence on nanocluster bonding is a promising area for further investigation with techniques such as STM, which can provide topographical maps of electronic DOS.

7.4 Chemical and electronic investigations into in-situ co-deposited chemically synthesised Au and Ru nanoclusters under vacuum conditions

A proof-of-concept investigation was conducted into the viability of co-depositing two nanocluster species, Au₉ and Ru₃, onto pre-treated ALD TiO₂ substrates with all steps performed under vacuum conditions. The respective deposition techniques, Ru₃ vapour deposition and Au₉ PNCD, preserved nanocluster properties and were associated with a reduction in Ti 3+ defect concentrations. However, several issues were encountered with heating effects on Ru₃ nanoclusters, which led to almost complete agglomeration of the Ru nanoclusters, and with isolation of each deposition step. After Au nanoclusters were deposited through PNCD, XPS scans detected increased contributions from Ru, understood to originate from Ru nanoclusters re-vaporised during PNCD. This cross-deposition negatively impacted the analysis and interpretation of the resultant MIES and UPS data. Several potential improvements to the experimental design are discussed to mitigate these effects in future studies.

XPS, UPS and MIES spectroscopy on co-deposited nanocluster-semiconductor systems are presented for the initial Ru₃ deposition and the subsequent final state of co-deposited nanoclusters after Au₉ PNCD. In both cases, weighting factor sums across the sample series indicated difficulties in fitting specific samples. MIES analysis successfully deconvoluted Ru₃-associated

basis spectra, which largely agreed with previous MIES studies on similar systems. For the co-deposited system, MIES deconvolution pointed to three basis spectra associated with surface species for Ru, Au and TiO₂. The key energy features in these spectra displayed similarities with previous observations of single-species nanocluster depositions onto ALD TiO₂ for both Au₉ and Ru₃. Although evidence was presented indicating that Au₉ DOS did exhibit shifted electronic DOS peak positions after co-deposition with Ru₃ nanoclusters, indicating that cluster-cluster electronic modification was possibly occurring.

UPS measurements were more successful across both sample series, with higher weighting factor sums for a two-basis SVD fitting regime. Of the two species, one correlated strongly with literature reports of TiO₂. The second basis spectra for both Ru₃ and co-deposited sample series were associated with an extension of electronic DOS between 0-4 eV and strongly correlated with Ru elemental concentration taken from XPS and a weak correlation with Au species in the co-deposited sample. Construction of a difference spectrum between UPS of the two series revealed that the co-deposited system displayed a suppressed DOS in the 0-4 eV region when compared to the Ru₃-only deposition, providing the first evidence of modification of substrate electronic DOS through co-deposition of nanoclusters.

This project overall has developed methods, techniques and analysis that, when combined have allowed for previously unseen aspects of chemically synthesised, Au and Ru nanoclusters deposited onto photocatalytic substrates to be analysed. The development of innovations, including a simple, clean and modifiable TiO₂ nanoparticulate substrate, and the PNCD method for depositing chemically synthesised nanoclusters *in-situ* under vacuum conditions, allowed for the use and analysis of MIES/UPS on complex systems and interactions. These methods facilitated the investigation of surface defect-nanocluster bonds and their influence on Au nanocluster DOS. Such *in-situ* methods also allowed for the study of complex, two-nanocluster systems and the detection of interactions and changes in their electronic structure through co-deposition processes. The promise of these techniques is evident from these findings, and the promise they hold in exploring a variety of nanoclusters and substrate pairings using surface-sensitive techniques could open pathways to further understanding of other systems, both for photocatalysis and in other fields.

- [1] R.E. Smalley, Future Global Energy Prosperity: The Terawatt Challenge, *MRS Bulletin* 30 (2005) 412-417.
- [2] S.C. Roy, O.K. Varghese, M. Paulose, C.A. Grimes, Toward Solar Fuels: Photocatalytic Conversion of Carbon Dioxide to Hydrocarbons, *ACS Nano* 4 (2010) 1259-1278.
- [3] A. Clerici, B. Cova, G. Callegari, Decarbonization of the Electrical Power Sector in Europe: An Asset, an Opportunity or a Problem?, *Energy & Environment* 26 (2015) 127-142.
- [4] I.E. Agency, *Energy Technology Perspectives 2023*, IEA, Paris, 2023.
- [5] *Statistical Review of World Energy 2012*, in: B. Dudley (Ed.), Pureprint Group Limited, 2012.
- [6] N.S. Lewis, D.G. Nocera, Powering the planet: Chemical challenges in solar energy utilization, *Proceedings of the National Academy of Sciences* 103 (2006) 15729-15735.
- [7] I. Ganesh, Solar fuels vis-à-vis electricity generation from sunlight: The current state-of-the-art (a review), *Renewable and Sustainable Energy Reviews* 44 (2015) 904-932.
- [8] G. Centi, S. Perathoner, Opportunities and prospects in the chemical recycling of carbon dioxide to fuels, *Catalysis Today* 148 (2009) 191-205.
- [9] J.D. Janna Olmos, J. Kargul, A quest for the artificial leaf, *The International Journal of Biochemistry & Cell Biology* 66 (2015) 37-44.
- [10] M. Kato, J.Z. Zhang, N. Paul, E. Reisner, Protein film photoelectrochemistry of the water oxidation enzyme photosystem II, *Chemical Society reviews* 43 (2014) 6485-6497.
- [11] A. Magnuson, M. Anderlund, O. Johansson, P. Lindblad, R. Lomoth, T. Polivka, S. Ott, K. Stensjö, S. Styring, V. Sundström, L. Hammarström, Biomimetic and Microbial Approaches to Solar Fuel Generation, *Accounts of Chemical Research* 42 (2009) 1899-1909.
- [12] C. Graves, S.D. Ebbesen, M. Mogensen, K.S. Lackner, Sustainable hydrocarbon fuels by recycling CO₂ and H₂O with renewable or nuclear energy, *Renewable and Sustainable Energy Reviews* 15 (2011) 1-23.
- [13] M.L. Martin, M.J. Connolly, F.W. DelRio, A.J. Slifka, Hydrogen embrittlement in ferritic steels, *Applied Physics Reviews* 7 (2020) 041301.
- [14] K.P. Keboletse, F. Ntuli, O.P. Oladijo, Influence of coal properties on coal conversion processes-coal carbonization, carbon fiber production, gasification and liquefaction technologies: a review, *International Journal of Coal Science & Technology* 8 (2021) 817-843.
- [15] K. Ayers, N. Danilovic, R. Ouimet, M. Carmo, B. Pivovar, M. Bornstein, Perspectives on low-temperature electrolysis and potential for renewable hydrogen at scale, *Annual review of chemical and biomolecular engineering* 10 (2019).
- [16] K. Zeng, D. Zhang, Recent progress in alkaline water electrolysis for hydrogen production and applications, *Progress in Energy and Combustion Science* 36 (2010) 307-326.
- [17] D.M.F. Santos, C.A.C. Sequeira, J.L. Figueiredo, Hydrogen production by alkaline water electrolysis, *Química Nova* 36 (2013).
- [18] A. Gupta, B. Likozar, R. Jana, W.C. Chanu, M.K. Singh, A review of hydrogen production processes by photocatalytic water splitting – From atomistic catalysis design to optimal reactor engineering, *International Journal of Hydrogen Energy* 47 (2022) 33282-33307.
- [19] A.M.K. Fehr, A. Agrawal, F. Mandani, C.L. Conrad, Q. Jiang, S.Y. Park, O. Alley, B. Li, S. Sidhik, I. Metcalf, C. Botello, J.L. Young, J. Even, J.C. Blancon, T.G. Deutsch, K. Zhu, S. Albrecht, F.M. Toma, M. Wong, A.D. Mohite, Integrated halide perovskite photoelectrochemical cells with solar-driven water-splitting efficiency of 20.8%, *Nature Communications* 14 (2023) 3797.
- [20] J. Luo, J.-H. Im, M.T. Mayer, M. Schreier, M.K. Nazeeruddin, N.-G. Park, S.D. Tilley, H.J. Fan, M. Grätzel, Water photolysis at 12.3% efficiency via perovskite photovoltaics and Earth-abundant catalysts, *Science* 345 (2014) 1593-1596.
- [21] K. Iizuka, T. Wato, Y. Miseki, K. Saito, A. Kudo, Photocatalytic reduction of carbon dioxide over Ag cocatalyst-loaded ALa₄Ti₄O₁₅ (A = Ca, Sr, and Ba) using water as a reducing reagent, *Journal of the American Chemical Society* 133 (2011) 20863-20868.
- [22] I.R. Hamdani, A.N. Bhaskarwar, Recent progress in material selection and device designs for photoelectrochemical water-splitting, *Renewable and Sustainable Energy Reviews* 138 (2021) 110503.
- [23] A. Fujishima, K. Honda, Electrochemical Photolysis of Water at a Semiconductor Electrode, *Nature* 238 (1972) 37-38.

- [24] F. Fresno, R. Portela, S. Suárez, J.M. Coronado, Photocatalytic materials: recent achievements and near future trends, *J. Mater. Chem. A* 2 (2014) 2863-2884.
- [25] J.Y. Lei, Y. Chen, F. Shen, L.Z. Wang, Y.D. Liu, J.L. Zhang, Surface modification of TiO₂ with g-C₃N₄ for enhanced UV and visible photocatalytic activity, *J. Alloy. Compd.* 631 (2015) 328-334.
- [26] N. Serpone, Is the Band Gap of Pristine TiO₂ Narrowed by Anion- and Cation-Doping of Titanium Dioxide in Second-Generation Photocatalysts?, *The Journal of Physical Chemistry B* 110 (2006) 24287-24293.
- [27] M.M. Khan, S.A. Ansari, D. Pradhan, M.O. Ansari, D.H. Han, J. Lee, M.H. Cho, Band gap engineered TiO₂ nanoparticles for visible light induced photoelectrochemical and photocatalytic studies, *Journal of Materials Chemistry A* 2 (2014) 637-644.
- [28] J.Z. Bloh, R. Dillert, D.W. Bahnemann, Designing Optimal Metal-Doped Photocatalysts: Correlation between Photocatalytic Activity, Doping Ratio, and Particle Size, *The Journal of Physical Chemistry C* 116 (2012) 25558-25562.
- [29] R. Kydd, J. Scott, W.Y. Teoh, K. Chiang, R. Amal, Understanding photocatalytic metallization of preadsorbed ionic gold on titania, ceria, and zirconia, *Langmuir : the ACS journal of surfaces and colloids* 26 (2010) 2099-2106.
- [30] W.N. Wang, W.J. An, B. Ramalingam, S. Mukherjee, D.M. Niedzwiedzki, S. Gangopadhyay, P. Biswas, Size and structure matter: enhanced CO₂ photoreduction efficiency by size-resolved ultrafine Pt nanoparticles on TiO₂ single crystals, *Journal of the American Chemical Society* 134 (2012) 11276-11281.
- [31] T. Tsukuda, H. Häkkinen, *Protected Metal Clusters: From Fundamentals to Applications*, Elsevier Science 2015.
- [32] L. Howard-Fabretto, G.G. Andersson, Metal Clusters on Semiconductor Surfaces and Application in Catalysis with a Focus on Au and Ru, *Advanced Materials* 32 (2020) 1904122.
- [33] U. Heiz, *Nanocatalysis*, Dordrecht : Springer, Dordrecht, 2007.
- [34] P. Lu, Polymer-protected Ni/Pd bimetallic nano-clusters: preparation, characterization and catalysis for hydrogenation of nitrobenzene, *J. Phys. Chem. B* 103 (1999) 9673-9682.
- [35] A. Kulkarni, R.J. Lobo-Lapidus, B.C. Gates, Metal clusters on supports: synthesis, structure, reactivity, and catalytic properties, *Chemical communications* 46 (2010) 5997-6015.
- [36] J. Wang, G. Wang, J. Zhao, Density-functional study of $\{\text{Au}\}_n$ ($n=2\text{--}20$) clusters: Lowest-energy structures and electronic properties, *Physical Review B* 66 (2002) 035418.
- [37] B. Yoon, P. Koskinen, B. Huber, O. Kostko, B. von Issendorff, H. Hakkinen, M. Moseler, U. Landman, Size-dependent structural evolution and chemical reactivity of gold clusters, *Chemphyschem : a European journal of chemical physics and physical chemistry* 8 (2007) 157-161.
- [38] G. Portale, L. Sciortino, C. Albonetti, F. Giannici, A. Martorana, W. Bras, F. Biscarini, A. Longo, Influence of metal-support interaction on the surface structure of gold nanoclusters deposited on native SiO_x/Si substrates, *Physical Chemistry Chemical Physics* 16 (2014) 6649-6656.
- [39] G.E. Johnson, C. Wang, T. Priest, J. Laskin, Monodisperse Au₁₁ clusters prepared by soft landing of mass selected ions, *Analytical chemistry* 83 (2011) 8069-8072.
- [40] Y. Negishi, W. Kurashige, Y. Niihori, K. Nobusada, Toward the creation of stable, functionalized metal clusters, *Physical chemistry chemical physics : PCCP* 15 (2013) 18736-18751.
- [41] J.M. Pettibone, J.W. Hudgens, Predictive gold nanocluster formation controlled by metal-ligand complexes, *Small* 8 (2012) 715-725.
- [42] A. Cho, Connecting the Dots to Custom Catalysts, *Science* 299 (2003) 1684-1685.
- [43] M. Turner, V.B. Golovko, O.P.H. Vaughan, P. Abdulkin, A. Berenguer-Murcia, M.S. Tikhov, B.F.G. Johnson, R.M. Lambert, Selective oxidation with dioxygen by gold nanoparticle catalysts derived from 55-atom clusters, *Nature* 454 (2008) 981-983.
- [44] D.P. Anderson, J.F. Alvino, A. Gentleman, H.A. Qahtani, L. Thomsen, M.I. Polson, G.F. Metha, V.B. Golovko, G.G. Andersson, Chemically-synthesised, atomically-precise gold clusters deposited and activated on titania, *Physical chemistry chemical physics : PCCP* 15 (2013) 3917-3929.
- [45] P.P. Edwards, J.M. Thomas, *Gold in a Metallic Divided State—From Faraday to Present-Day Nanoscience*, *Angewandte Chemie International Edition* 46 (2007) 5480-5486.

- [46] L. Liu, A. Corma, Metal Catalysts for Heterogeneous Catalysis: From Single Atoms to Nanoclusters and Nanoparticles, *Chemical Reviews* 118 (2018) 4981-5079.
- [47] Z.-J. Guan, J.-J. Li, F. Hu, Q.-M. Wang, Structural Engineering toward Gold Nanocluster Catalysis, *Angewandte Chemie International Edition* 61 (2022) e202209725.
- [48] P.H. Hess, P.H. Parker, Polymers for stabilization of colloidal cobalt particles, *Journal of Applied Polymer Science* 10 (1966) 1915-1927.
- [49] G. Carotenuto, F. Nicolais, Synthesis of Polymer-Embedded Metal, Semimetal, or Sulfide Clusters by Thermolysis of Mercaptide Molecules Dissolved in Polymers, *Recent Patents on Materials Science* 1 (2008) 1-11.
- [50] G. Schmid, Clusters and colloids: bridges between molecular and condensed material, *Endeavour* 14 (1990) 172-178.
- [51] T. Tsukuda, Toward an Atomic-Level Understanding of Size-Specific Properties of Protected and Stabilized Gold Clusters, *Bulletin of the Chemical Society of Japan* 85 (2012) 151-168.
- [52] P. Pyykko, Structural properties: Magic nanoclusters of gold, *Nat Nano* 2 (2007) 273-274.
- [53] G. Schmid, N. Klein, Novel Modifications of Gold, Rhodium, and Ruthenium—M13 Clusters as Building Blocks of “Superclusters”, *Angewandte Chemie International Edition in English* 25 (1986) 922-923.
- [54] G. Schmid, Large clusters and colloids. Metals in the embryonic state, *Chemical Reviews* 92 (1992) 1709-1727.
- [55] M.A. Lopez-Quintela, J. Rivas, Chemical reactions in microemulsions - a powerful method to obtain ultrafine particles, *J. Colloid Interface Sci.* 158 (1993) 446-451.
- [56] M.A. López-Quintela, Synthesis of nanomaterials in microemulsions: formation mechanisms and growth control, *Current Opinion in Colloid & Interface Science* 8 (2003) 137-144.
- [57] D.V. Leff, P.C. Ohara, J.R. Heath, W.M. Gelbart, Thermodynamic Control of Gold Nanocrystal Size: Experiment and Theory, *The Journal of Physical Chemistry* 99 (1995) 7036-7041.
- [58] L.K. Ono, D. Sudfeld, B.R. Cuenya, In situ gas-phase catalytic properties of TiC-supported size-selected gold nanoparticles synthesized by diblock copolymer encapsulation, *Surf. Sci.* 600 (2006) 5041-5050.
- [59] L. Shang, S. Dong, G.U. Nienhaus, Ultra-small fluorescent metal nanoclusters: Synthesis and biological applications, *Nano Today* 6 (2011) 401-418.
- [60] S. Qu, H. Yang, D. Ren, S. Kan, G. Zou, D. Li, M. Li, Magnetite Nanoparticles Prepared by Precipitation from Partially Reduced Ferric Chloride Aqueous Solutions, *Journal of Colloid and Interface Science* 215 (1999) 190-192.
- [61] H.H. Ingelsten, R. Bagwe, A. Palmqvist, M. Skoglundh, C. Svanberg, K. Holmberg, D.O. Shah, Kinetics of the formation of nano-sized platinum particles in water-in-oil microemulsions, *Journal of Colloid and Interface Science* 241 (2001) 104-111.
- [62] V. USKOKOVIĆ, M. DROFENIK, SYNTHESIS OF MATERIALS WITHIN REVERSE MICELLES, *Surface Review and Letters* 12 (2005) 239-277.
- [63] J.P. Wilcoxon, B.L. Abrams, Synthesis, structure and properties of metal nanoclusters, *Chemical Society reviews* 35 (2006) 1162-1194.
- [64] J.P. Wilcoxon, Method for the preparation of metal colloids in inverse micelles and product preferred by the method, Google Patents, 1992.
- [65] P. de la Iglesia, V.W. Jaeger, Y. Xi, J. Pfaendtner, L.D. Pozzo, Structure Characterization and Properties of Metal–Surfactant Complexes Dispersed in Organic Solvents, *Langmuir : the ACS journal of surfaces and colloids* 31 (2015) 9006-9016.
- [66] X. Lin, C. Sorensen, K. Klabunde, Digestive ripening, nanophase segregation and superlattice formation in gold nanocrystal colloids, *Journal of Nanoparticle Research* 2 (2000) 157-164.
- [67] M. Boutonnet, J. Kizling, P. Stenius, THE PREPARATION OF MONODISPERSE COLLOIDAL METAL PARTICLES FROM MICRO-EMULSIONS, *Colloids and Surfaces* 5 (1982) 209-225.
- [68] H. Hirai, Y. Nakao, N. Toshima, Preparation of Colloidal Rhodium in Poly(vinyl Alcohol) by Reduction with Methanol, *Journal of Macromolecular Science: Part A - Chemistry* 12 (1978) 1117-1141.
- [69] J.A. Lopez-Sanchez, N. Dimitratos, C. Hammond, G.L. Brett, L. Kesavan, S. White, P. Miedziak, R. Tiruvalam, R.L. Jenkins, A.F. Carley, D. Knight, C.J. Kiely, G.J. Hutchings, Facile removal of stabilizer-ligands from supported gold nanoparticles, *Nature chemistry* 3 (2011) 551-556.

- [70] N. Toshima, T. Yonezawa, Bimetallic nanoparticles - novel materials for chemical and physical applications, *New J. Chem.* 22 (1998) 1179-1201.
- [71] N. Toshima, T. Yonezawa, K. Kushihashi, Polymer-protected palladium-platinum bimetallic clusters: preparation, catalytic properties and structural considerations, *Journal of the Chemical Society, Faraday Transactions* 89 (1993) 2537-2543.
- [72] T. Yonezawa, N. Toshima, Mechanistic consideration of formation of polymer-protected nanoscopic bimetallic clusters, *Journal of the Chemical Society, Faraday Transactions* 91 (1995) 4111-4119.
- [73] M. Haruta, T. Kobayashi, H. Sano, N. Yamada, Novel gold catalysts for the oxidation of carbon monoxide at a temperature far below 0[deg]C, *Chem. Lett. (Jpn)* 16 (1987) 405-408.
- [74] H. Tsunoyama, N. Ichikuni, T. Tsukuda, Microfluidic Synthesis and Catalytic Application of PVP-Stabilized, ~1 nm Gold Clusters, *Langmuir : the ACS journal of surfaces and colloids* 24 (2008) 11327-11330.
- [75] (!!! INVALID CITATION !!! {}).
- [76] P. Pyykko, Relativistic effects in structural chemistry, *Chemical Reviews* 88 (1988) 563-594.
- [77] P. Pyykkö, Theoretical chemistry of gold, *Angewandte Chemie International Edition* 43 (2004) 4412-4456.
- [78] S. Palmal, S.K. Basiruddin, A.R. Maity, S.C. Ray, N.R. Jana, Thiol-Directed Synthesis of Highly Fluorescent Gold Clusters and Their Conversion into Stable Imaging Nanoprobes, *Chemistry – A European Journal* 19 (2013) 943-949.
- [79] R.L. Whetten, M.N. Shafiqullin, J.T. Khoury, T.G. Schaaff, I. Vezmar, M.M. Alvarez, A. Wilkinson, Crystal Structures of Molecular Gold Nanocrystal Arrays, *Accounts of Chemical Research* 32 (1999) 397-406.
- [80] H. Tsunoyama, Y. Negishi, T. Tsukuda, Chromatographic Isolation of "Missing" Au₅₅ Clusters Protected by Alkanethiolates, *Journal of the American Chemical Society* 128 (2006) 6036-6037.
- [81] T.G. Schaaff, G. Knight, M.N. Shafiqullin, R.F. Borkman, R.L. Whetten, Isolation and Selected Properties of a 10.4 kDa Gold:Glutathione Cluster Compound, *The Journal of Physical Chemistry B* 102 (1998) 10643-10646.
- [82] M. Walter, J. Akola, O. Lopez-Acevedo, P.D. Jadzinsky, G. Calero, C.J. Ackerson, R.L. Whetten, H. Gronbeck, H. Hakkinen, A unified view of ligand-protected gold clusters as superatom complexes, *Proceedings of the National Academy of Sciences of the United States of America* 105 (2008) 9157-9162.
- [83] K.J. Taylor, C.L. Pettiette-Hall, O. Cheshnovsky, R.E. Smalley, Ultraviolet photoelectron spectra of coinage metal clusters, *The Journal of Chemical Physics* 96 (1992) 3319-3329.
- [84] P. Pyykkö, Understanding the eighteen-electron rule, *Journal of Organometallic Chemistry* 691 (2006) 4336-4340.
- [85] B. Kiran, P. Jena, X. Li, A. Grubisic, S.T. Stokes, G. Ganteför, K.H. Bowen, R. Burgert, H. Schnöckel, Magic rule for Al_nH_m magic clusters, *Physical review letters* 98 (2007) 256802.
- [86] J. Hartig, A. Stößer, P. Hauser, H. Schnöckel, A Metalloid [Ga₂₃{N(SiMe₃)₂}₁₁] Cluster: The Jellium Model Put to Test, *Angewandte Chemie International Edition* 46 (2007) 1658-1662.
- [87] P.D. Jadzinsky, G. Calero, C.J. Ackerson, D.A. Bushnell, R.D. Kornberg, Structure of a thiol monolayer-protected gold nanoparticle at 1.1 Å resolution, *Science* 318 (2007) 430-433.
- [88] Y. Negishi, K. Nobusada, T. Tsukuda, Glutathione-Protected Gold Clusters Revisited: Bridging the Gap between Gold(I)-Thiolate Complexes and Thiolate-Protected Gold Nanocrystals, *Journal of the American Chemical Society* 127 (2005) 5261-5270.
- [89] J.M. Soler, M.R. Beltrán, K. Michaelian, I.L. Garzón, P. Ordejón, D. Sánchez-Portal, E. Artacho, Metallic bonding and cluster structure, *Physical Review B* 61 (2000) 5771-5780.
- [90] N.K. Chaki, Y. Negishi, H. Tsunoyama, Y. Shichibu, T. Tsukuda, Ubiquitous 8 and 29 kDa Gold:Alkanethiolate Cluster Compounds: Mass-Spectrometric Determination of Molecular Formulas and Structural Implications, *Journal of the American Chemical Society* 130 (2008) 8608-8610.
- [91] Z. Xu, F.S. Xiao, S.K. Purnell, O. Alexeev, S. Kawi, S.E. Deutsch, B.C. Gates, Size-dependent catalytic activity of supported metal clusters, *Nature* 372 (1994) 346-348.
- [92] D.-e. Jiang, W. Luo, M.L. Tiago, S. Dai, In search of a structural model for a thiolate-protected Au₃₈ cluster, *The Journal of Physical Chemistry C* 112 (2008) 13905-13910.

- [93] W.W. Xu, Y. Gao, X.C. Zeng, <div xmlns="http://www.w3.org/1999/xhtml">Unraveling structures of protection ligands on gold nanoparticle Au₆₈(SH)₃₂</div>, *Science Advances* 1 (2015).
- [94] M.W. Heaven, A. Dass, P.S. White, K.M. Holt, R.W. Murray, Crystal structure of the gold nanoparticle [N (C₈H₁₇)₄][Au₂₅ (SCH₂CH₂Ph)₁₈], *Journal of the American Chemical Society* 130 (2008) 3754-3755.
- [95] S. Antonello, M. Hesari, F. Polo, F. Maran, Electron transfer catalysis with monolayer protected Au(2)(5) clusters, *Nanoscale* 4 (2012) 5333-5342.
- [96] Y. Zhu, H. Qian, R. Jin, An atomic-level strategy for unraveling gold nanocatalysis from the perspective of Au(n)(SR)_m nanoclusters, *Chemistry* 16 (2010) 11455-11462.
- [97] R.H. Adnan, J.M.L. Madrdejós, A.S. Alotabi, G.F. Metha, G.G. Andersson, A Review of State of the Art in Phosphine Ligated Gold Clusters and Application in Catalysis, *Advanced Science* 9 (2022) 2105692.
- [98] <siegbahn-lecture.pdf>.
- [99] C.C. Chusuei, X. Lai, K.A. Davis, E.K. Bowers, J.P. Fackler, D.W. Goodman, A Nanoscale Model Catalyst Preparation: Solution Deposition of Phosphine-Stabilized Gold Clusters onto a Planar TiO₂(110) Support, *Langmuir : the ACS journal of surfaces and colloids* 17 (2001) 4113-4117.
- [100] F. Wen, U. Englert, B. Gutrath, U. Simon, Crystal Structure, Electrochemical and Optical Properties of [Au₉(PPh₃)₈](NO₃)₃, *European Journal of Inorganic Chemistry* 2008 (2008) 106-111.
- [101] M. Turner, V.B. Golovko, O.P. Vaughan, P. Abdulkin, A. Berenguer-Murcia, M.S. Tikhov, B.F. Johnson, R.M. Lambert, Selective oxidation with dioxygen by gold nanoparticle catalysts derived from 55-atom clusters, *Nature* 454 (2008) 981-983.
- [102] S. Hong, G. Shafai, M. Bertino, T.S. Rahman, Toward an Understanding of Ligand Selectivity in Nanocluster Synthesis, *The Journal of Physical Chemistry C* 115 (2011) 14478-14487.
- [103] J. Chen, Q.F. Zhang, T.A. Bonaccorso, P.G. Williard, L.S. Wang, Controlling gold nanoclusters by diphospine ligands, *Journal of the American Chemical Society* 136 (2014) 92-95.
- [104] S. Bhardwaj, R. Itteboina, T.K. Sau, Observing Ultra-Small Gold Cluster to Plasmonic Nanoparticle Evolution in a One-Pot Aqueous Synthesis, *ChemistrySelect* 1 (2016) 3091-3096.
- [105] I.V. Graf, J.W. Bacon, M.B. Consugar, M.E. Curley, L.N. Ito, L.H. Pignolet, Cluster chemistry on surfaces: Characterization and catalytic studies of phosphine-stabilized platinum-gold clusters on silica and alumina supports, *Inorganic Chemistry* 35 (1996) 689-694.
- [106] H. Yang, Y. Wang, J. Lei, L. Shi, X. Wu, V. Mäkinen, S. Lin, Z. Tang, J. He, H. Hakkinen, L. Zheng, N. Zheng, Ligand-stabilized Au₁₃Cu(x) (x = 2, 4, 8) bimetallic nanoclusters: ligand engineering to control the exposure of metal sites, *Journal of the American Chemical Society* 135 (2013) 9568-9571.
- [107] G. Schmid, M. Baumle, M. Geerkens, I. Heim, C. Osemann, T. Sawitowski, Current and future applications of nanoclusters, *Chemical Society reviews* 28 (1999) 179-185.
- [108] W. Yoshitake, Atomically precise cluster catalysis towards quantum controlled catalysts, *Science and Technology of Advanced Materials* 15 (2014) 063501.
- [109] S. Vajda, M.J. Pellin, J.P. Greeley, C.L. Marshall, L.A. Curtiss, G.A. Ballentine, J.W. Elam, S. Catillon-Mucherie, P.C. Redfern, F. Mehmood, P. Zapol, Subnanometre platinum clusters as highly active and selective catalysts for the oxidative dehydrogenation of propane, *Nature materials* 8 (2009) 213-216.
- [110] Y. Lei, F. Mehmood, S. Lee, J. Greeley, B. Lee, S. Seifert, R.E. Winans, J.W. Elam, R.J. Meyer, P.C. Redfern, D. Teschner, R. Schlogl, M.J. Pellin, L.A. Curtiss, S. Vajda, Increased silver activity for direct propylene epoxidation via subnanometer size effects, *Science* 328 (2010) 224-228.
- [111] L. D'Souza, M. Noeske, R.M. Richards, U. Kortz, Polyoxotungstate stabilized palladium, gold, and silver nanoclusters: a study of cluster stability, catalysis, and effects of the stabilizing anions, *J Colloid Interface Sci* 394 (2013) 157-165.
- [112] C. Kerpál, D.J. Harding, D.M. Rayner, J.T. Lyon, A. Fielicke, Far-IR Spectra and Structures of Small Cationic Ruthenium Clusters: Evidence for Cubic Motifs, *The Journal of Physical Chemistry C* 119 (2015) 10869-10875.

- [113] Y. Xia, Y. Xiong, B. Lim, S.E. Skrabalak, Shape-Controlled Synthesis of Metal Nanocrystals: Simple Chemistry Meets Complex Physics?, *Angewandte Chemie International Edition* 48 (2009) 60-103.
- [114] P.A. DeSario, J.J. Pietron, D.E. DeVantier, T.H. Brintlinger, R.M. Stroud, D.R. Rolison, Plasmonic enhancement of visible-light water splitting with Au-TiO₂ composite aerogels, *Nanoscale* 5 (2013) 8073-8083.
- [115] M. Chen, Y. Cai, Z. Yan, D.W. Goodman, On the origin of the unique properties of supported Au nanoparticles, *Journal of the American Chemical Society* 128 (2006) 6341-6346.
- [116] D.W. Goodman, M.S. Chen, COLL 448-Catalytically active gold: From nano-particles to ultra-thin films, *Abstracts of Papers of the American Chemical Society* 232 (2006).
- [117] Y. Negishi, T. Nakazaki, S. Maloa, S. Takano, Y. Niihori, W. Kurashige, S. Yamazoe, T. Tsukuda, H. Hakkinen, A Critical Size for Emergence of Nonbulk Electronic and Geometric Structures in Dodecanethiolate-Protected Au Clusters, *Journal of the American Chemical Society* 137 (2015) 1206-1212.
- [118] A. Wang, J. Li, T. Zhang, Heterogeneous single-atom catalysis, *Nature Reviews Chemistry* 2 (2018) 65-81.
- [119] R. Jin, G. Li, S. Sharma, Y. Li, X. Du, Toward Active-Site Tailoring in Heterogeneous Catalysis by Atomically Precise Metal Nanoclusters with Crystallographic Structures, *Chem Rev* 121 (2021) 567-648.
- [120] M. Haruta, Low-temperature oxidation of CO over gold supported on TiO₂, [agr]-Fe₂O₃, and Co₃O₄, *J. Catalys.* 144 (1993) 175-192.
- [121] N. Lopez, J.K. Nørskov, Catalytic CO Oxidation by a Gold Nanoparticle: A Density Functional Study, *Journal of the American Chemical Society* 124 (2002) 11262-11263.
- [122] Z. Wu, J. Chen, R. Jin, One-Pot Synthesis of Au₂₅(SG)₁₈ 2- and 4-nm Gold Nanoparticles and Comparison of Their Size-Dependent Properties, *Advanced Functional Materials* 21 (2011) 177-183.
- [123] S. Shirakawa, M. Osaki, Y. Nagai, Y.F. Nishimura, K. Dohmae, S.i. Matsumoto, H. Hirata, XAFS study on promoting effect of Au via NiO reduction in Au-Ni bimetallic clusters, *Catalysis Today*.
- [124] M. Akutsu, K. Koyasu, J. Atobe, N. Hosoya, K. Miyajima, M. Mitsui, A. Nakajima, Experimental and Theoretical Characterization of Aluminum-Based Binary Superatoms of Al₁₂X and Their Cluster Salts, *The Journal of Physical Chemistry A* 110 (2006) 12073-12076.
- [125] A.S. Alotabi, Y. Yin, A. Redaa, S. Tesana, G.F. Metha, G.G. Andersson, Cr₂O₃ layer inhibits agglomeration of phosphine-protected Au₉ clusters on TiO₂ films, *The Journal of Chemical Physics* 155 (2021) 164702.
- [126] A.S. Alotabi, Y. Yin, A. Redaa, S. Tesana, G.F. Metha, G.G. Andersson, Effect of TiO₂ Film Thickness on the Stability of Au₉ Clusters with a CrO_x Layer, *Nanomaterials* 12 (2022) 3218.
- [127] K. Maeda, K. Teramura, D. Lu, N. Saito, Y. Inoue, K. Domen, Noble-metal/Cr(2)O(3) core/shell nanoparticles as a cocatalyst for photocatalytic overall water splitting, *Angew Chem Int Ed Engl* 45 (2006) 7806-7809.
- [128] Q. Wang, K. Domen, Particulate Photocatalysts for Light-Driven Water Splitting: Mechanisms, Challenges, and Design Strategies, *Chemical Reviews* 120 (2020) 919-985.
- [129] T. Takata, C. Pan, M. Nakabayashi, N. Shibata, K. Domen, Fabrication of a Core-Shell-Type Photocatalyst via Photodeposition of Group IV and V Transition Metal Oxyhydroxides: An Effective Surface Modification Method for Overall Water Splitting, *Journal of the American Chemical Society* 137 (2015) 9627-9634.
- [130] A.M. Argo, B.C. Gates, MgO-supported Rh₆ and Ir₆: Structural characterization during the catalysis of ethene hydrogenation, *Journal of Physical Chemistry B* 107 (2003) 5519-5528.
- [131] B.C. Gates, Supported metal cluster catalysts, *Journal of Molecular Catalysis A: Chemical* 163 (2000) 55-65.
- [132] A. Kulkarni, R.J. Lobo-Lapidus, B.C. Gates, Metal clusters on supports: synthesis, structure, reactivity, and catalytic properties, *Chemical communications* 46 (2010) 5997-6015.
- [133] C. Moreno-Castilla, M.A. Salas-Peregrín, F.J. López-Garzón, Hydrogenation of carbon oxides by Ru/activated carbon catalysts obtained from Ru₃(CO)₁₂: effect of pretreatment on their dispersion, composition and activity, *Journal of Molecular Catalysis A: Chemical* 95 (1995) 223-233.

- [134] R. Pierantozzi, E.G. Valagene, A.F. Nordquist, P.N. Dyer, Support and cluster effects on synthesis gas conversion with supported ruthenium clusters, *Journal of Molecular Catalysis* 21 (1983) 189-202.
- [135] J.G. Shen, M. Ichikawa, Intrazeolite Anchoring of Co, Ru, and [Ru– Co] Carbonyl Clusters: Synthesis, Characterization, and Their Catalysis for CO Hydrogenation, *The Journal of Physical Chemistry B* 102 (1998) 5602-5613.
- [136] Z. Song, T. Cai, J.C. Hanson, J.A. Rodriguez, J. Hrbek, Structure and reactivity of Ru nanoparticles supported on modified graphite surfaces: A study of the model catalysts for ammonia synthesis, *Journal of the American Chemical Society* 126 (2004) 8576-8584.
- [137] W. Ouyang, M.J. Muñoz-Batista, A. Kubacka, R. Luque, M. Fernández-García, Enhancing photocatalytic performance of TiO₂ in H₂ evolution via Ru co-catalyst deposition, *Applied Catalysis B: Environmental* 238 (2018) 434-443.
- [138] G. Ding, S. Chu, D. Lin, R. He, Y. Jiang, Y. Lu, Coupling surfactant-free Ru nanoclusters with defect carbon for efficient pH-universal hydrogen evolution, *Catalysis Communications* 162 (2022) 106401.
- [139] L. Yang, P. Gao, J. Lu, W. Guo, Z. Zhuang, Q. Wang, W. Li, Z. Feng, Mechanism analysis of Au, Ru noble metal clusters modified on TiO₂ (101) to intensify overall photocatalytic water splitting, *RSC advances* 10 (2020) 20654-20664.
- [140] S.M. Kozlov, H.A. Aleksandrov, J. Goniakowski, K.M. Neyman, Effect of MgO(100) support on structure and properties of Pd and Pt nanoparticles with 49-155 atoms, *J Chem Phys* 139 (2013) 084701.
- [141] I.X. Green, W. Tang, M. Neurock, J.T. Yates, Jr., Spectroscopic observation of dual catalytic sites during oxidation of CO on a Au/TiO₂ catalyst, *Science* 333 (2011) 736-739.
- [142] H. Häkkinen, S. Abbet, A. Sanchez, U. Heiz, U. Landman, Structural, Electronic, and Impurity-Doping Effects in Nanoscale Chemistry: Supported Gold Nanoclusters, *Angewandte Chemie International Edition* 42 (2003) 1297-1300.
- [143] K. Maeda, A. Xiong, T. Yoshinaga, T. Ikeda, N. Sakamoto, T. Hisatomi, M. Takashima, D. Lu, M. Kanehara, T. Setoyama, T. Teranishi, K. Domen, Photocatalytic Overall Water Splitting Promoted by Two Different Cocatalysts for Hydrogen and Oxygen Evolution under Visible Light, *Angewandte Chemie International Edition* 49 (2010) 4096-4099.
- [144] A. Xiong, T. Yoshinaga, T. Ikeda, M. Takashima, T. Hisatomi, K. Maeda, T. Setoyama, T. Teranishi, K. Domen, Effect of Hydrogen and Oxygen Evolution Cocatalysts on Photocatalytic Activity of GaN:ZnO, *European Journal of Inorganic Chemistry* 2014 (2014) 767-772.
- [145] T. Yoshinaga, M. Saruyama, A. Xiong, Y. Ham, Y. Kuang, R. Niishiro, S. Akiyama, M. Sakamoto, T. Hisatomi, K. Domen, T. Teranishi, Boosting photocatalytic overall water splitting by Co doping into Mn₃O₄ nanoparticles as oxygen evolution cocatalysts, *Nanoscale* 10 (2018) 10420-10427.
- [146] D. Wang, R. Li, J. Zhu, J. Shi, J. Han, X. Zong, C. Li, Photocatalytic Water Oxidation on BiVO₄ with the Electrocatalyst as an Oxidation Cocatalyst: Essential Relations between Electrocatalyst and Photocatalyst, *The Journal of Physical Chemistry C* 116 (2012) 5082-5089.
- [147] R.H. Adnan, G.G. Andersson, M.I.J. Polson, G.F. Metha, V.B. Golovko, Factors influencing the catalytic oxidation of benzyl alcohol using supported phosphine-capped gold nanoparticles, *Catal. Sci. Technol.* 5 (2015) 1323-1333.
- [148] M. Chen, A. Santra, D. Goodman, Structure of thin SiO₂ films grown on Mo (112), *Physical Review B* 69 (2004) 155404.
- [149] Z. Wu, R. Jin, On the ligand's role in the fluorescence of gold nanoclusters, *Nano letters* 10 (2010) 2568-2573.
- [150] S.V. Ingale, P.B. Wagh, A.K. Tripathi, A.S. Dudwadkar, S.S. Gamre, P.T. Rao, I.K. Singh, S.C. Gupta, Photo catalytic oxidation of TNT using TiO₂-SiO₂ nano-composite aerogel catalyst prepared using sol-gel process, *Journal of Sol-Gel Science and Technology* 58 (2011) 682-688.
- [151] Ö. Metin, S. Özkar, S. Sun, Monodisperse nickel nanoparticles supported on SiO₂ as an effective catalyst for the hydrolysis of ammonia-borane, *Nano Research* 3 (2010) 676-684.
- [152] G. Chen, H. Yang, B. Wu, Y. Zheng, N. Zheng, Supported monodisperse Pt nanoparticles from [Pt₃(CO)₃(μ₂-CO)₃]₅(²⁻) clusters for investigating support-Pt interface effect in catalysis, *Dalton transactions* 42 (2013) 12699-12705.
- [153] S.H. Tamboli, R.B. Patil, S.V. Kamat, V. Puri, R.K. Puri, Modification of optical properties of MgO thin films by vapour chopping, *J. Alloy. Compd.* 477 (2009) 855-859.

- [154] H. Heidari, M. Abedini, A. Nemati, M.M. Amini, Nanocrystalline Magnesium Oxide as a Versatile Heterogeneous Catalyst for the Meerwein–Ponndorf–Verley Reduction of Cyclohexanone into Cyclohexanol: Effect of Preparation Method of Magnesium Oxide on Yield, *Catalysis Letters* 130 (2009) 266-270.
- [155] M. Julkapli Nurhidayatullaili, S. Bagheri, Magnesium oxide as a heterogeneous catalyst support, *Reviews in Inorganic Chemistry*, 2016, pp. 1.
- [156] P.B. Devaraja, D.N. Avadhani, H. Nagabhushana, S.C. Prashantha, S.C. Sharma, B.M. Nagabhushana, H.P. Nagaswarupa, B.D. Prasad, Luminescence properties of MgO: Fe³⁺ nanopowders for WLEDs under NUV excitation prepared via propellant combustion route, *Journal of Radiation Research and Applied Sciences* 8 (2015) 362-373.
- [157] A. Parmaliana, F. Arena, F. Frusteri, N. Giordano, Temperature-programmed reduction study of NiO-MgO interactions in magnesia-supported Ni catalysts and NiO-MgO physical mixture, *Journal of the Chemical Society, Faraday Transactions* 86 (1990) 2663-2669.
- [158] S. Abbet, A.M. Ferrari, L. Giordano, G. Pacchioni, H. Häkkinen, U. Landman, U. Heiz, Pd₁/MgO(1 0 0): a model system in nanocatalysis, *Surface Science* 514 (2002) 249-255.
- [159] M. Moseler, M. Walter, B. Yoon, U. Landman, V. Habibpour, C. Harding, S. Kunz, U. Heiz, Oxidation State and Symmetry of Magnesia-Supported Pd₁₃O_x Nanocatalysts Influence Activation Barriers of CO Oxidation, *Journal of the American Chemical Society* 134 (2012) 7690-7699.
- [160] G. Rossi, L. Anghinolfi, R. Ferrando, F. Nita, G. Barcaro, A. Fortunelli, Prediction of the structures of free and oxide-supported nanoparticles by means of atomistic approaches: the benchmark case of nickel clusters, *Physical chemistry chemical physics : PCCP* 12 (2010) 8564-8570.
- [161] M. Smerieri, J. Pal, L. Savio, L. Vattuone, R. Ferrando, S. Tosoni, L. Giordano, G. Pacchioni, M. Rocca, Spontaneous Oxidation of Ni Nanoclusters on MgO Monolayers Induced by Segregation of Interfacial Oxygen, *The Journal of Physical Chemistry Letters* 6 (2015) 3104-3109.
- [162] J. Guzman, B.C. Gates, Simultaneous Presence of Cationic and Reduced Gold in Functioning MgO-Supported CO Oxidation Catalysts: Evidence from X-ray Absorption Spectroscopy, *The Journal of Physical Chemistry B* 106 (2002) 7659-7665.
- [163] M. Ni, M.K.H. Leung, D.Y.C. Leung, K. Sumathy, A review and recent developments in photocatalytic water-splitting using TiO₂ for hydrogen production, *Renewable and Sustainable Energy Reviews* 11 (2007) 401-425.
- [164] A. Kongkanand, K. Tvrdy, K. Takechi, M. Kuno, P.V. Kamat, Quantum dot solar cells. Tuning photoresponse through size and shape control of CdSe-TiO₂ architecture, *Journal of the American Chemical Society* 130 (2008) 4007-4015.
- [165] M.G. Kibria, H.P.T. Nguyen, K. Cui, S. Zhao, D. Liu, H. Guo, M.L. Trudeau, S. Paradis, A.-R. Hakima, Z. Mi, One-Step Overall Water Splitting under Visible Light Using Multiband InGa_N/Ga_N Nanowire Heterostructures, *ACS Nano* 7 (2013) 7886-7893.
- [166] B. Samuneva, V. Kozhukharov, C. Trapalis, R. Kranold, Sol-gel processing of titanium-containing thin coatings, *Journal of Materials Science* 28 (1993) 2353-2360.
- [167] B.A. Morales, O. Novaro, T. López, E. Sánchez, R. Gómez, Effect of hydrolysis catalyst on the Ti deficiency and crystallite size of sol-gel-TiO₂ crystalline phases, *Journal of Materials Research* 10 (1995) 2788-2796.
- [168] S. Mahshid, M. Askari, M.S. Ghamsari, Synthesis of TiO₂ nanoparticles by hydrolysis and peptization of titanium isopropoxide solution, *Journal of Materials Processing Technology* 189 (2007) 296-300.
- [169] Y.L. Brama, Y. Sun, S.R.K. Dangeti, M. Mujahid, Response of sputtered titanium films on silicon to thermal oxidation, *Surface and Coatings Technology* 195 (2005) 189-197.
- [170] C.J. Tavares, J. Vieira, L. Rebouta, G. Hungerford, P. Coutinho, V. Teixeira, J.O. Carneiro, A.J. Fernandes, Reactive sputtering deposition of photocatalytic TiO₂ thin films on glass substrates, *Materials Science and Engineering: B* 138 (2007) 139-143.
- [171] I. Hadjoub, T. Touam, A. Chelouche, M. Atoui, J. Solard, M. Chakaroun, A. Fischer, A. Boudrioua, L.H. Peng, Post-deposition annealing effect on RF-sputtered TiO₂ thin-film properties for photonic applications, *Appl. Phys. A-Mater. Sci. Process.* 122 (2016) 8.
- [172] S. Mahshid, M. Askari, M. Sasani Ghamsari, N. Afshar, S. Lahuti, Mixed-phase TiO₂ nanoparticles preparation using sol-gel method, *J. Alloy. Compd.* 478 (2009) 586-589.

- [173] D. Reyes-Coronado, G. Rodriguez-Gattorno, M.E. Espinosa-Pesqueira, C. Cab, R. de Coss, G. Oskam, Phase-pure TiO₂ nanoparticles: anatase, brookite and rutile, *Nanotechnology* 19 (2008) 145605.
- [174] Z.Y. Li, N.P. Young, M. Di Vece, S. Palomba, R.E. Palmer, A.L. Bleloch, B.C. Curley, R.L. Johnston, J. Jiang, J. Yuan, Three-dimensional atomic-scale structure of size-selected gold nanoclusters, *Nature* 451 (2008) 46-48.
- [175] E. Scolan, C. Sanchez, Synthesis and characterization of surface-protected nanocrystalline titania particles, *Chemistry of Materials* 10 (1998) 3217-3223.
- [176] W.-N. Wang, W.-J. An, B. Ramalingam, S. Mukherjee, D.M. Niedzwiedzki, S. Gangopadhyay, P. Biswas, Size and Structure Matter: Enhanced CO₂ Photoreduction Efficiency by Size-Resolved Ultrafine Pt Nanoparticles on TiO₂ Single Crystals, *Journal of the American Chemical Society* 134 (2012) 11276-11281.
- [177] F. Gao, D.W. Goodman, Model catalysts: simulating the complexities of heterogeneous catalysts, *Annual review of physical chemistry* 63 (2012) 265-286.
- [178] C.-C. Kao, S.-C. Tsai, Y.-W. Chung, Surface electronic properties and CO hydrogenation activity of nickel deposited on rutile TiO₂(100) as a model supported catalyst, *Journal of Catalysis* 73 (1982) 136-146.
- [179] D.W. Goodman, "Catalytically active Au on Titania:" yet another example of a strong metal support interaction (SMSI)?, *Catalysis Letters* 99 (2004) 1-4.
- [180] A. Vijay, G. Mills, H. Metiu, Adsorption of gold on stoichiometric and reduced rutile TiO₂ (110) surfaces, *The Journal of Chemical Physics* 118 (2003) 6536-6551.
- [181] M. Chen, D.W. Goodman, Catalytically active gold on ordered titania supports, *Chemical Society reviews* 37 (2008) 1860-1870.
- [182] M.M. Hasan, A.S.M.A. Haseeb, R. Saidur, H.H. Masjuki, M. Hamdi, Influence of substrate and annealing temperatures on optical properties of RF-sputtered TiO₂ thin films, *Optical Materials* 32 (2010) 690-695.
- [183] L. Dreesen, F. Cecchet, S. Lucas, DC Magnetron Sputtering Deposition of Titanium Oxide Nanoparticles: Influence of Temperature, Pressure and Deposition Time on the Deposited Layer Morphology, the Wetting and Optical Surface Properties, *Plasma Processes and Polymers* 6 (2009) S849-S854.
- [184] V. Singh, I.J. Beltran, J.C. Ribot, P. Nagpal, Photocatalysis deconstructed: design of a new selective catalyst for artificial photosynthesis, *Nano letters* 14 (2014) 597-603.
- [185] G.G. Andersson, V.B. Golovko, J.F. Alvino, T. Bennett, O. Wrede, S.M. Mejia, H.S. Al Qahtani, R. Adnan, N. Gunby, D.P. Anderson, G.F. Metha, Phosphine-stabilised Au-9 clusters interacting with titania and silica surfaces: The first evidence for the density of states signature of the support-immobilised cluster, *J. Chem. Phys.* 141 (2014) 12.
- [186] V.D. Borman, M.A. Pushkin, V.N. Tronin, V.I. Troyan, Evolution of the electronic properties of transition metal nanoclusters on graphite surface, *Journal of Experimental and Theoretical Physics* 110 (2010) 1005-1025.
- [187] Z. Zhang, W. Tang, M. Neurock, J.T. Yates, Electric Charge of Single Au Atoms Adsorbed on TiO₂(110) and Associated Band Bending, *The Journal of Physical Chemistry C* 115 (2011) 23848-23853.
- [188] T.A. Baker, X. Liu, C.M. Friend, The mystery of gold's chemical activity: local bonding, morphology and reactivity of atomic oxygen, *Physical chemistry chemical physics : PCCP* 13 (2011) 34-46.
- [189] D.P. Anderson, R.H. Adnan, J.F. Alvino, O. Shipper, B. Donoeva, J.Y. Ruzicka, H. Al Qahtani, H.H. Harris, B. Cowie, J.B. Aitken, V.B. Golovko, G.F. Metha, G.G. Andersson, Chemically synthesised atomically precise gold clusters deposited and activated on titania. Part II, *Physical chemistry chemical physics : PCCP* 15 (2013) 14806-14813.
- [190] S.D. Sartale, A.A. Ansari, S.J. Rezvani, Influence of Ti film thickness and oxidation temperature on TiO₂ thin film formation via thermal oxidation of sputtered Ti film, *Materials Science in Semiconductor Processing* 16 (2013) 2005-2012.
- [191] J.W. Mai, W. Liu, J.L. Qiu, F.J. Wu, H.F. Liu, W.Y. Zhou, Y.P. Fang, S.T. Zhang, Characterization and Enhanced Visible-Light Photocatalytic Properties of {001} Facets-Exposed TiO₂-Reduced Graphene Oxide Nanocomposites, *J. Nanosci. Nanotechnol.* 15 (2015) 4870-4876.

- [192] N. ARSHI, J. LU, C.G. LEE, J.H. YOON, B.H. KOO, F. AHMED, Thickness effect on properties of titanium film deposited by d.c. magnetron sputtering and electron beam evaporation techniques, *Bulletin of Materials Science* 36 (2013) 807-812.
- [193] L. Liu, B. Qiao, Y. Ma, J. Zhang, Y. Deng, Ferric hydroxide supported gold subnano clusters or quantum dots: enhanced catalytic performance in chemoselective hydrogenation, *Dalton transactions* (2008) 2542-2548.
- [194] B.B. Das, G.R. Rупpa, Sol-gel synthesis, crystal structure, and characterization of $Y_xBi_{2-x}Cd_{4-3x}O_7$ ($0.05 \leq x \leq 0.35$) nano-oxides, *Journal of Sol-Gel Science and Technology* 79 (2016) 596-605.
- [195] M. Bersani, K. Gupta, A.K. Mishra, R. Lanza, S.F.R. Taylor, H.U. Islam, N. Hollingsworth, C. Hardacre, N.H. de Leeuw, J.A. Darr, Combined EXAFS, XRD, DRIFTS, and DFT Study of Nano Copper Based Catalysts for CO₂ Hydrogenation, *ACS Catal.* 6 (2016) 5823-5833.
- [196] H.S. Al Qahtani, K. Kimoto, T. Bennett, J.F. Alvino, G.G. Andersson, G.F. Metha, V.B. Golovko, T. Sasaki, T. Nakayama, Atomically resolved structure of ligand-protected Au₉ clusters on TiO₂ nanosheets using aberration-corrected STEM, *The Journal of chemical physics* 144 (2016) 114703.
- [197] O. Stein, J. Ankri, M. Asscher, Surface diffusion of gold nanoclusters on Ru(0001): effects of cluster size, surface defects and adsorbed oxygen atoms, *Physical chemistry chemical physics : PCCP* 15 (2013) 13506-13512.
- [198] R.M. Rioux, H. Song, J.D. Hoefelmeyer, P. Yang, G.A. Somorjai, High-surface-area catalyst design: Synthesis, characterization, and reaction studies of platinum nanoparticles in mesoporous SBA-15 silica, *Journal of Physical Chemistry B* 109 (2005) 2192-2202.
- [199] S. Kunz, K. Hartl, M. Nesselberger, F.F. Schweinberger, G. Kwon, M. Hanzlik, K.J. Mayrhofer, U. Heiz, M. Arenz, Size-selected clusters as heterogeneous model catalysts under applied reaction conditions, *Physical chemistry chemical physics : PCCP* 12 (2010) 10288-10291.
- [200] T. Lee, J. Liu, N.-P. Chen, R.P. Andres, D.B. Janes, R. Reifemberger, Electronic Properties of Metallic Nanoclusters on Semiconductor Surfaces: Implications for Nanoelectronic Device Applications, *Journal of Nanoparticle Research* 2 (2000) 345-362.
- [201] X.M. Hu, P. von Blanckenhagen, Application of scanning tunneling microscopy to aluminum nanocluster deposition on silicon, *J. Vac. Sci. Technol. B* 17 (1999) 265-268.
- [202] S. Harinipriya, M.V. Sangaranarayanan, Stability of Scanning Tunneling Microscopy Tip-Induced Bimetallic Nanoclusters: Influence of Hardness and Composition on the Cohesive Energies, *The Journal of Physical Chemistry B* 108 (2004) 13944-13947.
- [203] M.J.J. Jak, C. Konstapel, A. van Kreuningen, J. Verhoeven, J.W.M. Frenken, Scanning tunnelling microscopy study of the growth of small palladium particles on TiO₂(110), *Surface Science* 457 (2000) 295-310.
- [204] Y. Fukamori, M. König, B. Yoon, B. Wang, F. Esch, U. Heiz, U. Landman, Fundamental Insight into the Substrate-Dependent Ripening of Monodisperse Clusters, *ChemCatChem* 5 (2013) 3330-3341.
- [205] A. Howard, C.E.J. Mitchell, R.G. Egdell, Real time STM observation of Ostwald ripening of Pd nanoparticles on TiO₂(1 1 0) at elevated temperature, *Surface Science* 515 (2002) L504-L508.
- [206] J.D. Fuhr, A. Saul, J.O. Sofo, Scanning tunneling microscopy chemical signature of point defects on the MoS₂(0001) surface, *Physical Review Letters* 92 (2004) 4.
- [207] F. Sedona, S. Agnoli, M. Fanetti, I. Kholmanov, E. Cavaliere, L. Gavioli, G. Granozzi, Ordered Arrays of Au Nanoclusters by TiO_x Ultrathin Templates on Pt(111), *The Journal of Physical Chemistry C* 111 (2007) 8024-8029.
- [208] B. Qu, J.-H. Hu, H. Li, W.-J. Li, M.-L. Huang, Q.-H. Wu, Formation of Au nanocluster ordered array on Si(111)-7 × 7 surface, *Surface and Interface Analysis* 47 (2015) 926-929.
- [209] H. Hövel, I. Barke, Morphology and electronic structure of gold clusters on graphite: Scanning-tunneling techniques and photoemission, *Progress in Surface Science* 81 (2006) 53-111.
- [210] D. Fujita, K. Ohnishi, T. Ohgi, Discrete charging effects in gold nanoclusters grown on self-assembled monolayers, *Science and Technology of Advanced Materials* 3 (2002) 283-287.
- [211] M. Rastei, J. Bucher, P. Ignatiev, V. Stepanyuk, P. Bruno, Surface electronic states in Co nanoclusters on Au (111): Scanning tunneling spectroscopy measurements and ab initio calculations, *Physical Review B* 75 (2007) 045436.
- [212] A. Bettac, L. Köller, V. Rank, K.H. Meiwes-Broer, Scanning tunneling spectroscopy on deposited platinum clusters, *Surface Science* 402-404 (1998) 475-479.

- [213] C.M. Wang, V. Shutthanandan, Y. Zhang, S. Thevuthasan, G. Duscher, Atomic resolution imaging of Au nanocluster dispersed in TiO₂, SrTiO₃, and MgO, *Journal of the American Ceramic Society* 88 (2005) 3184-3191.
- [214] H.-J. Freund, G. Pacchioni, Oxide ultra-thin films on metals: new materials for the design of supported metal catalysts, *Chemical Society reviews* 37 (2008) 2224-2242.
- [215] A.A. Herzing, C.J. Kiely, A.F. Carley, P. Landon, G.J. Hutchings, Identification of active gold nanoclusters on iron oxide supports for CO oxidation, *Science* 321 (2008) 1331-1335.
- [216] C.M. Wang, V. Shutthanandan, Y. Zhang, S. Thevuthasan, L. Thomas, W.J. Weber, G. Duscher, Atomic level imaging of Au nanocluster dispersed in TiO₂ and SrTiO₃, *Nuclear Instruments and Methods in Physics Research Section B: Beam Interactions with Materials and Atoms* 242 (2006) 380-382.
- [217] P.E. Batson, Motion of Gold Atoms on Carbon in the Aberration-Corrected STEM, *Microscopy and Microanalysis* 14 (2008) 89-97.
- [218] C. Bosch-Navarro, Z.P.L. Laker, H.R. Thomas, A.J. Marsden, J. Sloan, N.R. Wilson, J.P. Rourke, Covalently Binding Atomically Designed Au₉ Clusters to Chemically Modified Graphene, *Angewandte Chemie International Edition* (2015) n/a-n/a.
- [219] L.D. Marks, Experimental studies of small particle structures, *Reports on Progress in Physics* 57 (1994) 603.
- [220] P.E. Batson, N. Dellby, O.L. Krivanek, Sub-angstrom resolution using aberration corrected electron optics, *Nature* 418 (2002) 617-620.
- [221] D. Bahena, N. Bhattarai, U. Santiago, A. Tlahuice, A. Ponce, S.B.H. Bach, B. Yoon, R.L. Whetten, U. Landman, M. Jose-Yacaman, STEM Electron Diffraction and High-Resolution Images Used in the Determination of the Crystal Structure of the Au₁₄₄(SR)₆₀ Cluster, *The Journal of Physical Chemistry Letters* 4 (2013) 975-981.
- [222] Y. Iwasawa, X-ray absorption fine structure for catalysts and surfaces, World Scientific 1996.
- [223] J. Liu, K.S. Krishna, Y.B. Losovyj, S. Chattopadhyay, N. Lozova, J.T. Miller, J.J. Spivey, C.S. Kumar, Ligand-stabilized and atomically precise gold nanocluster catalysis: a case study for correlating fundamental electronic properties with catalysis, *Chemistry* 19 (2013) 10201-10208.
- [224] L. Sciortino, F. Giannici, A. Martorana, A.M. Ruggirello, V.T. Liveri, G. Portale, M.P. Casaletto, A. Longo, Structural Characterization of Surfactant-Coated Bimetallic Cobalt/Nickel Nanoclusters by XPS, EXAFS, WAXS, and SAXS, *The Journal of Physical Chemistry C* 115 (2011) 6360-6366.
- [225] S.L. Christensen, M.A. MacDonald, A. Chatt, P. Zhang, H. Qian, R. Jin, Dopant location, local structure, and electronic properties of Au₂₄Pt (SR)₁₈ nanoclusters, *The Journal of Physical Chemistry C* 116 (2012) 26932-26937.
- [226] A.M. van der Eerden, T. Visser, T.A. Nijhuis, Y. Ikeda, M. Lepage, D.C. Koningsberger, B.M. Weckhuysen, Atomic XAFS as a tool to probe the electronic properties of supported noble metal nanoclusters, *Journal of the American Chemical Society* 127 (2005) 3272-3273.
- [227] M. Tada, S. Murata, T. Asakoka, K. Hiroshima, K. Okumura, H. Tanida, T. Uruga, H. Nakanishi, S.-i. Matsumoto, Y. Inada, M. Nomura, Y. Iwasawa, In Situ Time-Resolved Dynamic Surface Events on the Pt/C Cathode in a Fuel Cell under Operando Conditions, *Angewandte Chemie International Edition* 46 (2007) 4310-4315.
- [228] R. Toyoshima, H. Kondoh, In-situ observations of catalytic surface reactions with soft x-rays under working conditions, *Journal of Physics: Condensed Matter* 27 (2015) 083003.
- [229] R.M. Feenstra, Scanning tunneling spectroscopy, *Surface science* 299 (1994) 965-979.
- [230] A. Yu, S. Li, G. Czap, W. Ho, Tunneling-Electron-Induced Light Emission from Single Gold Nanoclusters, *Nano letters* 16 (2016) 5433-5436.
- [231] M. Valden, Onset of Catalytic Activity of Gold Clusters on Titania with the Appearance of Nonmetallic Properties, *Science* 281 (1998) 1647-1650.
- [232] C. Battistoni, G. Mattocono, F. Cariati, L. Naldini, A. Sgamellotti, XPS photoelectron spectra of cluster compounds of gold, *Inorganica Chimica Acta* 24 (1977) 207-210.
- [233] E. McCafferty, J.P. Wightman, Determination of the concentration of surface hydroxyl groups on metal oxide films by a quantitative XPS method, *Surface and Interface Analysis* 26 (1998) 549-564.
- [234] J.T. Mayer, U. Diebold, T.E. Madey, E. Garfunkel, Titanium and reduced titania overlayers on titanium dioxide(110), *Journal of Electron Spectroscopy and Related Phenomena* 73 (1995) 1-11.

- [235] D.P. Anderson, J.F. Alvino, A. Gentleman, H. Al Qahtani, L. Thomsen, M.I.J. Polson, G.F. Metha, V.B. Golovko, G.G. Andersson, Chemically-synthesised, atomically-precise gold clusters deposited and activated on titania, *Physical Chemistry Chemical Physics* 15 (2013) 3917-3929.
- [236] X.Y. Xin, T. Xu, J. Yin, L. Wang, C.Y. Wang, Management on the location and concentration of Ti³⁺ in anatase TiO₂ for defects-induced visible-light photocatalysis, *Appl. Catal. B-Environ.* 176 (2015) 354-362.
- [237] S. Zhao, Y. Zhou, K. Zhao, Z. Liu, P. Han, S. Wang, W. Xiang, Z. Chen, H. Lü, B. Cheng, Violet luminescence emitted from Ag-nanocluster doped ZnO thin films grown on fused quartz substrates by pulsed laser deposition, *Physica B: Condensed Matter* 373 (2006) 154-156.
- [238] S. DiCenzo, S. Berry, E. Hartford, Photoelectron spectroscopy of single-size Au clusters collected on a substrate, *Physical Review B* 38 (1988) 8465-8468.
- [239] S. Hajati, V. Zaporozhchenko, F. Faupel, S. Tougaard, Characterization of Au nano-cluster formation on and diffusion in polystyrene using XPS peak shape analysis, *Surface science* 601 (2007) 3261-3267.
- [240] F. Durap, M. Zahmakıran, S. Özkar, Water soluble laurate-stabilized ruthenium (0) nanoclusters catalyst for hydrogen generation from the hydrolysis of ammonia-borane: high activity and long lifetime, *international journal of hydrogen energy* 34 (2009) 7223-7230.
- [241] Z. Jiang, W. Zhang, L. Jin, X. Yang, F. Xu, J. Zhu, W. Huang, Direct XPS Evidence for Charge Transfer from a Reduced Rutile TiO₂(110) Surface to Au Clusters, *The Journal of Physical Chemistry C* 111 (2007) 12434-12439.
- [242] J.W. Niemantsverdriet, *Spectroscopy in catalysis : an introduction*, Weinheim ; New York : VCH, Weinheim ; New York, 1993.
- [243] H. Morgner, The Characterization of Liquid and Solid Surfaces with Metastable Helium Atoms, in: B. Benjamin, W. Herbert (Eds.), *Advances In Atomic, Molecular, and Optical Physics*, Academic Press 2000, pp. 387-488.
- [244] J.F. Moulder, J. Chastain, *Handbook of X-ray Photoelectron Spectroscopy: A Reference Book of Standard Spectra for Identification and Interpretation of XPS Data*, Physical Electronics Division, Perkin-Elmer Corporation 1992.
- [245] S.M. Sze, *The Physics of Semiconductor Devices*, Springer Proceedings in Physics (2019).
- [246] Y. Harada, S. Masuda, H. Ozaki, Electron Spectroscopy Using Metastable Atoms as Probes for Solid Surfaces, *Chemical Reviews* 97 (1997) 1897-1952.
- [247] H. Morgner, The quantitative characterization of liquid and solid surfaces with metastable helium atoms, 1999.
- [248] H. Morgner, The Characterization of Liquid and Solid Surfaces with Metastable Helium Atoms, in: B. Bederson, H. Walther (Eds.), *Advances In Atomic, Molecular, and Optical Physics*, Academic Press 2000, pp. 387-488.
- [249] L.N. Kantorovich, A.L. Shluger, P.V. Sushko, A.M. Stoneham, The prediction of metastable impact electronic spectra (MIES): perfect and defective MgO(001) surfaces by state-of-the-art methods, *Surface Science* 444 (2000) 31-51.
- [250] D.A. Skoog, F.J. Holler, S.R. Crouch, *Principles of Instrumental Analysis*, Cengage Learning 2017.
- [251] A. Barron, A. Agrawal, *Physical Methods in Chemistry and Nano Science. Volume 5: Molecular and Solid State Structure*, MiDAS Green Innovation, Limited 2020.
- [252] P.B. Hirsch, A. Howie, *Electron Microscopy of Thin Crystals*, R. E. Krieger Publishing Company 1977.
- [253] N.R. Wilson, J.V. Macpherson, Carbon nanotube tips for atomic force microscopy, *Nature nanotechnology* 4 (2009) 483-491.
- [254] P. Eaton, P. West, *Atomic Force Microscopy*, OUP Oxford 2010.
- [255] A.N. Shipway, E. Katz, I. Willner, Nanoparticle arrays on surfaces for electronic, optical, and sensor applications, *Chemphyschem : a European journal of chemical physics and physical chemistry* 1 (2000) 18-52.
- [256] M. Pelaez, N.T. Nolan, S.C. Pillai, M.K. Seery, P. Falaras, A.G. Kontos, P.S. Dunlop, J.W. Hamilton, J.A. Byrne, K. O'shea, A review on the visible light active titanium dioxide photocatalysts for environmental applications, *Applied Catalysis B: Environmental* 125 (2012) 331-349.
- [257] M. Cargnello, T.R. Gordon, C.B. Murray, Solution-Phase Synthesis of Titanium Dioxide Nanoparticles and Nanocrystals, *Chemical Reviews* 114 (2014) 9319-9345.

- [258] B. Mahltig, H. Böttcher, K. Rauch, U. Dieckmann, R. Nitsche, T. Fritz, Optimized UV protecting coatings by combination of organic and inorganic UV absorbers, *Thin Solid Films* 485 (2005) 108-114.
- [259] M. Pelaez, N.T. Nolan, S.C. Pillai, M.K. Seery, P. Falaras, A.G. Kontos, P.S.M. Dunlop, J.W.J. Hamilton, J.A. Byrne, K. O'Shea, M.H. Entezari, D.D. Dionysiou, A review on the visible light active titanium dioxide photocatalysts for environmental applications, *Applied Catalysis B: Environmental* 125 (2012) 331-349.
- [260] M.A. Hossain, M. Rahman, A Review of Nano Particle Usage on Textile Material against Ultra Violet Radiation, *Journal of Textile Science and Technology* 1 (2015) 93.
- [261] V.A. Versteeg, C.T. Avedisian, R. Raj, Metalorganic chemical vapor deposition by pulsed liquid injection using an ultrasonic nozzle: titanium dioxide on sapphire from titanium (IV) isopropoxide, *Journal of the American Ceramic Society* 78 (1995) 2763-2768.
- [262] L. Bergamonti, I. Alfieri, A. Lorenzi, A. Montenero, G. Predieri, R. Di Maggio, F. Girardi, L. Lazzarini, P.P. Lottici, Characterization and photocatalytic activity of TiO₂ by sol-gel in acid and basic environments, *Journal of Sol-Gel Science and Technology* 73 (2015) 91-102.
- [263] V. Pore, A. Rahtu, M. Leskelä, M. Ritala, T. Sajavaara, J. Keinonen, Atomic Layer Deposition of Photocatalytic TiO₂ Thin Films from Titanium Tetramethoxide and Water, *Chemical Vapor Deposition* 10 (2004) 143-148.
- [264] L. Chen, M.E. Graham, G. Li, K.A. Gray, Fabricating highly active mixed phase TiO₂ photocatalysts by reactive DC magnetron sputter deposition, *Thin Solid Films* 515 (2006) 1176-1181.
- [265] J. Carter, P. Shah, E. Nowicka, S. Freakley, D. Morgan, S. Golunski, G. Hutchings, Enhanced Activity and Stability of Gold/Ceria-Titania for the Low-Temperature Water-Gas Shift Reaction, *Frontiers in Chemistry* 7 (2019).
- [266] G. Krishnan, N. Eom, R.M. Kirk, V.B. Golovko, G.F. Metha, G.G. Andersson, Investigation of Phosphine Ligand Protected Au₁₃ Clusters on Defect Rich Titania, *The Journal of Physical Chemistry C* (2019).
- [267] H.S. Al Qahtani, G.F. Metha, R.B. Walsh, V.B. Golovko, G.G. Andersson, T. Nakayama, Aggregation Behavior of Ligand-Protected Au₉ Clusters on Sputtered Atomic Layer Deposition TiO₂, *The Journal of Physical Chemistry C* 121 (2017) 10781-10789.
- [268] G. Li, L. Yang, Y. Jin, L. Zhang, Structural and optical properties of TiO₂ thin film and TiO₂+ 2 wt.% ZnFe₂O₄ composite film prepared by rf sputtering, *Thin Solid Films* 368 (2000) 163-167.
- [269] D. Rafieian, W. Ogieglo, T. Savenije, R.G.H. Lammertink, Controlled formation of anatase and rutile TiO₂ thin films by reactive magnetron sputtering, *AIP Advances* 5 (2015) 097168.
- [270] A.P. Singh, N. Kodan, B.R. Mehta, Enhancing the photoelectrochemical properties of titanium dioxide by thermal treatment in oxygen deficient environment, *Appl. Surf. Sci.* 372 (2016) 63-69.
- [271] U.I. Gaya, A.H. Abdullah, Heterogeneous photocatalytic degradation of organic contaminants over titanium dioxide: a review of fundamentals, progress and problems, *Journal of Photochemistry and Photobiology C: Photochemistry Reviews* 9 (2008) 1-12.
- [272] J.F. Moulder, W.F. Stickle, P.E. Sobol, K.D. Bomben, *Handbook of X-Ray Photoelectron Spectroscopy*, Physical Electronics, Inc., Eden Prairie, Minnesota 55344, United States of America, 1995.
- [273] A. Jain, S.P. Ong, G. Hautier, W. Chen, W.D. Richards, S. Dacek, S. Cholia, D. Gunter, D. Skinner, G. Ceder, K.A. Persson, Commentary: The Materials Project: A materials genome approach to accelerating materials innovation, *APL Materials* 1 (2013) 011002.
- [274] S.P. Ong, W.D. Richards, A. Jain, G. Hautier, M. Kocher, S. Cholia, D. Gunter, V.L. Chevrier, K.A. Persson, G. Ceder, Python Materials Genomics (pymatgen): A robust, open-source python library for materials analysis, *Computational Materials Science* 68 (2013) 314-319.
- [275] D. Briggs, M.P. Seah, *Practical Surface Analysis*, Macmillan Publishers Limited. All rights reserved, 1990.
- [276] T.L. Barr, S. Seal, Nature of the use of adventitious carbon as a binding energy standard, *Journal of Vacuum Science & Technology A* 13 (1995) 1239-1246.
- [277] Y. Brama, Y. Sun, S. Dangeti, M. Mujahid, Response of sputtered titanium films on silicon to thermal oxidation, *Surface and coatings technology* 195 (2005) 189-197.
- [278] G. Battaglin, G.D. Mea, G.D. Marchi, P. Mazzoldi, A. Miotello, M. Guglielmi, Field-assisted sodium migration in glasses during medium-energy proton irradiation, *Journal of Physics C: Solid State Physics* 15 (1982) 5623-5627.

- [279] R.A. Abbott, T.I. Kamins, Sodium migration through electron-gun evaporated Al₂O₃ and double layer Al₂O₃ · SiO₂ structures, *Solid-State Electronics* 13 (1970) 565-576.
- [280] S. Lee, G.W. Zajac, D.W. Goodman, A study of the electronic structure and reactivity of V/TiO₂(110) with metastable impact electron spectroscopy (MIES) and ultraviolet photoelectron spectroscopy (UPS), *Topics in Catalysis* 38 (2006) 127-132.
- [281] S. Wendt, P.T. Sprunger, E. Lira, G.K.H. Madsen, Z. Li, J.Ø. Hansen, J. Matthiesen, A. Blekinge-Rasmussen, E. Lægsgaard, B. Hammer, F. Besenbacher, The Role of Interstitial Sites in the Ti3d Defect State in the Band Gap of Titania, *Science* 320 (2008) 1755-1759.
- [282] S. Krischok, J. Schaefer, O. Höfft, V. Kempter, Lithium adsorption on TiO₂: studies with electron spectroscopies (MIES and UPS), *Surface and interface analysis* 37 (2005) 83-89.
- [283] S. Krischok, J. Günster, D.W. Goodman, O. Höfft, V. Kempter, MIES and UPS(Hel) studies on reduced TiO₂(110), *Surface and Interface Analysis* 37 (2005) 77-82.
- [284] S. Krischok, O. Höfft, V. Kempter, Interaction of alkali atoms with water multilayers adsorbed on TiO₂ (1 1 0): a study with MIES and UPS, *Surface science* 532 (2003) 370-376.
- [285] S. Krischok, J. Günster, D. Goodman, O. Höfft, V. Kempter, MIES and UPS (Hel) studies on reduced TiO₂ (110), *Surface and interface analysis* 37 (2005) 77-82.
- [286] T. Higaki, Q. Li, M. Zhou, S. Zhao, Y. Li, S. Li, R. Jin, Toward the Tailoring Chemistry of Metal Nanoclusters for Enhancing Functionalities, *Accounts of Chemical Research* 51 (2018) 2764-2773.
- [287] Y. Negishi, Y. Matsuura, R. Tomizawa, W. Kurashige, Y. Niihori, T. Takayama, A. Iwase, A. Kudo, Controlled Loading of Small Au_n Clusters (n= 10–39) onto BaLa₄Ti₄O₁₅ Photocatalysts: Toward an Understanding of Size Effect of Cocatalyst on Water-Splitting Photocatalytic Activity, *The Journal of Physical Chemistry C* 119 (2015) 11224-11232.
- [288] T. Bernhardt, U. Heiz, U. Landman, Chemical and Catalytic Properties of Size-Selected Free and Supported Clusters, *Nanocatalysis*, Springer2007, pp. 1-191.
- [289] Y. Negishi, Y. Matsuura, R. Tomizawa, W. Kurashige, Y. Niihori, T. Takayama, A. Iwase, A. Kudo, Controlled loading of small Au_n clusters (n = 10-39) onto BaLa₄Ti₄O₁₅ photocatalysts: Toward an understanding of size effect of cocatalyst on water-splitting photocatalytic activity, *J. Phys. Chem. C* 119 (2015) 11224-11432.
- [290] W. Kurashige, R. Kumazawa, D. Ishii, R. Hayashi, Y. Niihori, S. Hossain, L.V. Nair, T. Takayama, A. Iwase, S. Yamazoe, Au₂₅-Loaded BaLa₄Ti₄O₁₅ Water-Splitting Photocatalyst with Enhanced Activity and Durability Produced Using New Chromium Oxide Shell Formation Method, *The Journal of Physical Chemistry C* 122 (2018) 13669-13681.
- [291] W. Li, Q. Ge, X. Ma, Y. Chen, M. Zhu, H. Xu, R. Jin, Mild Activation of CeO₂-Supported Gold Nanoclusters and Insight into the Catalytic Behavior in CO Oxidation, *Nanoscale* 8 (2016) 2378-2385.
- [292] B.C. Gates, Supported gold catalysts: new properties offered by nanometer and sub-nanometer structures, *Chemical communications* 49 (2013) 7876-7877.
- [293] W.E. Kaden, T. Wu, W.A. Kunkel, S.L. Anderson, Electronic structure controls reactivity of size-selected Pd clusters adsorbed on TiO₂ surfaces, *Science* 326 (2009) 826-829.
- [294] D.M. Foster, R. Ferrando, R.E. Palmer, Experimental Determination of the Energy Difference Between Competing Isomers of Deposited, Size-Selected Gold Nanoclusters, *Nature Communications* 9 (2018) 1323.
- [295] T. Bennett, R.H. Adnan, J.F. Alvino, R. Kler, V.B. Golovko, G.F. Metha, G.G. Andersson, Effect of Gold Nanoclusters on the Production of Ti³⁺ Defect Sites in Titanium Dioxide Nanoparticles under Ultraviolet and Soft X-ray Radiation, *The Journal of Physical Chemistry C* 119 (2015) 11171-11177.
- [296] S. Krumdieck, Pulsed-Pressure MOCVD Science, Materials and Technology, *ECS Transactions* 25 (2009) 1209-1219.
- [297] H.M. Cave, S.P. Krumdieck, M.C. Jermy, Development of a Model for High Precursor Conversion Efficiency Pulsed-Pressure Chemical Vapor Deposition (PP-CVD) Processing, *Chemical Engineering Journal* 135 (2008) 120-128.
- [298] J.-Y. Ruzicka, F. Abu Bakar, C. Hoeck, R. Adnan, C. McNicoll, T. Kemmitt, B.C. Cowie, G.F. Metha, G.G. Andersson, V.B. Golovko, Toward Control of Gold Cluster Aggregation on TiO₂ via Surface Treatments, *The Journal of Physical Chemistry C* 119 (2015) 24465-24474.
- [299] F. Ostendorf, C. Schmitz, S. Hirth, A. Kühnle, J.J. Kolodziej, M. Reichling, How Flat is an Air-Cleaved Mica Surface?, *Nanotechnology* 19 (2008) 305705.

- [300] J. Mayer, U. Diebold, T. Madey, E. Garfunkel, Titanium and Reduced Titania Overlayers on Titanium Dioxide (110), *Journal of Electron Spectroscopy and Related Phenomena* 73 (1995) 1-11.
- [301] R.G. Acres, A.V. Ellis, J. Alvino, C.E. Lenahan, D.A. Khodakov, G.F. Metha, G.G. Andersson, Molecular Structure of 3-Aminopropyltriethoxysilane Layers Formed on Silanol-Terminated Silicon Surfaces, *The Journal of Physical Chemistry C* 116 (2012) 6289-6297.
- [302] H.S. Al Qahtani, R. Higuchi, T. Sasaki, J.F. Alvino, G.F. Metha, V.B. Golovko, R. Adnan, G.G. Andersson, T. Nakayama, Grouping and aggregation of ligand protected Au 9 clusters on TiO₂ nanosheets, *RSC Advances* 6 (2016) 110765-110774.
- [303] D.F. Dever, A. Finch, E. Grunwald, The Vapor Pressure of Methanol, *The Journal of Physical Chemistry* 59 (1955) 668-669.
- [304] D.R. Lide, *CRC Handbook of Chemistry and Physics*, 86th Edition, Taylor & Francis 2005.
- [305] R. Boichot, S. Krumdieck, Numerical Modeling of the Droplet Vaporization for Design and Operation of Liquid-pulsed CVD Chemical Vapor Deposition 21 (2015) 375-384.
- [306] P. Kunwar, J. Hassinen, G. Bautista, R.H.A. Ras, J. Toivonen, Direct Laser Writing of Photostable Fluorescent Silver Nanoclusters in Polymer Films, *ACS Nano* 8 (2014) 11165-11171.
- [307] L. Shang, J. Xu, G.U. Nienhaus, Recent advances in synthesizing metal nanocluster-based nanocomposites for application in sensing, imaging and catalysis, *Nano Today* 28 (2019) 100767.
- [308] G. Li, R. Jin, Atomically Precise Gold Nanoclusters as New Model Catalysts, *Acc. Chem. Res.* 46 (2013) 1749-1758.
- [309] J.F. Alvino, T. Bennett, D. Anderson, B. Donoeva, D. Ovoshchnikov, R.H. Adnan, D. Appadoo, V. Golovko, G. Andersson, G.F. Metha, Far-infrared absorption spectra of synthetically-prepared, ligated metal clusters with Au₆, Au₈, Au₉ and Au₆Pd metal cores, *RSC Advances* 3 (2013) 22140-22149.
- [310] A. Kulkarni, R.J. Lobo-Lapidus, B.C. Gates, Metal clusters on supports: synthesis, structure, reactivity, and catalytic properties, *Chemical communications* 46 (2010) 5997.
- [311] M.A. Duncan, *Journal of Cluster Science* 8 (1997) 239-266.
- [312] H. Himeno, K. Miyajima, T. Yasuike, F. Mafuné, Gas Phase Synthesis of Au Clusters Deposited on Titanium Oxide Clusters and Their Reactivity with CO Molecules, *The Journal of Physical Chemistry A* 115 (2011) 11479-11485.
- [313] P. Grammatikopoulos, S. Steinhauer, J. Vernieres, V. Singh, M. Sowwan, Nanoparticle design by gas-phase synthesis, *Advances in Physics: X* 1 (2016) 81-100.
- [314] X. Zhao, J. Hrbek, J. Rodriguez, The decomposition and chemistry of Ru₃(CO)₁₂ on TiO₂(110) studied with X-ray photoelectron spectroscopy and temperature programmed desorption, *Surface Science* 575 (2005) 115-124.
- [315] Q. Tang, G. Hu, V. Fung, D.-e. Jiang, Insights into Interfaces, Stability, Electronic Properties, and Catalytic Activities of Atomically Precise Metal Nanoclusters from First Principles, *Acc. Chem. Res.* 51 (2018) 2793-2802.
- [316] K. Basu, S. Paul, R. Jana, A. Datta, A. Banerjee, Red-Emitting Copper Nanoclusters: From Bulk-Scale Synthesis to Catalytic Reduction, *ACS Sustainable Chemistry & Engineering* 7 (2019) 1998-2007.
- [317] R.W. Joyner, J.B. Pendry, D.K. Saldin, S.R. Tennison, Metal-support interactions in heterogeneous catalysis, *Surface science* 138 (1984) 84-94.
- [318] M. Valero, P. Raybaud, P. Sautet, Interplay between molecular adsorption and metal-support interaction for small supported metal clusters: CO and C₂H₄ adsorption on Pd₄/γPd₄/γ-Al₂O₃, *Journal of Catalysis* 247 (2007) 339-355.
- [319] W. Guo, J. Zou, B. Guo, J. Xiong, C. Liu, Z. Xie, L. Wu, Pd nanoclusters/TiO₂(B) nanosheets with surface defects toward rapid photocatalytic dehalogenation of polyhalogenated biphenyls under visible light, *Applied Catalysis B: Environmental* 277 (2020) 119255.
- [320] X.Y. Liu, A. Wang, T. Zhang, C.-Y. Mou, Catalysis by gold: New insights into the support effect, *Nano Today* 8 (2013) 403-416.
- [321] U. Diebold, The surface science of titanium dioxide, *Surface Science Reports* 48 (2003) 53-229.
- [322] E. Wahlström, N. Lopez, R. Schaub, P. Thostrup, A. Rønnau, C. Africh, E. Lægsgaard, J.K. Nørskov, F. Besenbacher, Bonding of Gold Nanoclusters to Oxygen Vacancies on RutileTiO₂(110), *Physical Review Letters* 90 (2003).

- [323] G. Krishnan, H.S. Al Qahtani, J. Li, Y. Yin, N. Eom, V.B. Golovko, G.F. Metha, G.G. Andersson, Investigation of Ligand-Stabilized Gold Clusters on Defect-Rich Titania, *The Journal of Physical Chemistry C* 121 (2017) 28007-28016.
- [324] J. Daughtry, G.G. Andersson, G.F. Metha, S. Tesana, T. Nakayama, Sub-monolayer Au 9 cluster formation via pulsed nozzle cluster deposition, *Nanoscale Advances* 2 (2020) 4051-4061.
- [325] J. Daughtry, A.S. Alotabi, L. Howard-Fabretto, G.G. Andersson, Composition and properties of RF-sputter deposited titanium dioxide thin films, *Nanoscale Advances* 3 (2021) 1077-1086.
- [326] H. Morgner, The characterization of liquid and solid surfaces with metastable helium atoms, *Advances in atomic, molecular, and optical physics* 42 (2000) 387-488.
- [327] J.Y. Ruzicka, F. Abu Bakar, C. Hoeck, R. Adnan, C. McNicoll, T. Kemmitt, B.C. Cowie, G.F. Metha, G.G. Andersson, V.B. Golovko, Toward Control of Gold Cluster Aggregation on TiO₂ via Surface Treatments, *J. Phys. Chem. C* 119 (2015) 24465-24474.
- [328] D.P. Anderson, R.H. Adnan, J.F. Alvino, O. Shipper, B. Donoeva, J.-Y. Ruzicka, H. Al Qahtani, H.H. Harris, B. Cowie, J.B. Aitken, V.B. Golovko, G.F. Metha, G.G. Andersson, Chemically synthesised atomically precise gold clusters deposited and activated on titania. Part II, *Phys. Chem. Chem. Phys.* 15 (2013) 14806-14813.
- [329] G. Daniel, Electron Mean Free Path in Elemental Metals, *Journal of Applied Physics* 119 (2016) 085101.
- [330] B.A. Chambers, C. Neumann, A. Turchanin, C.T. Gibson, G.G. Andersson, The Direct Measurement of the Electronic Density of States of Graphene using Metastable Induced Electron Spectroscopy, *2D Materials* 4 (2017) 025068.
- [331] S. Krischok, O. Höfft, J. Gunster, J. Stultz, D. W. Goodman, V. Kempter, H₂O Interaction with Bare and Li-Precovered TiO₂: Studies with Electron-Spectroscopy (MIES and UPS HEI and HEII), *Surface Science* 495 (2001) 8-18.
- [332] G. Beamson, D. Briggs, High Resolution XPS of Organic Polymers: The Scienta ESCA300 Database, Wiley 1992.
- [333] H. Onishi, C. Egawa, T. Aruga, Y. Iwasawa, Adsorption of Na atoms and oxygen-containing molecules on MgO(100) and (111) surfaces, *Surface Science* 191 (1987) 479-491.
- [334] T. Hanawa, M. Ota, Calcium phosphate naturally formed on titanium in electrolyte solution, *Biomaterials* 12 (1991) 767-774.
- [335] R.P. Netterfield, P.J. Martin, C.G. Pacey, W.G. Sainy, D.R. McKenzie, G. Auchterlonie, Ion-assisted deposition of mixed TiO₂-SiO₂ films, *Journal of Applied Physics* 66 (1989) 1805-1809.
- [336] C. Battistoni, G. Mattogno, D.M.P. Mingos, Characterization of some gold cluster compounds by X-Ray photoelectron spectroscopy, *Journal of Electron Spectroscopy and Related Phenomena* 33 (1984) 107-113.
- [337] D.M. Laurent, X. Fengting, G.N. Ralph, C.Y. Judith, Preparation of TiO₂-supported Au nanoparticle catalysts from a Au₁₃ cluster precursor: Ligand removal using ozone exposure versus a rapid thermal treatment, *Journal of Catalysis* 243 (2006) 64-73.
- [338] J.J. Pireaux, M. Chtaïb, J.P. Delrue, P.A. Thiry, M. Liehr, R. Caudano, Electron spectroscopic characterization of oxygen adsorption on gold surfaces: I. Substrate impurity effects on molecular oxygen adsorption in ultra high vacuum, *Surface Science* 141 (1984) 211-220.
- [339] M. Marschewski, C. Otto, L. Wegewitz, O. Höfft, A. Schmidt, W. Maus-Friedrichs, Adsorption analysis of thin films of terephthalic acid on Au and Al studied by MIES, UPS and XPS, *Applied Surface Science* 339 (2015) 9-14.
- [340] G.G. Andersson, V.B. Golovko, J.F. Alvino, T. Bennett, O. Wrede, S.M. Mejia, H.S.A. Qahtani, R. Adnan, N. Gunby, D.P. Anderson, G.F. Metha, Phosphine-stabilised Au₉ clusters interacting with titania and silica surfaces: The first evidence for the density of states signature of the support-immobilised cluster, *The Journal of Chemical Physics* 141 (2014) 014702.
- [341] S.-H. Yoo, N. Siemer, M. Todorova, D. Marx, J. Neugebauer, Deciphering Charge Transfer and Electronic Polarization Effects at Gold Nanocatalysts on Reduced Titania Support, *The Journal of Physical Chemistry C* 123 (2019) 5495-5506.
- [342] N. Saadatjou, A. Jafari, S. Sahebdehfar, Ruthenium Nanocatalysts for Ammonia Synthesis: A Review, *Chemical Engineering Communications* 202 (2015) 420-448.
- [343] H. Hu, J.H. Xin, H. Hu, X. Wang, D. Miao, Y. Liu, Synthesis and stabilization of metal nanocatalysts for reduction reactions – a review, *Journal of Materials Chemistry A* 3 (2015) 11157-11182.

- [344] Z. Xi, D.P. Erdosy, A. Mendoza-Garcia, P.N. Duchesne, J. Li, M. Muzzio, Q. Li, P. Zhang, S. Sun, Pd nanoparticles coupled to WO₂. 72 nanorods for enhanced electrochemical oxidation of formic acid, *Nano letters* 17 (2017) 2727-2731.
- [345] S.B. Somvanshi, S.B. Somvanshi, P.B. Kharat, Nanocatalyst: A Brief Review on Synthesis to Applications, *Journal of Physics: Conference Series* 1644 (2020) 012046.
- [346] J. Yang, B. Chen, X. Liu, W. Liu, Z. Li, J. Dong, W. Chen, W. Yan, T. Yao, X. Duan, Efficient and robust hydrogen evolution: phosphorus nitride imide nanotubes as supports for anchoring single ruthenium sites, *Angewandte Chemie* 130 (2018) 9639-9644.
- [347] L. Howard-Fabretto, G.G. Andersson, Metal clusters on semiconductor surfaces and application in catalysis with a focus on Au and Ru, *Advanced Materials* 32 (2020) 1904122.
- [348] U. Landman, W. Luedtke, Small is different: energetic, structural, thermal, and mechanical properties of passivated nanocluster assemblies, *Faraday discussions* 125 (2004) 1-22.
- [349] F. Wang, Y. Wang, Y.-H. Liu, P.J. Morrison, R.A. Loomis, W.E. Buhro, Two-dimensional semiconductor nanocrystals: properties, templated formation, and magic-size nanocluster intermediates, *Accounts of chemical research* 48 (2015) 13-21.
- [350] C.M. Aikens, R. Jin, X. Roy, T. Tsukuda, From atom-precise nanoclusters to superatom materials, AIP Publishing LLC, 2022, pp. 170401.
- [351] J. Liu, D. Cao, H. Xu, D. Cheng, From double-atom catalysts to single-cluster catalysts: A new frontier in heterogeneous catalysis, *Nano Select* 2 (2021) 251-270.
- [352] M.O.J. Jäger, E.V. Morooka, F. Federici Canova, L. Himanen, A.S. Foster, Machine learning hydrogen adsorption on nanoclusters through structural descriptors, *npj Computational Materials* 4 (2018) 37.
- [353] J.C. Burgos, S.M. Mejía, G.F. Metha, Effect of Charge and Phosphine Ligands on the Electronic Structure of the Au₈ Cluster, *ACS Omega* 4 (2019) 9169-9180.
- [354] V.Q. Vuong, J.M.L. Madrdejós, B. Aradi, B.G. Sumpter, G.F. Metha, S. Irle, Density-functional tight-binding for phosphine-stabilized nanoscale gold clusters, *Chemical Science* 11 (2020) 13113-13128.
- [355] R. Jin, G. Li, S. Sharma, Y. Li, X. Du, Toward Active-Site Tailoring in Heterogeneous Catalysis by Atomically Precise Metal Nanoclusters with Crystallographic Structures, *Chemical Reviews* 121 (2021) 567-648.
- [356] H. Mousavi, Y. Yin, L. Howard-Fabretto, S.K. Sharma, V. Golovko, G.G. Andersson, C.J. Shearer, G.F. Metha, Au₁₀₁-rGO nanocomposite: immobilization of phosphine-protected gold nanoclusters on reduced graphene oxide without aggregation, *Nanoscale Advances* 3 (2021) 1422-1430.
- [357] L. Howard-Fabretto, Spectroscopic studies of size-selected Ru and Pt clusters on Titania, Flinders University, College of Science and Engineering, 2021.
- [358] L. Howard-Fabretto, T.J. Gorey, G. Li, S. Tesana, G.F. Metha, S.L. Anderson, G.G. Andersson, Encapsulation of Size-Selected Ru₃ Clusters into RF-Deposited TiO₂, *American Chemical Society (ACS)*, 2022.
- [359] O.M.E. Ylivaara, A. Langner, X. Liu, D. Schneider, J. Julin, K. Arstila, S. Sintonen, S. Ali, H. Lipsanen, T. Sajavaara, S.-P. Hannula, R.L. Puurunen, Mechanical and optical properties of as-grown and thermally annealed titanium dioxide from titanium tetrachloride and water by atomic layer deposition, *Thin Solid Films* 732 (2021) 138758.
- [360] N.K. Chaki, S.G. Sudrik, H.R. Sonawane, K. Vijayamohanan, Single phase preparation of monodispersed silver nanoclusters using a unique electron transfer and cluster stabilising agent, triethylamine, *Chemical communications* (2002) 76-77.
- [361] L. Howard-Fabretto, T.J. Gorey, G. Li, S. Tesana, G.F. Metha, S.L. Anderson, G.G. Andersson, The interaction of size-selected Ru₃ clusters with RF-deposited TiO₂: probing Ru-CO binding sites with CO-temperature programmed desorption, *Nanoscale Advances* 3 (2021) 3537-3553.
- [362] D. Chandra, M.L. Garner, K.H. Lau, Vapor pressures of osmium, rhodium, and ruthenium carbonyls, *Journal of Phase Equilibria* 20 (1999) 565-572.
- [363] J. Daughtry, G.G. Andersson, G.F. Metha, S. Tesana, T. Nakayama, Sub-monolayer Au₉ cluster formation via pulsed nozzle cluster deposition, *Nanoscale Advances* 2 (2020) 4051-4061.
- [364] R.B. Walsh, A. Nelson, W.M. Skinner, D. Parsons, V.S. Craig, Direct measurement of van der Waals and diffuse double-layer forces between titanium dioxide surfaces produced by atomic layer deposition, *The Journal of Physical Chemistry C* 116 (2012) 7838-7847.

- [365] L. Howard-Fabretto, T.J. Gorey, G. Li, S. Tesana, G.F. Metha, S.L. Anderson, G.G. Andersson, The interaction of size-selected Ru 3 clusters with RF-deposited TiO 2: probing Ru–CO binding sites with CO-temperature programmed desorption, *Nanoscale Advances* (2021).
- [366] D. Chandra, M. Garner, K. Lau, Vapor pressures of osmium, rhodium, and ruthenium carbonyls, *Journal of phase equilibria* 20 (1999) 565-572.
- [367] M.C. Biesinger, B.P. Payne, A.P. Grosvenor, L.W.M. Lau, A.R. Gerson, R.S.C. Smart, Resolving surface chemical states in XPS analysis of first row transition metals, oxides and hydroxides: Cr, Mn, Fe, Co and Ni, *Appl. Surf. Sci.* 257 (2011) 2717-2730.
- [368] D.J. Miller, M.C. Biesinger, N.S. McIntyre, Interactions of CO₂ and CO at fractional atmosphere pressures with iron and iron oxide surfaces: one possible mechanism for surface contamination?, *Surface and Interface Analysis* 33 (2002) 299-305.
- [369] D.J. Morgan, Resolving ruthenium: XPS studies of common ruthenium materials, *Surface and Interface Analysis* 47 (2015) 1072-1079.
- [370] Y.J. Kim, Y. Gao, S.A. Chambers, Core-level X-ray photoelectron spectra and X-ray photoelectron diffraction of RuO₂ (110) grown by molecular beam epitaxy on TiO₂ (110), *Appl. Surf. Sci.* 120 (1997) 250-260.
- [371] J. Riga, C. Tenret-Noel, J.-J. Pireaux, R. Caudano, J. Verbist, Y. Gobillon, Electronic structure of rutile oxides TiO₂, RuO₂ and IrO₂ studied by X-ray photoelectron spectroscopy, *Physica Scripta* 16 (1977) 351.
- [372] D.R.G. Mitchell, G. Triani, Z. Zhang, Hydrothermal crystallization of amorphous titania films deposited using low temperature atomic layer deposition, *Thin Solid Films* 516 (2008) 8414-8423.
- [373] K. Miyajima, F. Mafuné, Thermal decomposition of triruthenium dodecacarbonyl investigated by variable-temperature mass spectrometry in the gas phase, *Chemical Physics Letters* 786 (2022) 139191.
- [374] P.W. James Keeler, *Chemical Structure and Reactivity: An Integrated Approach*, 2nd Edition ed., Oxford University Press, Oxford, UK, 2013.
- [375] D.C. Meier, G.A. Rizzi, G. Granozzi, X. Lai, D.W. Goodman, Ru 3 (CO) 12 Adsorption and Decomposition on TiO 2, *Langmuir : the ACS journal of surfaces and colloids* (2002).